

FLUORESCENCE-BASED
HIGH-RESOLUTION TRACKING OF
NANOPARTICLES

Von der
UNIVERSITÄT BAYREUTH
zur Erlangung des Grades eines
DOKTORS DER NATURWISSENSCHAFTEN
(Dr. rer. nat.)
genehmigte Abhandlung

von
DANIEL ZALAMI
geboren in Tönisvorst

1. Gutachter: Prof. Jürgen Köhler
2. Gutachter: Prof. Matthias Weiss

Tag der Einreichung: 06.05.2021
Tag des Kolloquiums: 05.11.2021

ABSTRACT / KURZDARSTELLUNG

ENGLISH

High-precision tracking of nanoparticles via fluorescence-optical methods is a current research area with many applications. While optical methods are usually characterized by causing minimal damage to the sample, their ability to resolve the sample spatially is limited. Therefore, many modern measurement methods make use of tricks to circumvent the diffraction limit and to obtain information at the nanometer scale.

In this dissertation, a fluorescence optical method for tracking single nanoparticles, called single-particle orbit tracking (SPOT), is further developed, investigated, and applied. One focus of those new developments was to update the existing experimental setup so that three-dimensional localization can take place instead of only two-dimensional tracking. Another important point of improvement was the extension of the control logic to include additional parameters and signals. The required technical modifications demanded a renewed mathematical modeling of the method, as well as analysis of the measurement errors and setup performance. While the temporal resolution of the experimental setup could be improved, an axial localization of the particles was only achievable at the expense of the accuracy in the lateral direction.

Reference samples were used to experimentally validate the upgraded technique and to point out existing issues. A major problem in the application of SPOT lies in measurement artifacts, which can, for example, mask existing anomalies in the diffusion behavior of the tracked nanoparticles and would lead to misinterpretations in unknown systems. Parameter studies with variation of easily accessible quantities, such as the solvent viscosity, the particle size or the considered time scales, offer possible remedies and concurrently show the importance of reference systems.

A new field of research is the investigation of the diffusion behavior of nanoparticles in complex filter materials. In this work, SPOT was used to study nanoparticles in a nanoporous triblock terpolymer-based membrane. Using conventional methods, the non-destructive characterization of such a system at room-temperature and in a liquid-filled state, is a great challenge. With SPOT, however, the size distribution of the voids could be determined non-invasively. For this purpose, nanometer-sized polymer particles were tracked during their thermal movement through the pore structure of the filter material. At the same time, indications of a suitable statistical model for the description of the particle motion were collected. Theoretical parameters for normal and anomalous diffusion in harmonic potentials were explicitly compared with experimentally determined values. It was shown that the particle motion can be described mainly by confined Brownian motion, but there exists a weak influence of anomalous diffusion components, which can be best described by the so-called *fractional Langevin equation*.

DEUTSCH

Die hochpräzise Nachverfolgung von Nanopartikeln mittels fluoreszenzoptischer Verfahren ist ein aktuelles Forschungsgebiet mit vielen Anwendungsbereichen. Während optische Verfahren sich meist dadurch auszeichnen, der Probe nur wenig zu schaden, so ist ihr räumliches Auflösungsvermögen begrenzt. Viele moderne Messmethoden bedienen sich daher Tricks, um die Beugungsgrenze zu umgehen, um dennoch Informationen auf der Nanometerskala zu gewinnen.

In dieser Dissertation wird eine fluoreszenzoptische Methode zur Verfolgung einzelner Nanopartikel, das sogenannte *single-particle orbit tracking* (SPOT), weiterentwickelt, näher untersucht und angewendet. Ein Schwerpunkt der Weiterentwicklung bestand darin, den bestehenden Versuchsaufbau derart zu modifizieren, sodass statt einer lediglich zweidimensionalen Nachverfolgung eine dreidimensionale Lokalisierung stattfinden kann. Eine weitere wichtige Verbesserung war die Erweiterung der Steuerungslogik um weitere Kenngrößen und Signale. Die erforderlichen technischen Modifikationen machten eine erneute mathematische Modellierung der Methode, sowie Analyse der Messfehler und Leistungsfähigkeit des Aufbaus notwendig. Während die zeitliche Auflösung verbessert werden konnte, so wurde eine axiale Lokalisierung der Teilchen nur auf Kosten der Genauigkeit in lateraler Richtung erreicht.

Anhand von Referenzproben wurde eine experimentelle Validierung der weiterentwickelten Technik durchgeführt und auf bestehende Probleme hingewiesen, bevor die Methode auf unbekannte Systeme angewendet wurde. Ein großes Problem in der Anwendung von SPOT, stellen Messartefakte dar, die beispielsweise vorliegende Anomalien im Diffusionsverhalten der verfolgten Nanopartikel überdecken können und bei unbekanntem Systemen zu Fehlinterpretationen führen würden. Parameterstudien mit Variation von leicht zugänglichen Größen, wie der Lösungsmittelviskosität, der Teilchengröße oder der betrachteten Zeitskalen, bieten Lösungsansätze und zeigen gleichzeitig die Wichtigkeit von Referenzsystemen auf.

Ein aktives Forschungsfeld ist die Untersuchung des Diffusionsverhaltens von Nanopartikeln in komplexen Filtermaterialien. In dieser Arbeit wurden mithilfe von SPOT Nanopartikel in einer nanoporösen Triblock Terpolymer-basierte Membran untersucht. Bei der Verwendung herkömmlicher Methoden stellt die zerstörungsfreie Charakterisierung eines solchen Systems bei Raumtemperatur und in flüssigkeitsgefülltem Zustand eine große Herausforderung dar. Mit SPOT konnte jedoch die Größenverteilung der Hohlräume auf nicht-invasive Art und Weise ermittelt werden. Hierzu wurden nanometergroße Polymerpartikel bei ihrer thermischen Bewegung durch die Porenstruktur des Filtermaterials verfolgt. Gleichzeitig konnten Indizien für ein passendes statistisches Modell zur Beschreibung der Teilchenbewegung gesammelt werden. Explizit wurden theoretische Kenngrößen für normale und anomale Diffusion in harmonischen Potentialen mit experimentell ermittelten Werten verglichen. Hierbei zeigte sich, dass die Teilchenbewegung zwar hauptsächlich durch eingeschränkte Brownsche Bewegung beschrieben wird, es jedoch einen kleineren Einfluss anomaler Diffusionskomponenten geben kann, der am besten mit der sogenannten *Fractional Langevin Equation* beschrieben wird.

CONTENTS

I	Main	1
1	Introduction	3
1.1	Single-particle tracking	5
1.2	State-of-the-art in active single-particle tracking	6
1.3	Challenges in the characterization of nanoporous filter materials	10
2	Nanoparticle diffusion	13
2.1	Brownian motion	13
2.2	Diffusion equation	16
2.3	Mean squared displacement	17
2.4	Anomalous diffusion	18
2.5	Confined diffusion	19
3	Method	23
3.1	Position-sensitive fluorescence rate modulation	24
3.2	Demodulation of the detected photon trace	26
3.3	Feedback controller	28
3.4	Trajectory reconstruction and analysis	31
4	Experimental setup	33
4.1	Optical setup	33
4.2	Nanopositioning stage	35
4.3	Setup controller	35
4.4	Comments about the setup	35
5	Materials	37
5.1	Fluorescent probes	37
5.2	Nanoporous triblock terpolymer membranes	41
5.3	Sample preparation	42
5.3.1	Nanoparticle suspensions for reference experiments	42
5.3.2	Polymer membranes infused with nanoparticle suspensions	43
6	Errors, limitations and artifacts	45
6.1	Beam scan path optimization	47
6.2	Localization error	50
6.2.1	Photon counting noise	52
6.2.2	Systematic localization error	53

6.2.3	Dynamic localization error	57
6.3	Tracking error	58
6.3.1	Localization errors induced tracking error	59
6.3.2	Stage vibration induced tracking error	61
6.4	Mean squared displacement in a feedback system	63
6.4.1	Oscillator driven by Brownian motion and measurement noise	65
6.4.2	Modeling of the simulated mean squared displacement	66
7	Reference experiments	69
7.1	Dynamic viscosities of different aqueous solutions	71
7.2	Anomaly detection	73
7.3	Conclusions from the reference experiments	77
8	Diffusion behavior of nanoparticles in complex filtration media	79
8.1	Preliminary work	79
8.2	Morphology inspection by environmental scanning electron microscopy	81
8.3	3D-SPOT within the porous bulk structure of the polymer membranes	83
8.4	Accessible void space distribution	85
8.5	Diffusion characteristics	87
8.6	Discussion of the 3D-SPOT experiments on complex filtration materials	94
9	Extensions of SPOT: Proof-of-concept experiments	95
9.1	Confined-space imaging with SPOT	95
9.2	Dual-Color 3D-SPOT	96
9.3	Fluorescence lifetime 3D-SPOT	101
10	Summary and outlook	103
II	Appendix	105
A	System theory and control systems	107
A.1	State-space formalism	107
A.2	Transfer function matrix formalism	109
A.3	System modeling of a driven oscillator	110
A.4	System identification	111
A.4.1	Unit impulse response (matrix)	111
A.4.2	Unit step response (matrix)	112
A.4.3	Frequency response (matrix)	112
A.5	Controller canonical form	113
A.6	Linear time-invariant discrete-time systems	114
A.7	Control systems	115
A.7.1	Full state feedback	115
A.7.2	Feedback based on the systems output	116
A.7.3	PID Controller	116
A.8	White noise in dynamical systems	118
B	Anomalous diffusion models	121
B.1	Continuous-time random walk	121

B.2	Fractional Brownian motion	123
B.3	Fractional Langevin equation	124
C	Methodological details	127
C.1	Molecule detection efficiency function	127
C.2	Statistical properties of the position estimator	128
C.3	Demodulation on a digital signal processor	135
C.4	Mean squared displacement computation based on fast Fourier transformation	136
C.5	Simulation of the 3D-SPOT method	136
C.6	Simulation of Brownian motion inside a sphere with hard walls	139
D	Technical details	141
D.1	Optical setup	141
D.2	Acusto optical deflector	143
D.3	Ray transfer matrix analysis	144
D.4	Nanopositioning stage	149
D.5	System identification of the nanopositioning stage-stage controller	151
D.6	ADwin	154
D.7	Software	156
D.8	Example of a SPOT measurement file	158
E	Supporting measurements	161
E.1	Rolling-ball viscometry	161
E.2	Refractive index matching	162
E.3	Environmental scanning electron microscope micrographs	164
E.4	2C3D-SPOT trajectories	167
	Abbreviations, symbols and conventions	169
	Bibliography	175

PART I | MAIN

1 | INTRODUCTION

In every breath, every drink, or every meal, a large number of nanometer-sized particles is taken up into our body. Even by touching things, nanoparticles can penetrate our organism, our cells. Skin, lungs, or the gastrointestinal tract are constantly exposed to the environment and the most likely entry points for those foreign substances. After entering the circulatory and lymphatic system, the particles may distribute in the entire body tissue and organs. Even if the vast majority causes little or no health effects, some intruders will occasionally cause appreciable harm to the organism depending on their composition and size.[1]

On earth, nanoparticles are produced by many natural processes like photochemical reactions, volcanic eruptions, fires, or erosion. But also extraterrestrial dust and living organisms (e.g., shedding of skin) are sources of nanoparticles. Moreover, some living beings are "nanoparticles" themselves, like bacteria and viruses, causing diseases like influenza[2], the acquired immunodeficiency syndrome[3], kidney stones[4], the severe acquired respiratory syndrome[5], or cervical cancer[6]. In particular, viruses appear as villainous intruders as they can exploit cellular processes to replicate themselves. However, also non-biological particles show toxic effects on cellular functions such as proliferation or metabolism.

While nature has been generating nanoparticles since the beginning of time, technology has only learned its intentional synthesis and use in modern times. While the proportion of human-made nanomaterials is steadily growing[7, 8], science still has many unanswered questions about the influences of nanometer-sized substances and the pathways they take.

This is for the reason that the nanometer scale is both rewarding and challenging at the same time. It corresponds approximately to the size of larger molecules, in particular proteins, those functional units that operate cell biology. But the scale is smaller than the length scale that can be resolved with light microscopy. Consequently, the complex mechanisms that underlie the essence of life remain hidden from direct observation.

Nowadays, this is no longer true. Modern microscopic techniques have opened up the sub-diffraction limit length scale with tricky detours and ingenious concepts. There are numerous examples that show how the diffraction limit can be circumvented, and nanoscopic effects can be studied. In the following, several of those examples will be introduced containing the method of *single-particle orbit tracking* (SPOT) that is central to this thesis.

Highlighted techniques, that circumvent the Abbe limit [9, 10] are *photoactivated localization microscopy* (PALM)[11], *stochastic optical reconstruction microscopy* (STORM)[12], *stimulated-emission-depletion* (STED)[13], or *reversible saturable/switchable optical (fluorescence) transitions* (RESOLFT)[14]. Those methods do not obey the diffraction limit anymore as they are driven by single-molecule/particle detection or the depletion of fluorescent states in a particular region. The new limitation is essentially the number of photons collected and the noise inherent to the detection process. Consequently, it is fair to call those microscopic techniques noise-limited. Very recent progress was achieved in

the research group of STEFAN W. HELL. They enhanced the resolution limit to 1 nm by (*minimal emission flux microscopy* (MINFLUX)[15], a method that is based on the absence of photons and will be explained in more detail in section 1.2. However, there are also more established methods that uncover dynamics below the length scale of the diffraction limit.

For example, measuring the efficiency of *fluorescence resonance energy transfer* (FRET) between two chromophores can resolve inter-chromophore distances with nanometer accuracy. The energy transfer can be recorded as a function of time and on the single-molecule level, but the method provides only relative positions. Moreover, there are special requirements for the spectral properties of the chromophores and, in practice, only a few molecule combinations, so-called "FRET-pairs", are relevant.

Another prevalent method is the *fluorescence correlation spectroscopy* (FCS). It is based on the acquisition of a fluctuating fluorescence signal that is (auto)correlated for further analysis. This kind of mathematical signal analysis reveals the time scale of the processes that are the source of the fluctuations. FCS was introduced in 1972 by MADGE, ELSON, and WEBB for an experiment, where the chemical reaction rates of DNA-drug intercalation was reported.[16] The application of this technique was immediately extended in a series of publications so that it served to determine particle concentrations and to calculate translational and rotational mobility.[17–20] However, FCS is not restricted to these origins of fluorescence fluctuations. It is sensitive to every process that causes temporal variations in the photon counting statistics, like blinking, bleaching, triplet-state dynamics, energy transfer or photon antibunching.[21–23] Usually, the spatial resolution of FCS is diffraction-limited, and it is often doubted whether this is a one-particle method in the strict sense because only the dynamics of ensemble means of one-particle movements are accessible. But the FCS-type of analysis can be applied to signals recorded with other methods like STED[24], *near-field scanning optical microscopy* (NSOM)[25], and *super-resolution optical fluctuation imaging* (SOFI)[26] providing dynamical information from nanoscale regions (~ 50 nm)[27]. The high temporal resolution (< 1 μ s), the high sensitivity to fluorescence level changes, as well as the possibility to study environmental influences have made FCS a popular and influential method to investigate molecular or single-particle dynamics not only in the life sciences[28, 29] but also in the material science[30].

Closely related to FCS is a wide-field technique, called *image correlation spectroscopy* (ICS)[31] that analyzes not a single focal point but a whole image series recorded by an (*electron-multiplying*) *charge-coupled device* ((EM)CCD) or *complementary metal-oxide-semiconductor* (CMOS) technology based camera. ICS appears in many flavors, depending on whether pixels are correlated in space, time, k -space, combinations of them, or between different color channels (ICS, tICS, kICS, STICS, ICCS)[32]. A remarkable variation of this method is *raster image correlation spectroscopy* (RICS), which uses the temporal information used in the construction of a confocal rasterized image to investigate fast correlations additionally.[33]

1.1 | SINGLE-PARTICLE TRACKING

More direct access to nanometer dynamics is gained via *single-particle tracking* (SPT) approaches. ROBERT BROWN's microscopic observation in 1828 of the thermally driven motion of pollen grains suspended in water is considered the first experiment of this category.[34] Apart from this exception, the actual use of SPT is much more recent, and the first video-based experiments are attributed to BRABANDER *et al.* in the late 1980s.[35, 36] They visualized the Rayleigh scattering of 40 nm-sized gold nanoparticles in living cells with *video-enhanced differential interference contrast microscopy* and extracted the particle tracks by image processing.[37] This approach became very popular due to the fact that bigger particles (e.g., polystyrene beads[38], latex beads[39], or silica particles[40], size range: 200 nm - 1 μ m) could be easily imaged with standard optical microscopy. Consequently, the technique was available to an extremely large number of research groups, which improved the data-extraction part of the experiment.[27] While the used particles could be detected with high temporal and spatial resolution due to their large scattering cross-section, their unwieldy size limited the accuracy with which biological processes could be investigated, and the next big step for SPT was the detection of single fluorescent molecules with conventional fluorescence microscopy at room temperature done by SCHMIDT *et al.*[41] The usage of single molecules as labels for proteins, DNA strands, mRNA, polymer chains, antibodies, and many other targets was quickly adapted to SPT experiments.

Since those days, the method has developed further and is now well established. However, the area remains dynamic and still brings new variants to light. In fact, SPT can also be conducted on absorption or scattering images. For example, a trending technique is a label-free method, called *interferometric scattering microscopy* (iSCAT) [42–45] or *coherent bright field microscopy* (COBRI)[46, 47].

Basically, single-particle tracking methods can be divided into two classes: Firstly, image series analyzed to extract the particle pathways *ex post facto* and secondly, measurement setups in which feedback loops have been implemented that track a single-particle in real-time. Methods of the second type are called *active single-particle tracking* approaches.

The most likely first experiment in which single microscopic particles were actively tracked using optical methods was carried out by HOWARD BERG in 1971.[48] He imaged individual *Escherichia coli* (*E. Coli*) bacteria onto six optical fibers. Each pair of fibers covered a spatial direction and was offset along the corresponding axis but still overlapping. The other ends of the fibers led to one photomultiplier each, whose analog signals were compared electronically so that movements of the bacterium were detected by differences of the signal pairs. A negative feedback loop controls the position of the specimen holder so that the image of the bacterium on the fibers remains locked. Compared to modern experiments, the object under investigation was gigantic and the resolution miserable, but one has to admit that the fundamental concepts have not changed much.

The microscopic method used in this thesis belongs to the active single-particle tracking approaches, and is named *single-particle orbit tracking* (SPOT). It inherits the concepts of HOWARD BERG's approach of localizing a particle optically and keeping it mechanically in a defined region. More elaborated considerations by JÖRG ENDERLEIN at the millennium change initialized the modern implementation, that was first realized by ENRICO GRATTON's group.[49] The new idea was to use a circular scanned laser focus to encode the particle position in a modulated fluorescence signal. It turned out that nanoparticles can be localized very precisely in this way and that they can be tracked with the assistance of feedback loops even in real-time.

1.2 | STATE-OF-THE-ART IN ACTIVE SINGLE-PARTICLE TRACKING

There are various alternatives to SPOT-approach that will be described in the context of this thesis, some of which differ only in the hardware implementation or other details, but also those that pursue fundamentally new concepts. Here, some highlights of the achievements of other groups are summarized, providing a state-of-the-art overview about active SPT.

BERLUND and MCHALE from the MABUCHI group described theoretically and in great detail a feedback controller design for single-particle tracking in a confocal microscope. [50, 51] Moreover, they worked out analytic expressions for the occurring fluorescence fluctuations recorded while tracking.[52] Finally, they called their analysis of the autocorrelation function from the recorded fluorescence signal *tracking-FCS*. [53] With tracking-FCS, MABUCHI and co-worker decoupled the timescales of diffusion and blinking of CdSe/ZnS quantum dots, which would otherwise avert an accurate analysis of the photon statistics in a classical FCS experiment. By doing this, they showed the suppression of short timescale fluorescence intermittency by 2-mercaptoethanol.[54] Furthermore, they studied intramolecular motion of single freely diffusing fluorescence-labeled double-stranded λ -phage DNA molecules with tracking-FCS.[55]

In the early days of developing feedback-based approaches for 3D-tracking of fluorescent particles, the mentioned MABUCHI group competed with the team of GRATTON in the field of experimental implementation. While the first mentioned have created an extremely useful and detailed theoretical framework for the method, the latter shone with inventiveness in applying and modifying the technique. GRATTON and co-workers called their approach *scanning-FCS* and were able to track fluorescent beads of 500 nm in agarose with 64 ms temporal and 20 nm spatial resolution already in 2003.[56]

The localization step of scanning-FCS differs to that of tracking-FCS in the way the demodulation is calculated. Instead of a continuous position calculation using lock-in summation, GRATTON's approach utilizes the *fast Fourier transformation* to extract positional information from the fluorescence signal. This algorithm is fast enough to perform the necessary calculations in real-time. A detailed analysis of the capabilities of scanning-FCS in its early stage was published in [49], where they measured the distances between (static) fluorescent particles with nanometer accuracy.

GRATTON's hardware implementation varies from the MABUCHI's group version in the way the orbit is created. GRATTON's group used Galvano mirrors instead of acousto-optical deflectors for the lateral deflection and an objective linear piezo scanner for the z -modulation. Since they excited their sample by two-photon excitation from a mode-locked titanium-sapphire laser, they could forgo detection pinholes and use wide-area detectors like photomultiplier tubes without impairing the signal-to-noise ratio significantly. Consequently, they did not need descanning of the detection beam path. In a more recent version of the setup, they were the first to use an *electrically tunable lens* to speed up the axial localization of 3D-orbital tracking.[57]

In addition, GRATTON and co-workers designed a variant of active SPT that can be implemented on many commercially available microscopes with only a few modifications needed. In this cost-efficient but slow version of orbital tracking, the particle was directed on circular paths around a fixed laser beam to achieve fluorescence modulation.[58]

The bandwidth of application is vast in the GRATTON group but mainly located in the

field of biology. They monitored the phagocytosis of fluorescent protein-coated beads by fibroblasts[59] or used the orbital tracking to move single gold nanoparticles systematically along collagen fibers and actin filaments inside Chinese hamster ovary K1 living cells, thereby mapping the biological fibers 3D topography with nanometer resolution.[60] In the scanning-FCS approach, the particles are not only tracked but also their photon emission traces are used to calculate correlation functions. GRATTON *et al.* set their photon counts in relation to the laser focus scan position by constructing two-dimensional photon carpets, where the first axis represents the total number of points along the orbit and the second axis represents the time of acquisition. Therefore, the complete photon counting trace, binned to scan positions, can be reconstructed by reading the photon carpet representation line by line. The benefit of this representation is that spatial and temporal information is encapsulated simultaneously. For example, the transport of single molecules through single *nuclear pores complexes* in intact cells was monitored by tracking the center of mass of the nuclear pores complex and autocorrelating the photon emissions from single scan positions and cross-correlating that of opposed one.[61, 62] This method was further applied to visualize the transcription kinetics variance of highly mobile identical genes. Therefore, GRATTON's group tracked a broad transgene array as a model system and resolved at distinct regions the synthesis of mRNA, which was only possible due to the high spatial and temporal resolution of the system.[63, 64]

The group of LAMB often cooperated with GRATTON and used a 3D orbital tracking approach for the study of biological problems as well. Their setup varied from the previously mentioned methods in the way the z -resolution was achieved. Instead of excitation in different planes, multiple detection planes were used that were generated by slightly misaligned detection pinholes.[65] Special to their implementation was an additional wide-field imaging channel and an incorporated stepping motor positioning stage that expanded the accessible tracking range to several centimeters.[66]

With these features available, they investigated not only processes within single living cells but also in entire organisms. The translational and rotational diffusion of single-walled carbon nanotubes in live HeLa cells was studied[67], the difference between 2D and 3D data analysis of trajectories occurring from anomalous diffusion of polyplexes in roundish amoeba or flattened HuH-7 human cells was pointed out[68], and the pathway of single *prototype foamy viruses* as they infect living cells was recorded.[69] In a more recent publication, they studied the mitochondrial trafficking in sensory neurons of zebrafish larvae over distances larger than 100 μm and imaged the environmental context in the superimposed wide-field channel. With their high spatial and temporal resolution, they were able to discriminate the already known fast components during active motion and a previously undetected motional state of slow velocity in antero- and retrograde direction.[66]

While the LAMB group achieved axial resolution with spatially separated detection volumes, this type of detection can also be utilized for the entire localization purpose. YANG and WERNER localized particle with a static laser and multiple detection volumes.[70–74] They compared signal heights from multiple detectors and used a nanopositioning stage to close the feedback loop. A technically demanding experiment was conducted by YANG and WELSHER.[75] They used two detector pairs for lateral localization and another one for the particle's axial position. By combining their real-time tracking with a three-channel *two-photon laser confocal scanning microscope* (2P-LSM), they randomly sample image planes of the environment on a coarser time and larger length scale. After sophisticated image reconstruction, they achieved a multi-resolution visualization of the early stages of cellular uptake of peptide-coated nanoparticles as a model system for cellular delivery strategies or

viral trafficking. This refined experiment combined nanometer/microsecond accuracy with a detailed mapping of the surrounding landscape.

Later, WELSHER used a different approach in his own research group. He and his collaborators generated a dynamically moving laser spot in three dimensions using a *two-dimensional electro-optic deflector* and a *tunable acoustic gradient lens*.^[76] The estimation filters used for the particle localization in their method, called *3D dynamic photon localization tracking* (3D-DyPLoT), are based on those developed for MOERNER's ABEL trap which will be explained in more detail later in this section.^[77] While the short-time localization originates from the squared area that is pegged from the laser focus scan path, a 2D piezoelectric stage expands the tracking range in the lateral direction and a high-speed objective lens positioner in the axial direction. For the detection, only one avalanche photodiode is necessary, which means that the optical setup is strongly simplified compared to setups like those of MABUCHI, LAMB, GRATTON and YANG. However, the main advantage of this method is the large observation area ($1\ \mu\text{m} \times 1\ \mu\text{m} \times 4\ \mu\text{m}$) that allows a particle to do large diffusive steps or intermediate timescale transitions into dark states without the tracking algorithm to lose it. Therefore, the piezoelectric stage has more time to execute the feedback step and the bandwidth limitation is less important. In a recent publication, the method was further developed to adaptively expand the size of the lateral scan path for changing diffusive conditions.^[78] The authors called the method *precision adaptive real-time tracking* (3D-PART) and applied it to monitor viral first contact of virus-like particles to the surface of live cells.

A method called *tracking single particles using nonlinear and multiplexed illumination* (TSUNAMI) capable of tracking in highly scattering environments was developed in the group of DUNN. ^[79] The particle localization of TSUNAMI is based on a barely overlapped tetrahedral arrangement of excitation volumes. The excitation volumes are created successively by laser pulses that are separated in time by 3.3 ns each. By time-correlated single-photon counting detection, each detected photon is assigned to a time gate that corresponds to a certain excitation volume, which can be used to calculate the particle position in three dimensions. The triangulated position is fed to a control loop that steers Galvano mirrors and an objective z -piezo scanner to the particle position. What must be guaranteed for this method to work is that the emitter's lifetime is shorter than the time gate of 3.3 ns. Otherwise, strong channel leakage would decrease the localization precision. Since TSUNAMI needs only one photomultiplier tube for localization, the technical complexity does not increase excessively if several color channels are detected simultaneously. The authors state an axial accuracy of better than 100 nm at a penetration depth of about 200 μm due to the used two-photon excitation.

Using this technique, the trafficking dynamics of *epidermal growth factor receptors* were measured in live cells at 16 nm lateral and 43 nm axial resolution, with track duration ranging from 2 to 10 min and vertical tracking depth of several micrometers.^[80]

In contrast to the previously discussed methods, where either the sample system is moved or the optics follow the particle's trajectory, in the next mentioned method external forces act on a particle to keep it within the detection volume. COHEN and MOERNER invented the *anti-Brownian electrokinetic* (ABEL) trap, which uses time-dependent electrical fields applied in a microfluidic cell to induce electrokinetic drifts that canceled out the thermal motion.^[81, 82] It was shown that the ABEL trap is capable of tracking single biomolecules in aqueous buffer solutions down to the 1 nm limit.^[83] The localization happens optically but its technical implementation changed over time. In the zeroth version, video-tracking was used and quickly replaced by a circular-scanned laser beam as

used in 2D-SPOT.[84, 85] After that, the scan path was optimized, considering the maximum information content of single photon detection.[83, 86] Digital signal filters had been introduced to yield a (near-)optimal single photon based localization algorithm.[77]

COHEN trapped single molecules of fluorescently-labeled λ -DNA and recorded the internal conformational dynamics inside the trap, which allowed them, for the first time, to measure the spectrum of internal conformational modes of a single relaxed polymer molecule. More recently, the MOERNER lab has trapped individual chaperonin molecules with the ABEL trap.[87] Incubating the chaperonins with fluorescently labeled ATP enabled the counting of bound ATP, molecule-by-molecule, and thus provided a detailed picture of the ATPs cooperative binding. The ABEL trap's major advantage is the dramatically enhanced acquisition time of emission from non-immobilized single proteins. In another recent study of the MOERNER group, the photophysical heterogeneity of phycolisomes quenched by orange carotenoid protein.[88]

Finally, there is the method of minimal emission fluxes, called MINFLUX, with its fundamentally different localization approach. While all previously mentioned methods need photons to localize a particle, in MINFLUX the absence of photons is used to tell about the particle's position. The excitation energy minimum of the doughnut-shaped excitation beam, known from the STED approach is placed at a known set of spatial coordinates around the molecule's proximity. The closer the distance between the minimum and the molecule's position, the fewer photons are detected. Iteratively decreasing the doughnut size and distance to the molecule increases the localization accuracy. Using, MINFLUX, the inventing group of HELL obtained the molecule's position with nanometer resolution.[15] Currently, MINFLUX is developing quickly. In 2018, it was able to resolve rapid molecular jumps in an artificial system with 2 nm resolution in about 400 μ s.[89] Very recently, experiments in fixed and live cells are conducted with about the same resolution, but in three dimensions and with two color channels.[90] As it is used for imaging and for tracking, it is assumed that the number of applications will increase significantly in the next years.

Summarizing this section, there are plenty of methods available for tracking single particles in real-time. As those methods differ in implementation, the basic concepts are the same. There is always a localization step consisting of probing for fluorescence at or from different spatial positions, the recorded fluorescence is processed to obtain the particle position, which is then finally fed back to compensate for the particle's motion. The major limitation of the temporal resolution is the number of detected photons from the emitter, whereas some methods also suffer from inertia effects of moving hardware components. Excluding MINFLUX, the spatial resolution resides in the same range of some tens of nanometer, depending on the integration time and sophistication of the filtration method. Almost all groups fight against correlations of tracking errors, which in principle should be avoided to get correct diffusion statistics.[51, 59, 74, 75, 91]

1.3 | CHALLENGES IN THE CHARACTERIZATION OF NANOPOROUS FILTER MATERIALS

The removal of plastic debris, especially from aquatic habitats, has recently attracted a lot of attention.[92] While the problems caused by larger pieces of plastic are obvious to everyone, in particular the so-called microplastics or nanoplastics are a hidden, but serious health problem.[93] There are many studies published that examine their harmful effect to living organisms.[94–96] The cleaning of liquids and gases that contain such particles is a difficult task. One important method to remove micro- or nanoparticles from a liquid or gas is *membrane filtration*. [95, 97, 98]

Of course, for effective filtration, the size of the membrane pores must be similar to or even smaller than that of the particles to be retained (see fig. 1.1). This means that the filter material that is meant to remove nanoparticles, must have a micro- or nanostructure of voids and pores. Therefore, the exact characterization of those materials and the examination of transport processes within them is challenging.

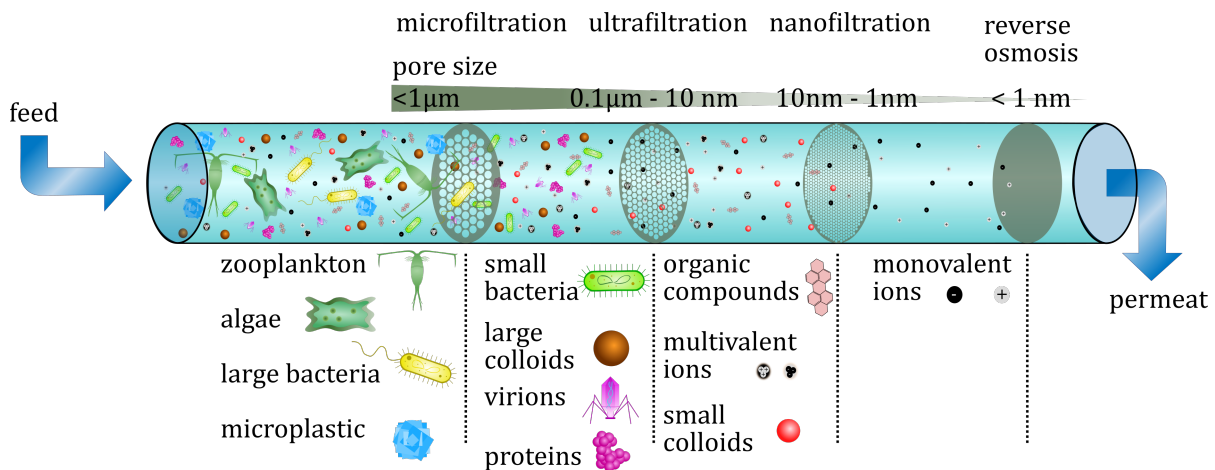


Figure 1.1.: Sketch of the different membrane filtration regimes and examples of particles that can be retained. *Microfiltration* uses pore sizes smaller than $1\mu\text{m}$ and is capable to retain particles like zooplankton, algae, larger bacteria and microplastic. Smaller particles that are only hardly visible under a light microscope, like little bacteria, virions or large colloids are able to pass a microfiltration membrane. However, they are hold back by *ultrafiltration*. Ultrafiltration is performed by membranes with pore sizes in the 10 to 100 nm range. Therefore, they can also be used for bigger proteins, but not to sort out smaller molecules or aggregates. Here, *nanofiltration* with pore sizes as small as 10 nm down to 1 nm comes into play. Those membranes are capable to remove smaller colloids, organic compounds and even multivalent ions from the feed. *Reverse osmosis* membranes exhibit the smallest pore sizes. Thus, all membranes with pores smaller than 1 nm are attributed to this category that is used to fully deionize water, even from monovalent ions.

Generic methods for characterizing micro- or nanoporous structures are *atomic force microscopy* (AFM) or *scanning electron microscopy* (SEM), that allow for imaging with high spatial resolution.[99–103] However, those methods, in particular SEM, need harsh preparation conditions, like drying, metal-coating, slicing or freezing and, moreover, both aforementioned techniques are restricted to the surface of the membrane material. In contrast, *solvent flow experiments* or *solute rejection tests* provide information about dominant length scales within a porous system in a liquid-filled state without having to destroy it.[104] Yet, those approaches reveal only ensemble averaged results, and, thus, the macroscopic transport properties of the system. A non-invasive approach that allows to obtain

the three-dimensional structure of a porous material without destruction is optical microscopy. One approach is to monitor the fluorescence of a concentrated dye solution that permeates a membrane by confocal laser scanning microscopy. High signals are obtained from observation volumes recorded from the void structure and a map of the porous network is obtained.[105, 106] Unfortunately, the resolution of such a map corresponds to the diffraction limit of light setting hard boundaries for the size of the structures that can be investigated by standard microscopy. For this reason, fluorescence-based high-resolution microscopy offer an attractive route to follow and is applied in the present work to a special category of membranes from the field of ultrafiltration. The experiments and results are described in chapter 8 and show that fluorescence-based high-resolution methods, like SPOT, offer an attractive approach to study nanoparticle motion on the nanometer length scale.

2 | NANOPARTICLE DIFFUSION

The temporal evolution of the spatial distribution of two or more substances with respect to each other is known as diffusion. By diffusion, a concentration gradient of two substances will be balanced out in time. The reason for that is the thermal motion of the molecules. They wiggle, rotate, and move from one place to another, and by doing this, they hit and strike each other (see fig. 2.1) redistributing their momentum and energy constantly. Even if a system is macroscopically in equilibrium, there are small scale fluctuations of energy and concentration.

Thermal motion of micro- and nanoscopic particles is a long known and extensively studied phenomenon. Since the very beginning with the stochastic description of normal diffusion, also known as *Brownian motion*, the development of the field was always connected to the experimental methods available to verify the predictions. Modern microscopic techniques, simulation methods, and mathematical approaches have accelerated the growth of this vast field. Changing from a thermally equilibrated system of mesoscopic particles and simple fluids to non-equilibrium systems of nanoscopic particles in more complex and even biological environments has uncovered significant deviations from normal diffusion.

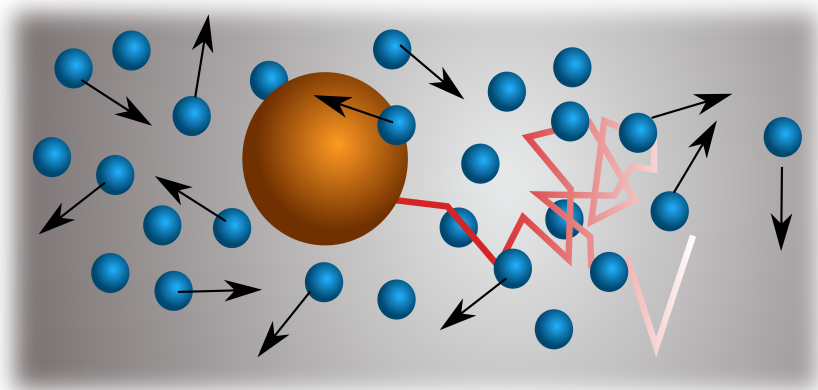


Figure 2.1.: Schematic illustration of the idea behind the Langevin equation. A single particle experiences a massive number of kicks. The directions and amplitudes of the kicks are randomly distributed and sum up to a single stochastic force that acts on an inertial particle that experiences friction when moving.

2.1 | BROWNIAN MOTION

A microscopic description of the diffusive pathway of a single particle that undergoes Brownian motion can be given with the help of a famous stochastic differential equation, called the *Langevin equation*.^[107] It relates the acceleration of a particle of mass m to two forces. First, to a stochastic fluctuating force of random kicks that pushed the particle into

random directions and with random magnitude and second, to a dissipative damping force that counteracts the accelerative kicks. In one dimension and with the friction coefficient ξ and the fluctuating kick-magnitude $\nu_{\text{bm}}(t)$, the Langevin stochastic differential equation can be written as

$$m\ddot{r}(t) = -\xi\dot{r}(t) + \nu_{\text{bm}}(t) . \quad (2.1)$$

Here, the kick term $\nu_{\text{bm}}(t)$ is a zero-mean, white noise process with covariance amplitude v_{bm} and obeys the following two statistical properties:

$$\mathcal{E}(\nu_{\text{bm}}(t)) = 0 , \quad \text{and} \quad (2.2)$$

$$\mathcal{E}(\nu_{\text{bm}}(t)\nu_{\text{bm}}(t')) = v_{\text{bm}}\delta(t - t') . \quad (2.3)$$

The notation $\mathcal{E}(x)$ is used to express the expectation value of the variable x and $\delta(x)$ is the Dirac delta distribution. Eq. (2.1) is a second-order stochastic differential equation that can be converted to a first-order stochastic differential equation system, which is, in fact, a state-space representation of the Langevin equation. A *linear time-invariant system* (LTI) in standard notation is written as

$$\dot{\mathbf{x}}(t) = \mathbf{A}\mathbf{x}(t) + \mathbf{B}_v\mathbf{u}(t) . \quad (2.4)$$

A detailed introduction into system theory and the occurring notation is given in the appendix A. In brief, $\mathbf{x}(t)$ is the system state variable, \mathbf{A} is the system matrix and \mathbf{B}_v the input matrix. The vector $\mathbf{u}(t)$ is the input, which is often identified with noise terms. The input (noise) covariance is expressed by \mathbf{V} . Comparing eq. (2.1) with eq. (2.4) and appendix A.8, the system state \mathbf{x} , as well as the system matrices, are easily identified as:

$$\mathbf{x}(t) = \begin{pmatrix} r(t) \\ \dot{r}(t) \end{pmatrix}, \quad \mathbf{u}(t) = \nu_{\text{bm}}(t), \quad \mathbf{A} = \begin{pmatrix} 0 & 1 \\ 0 & -\frac{\xi}{m} \end{pmatrix}, \quad \mathbf{B}_v = \begin{pmatrix} 0 \\ \frac{1}{m} \end{pmatrix} \quad \text{and} \quad \mathbf{V} = v_{\text{bm}} . \quad (2.5)$$

The kicks serve as the noisy input into the system, and the state variables contain the particle's position and velocity. Using the time-dependent Lyapunov equation (see appendix A.8),

$$\dot{\mathbf{Q}}(t) = \mathbf{A}(t)\mathbf{Q}(t) + \mathbf{Q}(t)\mathbf{A}^T(t) + \mathbf{B}_v(t)\mathbf{V}(t)\mathbf{B}_v^T(t) , \quad (2.6)$$

the temporal development of the process variance can be calculated. The system's process variance matrix (see appendix A.8) is written as

$$\mathbf{Q}(t) = \mathcal{E}(\mathbf{x}(t)\mathbf{x}^T(t)) = \begin{pmatrix} \mathcal{E}(r^2(t)) & \mathcal{E}(r(t)\dot{r}(t)) \\ \mathcal{E}(r(t)\dot{r}(t)) & \mathcal{E}(\dot{r}^2(t)) \end{pmatrix} \quad (2.7)$$

After inserting $\mathbf{Q}(t)$ into eq. (2.6), one obtains the following three differential equations:

$$\frac{d}{dt}\mathcal{E}(r^2(t)) = 2\mathcal{E}(r(t)\dot{r}(t)) \quad (2.8)$$

$$\frac{d}{dt}\mathcal{E}(r(t)\dot{r}(t)) = -\frac{\xi}{m}\mathcal{E}(r(t)\dot{r}(t)) + \mathcal{E}(\dot{r}^2(t)) \quad (2.9)$$

$$\frac{d}{dt}\mathcal{E}(\dot{r}^2(t)) = -\frac{2\xi}{m}\mathcal{E}(\dot{r}^2(t)) + \frac{v_{\text{bm}}}{m} \quad (2.10)$$

Provided that the initial conditions for the system are $\mathcal{E}(r^2(0)) = 0$, $\mathcal{E}(r(0)\dot{r}(0)) = 0$ and $\mathcal{E}(\dot{r}^2(0)) = \frac{v_{\text{bm}}}{2\xi m}$, these equations can be integrated. The solutions are

$$\mathcal{E}(r^2(t)) = \frac{v_{\text{bm}}}{\xi^2} \left\{ t - \frac{m}{\xi} \left[1 - \exp\left(-\frac{\xi}{m}t\right) \right] \right\}, \quad (2.11)$$

$$\mathcal{E}(\dot{r}(t)r(t)) = \frac{v_{\text{bm}}}{2\xi^2} \left[1 - \exp\left(-\frac{\xi}{m}t\right) \right] \quad \text{and} \quad (2.12)$$

$$\mathcal{E}(\dot{r}^2(t)) = \frac{v_{\text{bm}}}{2\xi^2 m}. \quad (2.13)$$

Comparing the equations above with the corresponding mathematical framework reveals that physical Brownian motion is indeed the integral of an *Ornstein-Uhlenbeck process*. [108] An Ornstein-Uhlenbeck process is a stochastic process of random steps with a small tendency to move back to its origin. [109] Several features of simple diffusion systems are easy to derive from eqns. (2.11)–(2.13).

From the fluctuation-dissipation theorem, it is known that the white-noise covariance is connected to the temperature \mathcal{T} and the friction ξ by [110]

$$v_{\text{bm}} = 2\xi k_B \mathcal{T}. \quad (2.14)$$

The symbol k_B , represents the *Boltzmann constant*. Consequently, the average squared velocity of a diffusing particle is a constant value $\mathcal{E}(\dot{r}^2(t)) = \frac{k_B T}{\xi m}$. For short times $t \ll \frac{m}{\xi}$, the particle moves like a free particle with $\mathcal{E}(r^2(t)) = \frac{2k_B \mathcal{T}}{\xi} t^2$. For long times $t \gg \frac{m}{\xi}$ or in the overdamped case, the scaling of the positional variance is proportional to time

$$\mathcal{E}(r^2(t)) = \frac{v_{\text{bm}}}{\xi^2} t = 2 \frac{k_B T}{\xi} t = 2Dt. \quad (2.15)$$

For the last identity, the common definition of the diffusion coefficient was used [111]

$$D = \frac{k_B \mathcal{T}}{\xi}. \quad (2.16)$$

In many applications, it is a good approximation to use the friction coefficient of a spherical particle with diameter a in a medium of the *dynamic viscosity* η given by

$$\xi = 3\pi\eta a. \quad (2.17)$$

For the long time limit or the overdamped case, the statistical process that describes Brownian motion merges from the integral of an Ornstein-Uhlenbeck process to an integral of a Wiener process, which is a stochastic, continuous-time process with normally distributed and statistically independent increments. [112] The corresponding Langevin equation is

$$\dot{r}(t) = \xi^{-1} \nu_{\text{bm}}(t) \quad (2.18)$$

and immediately solved by integration over the noise term

$$r(t) = r_0 + \xi^{-1} \int_0^t dt' \nu_{\text{bm}}(t'). \quad (2.19)$$

This equation can be used in computer simulations based on random number generation

to imitate a diffusive process (e.g., fig. 2.2). It should be noted that on a computer, the integration of a nowhere differentiable process is not straightforward, and errors are only small if the quantities to compute are observed on a time scale much larger than a single simulation step.

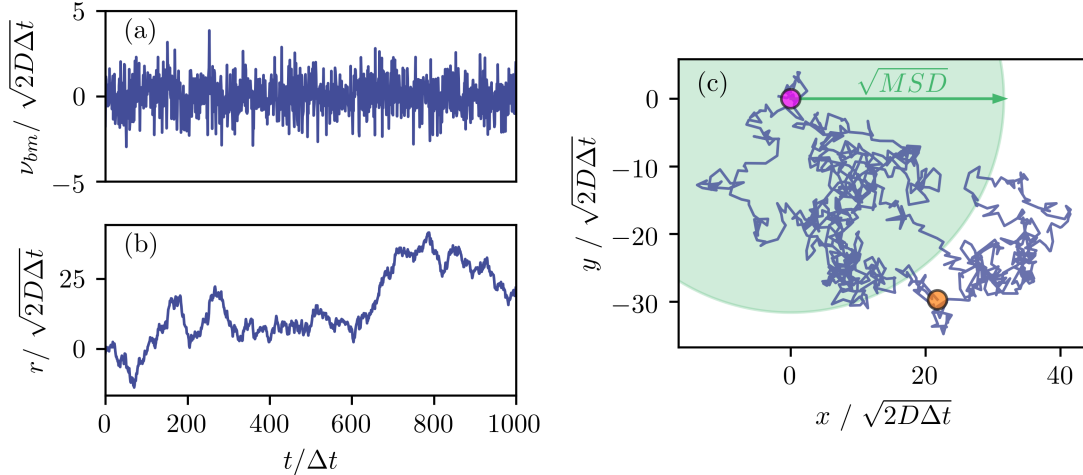


Figure 2.2.: Normalized example of a random walk. (a) Brownian noise term ν_{bm} that drives the particles motion. (b) Time series of the particle position in the overdamped case. (c) Two-dimensional (normalized) trajectory appearing as the typical irregular pathway. A green circle in the background represents the square-root of the mean squared displacement (MSD, see section 2.3) from the trajectory start position (violet sphere). An orange sphere marks the trajectory's last position.

2.2 | DIFFUSION EQUATION

The equations mentioned above described the realization of a process from a stochastic point of view. A different framework to handle such processes is the modeling of the evolution of probability distributions in time. Therefore, consider now the conditional probability density function $\mathcal{P}(r, t|r', t')$ of finding a particle at position r at time t provided that it resides in r' at time t' . In the overdamped case, the time evolution of this probability density function can be calculated with the so-called *Fokker-Planck* equation, which was already derived by ALBERT EINSTEIN and which is known as the *diffusion equation*[111]

$$\frac{\partial}{\partial t} \mathcal{P}(r, t|r', t') = D \frac{\partial^2}{\partial r^2} \mathcal{P}(r, t|r', t') . \quad (2.20)$$

From a macroscopic point of view, $\mathcal{P}(r, t|r', t')$ can be replaced by a concentration profile, and therefore it connects the micro- with the macroscale. The solution of the diffusion equation for a particle precisely located at $r' = 0$ for $t' = 0$ is

$$\mathcal{P}(r, t) = \mathcal{P}(r, t|0, 0) = \frac{1}{\sqrt{4\pi Dt}} \exp\left(-\frac{r^2}{4Dt}\right) \quad (2.21)$$

An illustration of the propagation of this probability density function in time and space is shown in fig. 2.3. Being the fundamental solution to the diffusion equation, eq. (2.21) can be utilized to calculate the solution of eq. (2.20) for other boundary or initial conditions as well.

In the literature, eq. (2.21) is linked to the *self-part of the Van Hove correlation function* known from condensed matter physics and used to analyze particle step distributions.[113, 114]

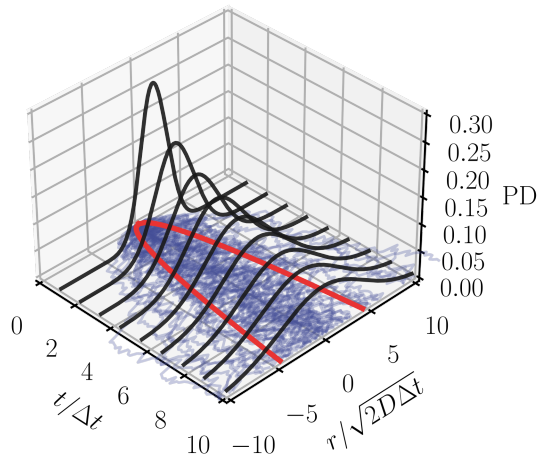


Figure 2.3.: Propagation of the probability density function (solid black line) of an overdamped Brownian diffusion process in time and space. In the t - r -plane a large number of Brownian walks are drawn in blue. Red lines show the square-root of the mean squared displacement (MSD, see section 2.3), indicating the growing standard deviation of the probability density function in time. The majority of the trajectory realizations accumulate within the area stacked out by the square-rooted MSD.

2.3 | MEAN SQUARED DISPLACEMENT

A frequently investigated quantity resulting from diffusion experiments is called the *mean squared displacement* (MSD). It measures the average squared distance that a particle covers with (lag) time (see fig. 2.2). Mathematically, the MSD is the second statistical moment of the particle position $r(t)$,

$$\text{MSD}(t) = \mathcal{E}(r^2(t)) = \int_{-\infty}^{\infty} r^2(t) \mathcal{P}(r, t) dr . \quad (2.22)$$

A theoretical expression for the MSD of overdamped Brownian motion was already calculated with the Langevin equation resulting in eq. (2.15), but can also be obtained by inserting eq. (2.21) into eq. (2.22). Experimentally, this quantity is approximated by an ensemble-average over many trajectories from (identical) particles. For the one-dimensional trajectories $r_i(t)$ of particles $i \in [0, N_{\text{particle}}]$, the ensemble-averaged MSD is written as

$$\langle \Delta r^2(t) \rangle_N = N_{\text{particles}}^{-1} \sum_{i=1}^{N_{\text{particles}}} [r_i(t) - r_i(0)]^2 . \quad (2.23)$$

In some single-particle experiments, only a minimal number of particles $N_{\text{particles}}$ are present, but the trajectories of the particles are very long. This is the situation present for SPOT. Therefore, temporal averaging of the displacements of a single pathway is more evident than the ensemble averaging. The time-averaged MSD of particle i is given by

$$\langle \Delta r^2(\tau) \rangle_{T,i} = \frac{1}{T - \tau} \int_{t=0}^{T-\tau} [r_i(t + \tau) - r_i(t)]^2 . \quad (2.24)$$

Here, the temporal variable was changed from absolute time t to lag time τ emphasizing the insignificance of the position measurement start time. For the statistics of a Brownian particle, both averages are related to the positional variance of a particle given by eq. (2.15). Note that for finite measurement times T and particle numbers N , the experimental MSDs are statistical measures. Provided that the measurement time T is long, and the particle number $N_{\text{particles}}$ is large, their expectation value is

$$\mathcal{E}\left(\langle\Delta r^2(\tau)\rangle_N\right) = \mathcal{E}\left(\langle\Delta r^2(\tau)\rangle_{T,i}\right) = 2D\tau \quad (2.25)$$

The definition of an *ergodic* process is that long-time averages and ensemble averages are identical[110], and it is seen that Brownian motion can be considered as an ergodic process.

2.4 | ANOMALOUS DIFFUSION

In general, the term "anomalous diffusion" denotes any deviation from the linear lag time dependency of the MSD, including phenomena like *ultraslow diffusion*, where the MSD scales with $[\log(\tau)]^{\tilde{\alpha}}$ with very different values for the exponent $\tilde{\alpha}$ [115] or diffusion with correlated jump length, where the MSD scales even faster than ballistic motion.[116] Most frequently, anomalous diffusion is identified by a power-law scaling of the MSD with respect to time

$$\text{MSD}_{\text{anomal}}(\tau) = 2D_\alpha\tau^\alpha, \quad (2.26)$$

with D_α being the *generalized diffusion coefficient* of physical dimension $\text{m}^2\text{s}^{-\alpha}$ and α being the *anomaly parameter*. [110] The anomaly parameter ranges between 0 and 2 and helps to categorize the type of diffusion. The regimes are *subdiffusion* $\alpha \in [0, 1[$, normal diffusion $\alpha = 1$, *superdiffusion* $\alpha \in]1, 2[$, and *ballistic motion* $\alpha = 2$. Examples for the different scaling regimes are shown in fig. 2.4. The empirical definition of anomalous diffusion does not specify the underlying physical processes, and different theoretical models can produce a power-law dependence of τ with the same α . In the appendices B.1–B.3, a small selection of anomalous diffusion models frequently encountered in literature are briefly introduced, focusing on the most important equations. Namely those anomalous diffusion models are the *continuous-time random walk* (CTRW), *fractional Brownian motion* (FBM) and motion according to a *fractional Langevin equation* (FLE).

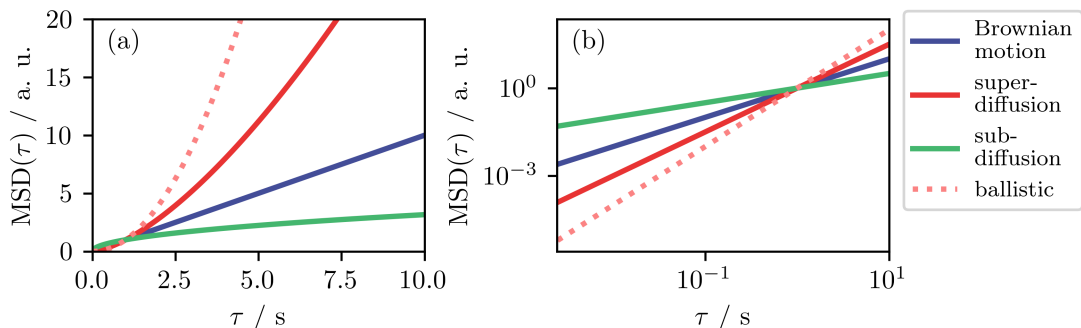


Figure 2.4.: Illustration of the different scaling of the MSD with respect to time in linear (a) and double-logarithmic (b) representation.

2.5 | CONFINED DIFFUSION

Many biological and technical important chemical or physical processes take place in finite domains, like the corralled motion of membrane proteins[117–121], diffusion inside the cell nucleus[122], substance mixing in microfluidic devices[123], or chemical reaction catalysis within constrained space.[124–127] While the confinement of molecular motion is often required by technology[128], it can also be counted as a key factor in the origin of life.[129] Some authors attribute the genesis of cells to the presence of a reaction container in the form of a primitive cell membrane.[130–132]

The space available for diffusion may be confined by geometrical obstacles and barriers or repulsive or attractive potentials. Depending on the complexity of the system, the particle undergoing confined diffusion may experience additional influences on its motion creating anomalous confined diffusion. One can think of a so-called *crowded fluid* (see [133]) inside a structured environment that is moving and interacting with the particle at the same time, creating arbitrarily complex diffusion characteristics.

As the confinement restricts the free expansion of the particle's trajectory, the corresponding MSD course flattens to a plateau value. For confined Brownian motion, the general expression for the MSD is given by

$$\text{MSD}_{\text{bm}}^{\text{confined}}(\tau) = \frac{L^2}{2} \left[1 - A_1 \exp\left(-\frac{A_2 2D\tau}{L^2}\right) \right]. \quad (2.27)$$

Here, L measures the length scale of the confinement and A_1 and A_2 are factors depending on the confinement shape. For $\tau \ll L^2/(2A_2D)$, the particle-wall interaction is negligible and the MSD scales like in the free-diffusion case proportional to the lag time τ . In [134], expressions for the MSD of Brownian motion confined in simple geometries with hard walls of varying dimensionality (one-dimensional diffusion on a straight, two-dimensional diffusion within a circle and three-dimensional diffusion within a sphere) are computed. All of those expression can be approximated by eq. (2.27) with a proper choice of A_1 and A_2 .

In many physical systems, hard walls and simple geometric shapes are not an adequate representation of reality. Instead, a particle exposed to a harmonic potential can be described by a Langevin equation modeling much softer confinement while keeping the equation as simple as possible. Assuming the origin-centered potential $U_\omega(r) = k_\omega r^2/2$ with spring constant k_ω , the not-overdamped particle position dynamic is given by

$$m\ddot{r}(t) = -\xi\dot{r} - k_\omega r + \nu_{\text{bm}}(t) \quad (2.28)$$

In [135], the state-space formalism is used to compute the MSD for a particle governed by these dynamics, yielding

$$\text{MSD}_{\text{bm,full}}^{\text{harm.pot}}(\tau) = \frac{2k_B T}{k_\omega} \left\{ 1 - \exp\left(-\frac{\xi\tau}{2m}\right) \left[\cos(\tilde{\omega}\tau) + \frac{\xi}{2m\tilde{\omega}} \sin(\tilde{\omega}\tau) \right] \right\} \quad (2.29)$$

with the frequency $\tilde{\omega} = \sqrt{k_\omega/m - \xi^2/(4m^2)}$. In the overdamped case, the MSD is not oscillating anymore and becomes

$$\text{MSD}_{\text{bm}}^{\text{harm.pot}}(\tau) = \frac{2k_B T}{k_\omega} \left[1 - \exp\left(-\frac{k_\omega\tau}{\xi}\right) \right]. \quad (2.30)$$

For long lag times, the MSD plateaus to the thermal value $\langle r^2 \rangle_{th} = k_B \mathcal{T} / k_\omega$, which does not depend on the particle properties but on the steepness of the potential. Evaluating the exponential term as a Taylor series for short lag times and stopping after the first order component, the MSD scales as $2D\tau$ again. Hence, the basic properties of the MSD are algebraic identical to the hard wall case.

The question arises, how would the MSD look like, if a Brownian law does not describe the particle's dynamics for short times. Indeed, more or less subtle discrepancies of the previously described behavior are observed for anomalous diffusion. A brief overview of the (time-averaged) MSDs for selected anomalous diffusion models (CTRW, FBM and FLE) is given to show the different scaling behavior. A more comprehensive review about this topic can be found in [136, 137], where most of the here presented results are extracted from.

For subdiffusive CTRW, the MSD does not converge to the thermal plateau, but grows according to [138]

$$\text{MSD}_{\text{ctrw}}^{\text{harm.pot}}(\tau) \approx \left(\langle r^2 \rangle_B - \langle r \rangle_B^2 \right) \frac{2 \sin(\pi\alpha)}{(1-\alpha)\alpha\pi} \left(\frac{\tau}{T} \right)^{1-\alpha} \quad (2.31)$$

with the first two moments of the Boltzmann distribution

$$\langle r^n \rangle_B = \frac{\int_{-\infty}^{\infty} r^n \exp\{-U_\omega(\mathbf{r})/(k_B \mathcal{T})\} dr}{\int_{-\infty}^{\infty} \exp\{-U_\omega(\mathbf{r})/(k_B \mathcal{T})\} dr} . \quad (2.32)$$

This is a power-law scaling that continues growing, even if the confinement is engaged. With this result being very counterintuitive, it was, however, proven with simulations[139] and found in experiments from optical tweezers[140]. Remarkably, eq. (2.31) does not require to know the detailed shape of the confining potential as it is incorporated into the moments of the Boltzmann distribution. In [141], analytical results for a cubic hard-wall potential are in accordance with the presented scaling.

The MSD for FBM in a harmonic potential was derived in [136] as

$$\begin{aligned} \text{MSD}_{\text{fbm}}^{\text{harm.pot}}(\tau) = & \frac{2\tilde{D}_\alpha \Gamma(\alpha + 1)}{k_\omega^\alpha} + 2\tilde{D}_\alpha \tau^\alpha - \frac{\tilde{D}_\alpha}{k_\omega^\alpha} \left[e^{k_\omega \tau} \Gamma(\alpha + 1, k_\omega \tau) + e^{-k_\omega \tau} \Gamma(\alpha + 1) \right] \\ & - \frac{k_\omega \tilde{D}_\alpha}{\alpha + 1} \tau^{\alpha+1} e^{-k_\omega \tau} M(\alpha + 1, \alpha + 2, k_\omega \tau) , \quad (2.33) \end{aligned}$$

using the *Gamma function* $\Gamma(x)$, the *complementary incomplete Gamma function* $\Gamma(z, x)$ and the so-called *Kummer function* $M(a, b, x)$, defined as

$$\Gamma(x) = \int_0^\infty e^{-t} t^{x-1} dt , \quad (2.34)$$

$$\Gamma(z, x) = \int_x^\infty e^{-t} t^{z-1} dt , \quad \text{and} \quad (2.35)$$

$$M(a, b, x) = \frac{\Gamma(b)}{\Gamma(b-a)\Gamma(a)} \int_0^1 e^{xt} t^{a-1} (1-t)^{b-a-1} dt , \quad (2.36)$$

respectively. The MSD converges to the thermal value $2 \langle r^2 \rangle_{\alpha, \text{th}} = 2\tilde{D}_\alpha \Gamma(\alpha + 1) / k_\omega^\alpha$ for large lag times. The approached level is α -dependent since the noise is external. The relaxation

dynamics can be approximated at $\tau \rightarrow \infty$ to uncover the asymptotic scaling law as

$$\text{MSD}_{\text{fbm}}^{\text{harm.pot}}(\tau) \approx 2 \langle r^2 \rangle_{\alpha, \text{th}} - \frac{\tilde{D}_\alpha \Gamma(\alpha + 1)}{k_\omega^2} e^{-k_\omega \tau} - \frac{2\alpha(\alpha - 1) \tilde{D}_\alpha}{k_\omega^2 \tau^{2-\alpha}}. \quad (2.37)$$

The second term is of leading order around $\alpha \approx 1$, for which the third term vanishes, and FBM converts to Brownian motion. Elsewhere, the MSD scales according to a power-law with the exponent $\alpha - 2$. Therefore, the MSD levels-off, but very slowly for superdiffusion and slightly faster for subdiffusion.

Motion following the subdiffusive FLE in the presence of a harmonic potential yields the MSD of shape

$$\text{MSD}_{\text{fle}}^{\text{harm.pot}}(\tau) = \frac{2k_B \mathcal{T}}{k_\omega} \left\{ 1 - E_{2-\alpha, 1} \left[-\frac{k_\omega}{\xi \Gamma(\alpha - 1)} \tau^{2-\alpha} \right] \right\}, \quad (2.38)$$

valid only in the overdamped limit. The appearing *generalized Mittag-Leffler function* $E_{a,b}(x)$ is defined by

$$E_{a,b}(x) = \sum_{n=0}^{\infty} \frac{x^n}{\Gamma(an + b)}. \quad (2.39)$$

This two-parameter Mittag-Leffler function interpolates between purely exponential and power-law-like scaling.[142] For $b = 1$, the second parameter can be suppressed in notation, and the resulting function is called the ordinary Mittag-Leffler function $E_a(x) = E_{a,b}(x)$.

Eq. (2.38) approaches the same α -independent thermal value for large lag times as in the Brownian motion case. At intermediate lag times, the MSD grows approximately as

$$\text{MSD}_{\text{fle}}^{\text{harm.pot}} \approx 2 \langle r^2 \rangle_{\text{th}} \left(1 - \frac{\xi}{k_\omega \tau^{2-\alpha}} \right). \quad (2.40)$$

and for short lag times, subdiffusive scaling is recovered.

Summarizing the MSD behavior for confined motion, there are two basic types of scaling. First of all, the exponential approaching to a constant plateau value and secondly a power-law that relaxes algebraically a lot slower. The generalized Mittag-Leffler function handles intermediate behavior that is not strictly captured by one of the two extremes. The timescale on which the MSD settles depends on the system's friction while the noise is considered internal by the underlying model. The plateau value contains information about the extent of the space between the surrounding barriers. An exotic exception of the two cases is the CTRW model, where the MSD does not level-off at any lag-time.

3 | METHOD

The following is a description of the basic concepts of SPOT, with the technical and mathematical details saved for later.

Repetitive scanning of a laser focus on a known pathway, for example the mentioned circle line, is used to imprint a carrier frequency onto the fluorescence rate of a particle such that the detected signal contains information on the particle's position. Once the focus is in close proximity to the particle, the fluorescence rate is high, and when the focus is far away, the number of detected photons per time bin decreases. In fig. 3.1 (a-c), this principle is illustrated for an orbital focus scan and a fixed particle emitting deterministic signals.

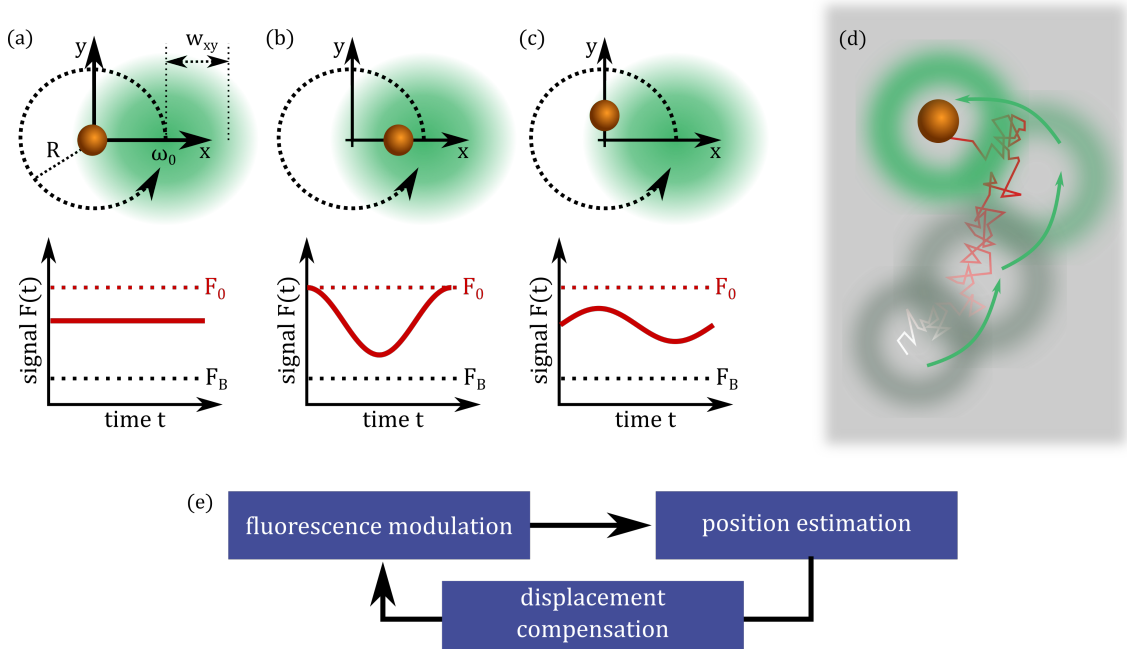


Figure 3.1.: (a-c) Sketch of the fluorescence rate modulation in an orbital scanning approach for lateral position estimation. Three scenarios are displayed (a,b,c) in which the position of a particle (orange sphere) is varied. A laser focus (blurry green disc) with a Gaussian intensity profile with $1/e^2$ -beam width w_{xy} is moved on a circle with radius R (black dotted line) starting at position $(R, 0)$. The angular frequency of the rotation is ω_0 . In scenario (a), the particle is located in the coordinate systems origin. The associated detected fluorescence signal $F(t)$, displayed on the plot below as a red line, is constant and resides between the peak fluorescence rate F_0 and the background signal F_B . Once the particle is displaced, the signal becomes modulated. In scenario (b), $F(t)$ describes a cosine-like shape with a deep modulation because the particle is positioned with a big displacement along the x -axis. In scenario (c), $F(t)$ progresses $\pi/2$ -phase shifted and with a less pronounced modulation depth corresponding to the smaller displacement just along the y -axis. (d) Sketch of the concept of a control loop that tries to minimize the distance between a diffusing particle and the orbit center. (e) Overview about the basic steps of the SPOT method, arranged in a feedback loop.

As the particle is in the orbit center (see fig. 3.1 (a)), the distance between the laser focus and the particle stays the same over a complete rotation cycle and a constant signal is detected. For the particle being displaced with respect to the orbit center (see fig. 3.1(b) and (c)), the signal becomes modulated with the modulation amplitude containing data about the particles radial displacement and the modulation phase defined by the angular position of the particle. Extracting this information with demodulation techniques provides an estimator for the particle's lateral position.

The modulation/demodulation idea can be extended to three dimensions (3D-SPOT) by switching quickly between two light orbits that are shifted with respect to each other along the common optical axis. Here, the reference position of the particle corresponds to the midpoint between the two orbits. This procedure is able to localize a mobile particle only for the time it diffuses through the detection volume.

By implementing of a feedback loop, that compensates for the particle's motion, the measurement time and trajectory length can be dramatically increased (fig. 3.1 (d)). The realization of a feedback loop can take various forms. The detection volume and excitation scan path may be shifted to be centered on the particle, external forces can be applied that act directly on the particle to move it back, or the sample cell may be driven to follow a mirror-inverted pathway and trap the freely moving particle within the laboratory coordinate system. The latter approach was embarked upon here.

Thus, SPOT is a control-theoretical problem, consisting of a position measurement through fluorescence modulation that is fed back to the sample holder to lock on this position, as displayed in fig. 3.1(e).

3.1 | POSITION-SENSITIVE FLUORESCENCE RATE MODULATION

First of all, an expression for the fluorescence signal $F(t)$ that is measured from a moderately excited distribution of chromophores with the concentration profile $c(t, \mathbf{r})$ must be developed.

Following literature, the recorded fluorescence signal depends on a so-called *molecule detection efficiency function* (MDF) that simultaneously considers the microscope's collection efficiency and excitation profile (see appendix C.1 for a brief motivation). A suitable expression for the MDF in a confocal microscope is developed in [143] by assuming a diverging Gaussian laser beam. DERTINGER *et al.* called it a modified Gaussian-Lorentz profile, which can be written as

$$\text{MDF}_{\text{mGL}}(\mathbf{r}) = \frac{\kappa(z)}{w^2(z)} \exp\left[-\frac{2}{w^2(z)}(x^2 + y^2)\right], \quad (3.1)$$

with the Cartesian z -coordinate co-aligned with the optical axis and the *collection efficiency amplitude* $\kappa(z)$ given by

$$\kappa(z) = 2 \int_0^{a_\circ} d\rho \frac{\rho}{\mathcal{R}^2(z)} \exp\left(-\frac{2\rho^2}{\mathcal{R}^2(z)}\right) = 1 - \exp\left(-\frac{2a_\circ^2}{\mathcal{R}^2(z)}\right). \quad (3.2)$$

The radial integration limits are chosen to reach from zero to a_\circ , which is the projection of the detection aperture diameter into the sample plane. The function $w(z)$ describes the axial dependency of the lateral beam diameter ($1/e^2$ -width). $\mathcal{R}(z)$ has an analog meaning but for the geometrical extend of the detection volume. Both functions are defined similarly

as

$$w(z) = w_{xy} \left[1 + \left(\frac{\lambda_{\text{exc}} z}{\pi w_{xy}^2 \tilde{n}} \right)^2 \right]^{1/2} = w_{xy} \left[1 + \left(\frac{z}{w_z} \right)^2 \right]^{1/2} \quad \text{and} \quad (3.3)$$

$$\mathcal{R}(z) = \mathcal{R}_0 \left[1 + \left(\frac{\lambda_{\text{em}} z}{\pi \mathcal{R}_0^2 \tilde{n}} \right)^2 \right]^{1/2} = \mathcal{R}_0 \left[1 + \left(\frac{z}{\mathcal{R}_z} \right)^2 \right]^{1/2}. \quad (3.4)$$

In this definition λ_{exc} and λ_{em} describe the central excitation and central emission wavelength, respectively. Furthermore, the refractive index of the immersion medium \tilde{n} appears in both definitions. The parameters w_{xy} and \mathcal{R}_0 are generally unknown model parameter and should be determined by fitting the model equations to a confocal scan of a single static particle. The characteristic length scales for axial beam divergence $w_z = \lambda_{\text{exc}} / (\pi w_{xy}^2 \tilde{n})$ and $\mathcal{R}_z = \lambda_{\text{em}} / (\pi \mathcal{R}_0^2 \tilde{n})$ are defined for simpler notation. There are many publications where this profile of the MDF was proven.[143–146] An example of a modified Gaussian-Lorentzian profile is shown in fig. 3.2.

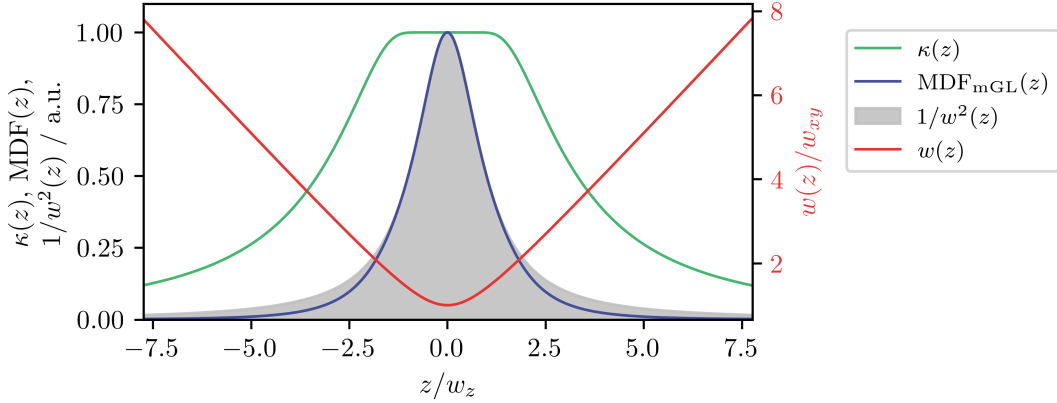


Figure 3.2.: Example of a modified Gaussian-Lorentzian computed for the parameter: $\lambda_{\text{exc}} = 520$ nm, $\lambda_{\text{em}} = 630$ nm, $w_{xy} = 190$ nm, $R_0 = 100$ nm, $\tilde{n} = 1.33$ and $a_{\odot} = 50 \mu\text{m}/60$. For comparison, the collection efficiency amplitude $\kappa(z)$, the axial dependency of the lateral beam width $w(z)$ and an unmodified Lorentzian profile $1/w^2(z)$ are added.

Ultimately, the fluorescence rate detected from the chromophore distribution in the presence of a homogeneous background fluorescence rate F_B is

$$F(t) = F_B + \int \text{MDF}(\mathbf{r}') c(t, \mathbf{r}') d^3r. \quad (3.5)$$

In a SPOT setup, the laser beam intensity profile is not centered at the same point as the collection efficiency, and the MDF has to be modified for a moving excitation profile. If the Gaussian-Lorentzian laser beam focus follows a prescribed trajectory written as $\mathbf{r}_L(t) = (x_L(t), y_L(t), z_L(t))$, the MDF becomes time-dependent, written as

$$\text{MDF}_{\text{mGL}}(t, \mathbf{r}) = \frac{\kappa(z)}{w^2(z - z_L(t))} \exp \left\{ -\frac{2[x - x_L(t)]^2}{w^2(z - z_L(t))} - \frac{2[y - y_L(t)]^2}{w^2(z - z_L(t))} \right\}. \quad (3.6)$$

Considering a very sharp-peaking chromophore distribution like it is realized by a single immobilized molecule or nanoparticle, $c(t, \mathbf{r})$ can be approximated by a Dirca-delta function

$\delta(\mathbf{r} - \mathbf{r}_p)$ peaking at the particle position \mathbf{r}_p . Inserting this and eq. (3.6) into eq. (3.5) yields in the detected fluorescence rate

$$F(t, \mathbf{r}_p) = F_B + \frac{F_0 w_{xy}^2 \kappa(z_p)}{w^2(z_p - z_L(t))} \exp \left\{ -\frac{2[x_p - x_L(t)]^2}{w^2(z_p - z_L(t))} - \frac{2[y_p - y_L(t)]^2}{w^2(z_p - z_L(t))} \right\} \quad (3.7)$$

The focus scan path $\mathbf{r}_L(t)$ will now be specified for the 3D-SPOT case, where it consists of two concentric rings shifted by d_z with respect to each other and created alternately. This can be written as two sinusoidal and $\pi/2$ -phase shifted pathways of amplitude R and angular frequency ω_0 in lateral directions and a square wave shaped switching of the z -coordinate with frequency $\omega_0/2$. Hence, the laser scan path is

$$\mathbf{r}_L(t) = \begin{pmatrix} x_L(t) \\ y_L(t) \\ z_L(t) \end{pmatrix} = \begin{pmatrix} R \cos(\omega_0 t) \\ R \sin(\omega_0 t) \\ d_z/2 \text{ sqw}(\omega_0 t/2) \end{pmatrix}. \quad (3.8)$$

The used square wave function $\text{sqw}(x)$ can be defined for instance by a Fourier series as

$$\text{sqw}(x) = \frac{4}{\pi} \sum_{k=1}^{\infty} \frac{\sin((2k-1)x)}{2k-1}. \quad (3.9)$$

Consequently, a pass of the total scan pattern takes $2T$ with $T = 2\pi/\omega_0$. An important characteristic of the functions for the particular spatial directions is that they are orthogonal functions so that the particle coordinates can be determined independently of each other through demodulation. With the scan path eq. (3.8), the fluorescence rate turns eq. (3.7) into

$$F(t, \mathbf{r}_p) = F_B + \frac{F_0 w_{xy}^2 \kappa(z_p)}{w^2 \left(z_p - \frac{d_z}{2} \text{sqw}\left(\frac{\omega_0 t}{2}\right) \right)} \exp \left\{ -\frac{2[(x_p - R \cos(\omega_0 t))^2 + (y_p - R \sin(\omega_0 t))^2]}{w^2 \left(z_p - \frac{d_z}{2} \text{sqw}\left(\frac{\omega_0 t}{2}\right) \right)} \right\}. \quad (3.10)$$

This is the fluorescence rate detected from a single particle significantly smaller than the laser beam waist and given for a beam scan path described by two parallel circle lines in a microscope where the MDF can be expressed by a modified Gaussian-Lorentzian profile.

3.2 | DEMODULATION OF THE DETECTED PHOTON TRACE

While the fluorescence rate is a deterministic function depending on the time and the actual particle position, the detected photon trace is a stochastic quantity. The random number $\Upsilon(t)$ records the arrivals of single photons and peaks to one (per second) every time t_i a photon is registered by the detector chip. A photon trace is therefore given as

$$\Upsilon(t) = \sum_i \delta(t - t_i). \quad (3.11)$$

With the chosen approach, a digital processor counts the rising edges of the voltage pulses emitted by the detector once a photon hits the active surface area of the APD chip.

Since a photon trace realization is random, its statistical properties must be defined. Because the probability of detecting a given number of photons in a given time interval is

Poisson distributed, $\Upsilon(t)$ can be related to the time-dependent fluorescence rate $F(t)$ by [147]

$$\mathcal{E}(\Upsilon(t)) = F(t) , \quad \text{and} \quad (3.12)$$

$$\mathcal{E}(\Upsilon(t_1)\Upsilon(t_2)) = F(t_1)F(t_2) + F(t_1)\delta(t_1 - t_2) . \quad (3.13)$$

In practice, a small signal chunk $\Upsilon(t')$ for $t' \in [t_0; t_0 + \tau]$ is recorded, and further processed. For example, the total number of detected photons $N_{ph}(t)$ is calculated. Mathematically, $N_{ph}(t)$ can be expressed as an integral over the photon trace

$$N_{ph}(t) = \int_{t_0}^{t_0+\tau} \Upsilon(t', \mathbf{r}_p) dt' . \quad (3.14)$$

The expected number of detected photons N_{ph} is finally given by

$$N_{ph} = \mathcal{E}(N_{ph}(t)) = \int_{t_0}^{t_0+\tau} F(t', \mathbf{r}_p) dt' \quad (3.15)$$

Due to the fluorescence rate modulation during the signal acquisition, information about the particle position are enclosed in the photon trace and extracted by phase-sensitive lock-in integration. An estimator $\hat{\mathbf{r}}_p$ for the particle position \mathbf{r}_p can be constructed by a transformation of the shape

$$\hat{\mathbf{r}}_p(t) = N_{ph}^{-1} \int_{t_0}^{t_0+\tau} \Upsilon(t', \mathbf{r}_p) \mathbf{demod}(t') dt' , \quad (3.16)$$

where the *demodulation vector function* $\mathbf{demod}(t)$ was introduced. The detailed realization of $\mathbf{demod}(t)$ depends on the MDF and the beam scan pattern that is used to modulate the fluorescence. For the present geometry and integration times of an integer multiple n_{sp} of the modulation period $2T$, the demodulation vector function is written as

$$\mathbf{demod}(t) = \begin{pmatrix} \frac{w_c^2}{2R_x^2} \cos(\omega_0 t) \\ \frac{w_c^2}{2R_y^2} \sin(\omega_0 t) \\ \frac{w_c^4 w_z^2}{d_z w_{xy}^2 (w_c^2 - 2R^2)} \text{sqw}\left(\frac{\omega_0}{2} t\right) \end{pmatrix} , \quad (3.17)$$

where an abbreviation of the lateral laser beam waist in the center plane of a two orbit geometry $w_c = w(d_z/2)$ was used. In the appendix, these equations are derived explicitly (see appendix C.2) and it is shown how to implement such a transformation on a real-time processor saving computation time (see appendix C.3).

The estimator of the particle position is a random variable, as it is based on probing the statistical quantity $\Upsilon(t', \mathbf{r}_p)$. However, the estimator's expectation value is, in fact, the particle position

$$\mathcal{E}(\hat{\mathbf{r}}_p(t)) \approx \mathbf{r}_p . \quad (3.18)$$

The variance of the estimator is determined by several factors. First of all, the integrated peak number of photons

$$N_{\max} = 2TF_0 \quad (3.19)$$

influences the estimator's accuracy. Moreover, the variance scales quadratic with the laser focus intensity profile's characteristic length scale along the corresponding axis w_{xy} or w_z and is further influenced by an externally controllable, dimensionless function representing

the geometry of the scan pattern in lateral direction as

$$\Lambda_{xy}(\xi_\rho, \xi_z) = \frac{(1 + \xi_z^2/4)^{3/2}}{\sqrt{8}\xi_\rho} \exp\left(\frac{\xi_\rho^2}{1 + \xi_z^2/4}\right), \quad (3.20)$$

and in axial direction as

$$\Lambda_z(\xi_\rho, \xi_p) = \frac{(1 + \xi_z^2/4)^{5/2}}{\xi_z(1 + \xi_z^2/4 - 2\xi_\rho^2)} \exp\left(\frac{\xi_\rho^2}{1 + \xi_z^2/4}\right). \quad (3.21)$$

Thus, the lateral and axial variance of the position estimator reads

$$\text{Var}(\hat{y}_p) \approx \text{Var}(\hat{x}_p) \approx \left(\frac{w_{xy}\Lambda_{xy}(R/w_{xy}, d_z/w_z)}{\sqrt{N_{\max}n_{sp}}}\right)^2 \quad \text{and} \quad (3.22)$$

$$\text{Var}(\hat{z}_p) \approx \left(\frac{w_z\Lambda_z(R/w_{xy}, d_z/w_z)}{\sqrt{N_{\max}}}\right)^2. \quad (3.23)$$

While the operator of the setup is free in the choice of $\Lambda_{xy}(\xi_\rho, \xi_p)$ or $\Lambda_z(\xi_\rho, \xi_p)$, the number of counted photons is only indirectly controllable. Thus, a suitable scan path geometry should be worked out to minimize the estimator's positional variance (see section 6.1). A detailed computation of the corresponding expressions can be found in the appendix C.2.

3.3 | FEEDBACK CONTROLLER

In the previous section, a fluorescence modulation technique was introduced to determine the position of a static particle with respect to the center of a laser focus scan path. If the particle moves slowly compared to the time needed for its localization, a moving particle can be localized. Sequential localization yields an estimate for the particle's trajectory $\hat{\mathbf{r}}(t)$. The measurement time of the trajectory is restricted to the residence time of the particle within the detection volume. To obtain trajectories rich in data points, long experimental times are needed.

One way to achieve this is to apply feedback to the system that compensates for the particle movement. As already mentioned, the approach here is based on the stage scanner that has the sample chamber attached to it. To track the particle, the sample scanning must happen in the reverse direction with respect to the particle movement, resulting in non-invasive trapping of the particle within a fixed detection volume. The interplay of the sample coordinate system that is attached to the stage and the laboratory reference frame is illustrated in fig. 3.3.

In this section, the feedback controller will be presented that allows for the trapping. For a basic introduction into system theory and control systems, a brief overview is given in the appendix A.

The transfer function formalism will be used in the following and therefore, the Laplace transformation will be defined first. The Laplace transformation of a function $f(t)$ is defined as

$$F(s) = \mathcal{L}\{f(t)\} = \int_0^\infty f(t) e^{-st} dt, \quad (3.24)$$

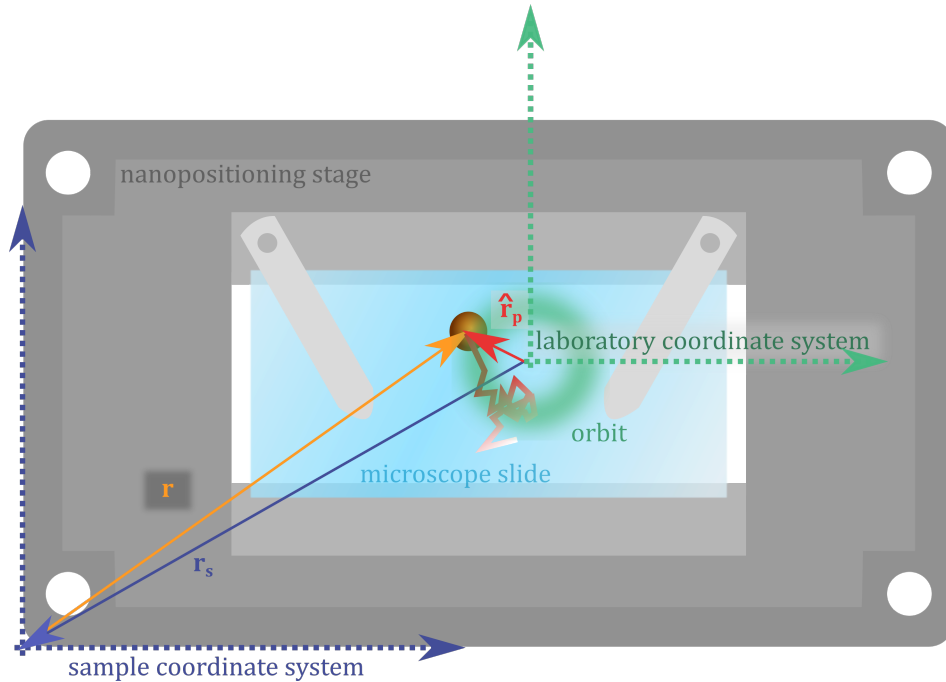


Figure 3.3.: Illustration of the relation between the sample stage and the laboratory coordinate system (not drawn to scale). The green coordinate system is fixed in space with its origin in the center of the detection volume. The orbital laser focus scan is centered around the laboratory coordinate systems origin. The sample coordinate system (blue) is fixed to that of the nanopositioning stage and moves on manipulation of the stage position r_s . Here the origin is selected arbitrarily in the lower left corner. The particle movement r takes place within the sample coordinate system, but the particle position is measured with respect to the laboratory coordinate system origin \hat{r}_p .

with the complex frequency $s \in \mathbb{C}$. The inverse Laplace transformation obeys

$$\mathcal{L}\{F(s)\}^{-1} = \frac{1}{2\pi i} \int_{c-j\infty}^{c+j\infty} F(s) e^{st} ds = \begin{cases} f(t) & \text{for } t > 0 \\ 0 & \text{for } t < 0 \end{cases}. \quad (3.25)$$

If available, Laplace transformed quantities are written as capital letters of the corresponding time domain variables.

In order to model, the feedback control system, the spatial particle coordinates and the stage axis are assumed to be completely independent from each other. Consequently, all equations in this section act on scalars and the final three-dimensional controller consists of three independent copies of the one-dimensional instances. In fig. 3.4, a block diagram helps to overview the control system.

The position of a particle $r(t)$ following Brownian motion in the overdamped regime is the integral over a Wiener process $\nu_{bm}(t)$ (see eq. (2.19)). The stage position $r_s(t)$ should follow this motion, and the error signal $e(t)$ is defined as

$$e(t) = r(t) - r_s(t). \quad (3.26)$$

The position estimator \hat{r}_p (see eq. (3.16), not drawn in fig. 3.4) measure this error signal corrupted by noise $n(t)$, which is modeled as Gaussian white noise given as the derivative

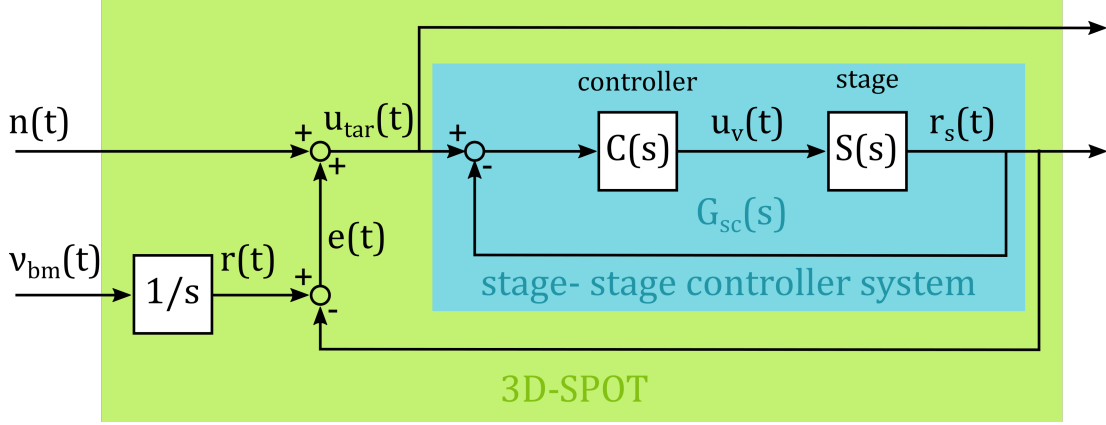


Figure 3.4.: Block diagram of the implemented feedback controller. Integration ($1/s$) of the driving Wiener process ν_{bm} yields the particle position $r(t)$. The difference between the particle’s position and the stage position $r_s(t)$ is the error signal $e(t)$ that is influence by counting noise $n(t)$. The error signal is used to determine the target control signal $u_{tar}(t)$ that is fed into a second control loop consisting of the stage controller with transfer function $C(s)$ and the stage itself with transfer function $S(s)$. The controller converts the target control signal u_{tar} to a control voltage $u_v(t)$. The stage responds with $r_s(t)$ to the control voltage which couples back to the error signal in the next loop iteration (inner and outer).

of a Wiener process $\nu_n(t)$ scaled with a noise density n

$$n(t) = n \frac{d\nu_n(t)}{dt} . \quad (3.27)$$

Hence, the signal that enters the stage controller, represented by the transfer function $C(s)$, is

$$u_{tar}(t) = e(t) + n(t) . \quad (3.28)$$

The controller converts this input signal to a voltage that drives the nanopositioning stage to the set point. This stage is represented by the transfer function $S(s)$, and its target is the particle position measurement in laboratory coordinates. In a second and faster control loop, the stage position is measured and fed back to the stage controller, where an internal proportional–integral–derivative (PID) controller is utilized to keep the stage on target. The combined stage–stage controller system is therefore represented by the transfer function $G_{sc}(s)$.

Continuing using the transfer function formalism, the input noise that drives the particles and influences the error signal translates to the stage position according to

$$\begin{aligned} R_s(s) &= G_{sc}(s) [E(s) + N(s)] \\ &= G_{sc}(s) [R_s(s) - R(s) + N(s)] \\ &= G_{sc}(s)R_s(s) - G_{sc}(s)s^{-1}\mathcal{L}\{\nu_{bm}(t)\} + G_{sc}(s)N(s) . \end{aligned} \quad (3.29)$$

After rearrangement, a direct relationship between the stage position and the noise sources is obtained

$$R_s(s) = \frac{G_{sc}(s)}{s[1 + G_{sc}(s)]}\mathcal{L}\{\nu_{bm}(t)\} + \frac{G_{sc}(s)}{1 + G_{sc}(s)}N(s) . \quad (3.30)$$

3.4 | TRAJECTORY RECONSTRUCTION AND ANALYSIS

A measured particle trajectory $\hat{\mathbf{r}}[k] = \hat{\mathbf{r}}(k\Delta t)$ with $k \in \{0, 1, 2 \dots N_{\text{pos}}\}$ is given as a sequence of N_{pos} positions recorded in equidistant time intervals Δt . A single position, written in Cartesian coordinates, is given as

$$\hat{\mathbf{r}}[k] = (\hat{r}_x[k], \hat{r}_y[k], \hat{r}_z[k]) . \quad (3.31)$$

The convention is used that discrete-time series are highlighted by an argument in rectangular brackets, that is the index of multiples of the sampling time interval.

The question arises, how to reconstruct the particle trajectory from the data generated by the SPOT measurement process? A SPOT measurement results in a file stored on a computer and looks like the example given in the appendix D.8. Besides the meta-information given in the file header, time series of the nanopositioning stage target position $\mathbf{u}_{\text{tar}}[k]$, the stage sensor output $\mathbf{r}_s[k]$ and the particle position with respect to the detection volume center $\hat{\mathbf{r}}_p[k]$, the detected photon number per channel, and the temperature and photodiode readout are stored as columns. The measured particle trajectory is defined by transforming the particle position from the laboratory reference frame to the sample chamber coordinates by

$$\hat{\mathbf{r}}[k] = \hat{\mathbf{r}}_p[k] - \mathbf{r}_s[k] . \quad (3.32)$$

The particle trajectory is used to compute further statistical quantities like the step-size distribution, the MSD or the (normalized) velocity autocorrelation function (nVACF).

The enumerated functions depend not on the absolute particle position, but on the particle displacements. Those displacements are represented by the increment vector specified for a particular lag time $\tau = k\Delta t$ and calculated as

$$\Delta\hat{\mathbf{r}}_k[i] = \hat{\mathbf{r}}[i+k] - \hat{\mathbf{r}}[i] , \quad (3.33)$$

with $i \in [0; N_{\text{pos}} - k]$. A histogram of all occurring displacements is called *step size distribution*. The step-size distribution considers the frequency of steps of a specific size and thus the average particle "velocity". However, it ignores temporal dependencies of the steps.

Those temporal dependencies are frequently studied with the help of the *normalized velocity autocorrelation* function (nVACF). According to [148, 149], the nVACF can be calculated as the averaged scalar product of successive increments vectors normalized by their absolute value via

$$\text{nVACF}_k[q] = \text{nVACF}_\tau(\Delta\tau = q\Delta t) = \frac{1}{N_{\text{pos}} - q} \sum_{i=0}^{N_{\text{pos}}-q} \frac{\Delta\hat{\mathbf{r}}_k[i]}{|\Delta\hat{\mathbf{r}}_k[i]|} \cdot \frac{\Delta\hat{\mathbf{r}}_k[i+q]}{|\Delta\hat{\mathbf{r}}_k[i+q]|} . \quad (3.34)$$

Positive values of nVACF indicate consecutive steps in the same direction, negative values in opposing directions. However, the most important function to elucidate the temporal evolution of the step sizes is the time-averaged MSD, that is calculated from a single trajectory as

$$\text{MSD}[k] = \text{MSD}(\tau = k\Delta t) = \frac{1}{N_{\text{pos}} - k} \sum_{i=0}^{N_{\text{pos}}-k} (\Delta\hat{\mathbf{r}}_k[i])^2 . \quad (3.35)$$

A fast way to compute the MSD for equally spaced lag-times is possible by splitting the sum in eq. (3.35) into correlation functions that can be calculated with the help of the

fast Fourier transformation (see appendix C.4 for more details).[150] Sometimes it may be interesting to investigate each spatial dimension separately. A three-dimensional MSD can therefore be dissected into three one-dimensional MSDs

$$\text{MSD}[k] = \text{MSD}_x[k] + \text{MSD}_y[k] + \text{MSD}_z[k] , \quad (3.36)$$

or one two-dimensional and one one-dimensional MSD, e.g.,

$$\text{MSD}[k] = \text{MSD}_{xy}[k] + \text{MSD}_z[k] . \quad (3.37)$$

Thus, the dimensionality of the MSD is named after the number of spatial dimensions of the underlying trajectory and labeled with the corresponding axis name.

4 | EXPERIMENTAL SETUP

The experimental setup of 3D-SPOT is basically an extension of a home-built fluorescence microscope that is controlled in real-time by feedback application. The optical setup is sectioned into four parts: A light sources unit, a beam deflection unit, a confocal microscope and a detection unit.

A schematic representation of the relevant components is illustrated in fig. 4.1. While a detailed technical description of the setup is given in the appendix D, the conceptual functioning will be explained in the following.

4.1 | OPTICAL SETUP

The light source unit consists of an application-dependent selection of lasers that are coupled into an optical single-mode fiber that transmits the laser light into a beam deflection unit. By doing this, lasers can be exchanged with a minimum of manual alignment needed in the remaining microscope units. Additionally, multiple lasers can be combined to a single beam that is perfectly co-aligned.

The beam deflection unit is required for creating two coaxial light orbits that are shifted with respect to each other along the optical axis in the detection volume. Therefore, the light path is split and combined again before it is guided to the confocal microscope body. On this way, three single-axis acousto-optical deflectors (AODs, see appendix D.2 for technical details) scan the beam in electronically controlled patterns. In each of the light pathways one of the two light orbits is generated. To switch back and forth between the orbits, the respective other beam is directed against the rim of an aperture with the help of the AODs. The desired axial displacement of the two light orbits along the optical axis is achieved by a slight deadjustment of two lenses within each branch. A detailed analysis of the relation between the angular deflection via the AODs, the (de-)adjustment of the lenses and the focus position within the sample plane is conducted with the help of *ray transfer matrix analysis* (see appendix D.3).

After entering the confocal microscope via a side-port, the deflected beam is guided by a dichroic mirror into an infinity-corrected microscope objective that focuses the light onto the sample that is mounted on a three-axis nanopositioning stage. The sample's fluorescence is collected by the same objective, passes the dichroic mirror and is imaged into the detection unit through a pinhole onto two avalanche photodiode (APD) based single-photon counting modules. Both detectors generate TTL pulses on the detection of a single-photon. Those pulses are counted by the electronics.

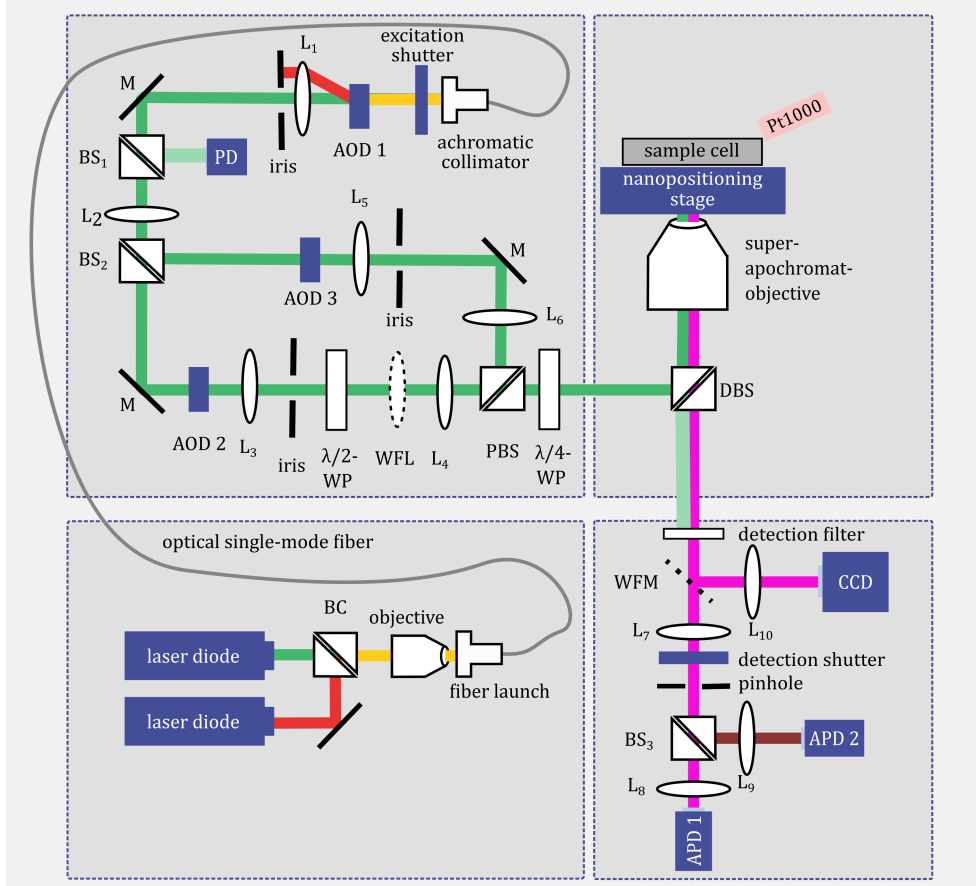


Figure 4.1.: Schematic representation of the optical setup for 3D-SPOT (not drawn to scale). The optical axes of the excitation beams are indicated by the green, red, and yellow bar representing its wavelength(s). The optical axis of the emission beam is drawn as a violet bar. Lenses with focal length f_i are indicated by L_i . Optical devices like lenses, objectives, filters, wave plates, etc. are drawn as white shapes. Several beam splitter/combiner are used: The excitation beam combiner (BC), non-polarizing 50:50 beam splitter cubes (BS_1 , BS_2 and BS_3), the polarizing beam splitter (PBS), and the dichroic mirror (DBS). Mirrors M or apertures like irises or pinholes are represented by black lines. Blue geometries indicate wired devices like the acousto-optical deflectors (AODs), a photodiode measuring the laser power for reference (PD), single-photon counting modules (APD 1 and 2), a charged-coupled device camera (CCD) and the nanopositioning stage. Dashed lines express the optional character of the wide-field lens (WFL) and wide-field mirror (WFM). A Pt1000-sensor element is used to record the room temperature next to the sample cell. Further explanations are given in the main text. A complete overview about the setup's electronics was waived in this figure for the sake of visual clarity, but it is illustrated in fig. D.9 in the appendix

4.2 | NANOPositionING STAGE

A critical component of the SPOT setup is the nanopositioning stage realized by a three-axis sample holder moved by piezoceramic actuators. Unfortunately, piezoceramic actuators suffer from several effects that hamper their usage in application.[151] For instance, the applied voltage is related to the displacement of the piezoceramic actuator by a hysteresis. Frequency components in the driver signal may excite mechanical vibrations. Furthermore, drift motion, known as creeping, occurs in situations where voltages are constantly applied over a long period of time, and limit the positional accuracy in the low-frequency range.

Because the positioning stage is so essential for the tracking performance, the initially used device was upgraded within this work's time span. A closed-loop device from *PI - physik instrumente* (P-545.3D8S, PInano Trak Piezo Tracking System, Physik Instrumente (PI) GmbH & Co. KG) replaced an open-loop system from *piezosystem jena* (Tritor 102, Piezosystem Jena). While many devices on the market are optimized in terms of spatial accuracy, which may be specified in the range below one nanometer, the application of SPOT requires fast response behavior. Long travel ranges enable simple usage and possibly long trajectories to record. This and some aspects concerning the type of construction and communication interfaces lead to the currently used device. The stage controller is equipped with a 20 kHz *proportional-integral-derivative* (PID) control loop and a notch filter removing frequencies in the range of the stage's resonance frequency from the driving signal.

More technical information and a detailed characterization of the stage is found in the appendix D.4 and appendix D.5, where also the stage-stage controller transfer function was identified.

4.3 | SETUP CONTROLLER

The core component of the setups control logic is an ADwin system (ADwin Gold II, Jäger Computergesteuerte Messtechnik GmbH). The ADwin is a self-sufficient, programmable digital signal processor that communicates with a PC (Windows 10, 64 bit), where a home-written graphical user interface (QtSPOT) enables the experimenter to configure the setups settings and to interact with the hardware without disturbing the real-time processing that happens on the ADwin's computation unit. The ADwin system sends the driver signals for the beam deflection to the AODs, sets the target values for the nanopositioning stage, receives the readout from the stage's position sensors and counts the photons detected by the APDs. Furthermore, it performs all computation needed for the localization and feedback application of the SPOT procedure and buffers the data, before they are transferred to the PC's hard drive.

More technical details about the ADwin system and the software realization can be found in the appendix D.6 and appendix D.7, respectively.

4.4 | COMMENTS ABOUT THE SETUP

The available hardware is sufficient to execute several further measurement methods, while switching between them needs on almost no manual intervention. For instance, FCS (with one, two, or moving laser beam foci), and 3D confocal scanning microscopy are already implemented. Just by pushing a button in the control software (QtSPOT), the setup changes

its operation mode. The AOD settings can be used to select an excitation wavelength by software. Switching to wide-field mode is just as easy and opens the door for camera-based SPT.

The addition of the axial fluorescence modulation increases the complexity of the setup tremendously. While 2D-SPOT needs only the focus width and orbit radius to be calibrated, 3D-SPOT requires the axial focus profile and the orbit distance. Especially because of the orbit separation being manipulated manually, time-consuming adjustment procedures are needed. Furthermore, the symmetry of both the excitation scan path and its arrangement in the detection volume must be guaranteed. It is necessary to check the properties of two foci and two orbits to match with high precision. Changing between excitation colors increases the number of calibration parameters.

Therefore, standardized calibration methods are an essential ingredient for the reliable operation of this setup. Some automated protocols are already implemented in the existing software.

5 | MATERIALS

In general, the sample systems that are used for SPOT experiments consist of two major ingredients. The first component is the fluorescent tracer which is the particle to be tracked by the method. Its properties like size, photo-physics and surface chemistry directly impacts the measurement accuracy and a proper particle choice is advised. The second component of the SPOT sample is the particle's environing medium. The medium's composition and its internal structure affects the diffusion behavior of the fluorescent probe. Depending on the experiments objective either a particle with known properties can be used to inspect its ambient conditions or the other way around.

In the context of this thesis, two different types of samples are employed: Isotropic nanoparticle suspensions, where individual fluorescent polystyrene spheres diffuse freely within homogeneous fluids and a nanoporous polymer membrane that is filled with a nanoparticle suspension and that confines the particles motion.

In this chapter, the fluorescent probes are explained and characterized first. Then, the polymer membranes used for the experiments in chapter 8 are introduced. In the last sections of this chapter, the actual sample preparation steps for the different experiments are summarized.

5.1 | FLUORESCENT PROBES

First, it needs to be specified what types of particles can and cannot be tracked by SPOT. An illustrative overview about the particle categories discussed in the following is given in fig. 5.1.

Organic dyes, for example, are synthetic molecules of low molecular weight and present in a wide variety of excitation and emission spectra. Dyes with very high quantum yields and extinction coefficients are available, like the very common fluorescein or rhodamine dye molecules.[158] Generic compounds like these have derivatives with tailored properties such as water solubility or photo-stability. Besides the flexibility of their photo-physical characteristics, dyes excel in their labeling properties. Due to their small size (~ 1 nm), labeling with an organic dye has minor influence on its target's biological function, for instance. In contrast, their small size (diffusing too fast) and limited photo-stability (photo-bleaching and blinking) hampers their usage as tracer particle for SPOT.

Naturally occurring fluorophores, like the *green fluorescent protein* (GFP)[159] and its many derivatives with tailored photo-physical properties (e.g. emitting in different spectral ranges, like the UV, yellow, orange, red, or infrared, showing enhanced photophysical properties like eGFP and eYFP or being even photo-activatable or -switchable [158, 160–165]) are in general larger than organic dyes and may be tracked with SPOT under the right experimental conditions. But in general, their applicability for SPOT is restricted similarly to organic dyes by their photo-stability.

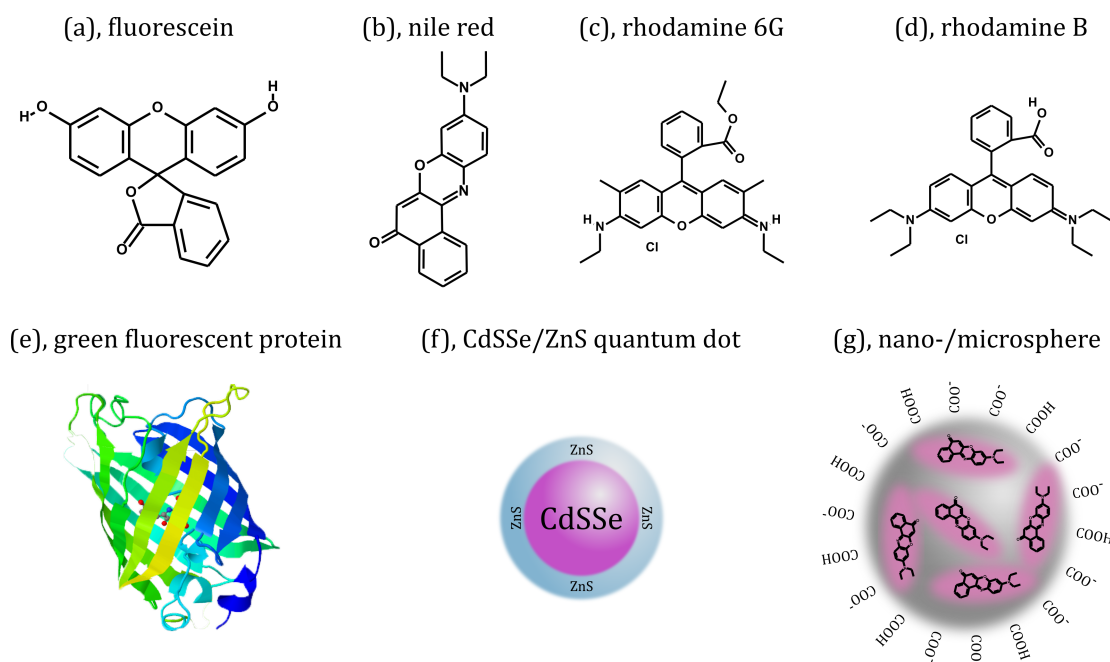


Figure 5.1.: Examples of fluorescent probes (not drawn to scale). The chemical structures of (a) fluorescein[152], (b) Nile red[153], and the two rhodamine derivatives, (c) rhodamine 6G[154] and (d) rhodamine B[155], are shown in the top row. In the bottom row, there is (e) the 3D structure of GFP (graphic taken from protein data bank with PDB ID: 1EMA[156, 157]) and schematic sketches of (f) a core-shell quantum dot and a (g) nano-/microsphere. As an example of the core-shell quantum dot, a CdSSe/ZnS compound was drawn and for the microsphere, a polystyrene bead labeled with Nile red and a carboxyl-modified surface. For near-neutral pH values, some carboxyl groups are charged (COO^-), and some are not ($COOH$).

However, there is a particle class of similar size that is very photo-stable. Quantum dots are nanoscale crystals (2-20 nm) of semiconductor materials with remarkable electronic and optical properties.[166, 167] In practice, samples containing quantum dots must be handled with care, as they contain heavy metals that are cytotoxic and may endanger the health of the experimenter or the investigated sample.[168–171] For experiments on the single nanocrystal level, it must be considered that quantum dots show similar blinking behavior like those of single-molecules.[172]

Less hazardous and not influenced by blinking are so-called *nano-* or *microspheres*. Those synthetic particles, sometimes also called *nanobeads*, are of spherical shape with a diameter in the nanometer or micrometer range. The used materials can vary strongly, but two important classes are silica-based or polymeric nanospheres. Both are not fluorescent and therefore have to be loaded with dyes for the purpose of fluorescence microscopy. In the case of polymeric particles, physical adsorption is a popular method to attach fluorescent dyes to preformed polymer particles.[173] As this adsorption is potentially reversible, dye leakage may occur, and copolymerization with reactive dyes has been developed to overcome this problem.[174] Today, many different fluorescent nanobeads are available commercially, leaving their exact preparation unknown as a business secret. In this thesis, fluorescent polymeric spheres significantly smaller than 1 μm and made of polystyrene are used. Polystyrene nanobeads are nontoxic and fairly biocompatible, disregarding the contemporary micro/nanoplastic debate. Furthermore, they are highly hydrophobic and can consequently be doped with a wide range of apolar fluorophores. However, their flexibility about surface modification is limited.[175] To stabilize nanospheres in aqueous environ-

ments, modification with carboxy groups are common because it allows for surface charge control via pH and ionic strength.[176] Carboxylated polymer particles are capable of forming amide bonds with amino groups of bioligands, which is a frequently used strategy to label proteins. But also other functional molecules like streptavidin can be coated on polystyrene particles.[177] Being loaded with large amounts of dye and with a flexible choice of size, nanobeads appear as the favorite tracer particle class for SPOT experiments.

The fluorescent probes that are used as tracer particles for SPOT experiments are listed in table 5.1 with the information provided by the respective manufacturer.

Table 5.1.: Listing of the used fluorescent particles and their specifications. Central excitation (exc.) and emission (em.) wavelength are defined by their spectral maximum. The nominal diameter \varnothing_{nom} is provided by the manufacturer.

product number	name	manufacturer	material	exc./nm	em./nm	$\varnothing_{\text{nom}}/\text{nm}$
F8786	FluoSpheres Nile Red, Fluorescent Microspheres	Thermo Fisher Scientific	polystyrene, carboxylate-modified	535	575	27 ± 4
F8783	FluoSpheres Dark Red, Fluorescent Microspheres	Thermo Fisher Scientific	polystyrene, carboxylate-modified	660	680	25 ± 4
T10711	TransFluoSpheres	Thermo Fisher Scientific	polystyrene, streptavidin-labeled	488	645	48 ± 6
CAF-050NM	Red Fluorescent Particles	Magsphere Inc.	polystyrene, carboxylate-modified	538	584	50 ± 18
CAF-100NM	Red Fluorescent Particles	Magsphere Inc.	polystyrene, carboxylate-modified	538	584	100 ± 20

The actual size distributions of a subset of the listed particles were determined by *dynamic light scattering* and the CONTIN analysis.[178] The obtained particle distributions are given in fig. 5.2. Measured diameters differ from the information provide by the manufacturers, which is not an unusual finding. Similar deviations between nominal and actual particle diameters have been found before.[179, 180]

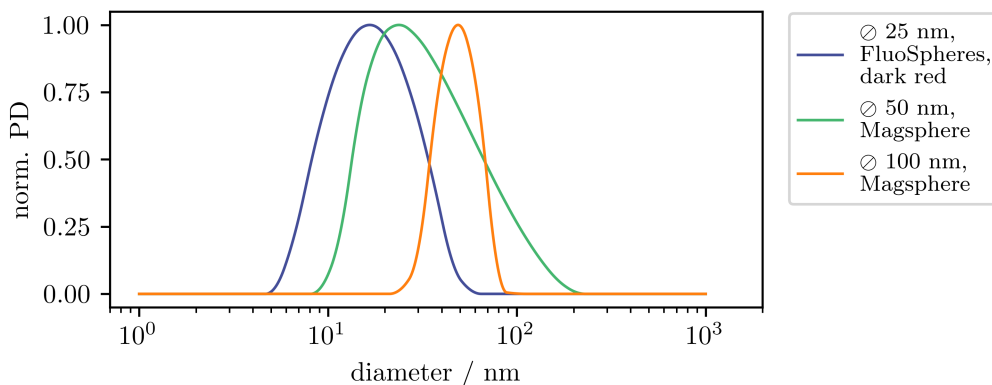


Figure 5.2.: Particle diameter distribution determined via the CONTIN analysis of dynamic light scattering experiments

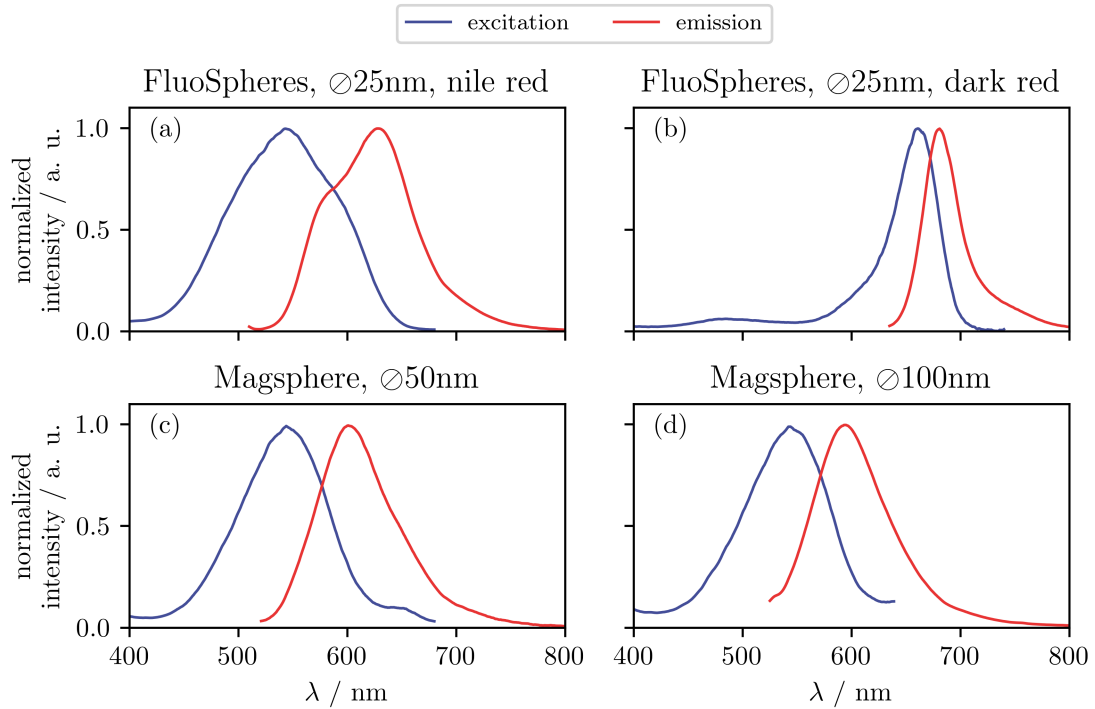


Figure 5.3.: Spectra recorded with a fluorescence spectrophotometer (Cary Eclipse fluorescence spectrophotometer, Varian Inc.) in buffered water. Excitation spectra are shown as solid blue lines and emission spectra as solid red lines. For a detailed description of the particles see table 5.1.

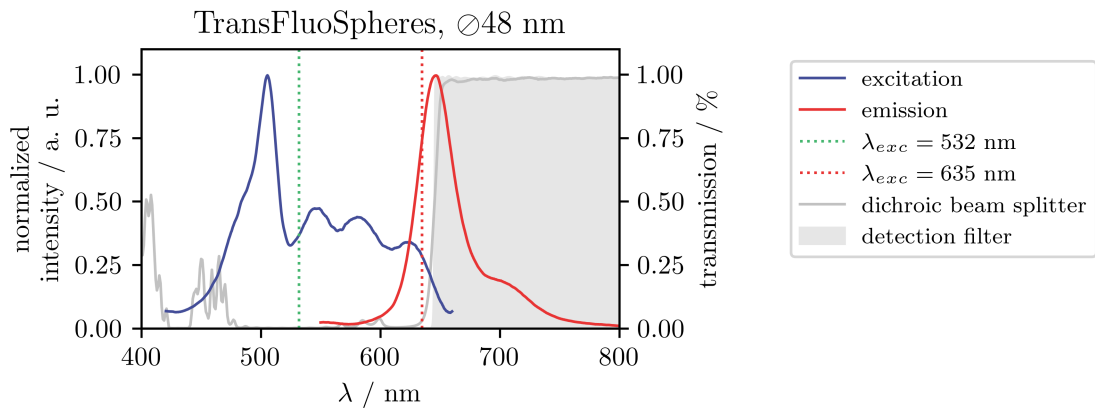


Figure 5.4.: Excitation (solid blue line) and emission (solid red line) spectrum of the TransFluoSpheres (see table 5.1) recorded with a fluorescence spectrophotometer (Cary Eclipse fluorescence spectrophotometer, Varian Inc.) in buffered water. In section 9.2, TransFluoSpheres are excited with two different laser wavelength (dashed green and red line), while maintaining the optical filter set (dichroic beam splitter: zt633rdc, Chroma Technology Corp., gray line; longpass detection filter: z633 RDC, AHF analysentechnik AG, light gray area)

Fluorescence emission and excitation spectra are recorded with a fluorescence spectrophotometer (Cary Eclipse fluorescence spectrophotometer, Varian Inc.) in buffered water (Phosphate-buffered saline, $pH = 7.4$) and shown in fig. 5.3. Obviously, the FluoSpheres labeled with the dye *nile red* (fig. 5.3 (a)) and the particles purchased from Magsphere Inc. (fig. 5.3 (c) and (d)) can be used with the same excitation wavelength (here: $\lambda_{\text{exc}} = 519 \text{ nm}$) and optical filters (dichroic mirror: DBS, z532 RDC, AHF analysentechnik AG; detection filter: HQ545LP, AHF analysentechnik AG). For the FluoSpheres labeled with the dye *dark red* a different spectral setting is necessary (excitation wavelength: $\lambda_{\text{exc}} = 635 \text{ nm}$; dichroic mirror: zt633rdc, Chroma Technology Corp.; detection filter: BLP01-633R-25, AHF analysentechnik AG).

In section 9.2, TransFluoSpheres are used in a dual-color excitation experiment, because of their special spectral characteristics (see fig. 5.4). Because of their special labeling with multiple dyes, energy transfer takes place and a broad band excitation spectrum is accompanied by a plain emission spectrum in the red spectral range. The particle's fluorescence spectrum in fig. 5.4 is supplemented with the spectral design of the dual-color experiment.

5.2 | NANOPOROUS TRIBLOCK TERPOLYMER MEMBRANES

In chapter 8, membranes formed via *self-assembly and non-solvent induced phase separation* (SNIPS [181], see below) from polystyrene-*block*-polyisoprene-*block*-poly(N-isopropylacrylamide) (PS₄₃-*b*-PI₄₀-*b*-PNIPAAm₁₇, subscripts denote the weight fractions of the corresponding segments, see fig. 5.5(a)) are used. This amphiphilic triblock terpolymer with a molar mass of $61\,100 \text{ g mol}^{-1}$ and a dispersity of 1.27 was synthesized via *nitroxide-mediated polymerization* in the group of FELIX H. SCHACHER. One reason for the choice of this material was that the PNIPAAm part is also known to show stimuli-responsive behavior. In future applications, such a system may not only serve as a static ultrafiltration substrate, but also as a stimuli-responsive gating membrane (see fig. 5.5(b)). With a *lower critical solution temperature* (LCST) between 30°C and 40°C in water, this polymer block expands to a relaxed chain for temperatures below the LCST and collapses to a dens coil for higher temperatures widening the membranes pores (see fig. 5.5(b)).[182, 183]

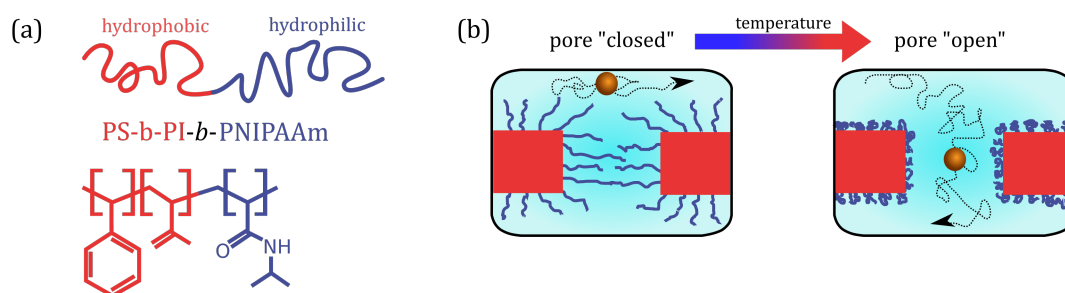


Figure 5.5.: (a) Structure of polystyrene-*block*-polyisoprene-*block*-poly(N-isopropylacrylamide). The two hydrophobic blocks are colored red, the hydrophilic block is drawn in blue. (b) Concept of a stimuli-responsive gating membrane inspired by [184]. Steric repulsion prevents a diffusing nanoparticle to pass the membrane pore. Heating the system above the LCST opens the pore, because the stimuli-responsive polymer chains collapse.

SNIPS is the combination of self-assembly of diblock copolymers with a industrially important production process of membranes for pressure-driven separation purposes, that is the *non-solvent-induced phase separation* (NIPS). In the fast process of isothermal NIPS, introduced by LOEB and SOURIRAJAN 50 years ago [185], a concentrated solution (10 - 25 wt%) of a polymer is cast on a substrate and subsequently immersed in a non-solvent bath. The residence time between the casting and the immersion in the bath is called the *open-time*. In the immersion bath, an exchange of the solvent and non-solvent results in a phase separation, where the polymer-rich phase forms the matrix structure and the polymer-poor phase becomes the voids during coagulation. In presence of a highly volatile solvent as a significant part of the casting solution, the formation of a dense skin on top of the porous structure is promoted. Membranes prepared by NIPS are therefore integrally asymmetric. In filter applications, the *top* or *skin layer* carries out the separation, while the substrate provides resilient mechanical properties with negligible resistance to the transmembrane flow. Parameters that influence the cross-section morphology are the used polymer, the selection of solvents and non-solvents, the selection of additives, the open-time and environmental parameters like ambient temperature and humidity.

Is the phase-inversion carried out with a block copolymer, the porous bulk material is formed as usual for the homopolymer case by liquid-liquid demixing. Furthermore, self-assembly occurs in the skin layer and produces an ordered structure, suitable parameter settings provided. That means a highly-ordered and thin top layer is supported from underneath by a non-ordered sponge-like bulk material.

5.3 | SAMPLE PREPARATION

In the following two sections, the actual sample preparations are described for the 3D-SPOT experiments presented in chapter 7 and chapter 8. All samples are applied as small drops (in general of about 25 μl) to a rectangular precision cover glass (24 \times 50 mm, thickness: (0.170 ± 0.005) mm, Paul Marienfeld GmbH & Co. KG) and sealed with vacuum grease (SGM494 Silicone Grease, ACC silicones) and a round coverslip (\varnothing 25 mm, thickness: 1.5H, Carl Roth GmbH + Co. KG). Thin rings punched out of a polydimethylsiloxane (PDMS) stamp resin served as spacers between the cover glass and the coverslip. Care was taken that the total weight of a sample cell resides in the range of 0.8 g to 1.0 g. A constant sample cell weight is important to maintain a reproducible response behavior of the nanopositioning stage which is mass dependent.

5.3.1 | NANOPARTICLE SUSPENSIONS FOR REFERENCE EXPERIMENTS

In chapter 7, reference experiments are conducted with nanoparticle suspensions in different aqueous solution media. Therefore, fluorescent polystyrene nanoparticles with a carboxylate-modified surface and nominal diameters of (27 ± 4) , (50 ± 18) and (100 ± 20) nm (F8786, FluoSpheres Fluorescent Microspheres, Thermo Fisher Scientific; CAF-050NM, Red Fluorescent Particles, Magsphere Inc.; CAF-100NM, Red Fluorescent Particles, Magsphere Inc.) are diluted in glycerol/water concentration series ranging from 50 vol% to 99 vol%, in dextran (15 wt% and 30 wt%), saccharose (60 wt%) and polyethylene glycol (30 wt% and 50 wt%) solutions. All samples were prepared with nominal nanoparticle number concentrations varying between 5 μM and 25 μM depending on the particle size.

For the glycerol solutions, pure glycerol (92.09 g mol^{-1} , product number: G5516, Sigma-Aldrich, Inc.) was mixed with high-purity water (Milli-Q). Powders of dextran (from *Leu-*

conostoc spp., 500 kDa, product number: 31392, Sigma-Aldrich, Inc.), saccharose (D(+)-Saccharose, 342 Da, product number: 4621.1, Carl Roth GmbH + Co. KG) and polyethylene glycol (Poly(ethylene glycol), 5000 to 7000 g mol⁻¹, product number: 81255, Sigma-Aldrich, Inc.) were solved in buffered water. The used buffer solution was a phosphate-buffered saline (0.01 M phosphate buffer, 0.0027 M potassium chloride, 0.137 M sodium chloride) with a *pH* of 7.4 at 25 °C that was prepared by solving 1 buffer tablet (phosphate buffered saline tablet, product number: p4417, Sigma-Aldrich, Inc.) in 200 ml high-purity water (Milli-Q).

5.3.2 | POLYMER MEMBRANES INFUSED WITH NANOPARTICLE SUSPENSIONS

In chapter 8, triblock terpolymer membranes are infused with a aqueous mixture containing the fluorescent nanoparticles. To prepare such samples several steps are needed.

First, the PS₄₃-*b*-PI₄₀-*b*-PNIPAAm₁₇-membranes with an area of several square centimeters were cut into small pieces ($\approx 0.5 \text{ cm} \times 0.5 \text{ cm}$) with a scalpel and stored in high-purity water (Milli-Q) at 4 °C. Later on, some cuttings were used for electron microscopy, as described in section 8.2, and for the SPOT experiments maintaining exactly the same batch.

In total, three different classes of fluorescent polystyrene nanoparticles with a carboxylate-modified surface are used, which all differ in size. Their nominal diameter were (25 ± 4) nm, (50 ± 18) nm and (100 ± 20) nm (F8783, FluoSpheres Fluorescent Microspheres, Thermo Fisher Scientific; CAF-050NM, Red Fluorescent Particles, Magsphere Inc.; CAF-100NM, Red Fluorescent Particles, Magsphere Inc.), respectively.

Nanoparticle were suspended in 2,2'-tiodiethanol (TDE, 122.19 g mol⁻¹, product number: 166782, Sigma-Aldrich, Inc.) mixed with an aqueous buffer in a ratio of about 1:1 vol/vol. The aqueous portion of the final buffer had a *pH* of 8 (sodium phosphate saline) at an ionic strength of 15 mM and the final mix showed an additional concentration of the non-ionic detergent Triton X-100 (Triton X-100, product number: 10789704001, Sigma-Aldrich, Inc.) of 0.1 vol%. The dynamic viscosity of the final mixture was determined to 4.9 mPa s with a rolling-ball viscometer (AMVn, Anton Paar GmbH) and density and sound velocimeter (DSA 500 M, Anton Paar). The temperature dependency of the dynamic viscosity for pure TDE and the aqueous buffer containing 53 vol% TDE are depicted in fig. E.2 in the appendix E.1). Using this buffer solution, nanoparticle suspensions with number concentrations of 7 pM were prepared.

Before infusing the membranes void space with the nanoparticle suspension, a piece of the membrane was taken out from its storage box filled with high-purity water and dried gently under nitrogen flow. Subsequently, a droplet ($\approx 10 \mu\text{L}$) of sodium phosphate buffer at a *pH* of 8.0 was placed on top of the membrane and allowed to soak in for 5 minutes. The membrane was dried again under nitrogen, wetted with 5 μL of the nanoparticle suspension.

6 | ERRORS, LIMITATIONS AND ARTIFACTS

3D-SPOT is a method that is affected by a number of error sources. Ignoring the occurring inaccuracies and problems leads to misinterpretations and reduces the ease of applying the method. For this reason, a closer examination of the error sources and performance constraints of the setup is indispensable.

In this chapter, it will be differentiated between *localization* and *tracking errors*. While a localization error is present even for a single estimation of the particle position, the tracking error describe the discrepancies between the real and measured particle position for repeated measurements. The inspected errors are the localization error due to photon-counting noise, the systematic localization error intrinsic to the used estimation equations, and the dynamic localization error occurring because of the particles movement during signal acquisition. Furthermore, the tracking error is considered that is produced by the interplay of all those localization errors. Finally, the system's feedback response behavior and its effects on the tracking error are studied.

The analysis is based on a comprehensive simulation of the measurement process. Technical details about the simulation are described in the appendix C.5. The simulation is a modularized implementation of the model described in chapter 3 incorporating nonlinearities in the signals and making it possible to switch individual effects on and off for separated discussion. In contrast to a real experiment, not only the measured particle position $\hat{\mathbf{r}}[k]$ is known, but also the "real" particle position $\mathbf{r}_p[k]$. This allows for a direct and quantitative observation of the localization errors. For feature-rich results, the real particle position is simulated on a finer time scale than the measurement sampling time. In order to compare the particle position estimate with the real particle position, the average real particle position $\bar{\mathbf{r}}[k]$ is computed for the trajectory part of a single scan path cycle (see eq. (C.68)). The tracking error vector $\boldsymbol{\chi}[k]$ is the difference between this averaged particle position and the reconstructed particle position.

$$\boldsymbol{\chi}[k] = \hat{\mathbf{r}}[k] - \bar{\mathbf{r}}[k] \quad (6.1)$$

The square root of Pythagorean sum over the components of the tracking error vector $\boldsymbol{\chi}[k]$ is the tracking error

$$\chi[k] = \sqrt{\chi_x[k]^2 + \chi_y[k]^2 + \chi_z[k]^2} . \quad (6.2)$$

It is helpful to look at the results of a single simulation run, as this shows more directly what is later studied in a systematic examination at a more condensed level. In fig. 6.1, an example of a simulated trajectory is shown. The simulation of SPOT generates a "measured" trajectory that successfully approximates the real particle trajectory. The error of the reproduced particle trajectory appears larger in axial than in lateral direction.

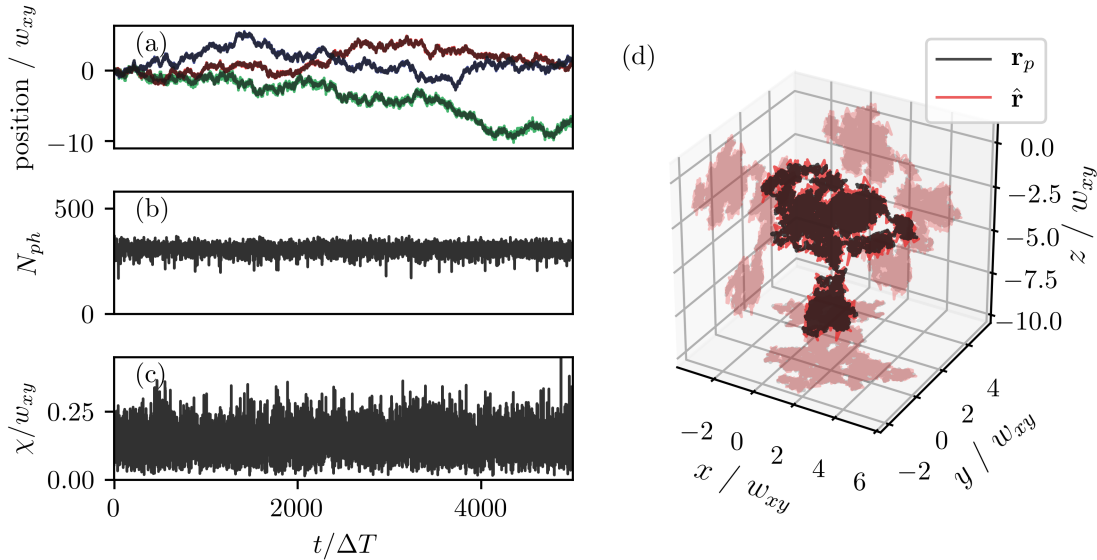


Figure 6.1.: Example of a simulation with 5×10^3 loop iterations. The real particle trajectory consists therefore of 160×10^3 positions. For a realistic view, all spatial quantities are scaled with the lateral beam width assuming $w_x = w_y = w_{xy}$ and $w_z = 3w_{xy}$. The input parameter were $D = 0.0035\Delta t w_{xy}^{-2}$, $F_0\Delta t = 500$, and $F_b\Delta t = 1$. The optimal focus scan path was used (see section 6.1). In (a), the real particle position r_i (black) and the estimated trajectory \hat{r}_i (x : blue, y : red, z : green) is plotted versus time. The temporal progress of (b) the number of detected photons per estimation cycle N_{ph} and (c) the tracking error amplitude χ are drawn. (d) Three-dimensional view of the real particle trajectory \mathbf{r} (black) and the measured one $\hat{\mathbf{r}}$ (red). Projections on two-dimensional planes are plotted with higher transparency.

This is expected due to the different spatial extent of the laser focus profile and shows that a separate analysis of the lateral and axial dimensions is needed. In the example, the number of detected photons N_{ph} per position estimation fluctuates around 350 with about 7.5% variation and is less than the input peak photon number $F_0\Delta t = 500$. This is reasonable since the particle is kept in the center of the scan path and will not be excited by the maximum focus intensity. The dependency of the measured photon count rate on the focus scan path shape is analyzed in section 6.1. The averaged tracking error of the entire track is $(0.128 \pm 0.054) w_{xy}$, which would amount to 30 to 40 nm in a real experiment. This value is expected to vary strongly with the input parameter of the concrete measurement/simulation scenario. The quantitative analysis of these dependencies is one of the purposes of the following chapters. Here, however, the approximate range of resolution becomes apparent, which is a two figure nanometer number that correspond to a length scale one order of magnitude lower than the classical diffraction limit.

A granular view about simulation results is given in fig. 6.2, where the actual particle position, the averaged real particle position of single signal acquisition interval and the estimated particle position are drawn alongside the inverted stage target position and its actual (inverted) response. Perfect localization accuracy would be reached if the estimated particle position would coincide with the averaged real particle position. However, the random nature of photon counting-based position estimation results in an inevitable lack of accuracy. Two important aspects can already be seen here. The position averaging smooths the path actually covered by the particle and the imprecision of the localization leads to an apparently stronger position fluctuation. The stretched laser focus size in the axial direction and the simultaneously worse position accuracy amplifies this overestimation

for the z -direction, as evident in a comparison of fig. 6.2 (b) to the lateral accuracy derived from fig. 6.2 (a). Because the (inverted) stage target position is set to the last known particle position, the target signal trajectory is compulsorily shifted by a total feedback period. According to the simulation settings a feedback period corresponds to three position estimation cycles. The lagging of the stage movement behind the target positions is striking and clearly visible in the inset of fig. 6.2 (a). This delayed motion is characterized by the stage-stage controller's frequency response and discussed in section 6.3.2. It is easy to deduce that the moving stage strongly influences the first position estimation after setting a new target. For this reason, the acquired fluorescence signal was ignored for position estimation in this period of time in the previous implementation of SPOT.[186]

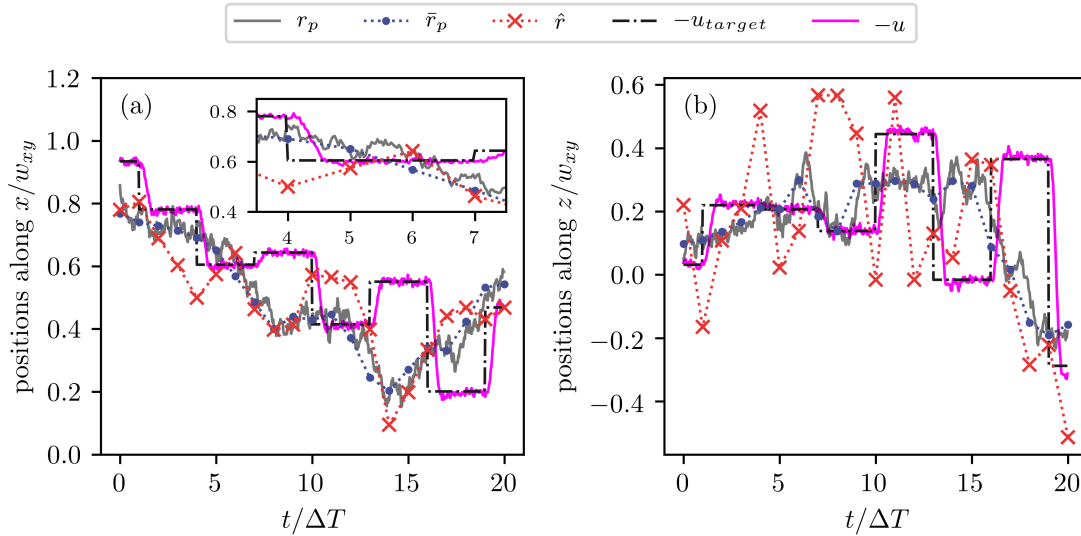


Figure 6.2.: Zoomed view on a simulation example generated with the same parameter as in fig. 6.1. (a) and (b) are the traces along the x -axis and z -axis, respectively. The real particle trajectory r is plotted as a solid gray line, the averaged real trajectory \bar{r} as blue dots connected with a dotted line, and the estimated particle trajectory \hat{r} is given as red crosses also connected by a dotted line. The stage follows the particle trajectory in an inverted coordinate system, therefore, the stages target position u_{target} (dash-dotted line) and the stages response u are multiplied by -1 before drawing. The inset in (a) provides a closer look at a smaller time window visualizing the stage response noise.

6.1 | BEAM SCAN PATH OPTIMIZATION

In order to achieve the highest possible degree of measurement accuracy of the particle position, even the smallest position deviations from the center point must show up in a strong modulation of the emission signal. The setscrew for this is the shape of the path on which the laser light focus is directed. It must be optimized to set the center point residing on the steepest flank of the intensity profile integrated over a total scan period. For 2D-SPOT, it turned out that an optimal choice of the orbit radius is $R_{\text{opt},(xy)} = w_{xy}/\sqrt{2}$. [51] The naive assumption for 3D-SPOT is that the same ratio between the (larger) lateral beam waist in the center plane w_c and the orbit radius still applies. But apparently, the linear dependency on the particle's z -position vanishes for $R = w_c/\sqrt{2}$, and axial localization becomes impossible (see eq. (3.17)). For 3D-SPOT with the assumed modified Gaussian-Lorentzian MDF and chosen scan pattern, a different parameter set will be the optimal

choice considering all particle coordinates. The lowest possible estimator variances are found by minimizing the lateral and axial scan path geometry functions $\Lambda_{xy}(R/w_{xy}, d_z/w_z)$ and $\Lambda_z(R/w_{xy}, d_z/w_z)$ mentioned in section 3.2.

The minimum of $\Lambda_{xy}(R/w_{xy}, d_z/w_z)$ is, in fact, obtained for an orbit radius of $R_{\text{opt},(xy)} = w_{xy}/\sqrt{2}$ and a inter-orbit distance of $d_{z,\text{opt},(xy)} = 0$ and the minimum of $\Lambda_z(R/w_{xy}, d_z/w_z)$ for $R_{\text{opt},(z)} = 0$ and $d_{z,\text{opt},(z)} = 2w_z/\sqrt{2}$. In fig. 6.3, the logarithm of the squared beam geometry functions are plotted, and the optimal parameter sets are marked in red. Some exemplary values are summarized in table 6.1.

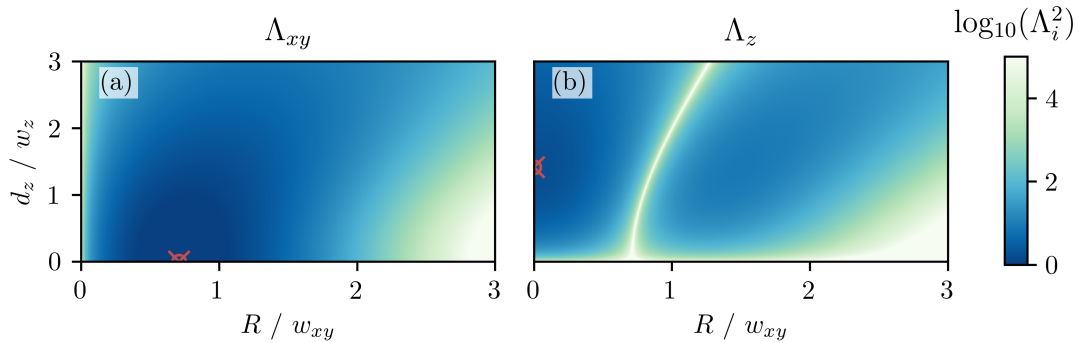


Figure 6.3.: Landscape of the functions (a) $\Lambda_{xy}(R/w_{xy}, d_z/w_z)$ and (b) $\Lambda_z(R/w_{xy}, d_z/w_z)$. The same color map applies to both plots. Deep blue areas indicate small function values and, therefore, good choices of parameters. For better visualization, the decadic logarithm of the squared scan path geometry functions is depicted, and values above 5 are cropped. The thin bright line in (b) breaches through areas of small function values indicate the singularity for $R = w_c/\sqrt{2}$

Table 6.1.: Examples of parameter settings for the scan path and corresponding geometry-function values.

R/w_{xy}	d_z/w_z	Λ_{xy}	Λ_z
$1/\sqrt{2}$	0	0.82	∞
0	$2/\sqrt{2}$	∞	1.30
$1/\sqrt{2}$	$2/\sqrt{2}$	1.28	5.44
0.30	1.20	1.99	1.62

The different scaling of the variances with w_{xy} and w_z does not allow for a direct comparison of the results of the beam geometry functions for the different spatial directions. The axial variance of the estimator is always larger because $w_z > w_{xy}$ due to optical reasons. Accepting this fact, one can follow different strategies and optimize, for example, just a single direction for an experiment where this direction is of higher relevance. In the following, a minimal total variance of the estimated particle position is aimed at. Therefore, the total variance is defined as the square root of the sum of the single coordinate variances

$$\sqrt{\text{Var}(\hat{\mathbf{r}}_p)} = \sqrt{\text{Var}(\hat{x}_p) + \text{Var}(\hat{y}_p) + \text{Var}(\hat{z}_p)}. \quad (6.3)$$

For a theoretical analysis of this quantity, it is necessary to connect the lateral and axial variances using a beam widths ratio like $w_z/w_{xy} = 3$, which is typical for practical applications. The final results are scaled with respect to w_{xy} and plotted in fig. 6.4(d) for comparison with simulation results shown in fig. 6.4(a-c). Simulation parameters are described in the figures captions.

The coincidence of the simulation and analytical results yield an optimal parameter choice of $R_{\text{opt}} = 0.3w_{xy}$ and $d_{z,\text{opt}} = 1.2w_z$. For this parameter set, the scan path geometry

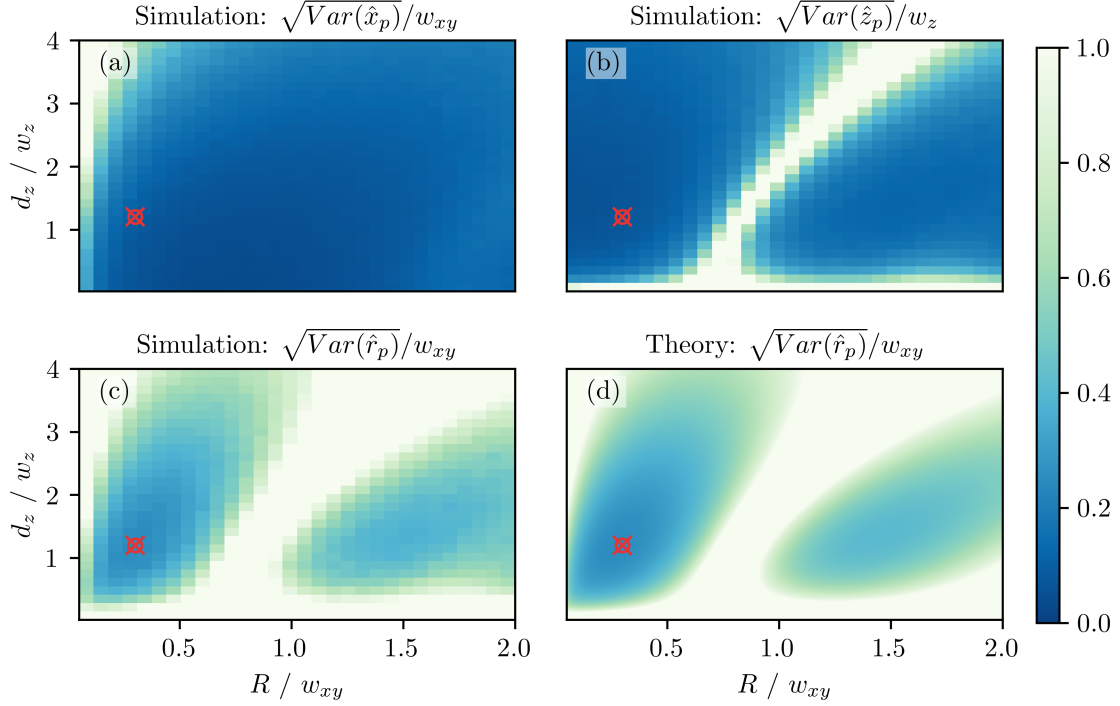


Figure 6.4.: Estimator variance of the particles (a) x - and (b) z -coordinate and (c,d) the total estimator variance for different choices of the orbit radius and orbit distance. (a, b, c) are the results of the same set of simulations with 500 signal and 1 background photon per scan period, a particle fixed at a randomly selected position close to the origin $\mathbf{r}_p = (0.05w_{xy}, 0.1w_{xy}, 0.2w_z)$, and no feedback applied. Each of the 30×30 simulations consists of 1000 localizations. The ratio between lateral and axial focus width was selected as $w_z/w_{xy} = 3$. For comparison, the theoretical results from eq. (6.3) are plotted in (d). All plots obey the same color scale with deep blue areas indicating zero and light yellow as 1. Values above 1 are cropped for better visualization. The red circled cross marks the parameter set of $R = 0.3w_{xy}$ and $d_z = 1.2w_z$, which appears as an optimal choice.

functions amount to about 2 for the lateral and 1.6 for the axial coordinates. This is a significant reduction of the maximal possible lateral accuracy for the benefit of higher axial reliability. Since the scaling length scale w_z is intrinsically larger than then w_{xy} , it makes sense to arrive at a compromise at the expense of lateral resolution. In all subsequent simulations, these ratios will be used and referred to as the "optimal scan path". The term "optimal" relates to its parameter set, creating this two parallel orbits, but it refers not to the laser focus pathway's general shape. It is expected that a different scan path is able to increase the accuracy further (see [78] or [187]).

In fig. 6.5(c) the integrated number of photons $N_{ph}(t)$ extracted from the simulations and its theoretical equivalent are plotted. The figure again reveals an exceptional agreement between the full signal simulation and the linear approximation. For the optimal parameters marked as a green circled cross, a reduced number of photons is detected. The factor between the number of photons that would be detected, if the laser focus and particle are centered in the middle of the detection volume and the integrated emission rate for the scanned laser focus is 0.64. When comparing photon detection rates measured with SPOT with related techniques like FCS, this is an important fact to know.

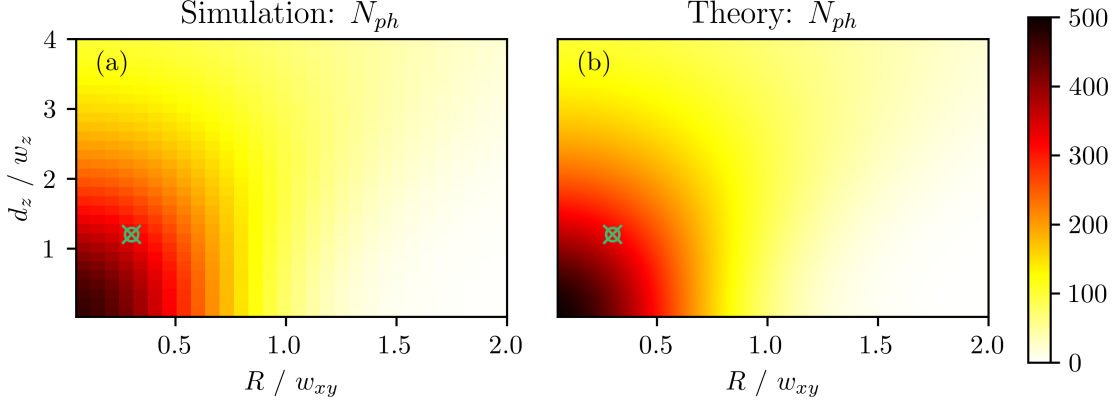


Figure 6.5.: Number of detected photons (color-coded) for (a) the same simulation as in fig. 6.4 and (b) calculated from eq. (C.33). The green cross marks the parameter set of $R = 0.3w_{xy}$ and $d_z = 1.2w_z$.

6.2 | LOCALIZATION ERROR

The localization error $\mathbf{e}_{\text{loc}}[k]$ is the discrepancy between the estimated particle position and the position of the particle at the end of the measurement cycle. This can be written as

$$\mathbf{e}_{\text{loc}}[k] = \hat{\mathbf{r}}[k] - \mathbf{r}_p(k\Delta t + \Delta t) = \begin{pmatrix} e_{\text{loc},x}[k] \\ e_{\text{loc},y}[k] \\ e_{\text{loc},z}[k] \end{pmatrix} = \begin{pmatrix} \hat{r}_x[k] - r_{p,x}(k\Delta t + \Delta t) \\ \hat{r}_y[k] - r_{p,y}(k\Delta t + \Delta t) \\ \hat{r}_z[k] - r_{p,z}(k\Delta t + \Delta t) \end{pmatrix}, \quad (6.4)$$

with the positive integer k indicating the measurement time interval of duration Δt . In the context of this thesis, this term excludes errors that are generated by the application of feedback and iterative position measurement. The localization error can be divided into a part that occurs even when the particle is not moving $\mathbf{r}_p(t) = \mathbf{r}_p$ and a part that arises only from the particle motion,

$$\mathbf{e}_{\text{loc}}[k] = \mathbf{e}_{\text{static}}[k] + \mathbf{e}_{\text{dynamic}}[k]. \quad (6.5)$$

Those contributions are called *static* $\mathbf{e}_{\text{static}}[k]$ and *dynamic localization errors* $\mathbf{e}_{\text{dynamic}}[k]$, respectively. The latter will be discussed in section 6.2.3. The static localization error is influenced by the statistic of the position estimator, which are already explicitly mentioned in section 3.2. But obviously, the demodulation of the emission signal for the determination of the particle position introduces an additional systematic localization error due to the neglect of higher harmonics in the fluorescence signal (see eqns. (C.30)–(C.32) in appendix C.2). The static localization error, therefore, consists of both a deterministic \mathbf{e}_{sys} and a random $\mathbf{e}_{\text{stat}}[k]$ contribution

$$\mathbf{e}_{\text{static}}[k] = \mathbf{e}_{\text{sys}} + \mathbf{e}_{\text{stat}}[k]. \quad (6.6)$$

An illustration of this two localization error components is given in fig. 6.6.

The static localization error varies in time due to its statistical contribution, while the systematic part depends parametric on the particle position. While the mean of $\mathbf{e}_{\text{stat}}[k]$ is zero, its variance is mainly affected by the previously discussed estimator variance, but

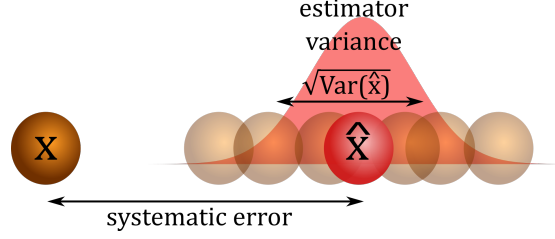


Figure 6.6.: Sketches of the static localization error that appears even for a not moving particle. Due to approximations in the position estimator equations, the real particle position is different from the estimated one. This systematic error is further intensified by the uncertainty due to the photon-counting noise, leading to a distribution of possible position estimation outcomes. The estimator variance shrinks with increasing integration time Δt .

also pointing instabilities of the laser beam and the deflection optic take part. Another statistical error source is the nanopositioning stage's positional noise. For the next sections, those additional statistical error sources are neglected, and only the photon-counting noise is considered so that

$$\text{Var}(e_{\text{stat},i}) = \text{Var}(\hat{r}_{p,i}) , \quad (6.7)$$

is valid.

A pure statistical error given by the variance $\text{Var}(e_{\text{stat}}) = \sigma^2$ appears as an offset of $2\sigma^2$ in the MSD in tracking applications.[188] The expected measured MSD in three dimensions is

$$\mathcal{E}(\langle \Delta \hat{r}^2[k] \rangle) = 6Dk\Delta t + 2\sigma^2 . \quad (6.8)$$

In fig. 6.7, simulation results visualize this relationship for two distinct statistical errors of $\sigma_1 = 0.1$ and $\sigma_2 = 0.2$, respectively. Notably, the offset yields in an apparent subdiffusion for short time scales.[189]

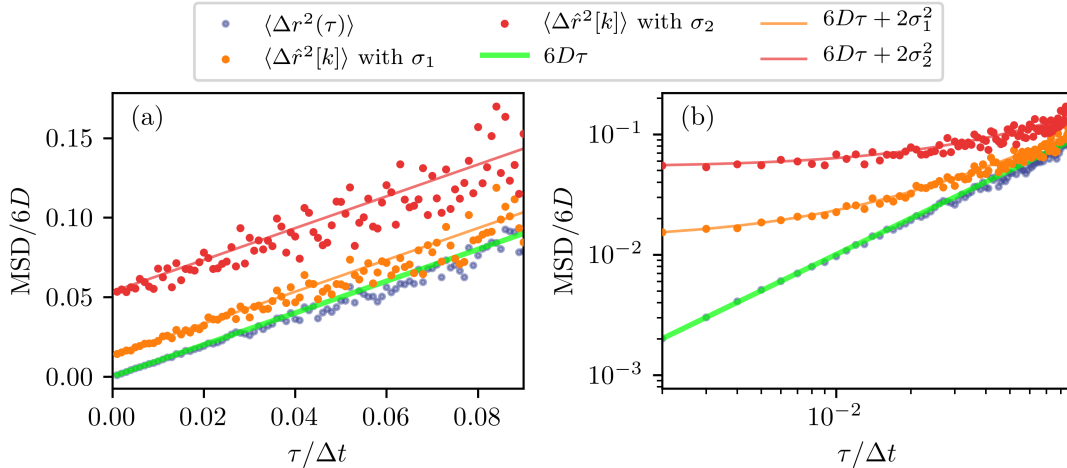


Figure 6.7.: MSD of two simulated particle trajectories with diffusion coefficient $D = 1$ and static localization variances $\sigma_1^2 = 0.1$ and $\sigma_2^2 = 0.2$ in (a) linear and (b) logarithmic representation. Trajectories consist of 3×10^3 positions. Blue dots represent the MSD from the actual particle trajectory, and orange and red those, measured with σ_1 or σ_2 , respectively. The solid light green line is a theoretical curve that follows $6D\tau$, the solid orange and red lines contain an offset of $2\sigma_1^2$ or $2\sigma_2^2$, respectively.

6.2.1 | PHOTON COUNTING NOISE

The dependency of the localization error on the integrated photon detection rate is inspected by simulations (see appendix C.5). The particle is fixed in the origin, but $N_{\max} = 2TF_0$ is varied between 0 and 1×10^5 photons. Each simulation is repeated 1000 times. The ratio $w_z/w_{xy} = 3$ and the optimal scan path is set. Any stage movement or feedback is deactivated. The results are fitted with

$$\frac{\sqrt{\text{Var}(\hat{r}_{p,i})}}{w_{xy}} = \frac{p_{i,0}}{\sqrt{N_{\max}}}, \quad (6.9)$$

and shown in fig. 6.8(a).

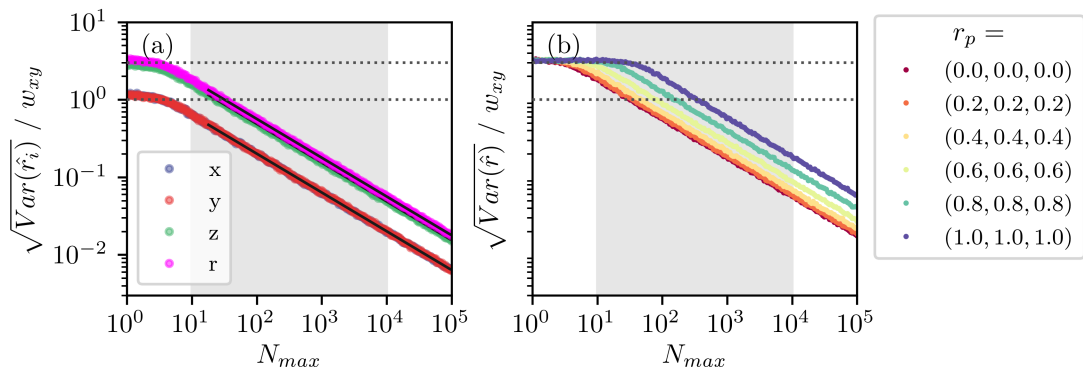


Figure 6.8.: (a) Square-root of the estimator variance $\sqrt{\text{Var}(\hat{r}_{p,i})}$ due to photon counting noise for a particle staying in the center of the detection volume. Blue, red, and green dots represent the standard deviation in x -, y -, and z -direction, respectively. Black dots are the Pythagorean sum of the single-axis standard deviations. Fits are drawn as solid black lines. Black dotted lines indicate the level of 1 and 3, which correspond to an uncertainty that is as big as the beam waist in the lateral and axial direction. The gray shaded area is the regime relevant in practical applications since more than 10 photons are needed for a position determination with an accuracy worth mentioning, and more than the limit of 10×10^3 photons per estimation cycle will hardly be exceeded if APDs are used and a temporal resolution in the millisecond range is targeted at. (b) Total estimator variance for different (static) particle positions. The variance is shifted to larger values for increasing particle displacements from the reference frame origin.

The error along the z -axis is larger than for the lateral particle coordinates and the three-dimensional particle position is, of course, more uncertain than the one-dimensional components. Moreover, it is clearly seen that the particle position estimator's standard deviation scales proportional to $1/\sqrt{N_{\max}}$ over the complete plotting range. The only exception from this is the very low photon number-range where no positional information is gained and the localization uncertainty exceeds maximum estimator outcome. The obtained fitting parameters $p_{i,0}$ are listed in table 6.2 and can be identified with the value of the scan path geometry functions $\Lambda_{xy}(0.3, 1.2) \approx 2$, $\Lambda_z(0.3, 1.2) \approx 1.6$ and the Pythagorean sum for the total variance. In order to get a feeling for the practical significance of the photon number, the standard deviation of the estimator is calculated for different beam waists and maximum photon numbers in table 6.3.

A typical parameter set with a beam waist of $w_x = w_y = 300$ nm and $w_z = 900$ nm and a number of $N_{\max} = 1000$ photons per localization period results in a localization uncertainty of about 19 nm in lateral and 46 nm in the axial direction. For a localization period of 4 ms, this requires the detection count rate to be as high as about 370 kcps, which

is a reasonable value for tracer particles like fluorescent beads or quantum dots, but not for most of the available single dye molecules or single fluorescent proteins.

Table 6.2.: Prefactors taken from the fitted relation between the estimator variance $\sqrt{\text{Var}(\hat{r}_{p,i})}$ and the integrated count rate N_{\max} (see eq. (6.9)).

Coordinate	$p_{i,0}$
$\hat{r}_{p,x}$	1.9932 ± 0.0008
$\hat{r}_{p,y}$	1.9994 ± 0.0008
$\hat{r}_{p,z}$	1.6313 ± 0.0009
$\hat{\mathbf{r}}_p$	5.6411 ± 0.0007

Table 6.3.: Standard deviation of the estimator $\sqrt{\text{Var}(\hat{r}_{p,i})}/\text{nm}$ for typical beam waists and a varying number of maximal photon numbers

Coordinate	w_i/nm	Number of photons N_{\max}					
		1	10	100	1000	10000	100000
$\sqrt{\text{Var}(\hat{x}_p)}/\text{nm}$,	200	399	126	40	13	4	1
$\sqrt{\text{Var}(\hat{y}_p)}/\text{nm}$	300	599	189	60	19	6	2
	400	799	253	80	25	8	3
$\sqrt{\text{Var}(\hat{z}_p)}/\text{nm}$	600	977	309	98	31	10	3
	900	1465	463	146	46	15	5
	1200	1953	618	195	62	20	6

In the next step, the localization of SPOT is simulated for multiple systematically varied particle positions, which individually remain fixed during a single simulation run. The results are plotted in fig. 6.8(b). Evidently, the estimator variance is shifted to larger uncertainties, if the particle is further away from the origin, while the scaling with the square root of the maximum photon number is conserved. Since the estimator can only reach certain maximum values depending on the prefactors of the demodulation vector function eq. (3.17), there is a cutoff at very large variances at insufficient photon numbers. The particle-position dependent growth of the estimator variance is a systematic error that is not handled by eqns. (3.22)–(3.23), but will be examined in the next section.

6.2.2 | SYSTEMATIC LOCALIZATION ERROR

The demodulation of the emission signal for particle position estimation is based on a first-order Taylor series approximation, which neglects higher harmonics in the modulated fluorescence signal and introduces a systematic localization error (see appendix C.2). This error occurs even in the absence of photon counting noise. The systematic localization error was already discovered for 2D-SPOT, where it yields in an increasing underestimation of the radial distance of the particle from the orbit center as this radial distance becomes larger.[51, 186]

If calculating the higher-order terms of the demodulation transformation, the increased complexity of 3D-SPOT outcrops as mixed terms of the radial ρ_p and axial z_p particle position component. Since the particle position estimator is a first-order approximation for particle positions near the origin, systematic errors will occur if the particle is located farther away. Simulations will help to identify the systematic error for the optimal focus scanning path in 3D-SPOT. Forgoing photon counting noise, the signals are assumed as smooth and deterministic. Stage movement and feedback are still kept deactivated.

Furthermore, the position of a static particle is varied along the x -axis for multiple fixed axial positions (see fig. 6.9 (a)) and then along the z -axis for multiple fixed radial displacements (see fig. 6.9 (b)). For each position, a full-order signal is calculated and consecutively demodulated with the lock-in detection based only on the first-order approximation of the photon emission rate. Due to the symmetry of the problem, results are presented in cylindrical particle coordinates. In fig. 6.10, the "measured" particle position $\hat{\mathbf{r}}_p = (\hat{\rho}_p, \hat{\varphi}_p, \hat{z}_p)$ is shown in dependency of the actual particle position $\mathbf{r}_p = (\rho_p, \varphi_p, z_p)$. In the top row of fig. 6.10, the calculated particle coordinates are shown as a function of the particle's radial position ρ_p and in the bottom row, as a function of the particle's axial position z_p . Due to the correlated dependencies, the other coordinate is varied parametrically. The azimuthal angle is always equal to 0.

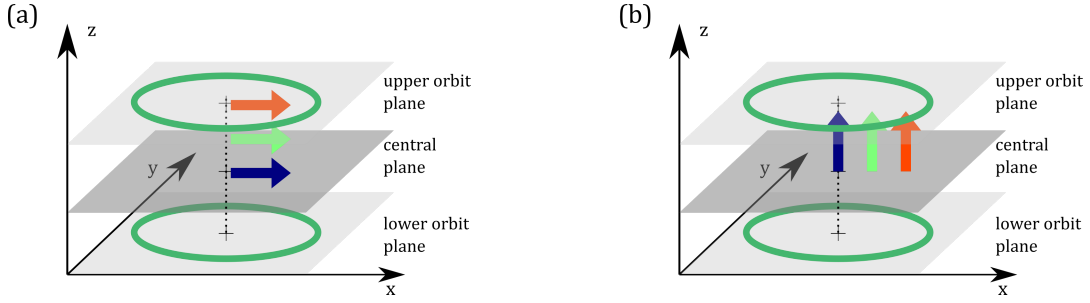


Figure 6.9.: Illustration of the simulation scenarios (not drawn to scale). (a) First, the distance of the particle to the optical axis is increased within multiple horizontal planes. So only the radial coordinate ρ_p is varied for a fixed axial position z_p . (b) In the second scenario, the particle is shifted axially along lines parallel to the optical axis.

Focusing on the estimated azimuthal angle of the particle position $\hat{\varphi}_p$ (fig. 6.10(b) and (e)), the estimator works perfectly. For zero radial displacement $\rho_p = 0$, the azimuthal angle is not defined, and $\hat{\varphi}_p$ diverges, but elsewhere the angle is correctly identified (Note that the measured positions for $\rho_p = 0$ are, therefore, not within the plotting range in fig. 6.10(b) and (e)). This is not surprising as the higher harmonic components in the fluorescence signal do not contribute to its phase (see eq. (C.20) in the appendix C.2).

Nevertheless, systematic errors occur in the estimation of the particle's radial distance from the origin $\hat{\rho}_p$. As in the 2D case, 3D-SPOT underestimates large radial displacements. Unfortunately, this underestimation is dependent on the z -plane of the particle position. More considerable distances from the central plane in the z -direction yield larger deviations from the real radial coordinate (fig. 6.10 (a)). This influence can be visualized in fig. 6.10 (d). Small radial and axial distances from the origin yield a correct match between real and computed coordinates. However, for larger radial distances from the center, the axial particle position contributes stronger to the measurement of ρ_p , yielding a stronger underestimation.

Similar behavior is obtained for the estimation of the axial particle position \hat{z}_p . For a particle shifted along the optical axis, the real z -position agrees well with the estimated one, at least within the ranges limited by $z_p \in \left[-\frac{d_z}{2}; \frac{d_z}{2}\right]$ (see fig. 6.10(f)). Interestingly, the z -coordinate of a particle displaced randomly within the central plane is always correctly detected. But problems start if neither ρ_p nor z_p is zero. The influence of the radial particle coordinate is very strong outside of the central plane. For $\rho_p = w_{wxy}$, there is even a change in signs, and the SPOT algorithm would move away the particle from from the detection volume in subsequent feedback steps.

In the previous realization of 2D-SPOT, the non-linearity of the particle's radial position

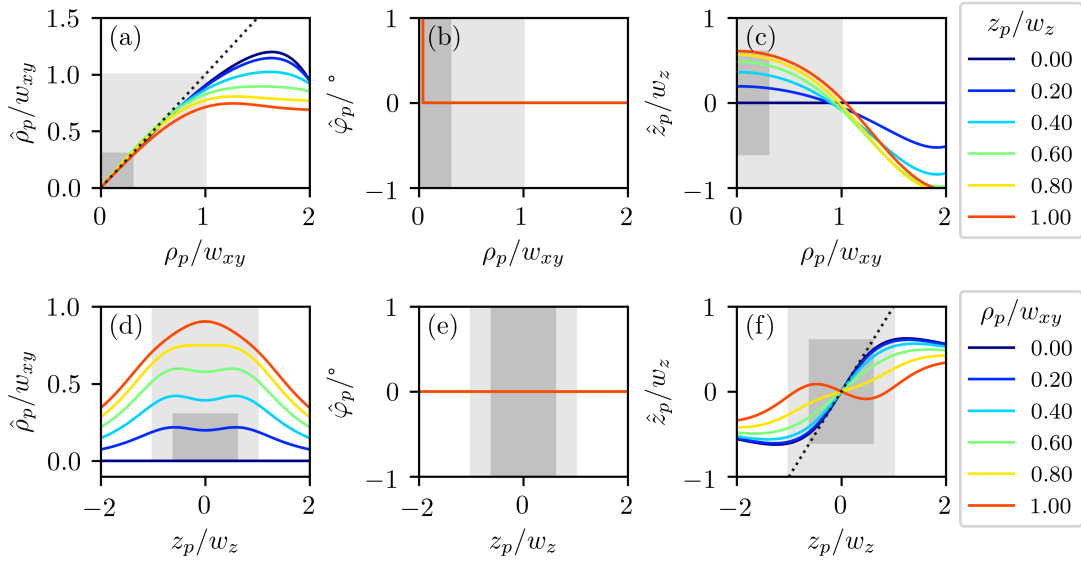


Figure 6.10.: Representation of the systematic localization error in (a, d) radial (b, e) azimuthal and (c, f) axial direction. The position resulting from the estimator equations is shown as a function of the actual particle position $\mathbf{r}_p = (\rho_p, \varphi_p, z_p)$. The results in the first row (a-c) show the simulation output for a particle shifted along the x -axis to vary only its radial distance ρ_p while keeping a fixed z -coordinate. Different colors correspond to different values of z_p . Figures in the second row (d-f) represent the outcome of simulations, where the axial position is varied for fixed radial displacements. Different radial distances are color-coded. The dark gray area labels the parameter range that is encapsulated by the laser focus centroid. The light gray area indicates the range of a cigar-shaped focal volume characterized by the length scales w_{xy} and w_z . In graphs (a) and (f), a black dotted line indicates the targeted linear relationship.

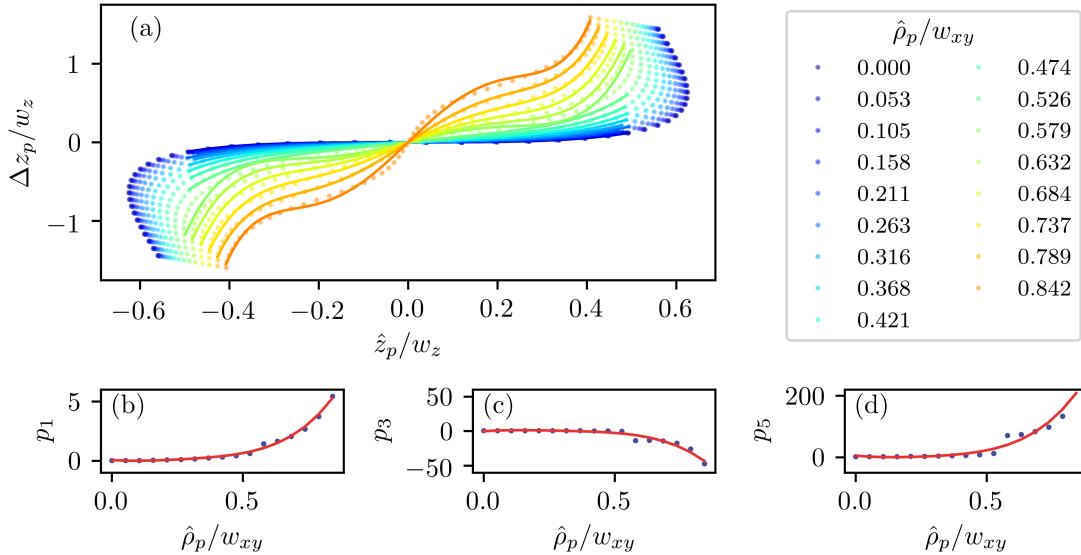


Figure 6.11.: (a) Systematic axial localization error in dependency of the estimated particle position \hat{z}_p (dots) for different radial displacements ρ_p (color-coded). The legend on the right-hand side applies. Solid lines in the same color represent the three-parameter fits of shape $p_1(\hat{\rho}_p/w_{xy})\hat{z}_p + p_3(\hat{\rho}_p/w_{xy})\hat{z}_p^3 + p_5(\hat{\rho}_p/w_{xy})\hat{z}_p^5$. Blue dots in figure (b), (c), and (d) are the coefficients p_1 , p_3 , and p_5 for the different radial displacements. Solid red lines are polynomial fits of fourth-degree to the data.

was corrected in real-time with the help of a fourth-order polynomial. In 3D-SPOT, there is the dilemma that both, z_p and ρ_p , influence the localization error in the axial and radial direction. A correction function that would map the estimated particle position to the real one is not injective and, thus, dependent on the sequence in which the correction is applied.

Due to the intrinsically worse resolution in the axial direction, the here chosen approach will neglect the radial error, and only correct the z -coordinate of the particle. The axial error $\Delta z_p = \hat{z}_p - z_p$ is fitted with a polynomial of shape

$$\frac{\Delta z_p}{w_z}(\hat{\rho}_p/w_{xy}, \hat{z}_p/w_z) = p_1(\hat{\rho}_p/w_{xy}) \left(\frac{\hat{z}_p}{w_z}\right) + p_3(\hat{\rho}_p/w_{xy}) \left(\frac{\hat{z}_p}{w_z}\right)^3 + p_5(\hat{\rho}_p/w_{xy}) \left(\frac{\hat{z}_p}{w_z}\right)^5. \quad (6.10)$$

Each coefficient $p_i(\hat{\rho}_p/w_{xy})$ is again modeled as a polynomial of fourth-order. The results of this analysis are summarized in fig. 6.11, and table 6.4. Provided that $\hat{\rho}_p$ and \hat{z}_p is measured, fig. 6.11(a) shows the value Δz_p that must be added to \hat{z}_p to obtain the correct axial position of the particle.

Table 6.4.: Fitting results of the fourth-degree polynomials of shape $\tilde{p}_a(\hat{\rho}_p/w_{xy})^4 + \tilde{p}_b(\hat{\rho}_p/w_{xy})^3 + \tilde{p}_c(\hat{\rho}_p/w_{xy})^2 + \tilde{p}_d(\hat{\rho}_p/w_{xy}) + \tilde{p}_e$ to determine the coefficients p_1 , p_3 , and p_5 of the z -correction polynomial.

	\tilde{p}_a	\tilde{p}_b	\tilde{p}_c	\tilde{p}_d	\tilde{p}_e
p_1	30.0908	-29.6365	12.9802	-1.6896	0.0510
p_3	-336.5471	368.3876	-164.8898	27.5561	-0.3175
p_5	1064.9361	-990.7676	466.5779	-84.1741	4.6803

The determined parametrization is applied to the simulation data, repeating the two scenarios illustrated in fig. 6.9. The results for \hat{z}_p are shown in fig. 6.12. One can see, that this correction yields a reduced influence of the radial and axial coordinate on the measurement accuracy for a wide range of particle positions. But for radial displacement greater than $0.85w_{xy}$, the fits do not converge properly, and the correction even increases the systematic error.

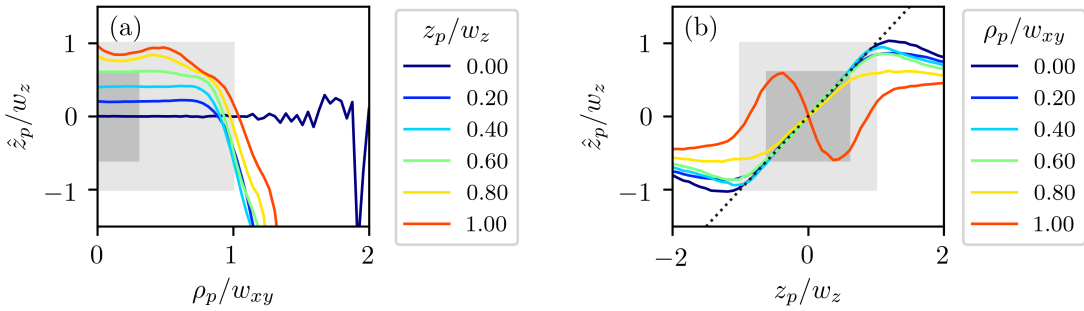


Figure 6.12.: (a) Estimate of the axial position \hat{z}_p of a particle shifted parallel to the x -axis for different axial displacements (color-coded) with the z -position correction applied. (b) Estimate of the axial position of a particle shifted parallel to the z -axis for different radial displacements (color-coded) with the z -position correction applied. The graphs relate to fig. 6.10 (c) and (f).

6.2.3 | DYNAMIC LOCALIZATION ERROR

The errors in determining the particle's position discussed so far are valid for an immobile particle. In contrast, the dynamic localization error considers a moving particle.[190] Due to the ongoing motion during signal acquisition, the center of mass position is measured instead of the actual one, yielding a reduced distance between successive localizations. In fig. 6.13, an illustration of the particle motion during signal acquisition shows the difference between the particle's actual position at the end of the measurement interval and the measured center of mass position.

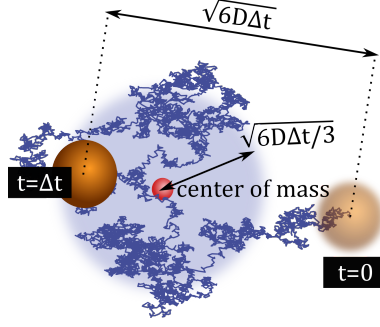


Figure 6.13.: Sketches of the dynamic localization error. Because of the finite photon counting integration time and the ongoing particle movement, the center of mass of a trajectory section is measured instead of the actual particle position. This so-called averaging error increases with integration time. While the particle covers a distance of $\sqrt{6D\Delta t}$, the measured position differs by $\sqrt{6D\Delta t/3}$ from the position at the end of the trajectory section.

In the overdamped limit, the particle position is given as an integral over the Wiener process $\boldsymbol{\nu}_{bm}(t)$ (see eq. (2.19)). The position measured within the measurement time Δt is the center of mass of the trajectory for $t \in [(k-1)\Delta t; k\Delta t]$ and written as

$$\hat{\mathbf{r}}[k] = \frac{1}{\Delta t} \int_{(k-1)\Delta t}^{k\Delta t} \mathbf{r}(t) dt = \frac{1}{\Delta t \xi} \int_{(k-1)\Delta t}^{k\Delta t} \int_0^t \boldsymbol{\nu}_{bm}(t') dt' dt . \quad (6.11)$$

The variance of the center of mass is

$$\begin{aligned} \text{Var}(\hat{\mathbf{r}}[k]) &= \mathcal{E}(\hat{\mathbf{r}}[k]^2) = \frac{1}{\Delta t^2 \xi^2} \int_{(k-1)\Delta t}^{k\Delta t} \int_0^t \int_{(k-1)\Delta t}^{k\Delta t} \int_0^{t''} \mathcal{E}(\boldsymbol{\nu}_{bm}(t') \boldsymbol{\nu}_{bm}(t''')) dt''' dt'' dt' dt \\ &= 6D\Delta t/3 . \end{aligned} \quad (6.12)$$

This is equal to the expected distance between the measured position and the actual position of the particle at the end of the measurement interval. In literature, it was shown that this averaging error leads to a systematic underestimation of the particles MSD.[191, 192] Hence, for three-dimensional Brownian motion, the expected measured MSD is

$$\mathcal{E}(\Delta \hat{\mathbf{r}}^2[k]) = 6D(k\Delta t - \Delta t/3) . \quad (6.13)$$

This effect is modeled with a simple simulation. A trajectory consisting of 3×10^6 three-dimensional data points was generated with Brownian motion statistics. Each segment of 1×10^3 positions is averaged to a single center of mass position, which entirely represents the measured trajectory. Afterwards, the MSD of the full trajectory is compared to that of the averaged one in fig. 6.14. In a linear representation (see fig. 6.14(a)), the measured MSD is just shifted towards smaller displacements but maintains its slope. Thus, the diffusion

coefficient can be extracted from the slope, making it is easy to correct for this artifact.[186] However, on a double-logarithmic representations (see fig. 6.14(b)) it is clearly seen that a simple offset appears at an apparent superdiffusion on short time scale and care must be taken in the respective discussion, if an actual anomaly is present.

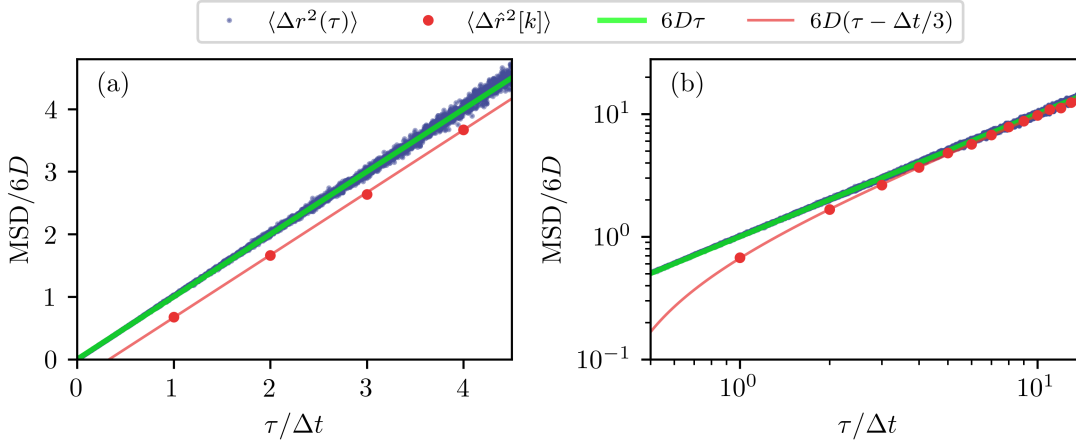


Figure 6.14.: MSD of a particle motion simulated according to the Brownian law, displayed in (a) linear and (b) logarithmic representation (blue dots) and the MSD of the same trajectory, but averaged for segments of 1000 positions (red dots). Green and red lines are the corresponding theoretical curves.

6.3 | TRACKING ERROR

In feedback-based tracking, localization errors yield a finite distance of the particle position and the origin after the movement compensation step. Thus, the next localization is influenced by the preceding measurement error, and those errors can accumulate or cancel each other out. The setup's overall ability to follow the motion is called total tracking error σ_t and defined via a root mean square relation

$$\sigma_t = \frac{1}{N_{\text{pos}}} \sqrt{\sum_{k=0}^{N_{\text{pos}}} (\hat{\mathbf{r}}[k] - \bar{\mathbf{r}}[k])^2} = \frac{1}{N_{\text{pos}}} \sqrt{\sum_{k=0}^{N_{\text{pos}}} \chi[k]^2} . \quad (6.14)$$

which compares the measured particle position $\hat{\mathbf{r}}[k]$ with the averaged actual particle position $\bar{\mathbf{r}}[k]$ (see eq. (C.68)). Unfortunately, this quantity is not accessible in practice as the real particle position is hidden. Therefore, simulations are used again to inspect the dependencies of this quantity. An example of serial measurement error-affected particle localization is illustrated in fig. 6.15. In the sketch, only the dynamic localization error is considered and it is seen that its relative contribution shrinks on larger time intervals. However, there are more effects to consider, especially the inertia of system components, such as the nanopositioning stage, that forces the tracked position to lag behind the real particle motion. In the following the interplay of photon counting noise, the systematic localization error and the averaging effects due to the finite duration of signal integration are analyzed first, and expanded by the influence of the system components' inertia in a second step.

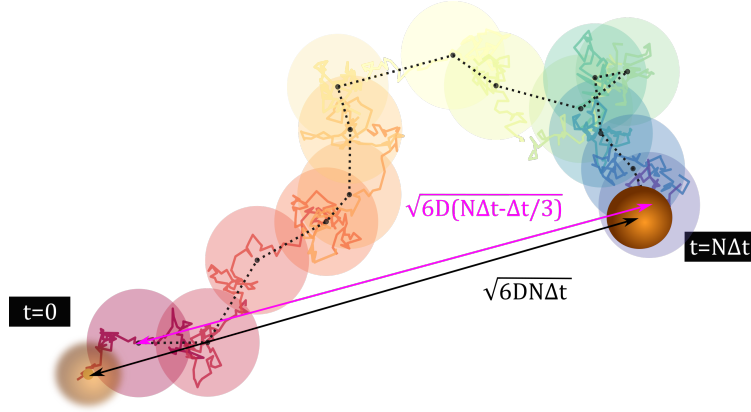


Figure 6.15.: Sketch of the tracking error, which occurs for serial particle localization. For example, finite measurement time intervals produce averaging effects and the resulting distance between the particle's initial and final position is reduced.

6.3.1 | LOCALIZATION ERRORS INDUCED TRACKING ERROR

The simulation described in the appendix C.5 is used with particle trajectories obeying Brownian motion statistics. The particle's maximum photon emission rate and diffusion coefficient are varied. The stage feedback is activated, but the stage position is still considered free of noise and infinitely fast responding. For each parameter pair a SPOT measurement of 300 position estimation cycles was simulated to compute the tracking error σ_t with eq. (6.14).

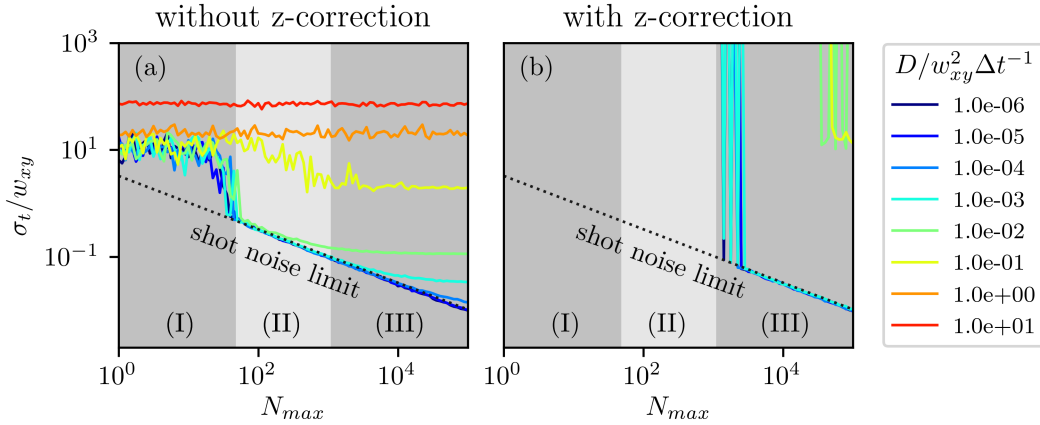


Figure 6.16.: Photon number dependency of the tracking error for various diffusion coefficients (color-coded, in units of squared lateral beam waists per estimation time). Results are from simulations of trajectories with 1×10^3 positions per data point and (a) z-correction active and (b) inactive. Focus width ratio $w_z/w_{xy} = 3$ is selected, and the stage response is instantaneous. Feedback was applied after 3 estimations. The dashed line represents the estimator variance limitation due to photon counting noise.

Figure 6.16 (a) shows the photon number dependency of the tracking error for various diffusion coefficients, where three intervals of peak photon numbers are distinguished. For less than $N_{\max} = 50$ photons (interval (I)), SPOT cannot estimate the particle position correctly. In interval (II), the range between 50 and 1000 peak photons per estimation cycle, the tracking error scales like the estimator standard deviation with $1/\sqrt{N_{\max}}$, but only if the diffusion coefficient is slow enough ($D < 1 \times 10^{-2} w_{xy}^2 \Delta t^{-1}$). For higher photon

numbers, the shot noise becomes smaller than the random motion error, and a photon count rate independent level is reached that is specific for the respective diffusion coefficient (interval (III)). Particles with diffusion coefficients greater than $1 \times 10^{-2} w_{xy}^2 \Delta t^{-1}$ are too fast to be followed, and their mean tracking error is outside the acceptable range.

Figure 6.16 (b) shows the same simulation but with the z -correction (see section 6.2.2) applied. The same trend with $1/\sqrt{N_{\max}}$ as in fig. 6.16 (a) is obtained, but with highly increased errors for weak emitting and fast particles. However, for peak detection rates of several thousand photons per estimation cycle (interval (III)), the tracking error is only determined by shot noise, and a great enhancement compared to the uncorrected case is recognized. Consequently, the worked out z -correction is capable to increase the tracking accuracy for mobile particles as well, but the controller has a higher demand for photons and lacks robustness for unfavorable conditions. Hence, the correction procedure is beneficial only in the count rate and diffusion coefficient range where tracking is already stable without its application.

Now, the tracking error is plotted against the diffusion coefficient for different peak photon numbers. Thus, fig. 6.17 (a) displays the same simulation as fig. 6.16 (a), but in a different representation.

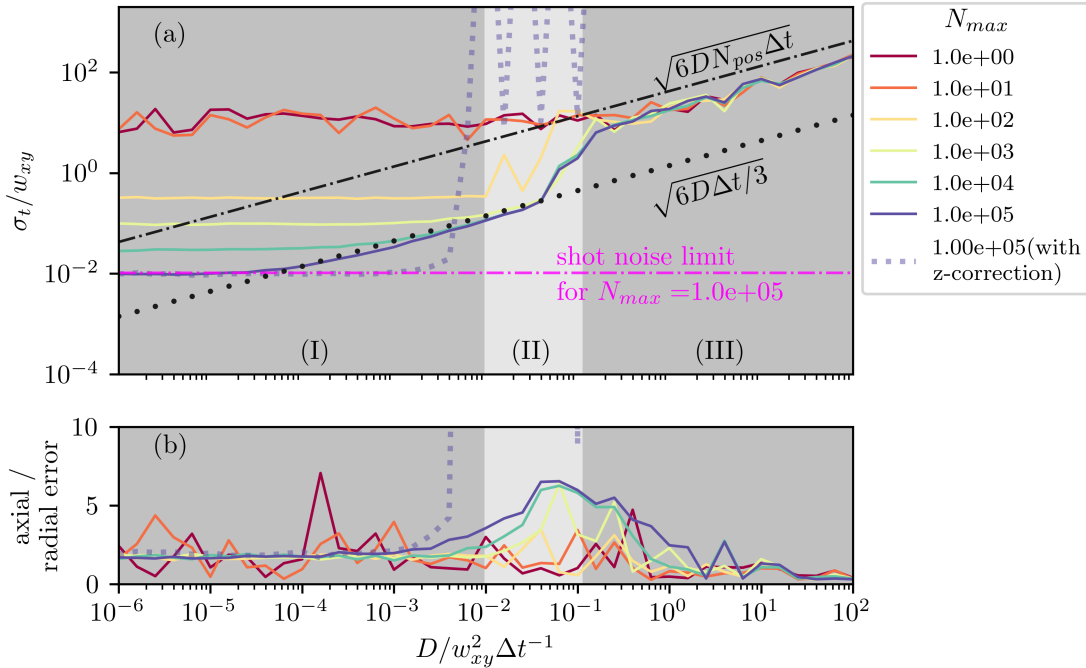


Figure 6.17.: (a) Dependency of the tracking error on the diffusion coefficient for various peak photon numbers (solid color-coded lines) based on the identical simulations shown in fig. 6.16. The purple dotted line corresponds to simulations with the z -correction applied and a peak photon number of $N_{\max} = 1 \times 10^5$. Furthermore, there are some auxiliary lines drawn. The dash-dotted black line corresponds to a distance that a freely diffusing particle would cover within the total simulation time, while the black dotted line corresponds to the averaging error. The shot noise limit for a peak photon number of $N_{\max} = 1 \times 10^5$ is plotted as a magenta dash-dotted horizontal line. (b) Ratio of the axial and the radial error.

No matter how slow a particle is, the peak photon number sets a fundamental limit to the accuracy, which decreases for increasing photon numbers. The diffusion coefficients are again categorized into three intervals. Interval (I) contains diffusion coefficients that are smaller than $1 \times 10^{-2} w_{xy}^2 \Delta t^{-1}$. Particles with a diffusion coefficient D in this range are

slow enough for the method to be followed, and the tracking error is a combination of the averaging error and the estimator uncertainty.

Diffusion coefficients in the range between $1 \times 10^{-2} w_{xy}^2 \Delta t^{-1}$ and $1 \times 10^{-1} w_{xy}^2 \Delta t^{-1}$ are assigned to interval (II). Here, the particle motion is likely to cover a distance of at least 50% of the lateral beam width within 3 estimation cycles, and the probability of losing it becomes very large. Thus, the obtained errors in the simulation correlate with the remaining trajectory length after a particle losing event. Particles with diffusion coefficients higher than $1 \times 10^{-1} w_{xy}^2 \Delta t^{-1}$ are in interval (III) and far too fast to be tracked. They behave like free particles right from the beginning of the simulation, and consequently, escape the detection volume according to free diffusion statistics with an error growing approximately like $\sqrt{6D\Delta t}$.

Notably, if the real particle trajectory's MSD would grow slower than proportional to τ , the "trackable" range of diffusion coefficients would shift to higher values, and the application range of SPOT is expanded. It is not surprising that depending on N_{\max} and D , there is a transition of tracking errors mainly given by shot noise or mainly affected by the averaging error. For less photons detected, the transition occurs at higher diffusion coefficients because the shot noise error is larger.

If the z -correction is applied (purple dotted line), the error introduced by diffusion is canceled out over a extensive range of diffusion coefficients, but the domain of diffusion coefficients that are too large to be tracked sets in earlier. For $D > 1 \times 10^{-2} w_{xy}^2 \Delta t^{-1}$ (interval (II)), a remarkably increased tracking error in the z -direction is present (see fig. 6.17 (b)), and the axial particle coordinates become unreliable. From the purple dotted line, it is clear that the z -tracking error increases dramatically and for smaller D with an active z -correction compared with an uncorrected axial localization. Apparently, the correction method enhances the axial error within this range, which is an observation that agrees well with the results in section 6.2.2. Here, the correction downgrades the axial accuracy for large lateral distances from the optical axis, which is, on average, the case for larger diffusion coefficients.

Summarizing, the diffusion coefficient of normally diffusing particles should not exceed $1 \times 10^{-2} w_{xy}^2 \Delta t^{-1}$. For instance, if $w_{xy} = 200$ nm and $\Delta t = 1.33$ ms, this diffusion coefficient limit would amount to $300 \text{ nm}^2 \text{ ms}^{-1}$ in real units or $675 \text{ nm}^2 \text{ ms}^{-1}$ for $w_{xy} = 300$ nm and $\Delta t = 1.33$ ms. Including more noise and error sources may reduce this limit even further. Because robustness is given priority over accuracy, the z -correction should generally be omitted. Its use is only recommended for very stable tracking conditions to push accuracy to the extreme.

6.3.2 | STAGE VIBRATION INDUCED TRACKING ERROR

In this section, the analysis is expanded by including the feedback dynamics considering the behavior of the nanopositioning stage and its controller. Time delays in the digital signal processing and the influence of the controller's notch filter are ignored since little is known about the technical details. Instead, the closed-loop feedback system consisting of the stage itself and the PID controller is regarded as a *linear time-invariant* subsystem with the stage target position $\mathbf{u}_{\text{tar}}(t)$ as input and the actual stage movement $\mathbf{r}_s(t)$ as output. This system was accurately identified (see appendix D.5) with a four-parameter transfer function which is cumbersome to deal with in a parameter study. To gain insight into the influence of the stage-stage controller system on the SPOT results, the forced oscillator transfer function (see eq. (A.29)) is used instead, reducing the number of parameters to

two, namely the *natural frequency* ω_n and the *damping coefficient* λ .

In fig. 6.18, the identical realization of a particle trajectory is plugged into simulations (see appendix C.5) using different parameter sets for the stage-stage controller transfer function. Inspecting the (inverted) stage motion reveals that the stage indeed follows the particle's movement but features strong oscillations for weak damping and low resonance frequencies. The same is true for the reconstructed particle trajectory, but the oscillation appear more irregular.

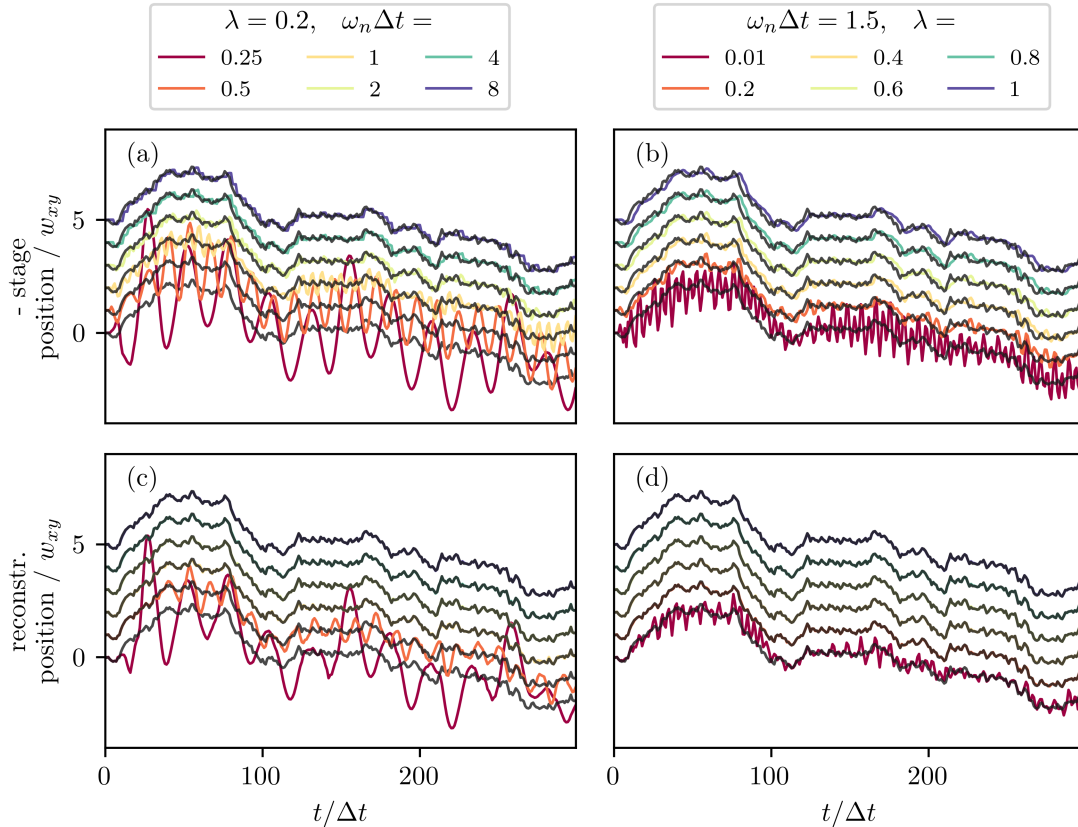


Figure 6.18.: Results for the x -coordinate of a 3D-SPOT simulation with deactivated photon counting noise or stage noise, but with a damped oscillatory transfer function used for the stage movement, characterized by the (dimensionless) resonance frequency $\omega_n \Delta t$ and the damping coefficient λ . The particle's diffusion coefficient was set to $0.01 w_{xy}^2 \Delta t^{-1}$. The inverted stage coordinate (colored lines) is compared with the real particle motion (black line) for (a) a fixed $\lambda = 0.2$ and a varying frequency $\omega_n \Delta t$ and (b) a fixed frequency $\omega_n \Delta t = 1.5$ and varying coefficient λ . In (c) and (d), the respective reconstructed particle trajectories are shown. Data sets are offset by 1 for better visibility.

In fig. 6.19, simulation results of a systematic variation of ω_n and λ for different diffusion coefficients are presented by plotting the tracking error. Because the computational effort is high, only short trajectories (300 estimation cycles) were simulated for varying diffusion coefficients. The same trend of the tracking error is obtained for all diffusion coefficients, but smaller D yield smaller tracking errors as already known. Careful interpretation of fig. 6.19 (a) is necessary. A system with a natural frequency multiple times higher than the reciprocal time of position estimation Δt^{-1} produces small. However, in practice, there is only little influence possible on ω_n , which can be understood as a setup-specific constant. Therefore, it is the position estimation time that must exceed the resonance time ω_n^{-1} .

The behavior for $\omega_n \Delta t \approx 1$ is characterized by a high volatility of the tracking error to the exact parameter configuration. For $\omega_n \Delta t \approx 2$, a dip in the curves for small diffusion coefficients indicates another setting where vibrations in the system are excited increasing the tracking error. From fig. 6.19 (b), the simple fact can be derived that a stiffer system (higher λ) reduces the susceptibility to oscillate and serves the purpose of tracking error reduction.

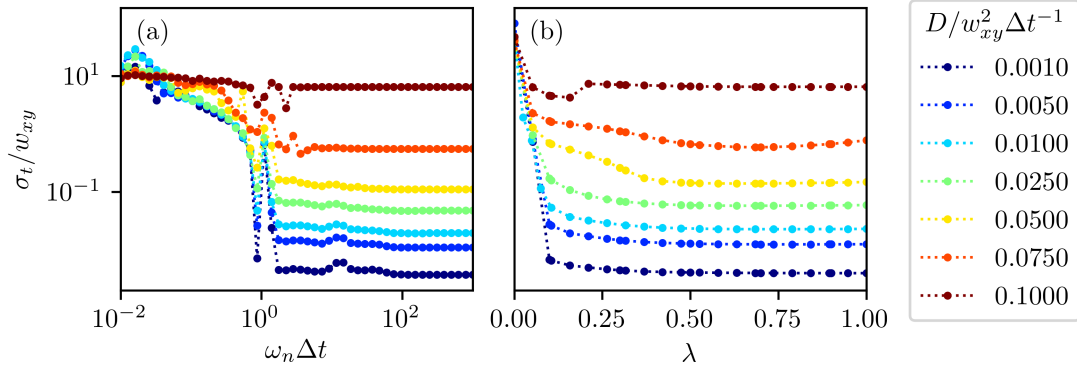


Figure 6.19.: Results of SPOT-simulations of a diffusing particle, including a damped oscillatory feedback response of the controller-stage system. The tracking error σ_τ is plotted versus (a) the natural frequency ω_n (fixed $\lambda = 0.2$) or the (b) damping coefficient λ (fixed $\omega_n = 1.5$) for different diffusion coefficients of the particle motion. Trajectories consisted of 300 position estimation cycles of duration Δt . Feedback is applied after each third localization period.

A more complicated transfer function of the stage-stage controller system would yield more complex parameter dependency, but two aspects are maintained. A system that can be pushed very fast, for example due to a higher resonance frequency and a stiff system that does not show large overshoot, reduces the tracking error. These two aspects have been addressed in the parameter configuration of the stage-controller (see appendix D.4).

6.4 | MEAN SQUARED DISPLACEMENT IN A FEEDBACK SYSTEM

The stage vibrations yield oscillations in the measured particle and stage trajectory and consequently also in derived quantities like the MSD. The problem with this is that those oscillations can be easily misinterpreted as transient step correlations of the actual particle motion physics. Hence, anomalous diffusion can be confused with stage oscillations. This problem is tackled by calculating the expected response statistics of the entire SPOT system actively tracking a normal diffusing particle with a realistic stage-stage controller transfer function. BERGLUND *et al.* developed the necessary mathematical framework which is used in the following.[52, 193] In section 3.3, the SPOT system feedback loop was modeled with transfer function formalism driven by white noise kicks $\nu_{bm}(t)$ and photon counting noise as input $n(t)$. All spatial axes are treated independently to reduce the analysis on a single spatial dimension. The stage position $r_s(t)$ is split into two parts, one that results from the particle motion $r_{s|p}(t)$ and one that results from the counting noise signal contribution

$r_{s|n}(t)$. With reference to eq. (3.30), the following equations are valid:

$$r_s(t) = r_{s|p}(t) + r_{s|n}(t), \quad (6.15)$$

$$R_{s|p}(s) = \frac{G_{sc}(s)}{s(1 + G_{sc}(s))} \mathcal{L}\{\nu_{bm}(t)\} \quad \text{and} \quad (6.16)$$

$$R_{s|n}(s) = \frac{G_{sc}(s)}{1 + G_{sc}(s)} N(s). \quad (6.17)$$

State-space realizations of these two systems are obtained by converting the transfer function to the system $\mathbf{A}_{n,p}$, input $\mathbf{B}_{n,p}$, and output matrices $\mathbf{C}_{n,p}$ in controller canonical form (see appendix A.5). The feed-forward matrix $\mathbf{D}_{n,p}$ is not necessary within this context and can be set to zero. The state and output equations are written in typical notation as

$$\dot{\mathbf{x}}_n(t) = \mathbf{A}_n \mathbf{x}_n(t) + \mathbf{B}_n u_n(t), \quad (6.18)$$

$$\dot{\mathbf{x}}_p(t) = \mathbf{A}_p \mathbf{x}_p(t) + \mathbf{B}_p u_p(t), \quad (6.19)$$

$$y_n(t) = \mathbf{C}_n \mathbf{x}_n, \quad \text{and} \quad (6.20)$$

$$y_p(t) = \mathbf{C}_p \mathbf{x}_p. \quad (6.21)$$

The index n refers to the measurement noise-driven system, while the index p denotes the system attributed to the particle motion. The meaning of the state vectors $\mathbf{x}_n(t)$ and $\mathbf{x}_p(t)$ are unknown at first hand, but not crucial for further discussion. The inputs are $u_n(t) = n(t)$ and $u_p(t) = \nu_{bm}(t)$, and the outputs are $y_n(t) = r_{s|n}(t)$ and $y_p(t) = r_{s|p}(t)$, respectively. All of those quantities are scalar functions. The steady-state process variances $\mathbf{Q}_{\infty|p}$ and $\mathbf{Q}_{\infty|n}$ are calculated by solving the Lyapunov equation (see eq. (A.75) in the appendix A.8) with the matrices defined above, and by using the covariance amplitudes $V_p = 2D$ (non-bold D is the diffusion coefficient, not to be confused with the feed-forward matrix) or $V_n = n^2$. For the photon counting noise part, the following statistical properties can be derived[52]

$$\mathcal{E}(r_{s|n}(t)) = 0, \quad (6.22)$$

$$\mathcal{E}(r_{s|n}(t + \tau)r_{s|n}(t)) = \mathbf{C}_n e^{\mathbf{A}_n \tau} \mathbf{Q}_{\infty|n} \mathbf{C}_n^T. \quad (6.23)$$

Note the occurrence of the *matrix exponential function* $e^{\mathbf{X}t}$ that is defined by its series expansion

$$e^{\mathbf{X}t} = \sum_{k=0}^{\infty} \frac{\mathbf{X}^k t^k}{k!}. \quad (6.24)$$

Unfortunately, the system attributed to the particle position noise is only marginally stable due to the transfer functions pole at the origin ($s = 0$ in eq. (6.16)). Therefore, it is wise to build the state-space model not for the actual stage position $\mathbf{r}_{s|p}(t)$ but for its first time derivative $\dot{\mathbf{r}}_{s|p}(t)$. Technically, this requires a multiplication by s removing the pole at the origin of $R_{s|p}(s)$. The modified system is denoted by the matrices $\tilde{\mathbf{A}}_p$, $\tilde{\mathbf{B}}_p$, $\tilde{\mathbf{C}}_p$ and $\tilde{\mathbf{Q}}_{\infty|p}$. The equation for the statistics of this marginally stable process are slightly more complex due to the required additional integration and can be written as[52]

$$\mathcal{E}(r_{s|p}(t)) = 0, \quad (6.25)$$

$$\mathcal{E}(r_{s|p}(t + \tau)r_{s|p}(t)) = \tilde{\mathbf{C}}_p \tilde{\mathbf{A}}_p^{-2} (e^{\tilde{\mathbf{A}}_p(t+\tau)} + e^{\tilde{\mathbf{A}}_p t} - e^{\tilde{\mathbf{A}}_p \tau} - 2\tilde{\mathbf{A}}_p t - \mathbf{1}) \tilde{\mathbf{Q}}_{\infty|p} \tilde{\mathbf{C}}_p^T. \quad (6.26)$$

Using these statistics, the contributions to the stage positional MSD are

$$\text{MSD}_n(\tau) = \mathcal{E} \left([r_{s|n}(t+\tau) - r_{s|n}(t)]^2 \right) = 2\mathbf{C}_n \left(\mathbb{1} - e^{\mathbf{A}_n\tau} \right) \mathbf{Q}_{\infty|n} \mathbf{C}_n^T, \quad (6.27)$$

$$\text{MSD}_p(\tau) = \mathcal{E} \left([r_{s|p}(t+\tau) - r_{s|p}(t)]^2 \right) = 2\tilde{\mathbf{C}}_p \tilde{\mathbf{A}}_p^{-2} \left(e^{\tilde{\mathbf{A}}_p\tau} - \tilde{\mathbf{A}}_p\tau - \mathbb{1} \right) \tilde{\mathbf{Q}}_{\infty|p} \tilde{\mathbf{C}}_p^T. \quad (6.28)$$

The total MSD of the stage position is therefore given as the sum of eq. (6.27) and eq. (6.28). This equation can be validated for example by reproducing the MSD for underdamped Brownian motion eq. (2.11) from section 2.1 by using eq. (6.28), $\mathbf{x} = \dot{r}$, $\mathbf{A}_p = -\xi m^{-1}$, $\mathbf{B}_p = m^{-1}$, $\mathbf{C}_p = 1$, and $V_p = v_{\text{BM}}$.

6.4.1 | OSCILLATOR DRIVEN BY BROWNIAN MOTION AND MEASUREMENT NOISE

The transfer function of a forced oscillator (see eq. (A.29)) should be considered as a model for the stage-stage controller system. It will turn out in this section that a closed analytical form of the MSD equation can be found. The state-space model of a driven oscillator is defined in controller canonical (see appendix A.5) form by

$$\mathbf{A}_n = \tilde{\mathbf{A}}_p = \begin{pmatrix} 0 & 1 \\ -\omega_n^2 & -2\lambda\omega_n \end{pmatrix}, \quad \mathbf{B}_n = \tilde{\mathbf{B}}_p = \begin{pmatrix} 0 \\ 1 \end{pmatrix} \quad \text{and} \quad \mathbf{C}_n = \tilde{\mathbf{C}}_p = \begin{pmatrix} \omega_n^2 & 0 \end{pmatrix} \quad (6.29)$$

with $y_n(t) = r_{s|n}(t)$ and $\tilde{y}_p(t) = \dot{r}_{s|p}(t)$. Hence, the steady-state process variance is calculated as

$$\mathbf{Q}_{\infty|n} = \begin{pmatrix} \frac{n^2}{4\lambda\omega_n^3} & 0 \\ 0 & \frac{n^2}{4\lambda\omega_n} \end{pmatrix} \quad \text{and} \quad \mathbf{Q}_{\infty|p} = \begin{pmatrix} \frac{D}{2\lambda\omega_n^3} & 0 \\ 0 & \frac{D}{2\lambda\omega_n} \end{pmatrix}. \quad (6.30)$$

Evaluation of the MSD for the forced oscillator by eq. (6.27) and eq. (6.28) yields

$$\text{MSD}_{n,\text{FO}}(\tau) = \frac{n^2\omega_n}{4\lambda} \left\{ 1 - e^{-\lambda\omega_n\tau} \left[\cosh(\omega_n\tau\sqrt{\lambda^2-1}) + \frac{\lambda \sinh(\omega_n\tau\sqrt{\lambda^2-1})}{\sqrt{\lambda^2-1}} \right] \right\} \quad (6.31)$$

and

$$\begin{aligned} \text{MSD}_{p,\text{FO}}(\tau) = 2D\tau + \frac{D(4\lambda^2-1)}{\lambda\omega_n} & \left[e^{-\lambda\omega_n\tau} \cosh(\omega_n\tau\sqrt{\lambda^2-1}) - 1 \right] \\ & + \frac{De^{-\lambda\omega_n\tau}}{\omega_n\sqrt{\lambda^2-1}} \sinh(\omega_n\tau\sqrt{\lambda^2-1}) (4\lambda^2-3), \end{aligned} \quad (6.32)$$

respectively. For large τ , the oscillatory influence of the stage response is expected to vanish and indeed, $\text{MSD}_{\text{FO},n}(\tau)$ approaches a constant value characterized by the noise density n

$$\lim_{\tau \rightarrow \infty} \text{MSD}_{n,\text{FO}}(\tau) = \frac{n^2\omega_n}{4\lambda} \quad (6.33)$$

and $\text{MSD}_{\text{FO},p}(\tau)$ converges to linear scaling observed for Brownian motion

$$\lim_{\tau \rightarrow \infty} \frac{\text{MSD}_{p,\text{FO}}(\tau)}{\tau} = 2D. \quad (6.34)$$

6.4.2 | MODELING OF THE SIMULATED MEAN SQUARED DISPLACEMENT

The described technique of calculating the MSD of the stage motion should be applied to simulation results like those shown in fig. 6.18. As already mentioned, the computational effort is high, and calculation time exceeded an acceptable level for more than 500 estimation cycles per trajectory. Thus, ensembles of 50 trajectories per parameter configuration are computed and processed to get their corresponding (time-averaged) MSD. Ensemble-averages of those time-averaged MSDs are compared with a model function by non-linear least-squares fitting. The fitting results, keeping the diffusion coefficient constant, are shown in fig. 6.20.

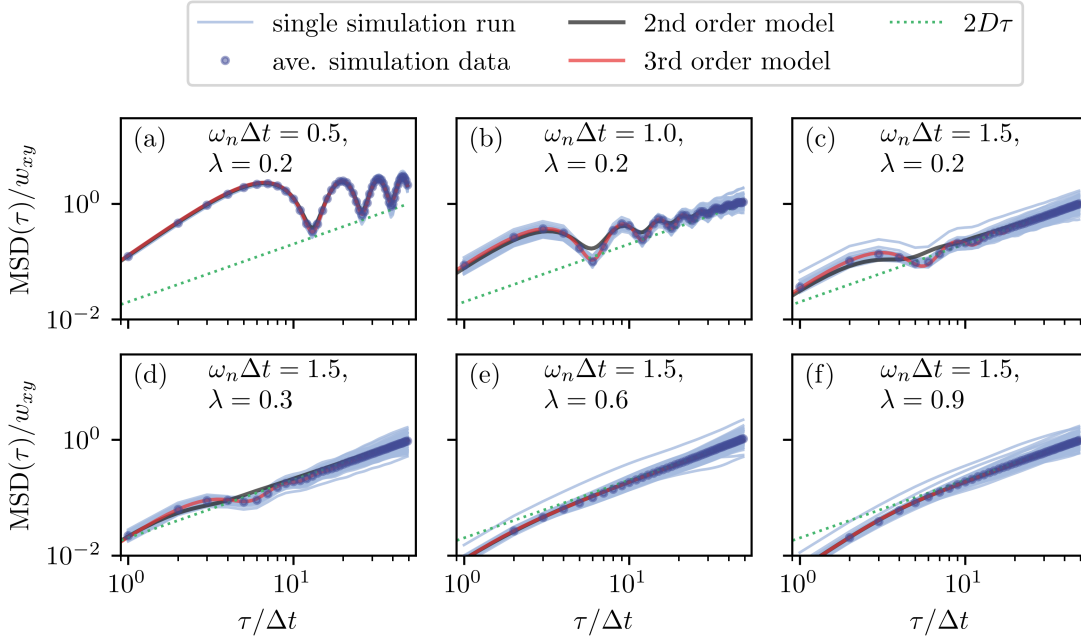


Figure 6.20.: One-dimensional MSD of the nanopositioning stage coordinates resulting from 3D-SPOT simulations with deactivated photon counting noise or stage noise, but with a damped oscillatory transfer function converting target positions to actual stage movements. The particle’s diffusion coefficient was set to $0.01w_{xy}^2\Delta t^{-1}$, target changes happen each three position estimation cycles, and the stage transfer function parameters are varied. In the top row, the damping coefficient is kept constant at $\lambda = 0.2$, while the frequency varies from $\omega_n\Delta t = 0.5$ to 1.5 . In contrast, in the bottom row, $\omega_n\Delta t$ is fixed at 1.5 , and the damping varies from $\lambda = 0.3$ to 0.9 . Solid light blue lines show single simulation runs consisting of 500 estimation cycles, while blue dots represent the average of 50 simulations each. The solid black and red solid line are the best fits by the forced oscillator and PI-controlled oscillator model, respectively. Green dotted lines are the standard result for the MSD of free Brownian motion scaling with $2D\tau$.

A comparison with the free diffusion result shows that the simulated MSD converges to the linear scaling for large τ but deviates for smaller τ significantly. The MSD shows strong oscillations for small damping coefficients, mostly surpassing the free diffusion case. Large damping coefficients yield an MSD that approaches the free diffusion limit from below. The time scale on which the oscillations occur correlates with the inputted ω_n . Contrary to BERGLUND *et al.*, a second-order model appears not sufficient to represent the full SPOT simulation in all details, even if it was a second-order transfer function used to simulate the stage-stage controller subsystem. The occurring modulation of the MSD is underestimated for certain parameter configurations. The model of a PI-controlled oscillator (see eq. (A.66), with $K_d = 0$ and $k_{dc} = 1$) is utilized containing four parameters,

namely the natural frequency ω_n , the damping λ , and the controller gains K_p and K_i . Such a transfer function is a third-order system written as

$$G_{\text{PI,osci}}(s) = \frac{(K_p s + K_i) \omega_n^2}{s^3 + 2\lambda\omega_n s^2 + (\omega_n^2 + K_p \omega_n^2) s + K_i \omega_n^2} \quad (6.35)$$

and represents the conversion of the particle motion and measurement noise input by the entire SPOT system ($G_{sc}(s)/(1 + G_{sc}(s))$) on the stage coordinate. The state-space realization in controller canonical form is defined by

$$\mathbf{A}_n = \tilde{\mathbf{A}}_p = \begin{pmatrix} 0 & 1 & 0 \\ 0 & 0 & 1 \\ -K_i \omega_n^2 & -\omega_n^2 - K_p \omega_n^2 & -2\lambda\omega_n \end{pmatrix} \quad (6.36)$$

$$\mathbf{B}_n = \tilde{\mathbf{B}}_p = \begin{pmatrix} 0 \\ 0 \\ 1 \end{pmatrix} \quad \text{and} \quad \mathbf{C}_n = \tilde{\mathbf{C}}_p = (K_i \omega_n^2 \quad K_p \omega_n^2 \quad 0), \quad (6.37)$$

while the feed-forward matrices $\mathbf{D}_n = \mathbf{D}_p = 0$ are again not required. The simulation does not include photon counting noise, thus only the particle motion-based system is considered. The steady-state process variance solves the corresponding Lyapunov equation with

$$\mathbf{Q}_{\infty|p} = \begin{pmatrix} -\frac{2\lambda D}{K_i \omega_n \beta_1} & 0 & \frac{D}{\beta_1} \\ 0 & -\frac{D}{\beta_1} & 0 \\ \frac{D}{\beta_1} & 0 & \frac{(1+K_p)\omega_n^2 D}{\beta_1} \end{pmatrix}. \quad (6.38)$$

using the abbreviation $\beta_1 = K_i \omega_n^2 - 2(1 + K_p)\lambda\omega_n^3$. Due to the complicated matrix exponential expression, it is not easy to obtain an analytical formula for the stage position MSD. However, eq. (6.28) can be evaluated numerically, making use of the Padé approximation.[194] The PI-controlled oscillator model is able to reproduce the simulation data with high accuracy while keeping the damping and diffusion coefficient at fixed values that are equal to the input data. In table 6.5, the parameters of the two different fitting models are contrasted.

Table 6.5.: Overview of the fitting results of the forced oscillator and PI-controlled oscillator model. Starred values (*) are kept fixed while fitting.

Input		Forced oscillator model			PI-controlled oscillator model				
$\omega_n \Delta t$	λ	$\omega_n \Delta t$	λ	adj. R ² /%	$\omega_n \Delta t$	λ (fixed)	K_i	K_p	adj. R ² /%
0.50	0.20	0.482	0.02	99.35	0.159	0.20*	0.453	8.182	99.82
1.00	0.20	1.057	0.06	97.93	0.643	0.20*	0.547	1.642	99.96
1.50	0.20	1.398	0.19	99.04	0.767	0.20*	0.423	1.100	99.83
1.50	0.30	1.693	0.33	93.65	0.729	0.30*	0.477	1.491	99.98
1.50	0.60	2.026	0.99	99.92	1.500*	0.60*	0.714	0.309	99.92
1.50	0.90	0.780	0.66	99.99	1.500*	0.90*	0.517	0.090	99.98

The adjusted R² value indicates the almost perfect correspondence between the PI-controlled oscillator model and the simulation results, while already, the forced oscillator model yields only small deviations. Unfortunately, it was not possible to reproduce the simulation input parameter accurately. The resonance frequency deviates strongly from the input settings. For large damping coefficients $\lambda \geq 0.6$, this is not crucial as the model is almost independent of ω_n , and the same result can be reproduced with different

resonance frequencies. For those cases, the second-order forced oscillator model is sufficient and coincides perfectly with the third-order PI-controlled oscillator model. To account for that, the resonance frequency ω_n was kept constant in the third-order model. However, for smaller damping coefficients $\lambda < 0.6$ where oscillations are present in the MSD, ω_n becomes important. The fitting displays smaller ω_n than originally inputted. The conclusion is that the full simulation covers more aspects than the linear model. For example, the discussed nonlinearities of the localization step and discrete-time stage position updates are not included.

Another important result of this section is that the first four MSD points that appear as the most meaningful in some studies (see [195]), are influenced most heavily by the stage-stage controller transfer function. Fitting a straight line or power-law to those points may yield falsified results for the diffusion coefficient and/or anomaly parameter. The best fitting range for a straight line or power-law is a use-case dependent compromise between the short lag time range influenced by measurement artifacts and the long lag time range characterized by a worse data basis for averaging.

7 | REFERENCE EXPERIMENTS

The large number of error sources and measurement artifacts discovered in theoretical considerations and computer simulations imply the conduction of reference measurements. Studying samples with known properties helps to identify which conclusions can or cannot be drawn from measurements about unknown systems.

For this purpose, a large set of trajectories of fluorescent polystyrene nanoparticles with nominal diameters of (27 ± 4) nm, (50 ± 18) nm and (100 ± 20) nm is recorded with 3D-SPOT in different aqueous solutions. Experiments are performed in a glycerol/water concentration series ranging from 50 vol% to 99 vol%, in dextran, saccharose and polyethylene glycol solutions (see section 5.3.1 for more details).

An example of a trajectory resulting from 3D-SPOT is depicted in fig. 7.1. It was a 50 nm sized particle in a 90 vol% glycerol/water mixture that was tracked for more than 2 minutes yielding 1×10^5 positions and a trace of the detected fluorescence (fig. 7.1 (c)). The three-dimensional particle trajectory (fig. 7.1 (a)) appears random, undirected and not bound to a certain region. Thus, its general appearance corresponds to that of a Brownian walk and meets the expectation. At first glance, the position variance of the three single-coordinate traces (fig. 7.1 (b)) appear similar, but slightly enlarged on intermediate time scales for the z -coordinate. The detected photon count rate is about 44 kcps on average. In fact, it is not constant in time, but decreases due to photo-bleaching. Single spikes of the fluorescence trace (e.g., at $t \approx 63$ s) may indicate an unstable tracking period arising from a second particle approaching the detection volume or a random accumulation of incorrect localizations.

Data like these are measured for the different nanoparticle/solution medium combinations. To achieve a successful tracking, smaller particles need more viscous solvents and, in consequence, it was not possible to test all combinations of solution medium and particle sizes. While the presented example does not suffer from obvious drift motion, some trajectories do. To correct for that, a straight line is fitted to each coordinate trace and subtracted subsequently. Additionally, positional oscillation with the frequency given by the stage's feedback period are removed by phase-sensitive lock-in analysis as described in [186]. From each recorded and corrected trajectory, the one-dimensional and time-averaged MSD is calculated for the x -, y -, and z -direction. MSDs are averaged for each concentration and particle size separately, where all spatial dimensions are considered equivalent as the solvents are isotropic.

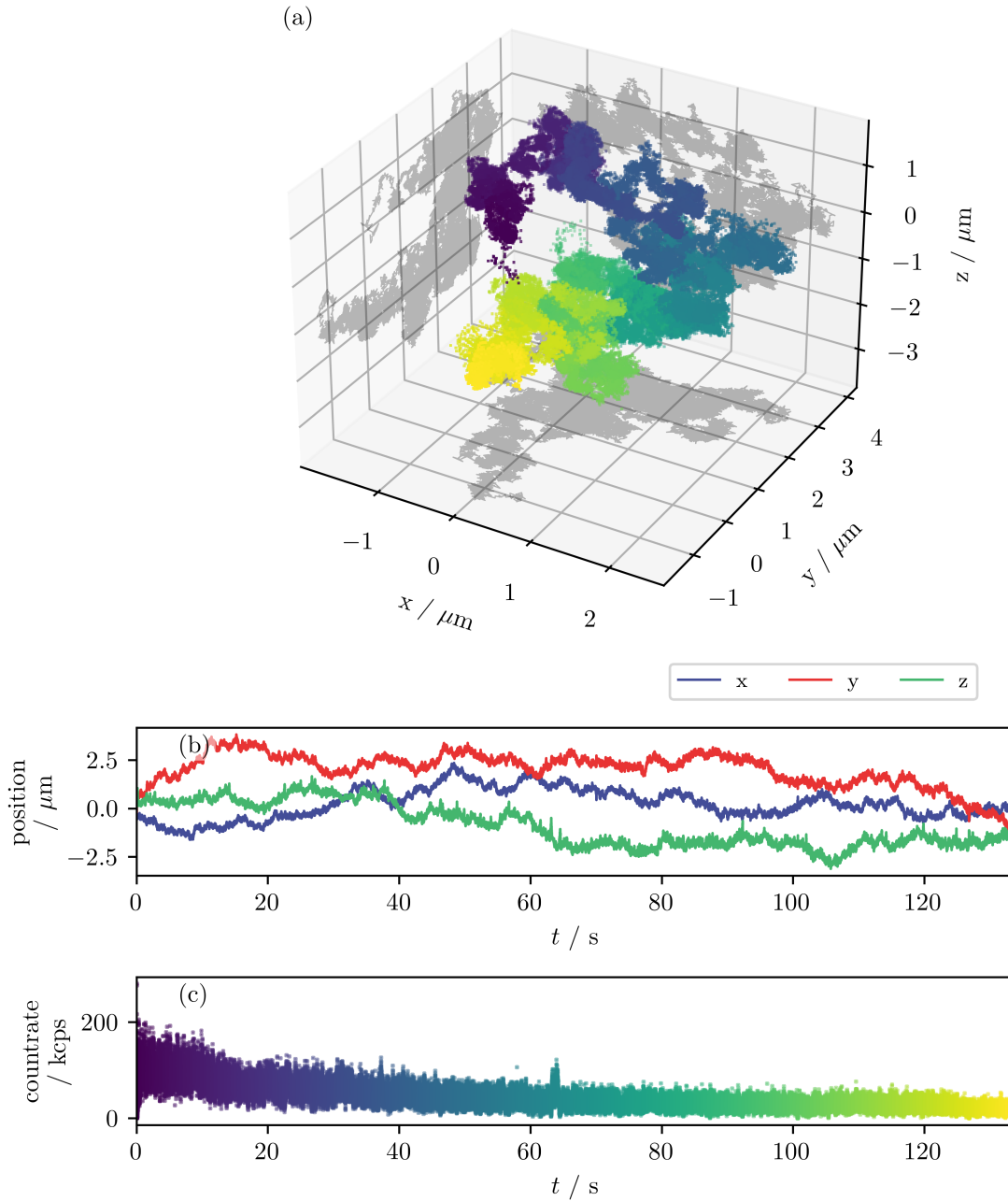


Figure 7.1.: Example of a trajectory recorded with 3D-SPOT. A 50 nm sized particle was followed in a 90% glycerol/water mixture for about 134s with 1.3ms temporal resolution. (a) Three dimensional representation of the recorded particle positions. The time is color-coded (dark blue to yellow) and two-dimensional projections are plotted alongside. (b) Time series of the particle coordinates. (c) Detected photon count rate with the same color-code as in (a).

7.1 | DYNAMIC VISCOSITIES OF DIFFERENT AQUEOUS SOLUTIONS

In order to confirm the quantitative use of the measured trajectories, the dynamic viscosity of the suspension fluids are determined and compared with reference values. For this purpose, it is necessary to derive the diffusion coefficient of the particles from the MSD. In this context, the results, in particular the MSDs, are examined with regard to artifacts of the measurement method. In fig. 7.2, the mean MSDs measured in the glycerol/water mixtures are shown with glycerol content increasing from (a) to (h).

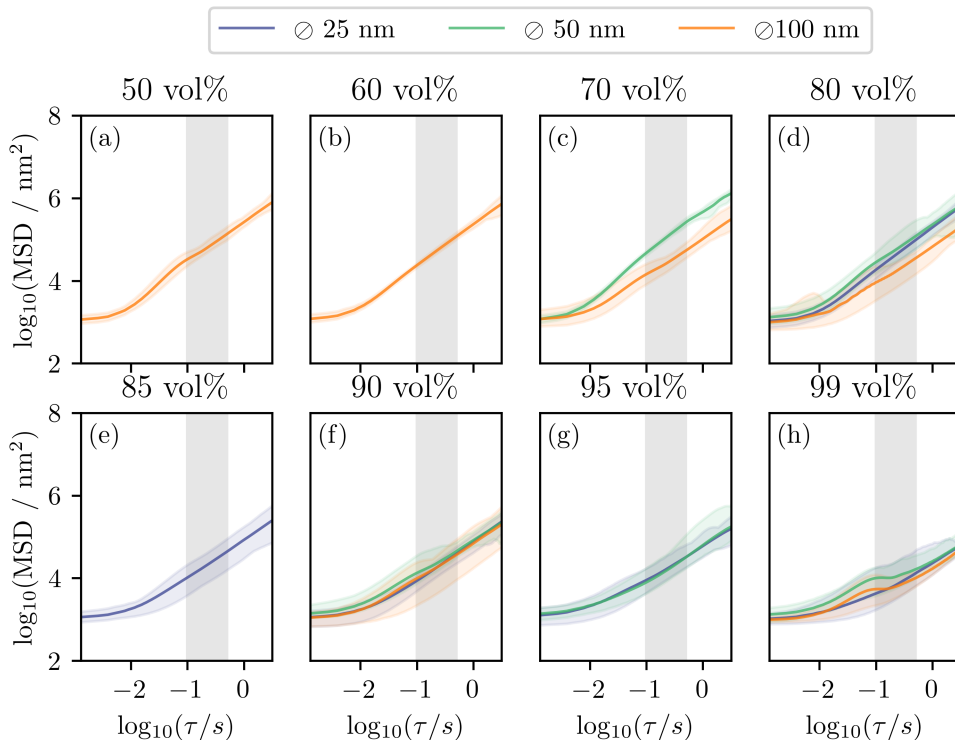


Figure 7.2.: Mean MSDs of trajectories in glycerol/water mixtures of various concentrations. Shaded areas indicate minimum-to-maximum ranges that contain the course of all individual MSDs from the data set. The gray region indicates the fitting range.

Simple linear scaling is expected for Brownian motion, but is not observed in the measurement data. Instead, for $\tau < 10$ ms, the averaging error yields to apparent subdiffusive scaling that transits to a linear scaling for larger lag times. Closer observation of the MSD course reveals a bending for the lowest and highest glycerol concentration at $\tau \approx 100$ ms. Figure 7.3 shows the MSDs for the sugar and polymer solutions in a matrix representation, where each row corresponds to a specific particle size and each column summarizes the result for a different substance. Lower concentrations (dotted lines) yield steeper MSDs. Once again, the bending for $\tau \approx 100$ ms is present and is strongly pronounced for the 30 wt% dextran and 50 wt% polyethylene glycol solution.

In the case of Brownian motion, the diffusion coefficient of a single particle can be determined from its MSD by straight line fitting. Due to the more complex course of the MSDs, the result will depend on the selected time range and a proper choice is very important. Here, the MSDs are fitted in the interval of 100 ms to 500 ms because this range is less affected by the short time measurement errors but still satisfactorily averaged.

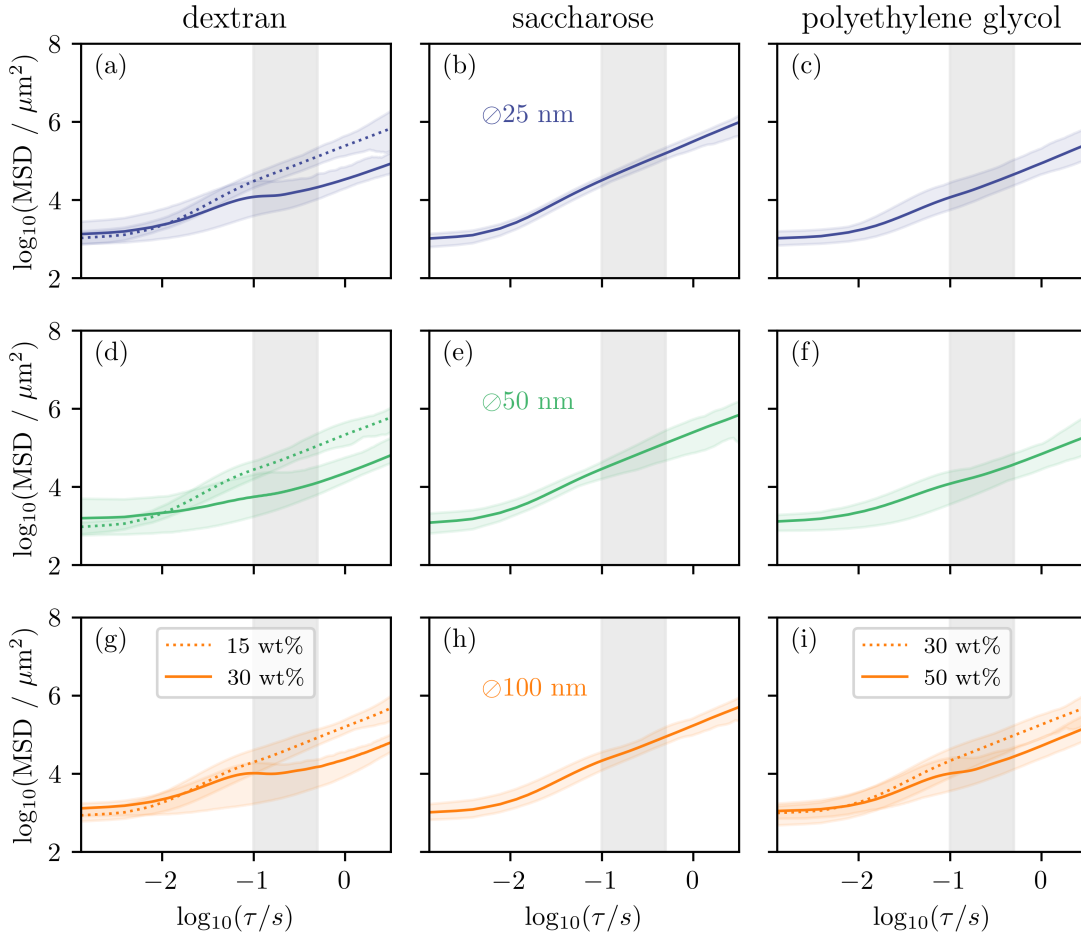


Figure 7.3.: MSDs for particles of different size (rows) solved in different media (columns): (a) Dextran, 25 nm; (b) saccharose, \varnothing 25 nm; (c) polyethylene glycol, \varnothing 25 nm; (d) dextran, \varnothing 50 nm; (e) saccharose, \varnothing 50 nm; (f) polyethylene glycol, \varnothing 50 nm; (g) dextran, \varnothing 100 nm; (h) saccharose, \varnothing 100 nm; (i) polyethylene glycol, \varnothing 100 nm. Shaded areas indicate minimum-to-maximum ranges that contain the course of all MSDs before averaging.

Moreover, the final outcome in this range is only weakly influenced by the MSD bending at $\tau \approx 100$ ms.

The slope of the linear model is converted to the individual diffusion coefficient D by eq. (2.15). Using the mean particle diameter measured with dynamic light scattering (see section 5.1), this diffusion coefficients are used to compute the dynamic viscosities η with the help of the Stokes-Einstein equation for spheres (combination of eq. (2.16) and eq. (2.17)). Those values obtained for η are compared in fig. 7.4 with data found in literature. References for glycerol are taken from SHEELY and CHENG[196, 197], a formula to calculate the viscosity of dextrans in aqueous solutions was extracted from CARRASCO[198], SWINDELLS and MIGLIORI provided the references for saccharose[199, 200], and data from REGUPATHI and HOLYST are used for comparison with the polyethylene glycol/water mixtures[201, 202]. Furthermore, a interpolation equation for the dynamic viscosity of glycerol was derived from rolling-ball viscometer measurements (see appendix E.1) and added to fig. 7.4 (a).

The viscosities resulting from 3D-SPOT do not show smooth curves, but the expected trends are visible for all three particle sizes. The scattering of some data points is large

due to the ensemble sizes and the width of the particle size distribution. Because slow particles are easier to catch in the initial particle search procedure of a 3D-SPOT measurement, 3D-SPOT has a bias towards slower (bigger and brighter) particles. This bias is pronounced for more difficult experimental situations which explains the deviation for the 100 nm particles in less viscous environments and produces an overestimation of the real viscosity. Provided that even literature data differ, the correspondence of the 3D-SPOT results and the reference curves are satisfactory.

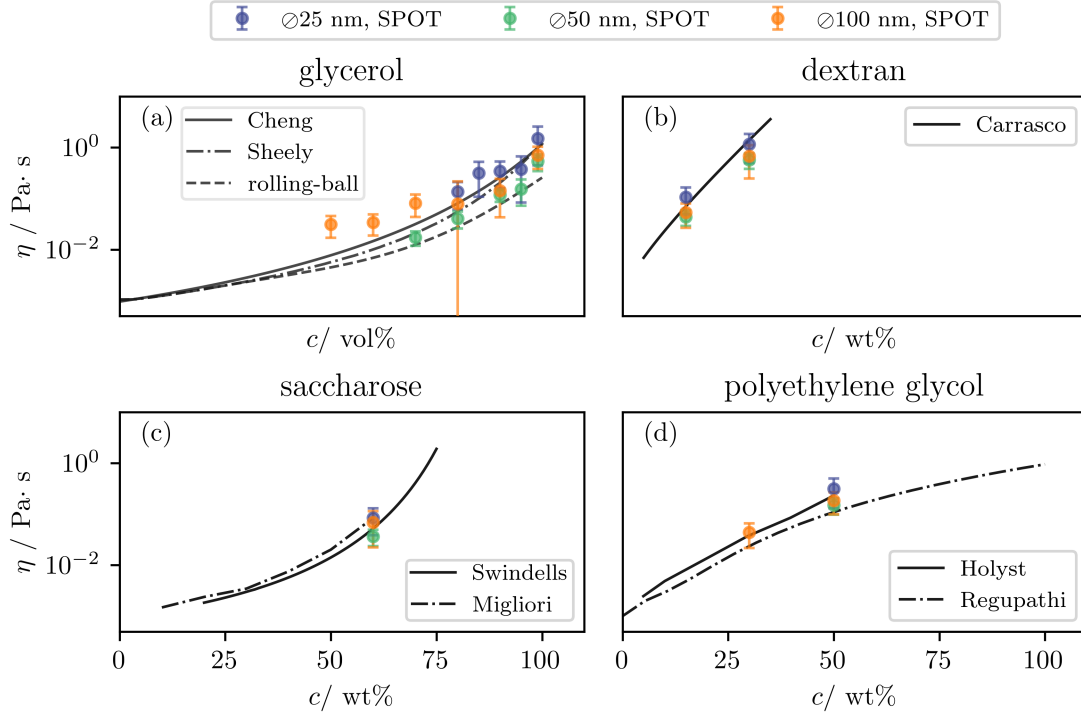


Figure 7.4.: Concentration dependency of the dynamic viscosity η of different aqueous solutions. 3D-SPOT results are depicted as dots with error bars in blue (25 nm), green (50 nm) and orange (100 nm) for (a) glycerol (b) dextran (c) saccharose and (d) polyethylene glycol, respectively. Literature resources are shown as solid and dash-dotted black lines. In the case of glycerol, also rolling-ball viscometer measurements are given (dashed black line).

7.2 | ANOMALY DETECTION

As seen in previous chapters, the intrinsic oscillations of the tracking procedure generate deviations from the linear scaling of the MSD even when measuring Brownian motion. These deviations can easily be misinterpreted as anomalous diffusion, which is why it will now be tested to what extent anomalies can be detected by 3D-SPOT. To infer the degree of anomaly on the time scale of interest, a straight-forward approach is to calculate the time-averaged MSD's logarithmic derivative as

$$\alpha(\tau) = \frac{d}{d \log_{10}(\tau)} \log_{10}(\text{MSD}(\tau)) . \quad (7.1)$$

In order to gain smooth varying $\alpha(\tau)$, the numerical fluctuations are removed following the procedure described in [203]. As an example, the MSDs that are created by simulation

of the SPOT method in the context of section 6.4 are converted to $\alpha(\tau)$ and plotted in fig. 7.5. While the curves approach the limit $\alpha(\tau) = 1$ for longer lag times, they differ from normal diffusion scaling depending on the setups transfer function parameters and not on the actual particle's diffusion characteristics.

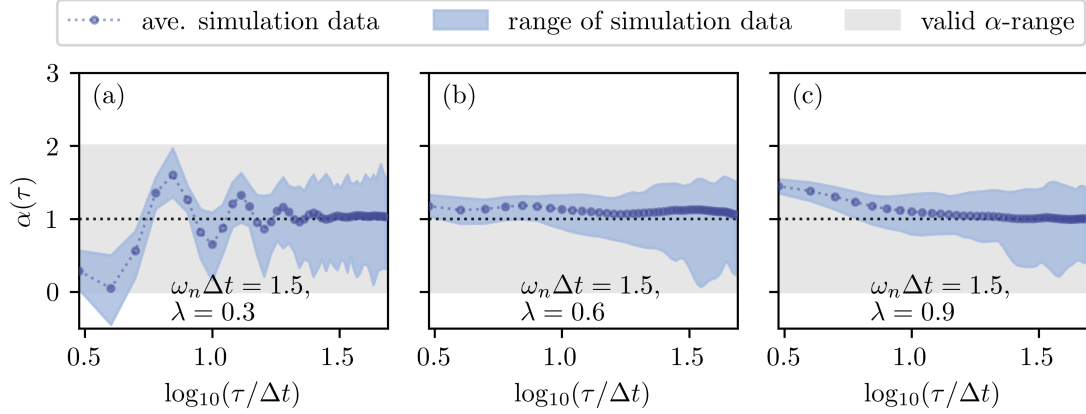


Figure 7.5.: Lag time dependent anomaly parameter determined for the simulation results presented in fig. 6.20(e)-(f). The light blue shaded area indicates the minimum-to-maximum range of the individual $\alpha(\tau)$ courses determined for each simulated MSD curve.

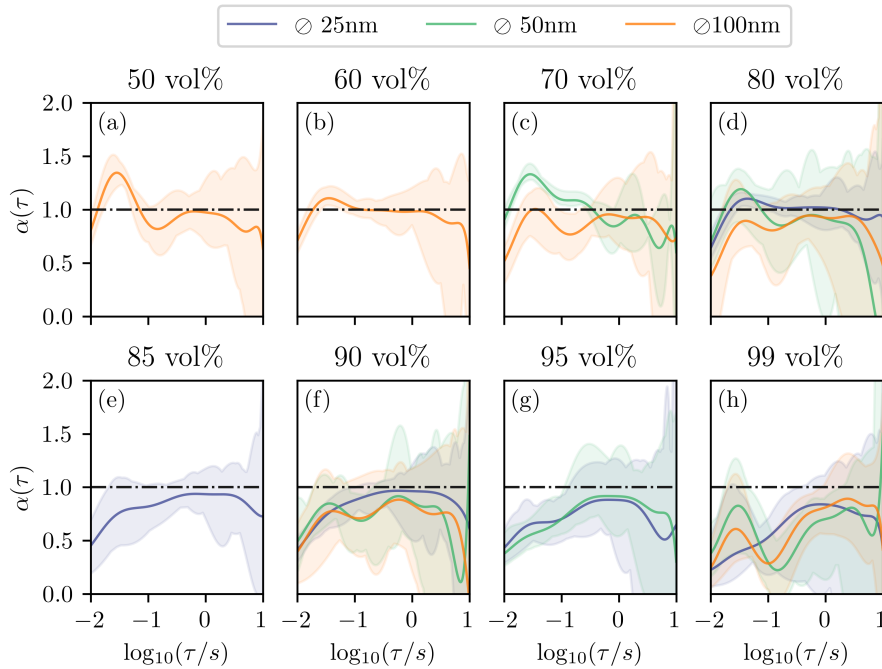


Figure 7.6.: Anomaly $\alpha(\tau)$ extracted from the MSD shown in fig. 7.3. Shaded areas represent the minimum-to-maximum ranges that contain the course of all $\alpha(\tau)$ before averaging.

In the same way, the reference experiments for 3D-SPOT are analyzed. In fig. 7.6, the lag time dependent anomaly parameter is shown for the glycerol concentration series measurement. While there are no reasons for the particle motion in glycerol/water mixtures to deviate from the linear τ -scaling of the MSD, there are significant anomalies detected. Especially in the short time regime ($\tau < 100$ ms), where the weighting of the localization

error is more severe, the MSD runs subdiffusive. Most concentration show an $\alpha(\tau)$ close to 1 in the range 100 ms to 1 s, a regime that is less influenced by the localization and tracking errors but still properly averaged. Lower particle diffusion coefficients (higher viscosities of the solution medium or larger particle diameter) lead to a later reach of the normal diffusion scaling. As already seen in fig. 7.2, the 50 vol% and 99 vol% glycerol/water mixtures show the strongest apparent anomalies.

It is not easy to quantitatively compare the complicated curves for $\alpha(\tau)$ and conclude which substance shows stronger anomalies than another. Therefore, an average anomaly $\bar{\alpha}$ is defined for the analogous lag time range of the diffusion coefficient determined in section 7.1. Hence, $\alpha(\tau)$ is averaged in the range $\tau \in [100 \text{ ms}; 500 \text{ ms}]$ for each individual one-dimensional MSD

$$\bar{\alpha} = \int_{100 \text{ ms}}^{500 \text{ ms}} \alpha(\tau) d\tau, \quad (7.2)$$

and presented in fig. 7.7 as box-and-whiskers plots.

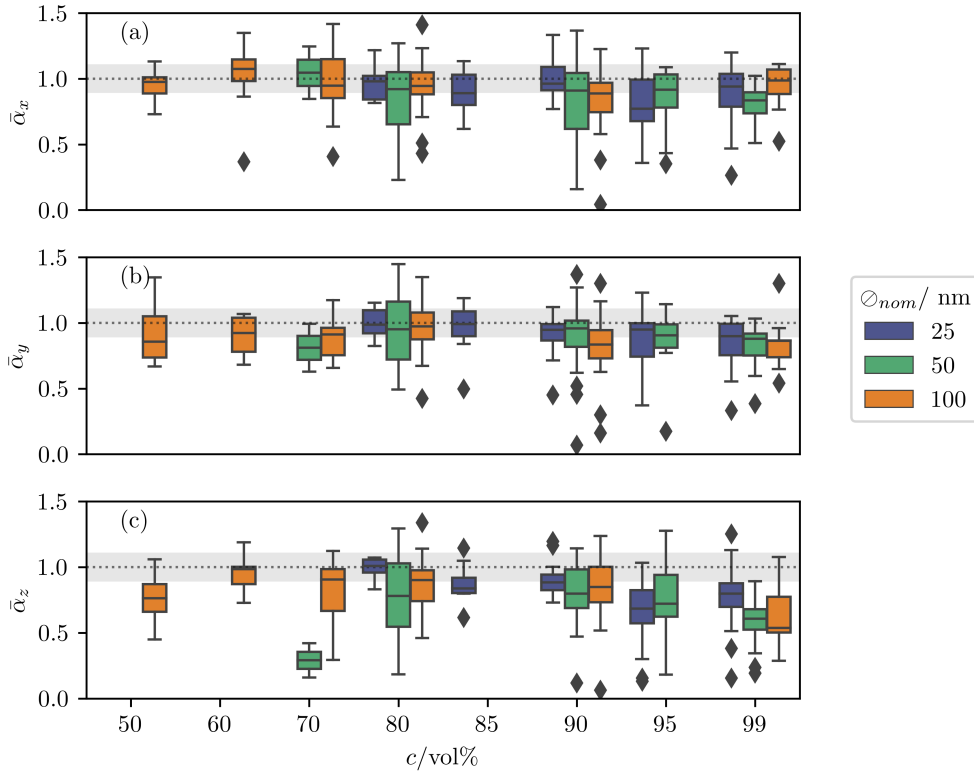


Figure 7.7.: Box-and-whiskers plots of the individual averaged anomalies extracted from the particles one-dimensional MSDs along (a) the x -direction, (b) the y -direction, and (c) the z -direction. A gray shaded area indicates a 10 % interval around the normal diffusive scaling range ($\bar{\alpha} = 1$, dotted black line). Whiskers corresponds to 1.5 of the interquartile range and outliers are displayed as diamonds.

The majority of the averaged anomaly parameters lies within a 10 % interval around $\bar{\alpha} = 1$ for the lateral coordinates ($\bar{\alpha}_x$ and $\bar{\alpha}_y$, see fig. 7.7 (a) and (b)). Most of the axial mean anomaly parameter ($\bar{\alpha}_z$, see fig. 7.7 (c)) differ significantly from the $\bar{\alpha}$ - interval accepted as normal diffusion. Hence, it is concluded that the larger tracking/localization error in z -direction compared to the lateral directions impede its usage for anomaly detection.

Repeating the same type of analysis on the aqueous sugar and polymer solutions, but ignoring the z -direction, the results shown in fig. 7.8 are obtained. For short lag times,

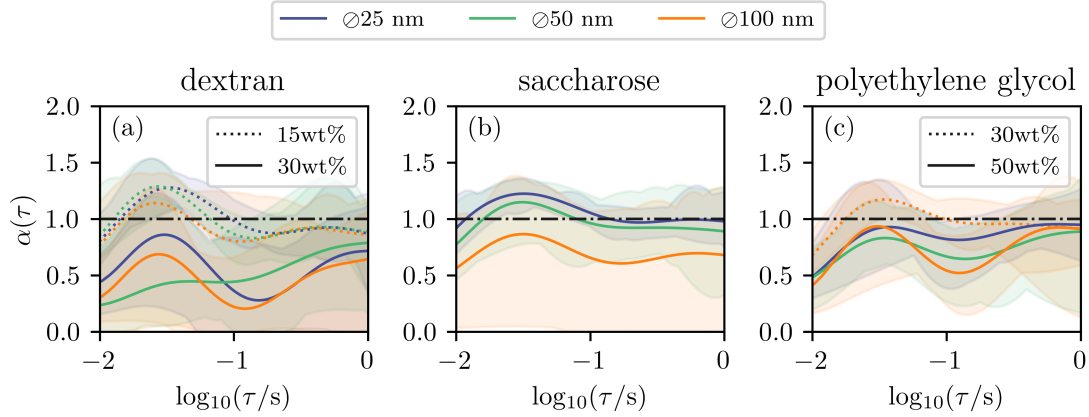


Figure 7.8.: Anomaly $\alpha(\tau)$ extracted from the lateral one-dimensional MSDs shown in fig. 7.3. (a) 15 wt% (dotted lines) and 30 wt% (solid lines) of dextran solved in water (b) 60 wt% saccharose solved in water and (c) 30 wt% and 50 wt% of polyethylene glycol solved in water. Shaded areas indicate minimum-to-maximum ranges that contain the course of all individual $\alpha(\tau)$.

subdiffusive scaling due to localization uncertainties is observed. For 15 wt% dextran, 60 wt% saccharose, or 30 wt% polyethylene glycol, the course of $\alpha(\tau)$ is close to 1 indicating Brownian motion. However, the anomaly parameter differs recognizably from 1 for the 30 wt% dextran solved in water. This is true for all used particle sizes. The 50 wt% polyethylene glycol solution show similar deviations from normal diffusion. But in contrast to the dextran measurements, $\alpha(\tau)$ approaches 1 within a few hundred millisecond.

Now, the averaged anomaly parameter is calculated and plotted in fig. 7.9, but only the lateral coordinates are considered. Since $\bar{\alpha}_{\text{lat}}$ is less sensitive to short time discrepancies from normal diffusion, but highly susceptible to $\alpha(\tau)$ for larger τ , the anomaly detections are slightly modified. In this representation, there is no detectable anomaly for both measured polyethylene glycol concentrations, but the broader scattering of the data for 15 wt% foreshadows concentration dependent diffusion anomalies in dextran solutions. In the case of 30 wt% dextran solved in water, stronger deviations from normal diffusion are obtained.

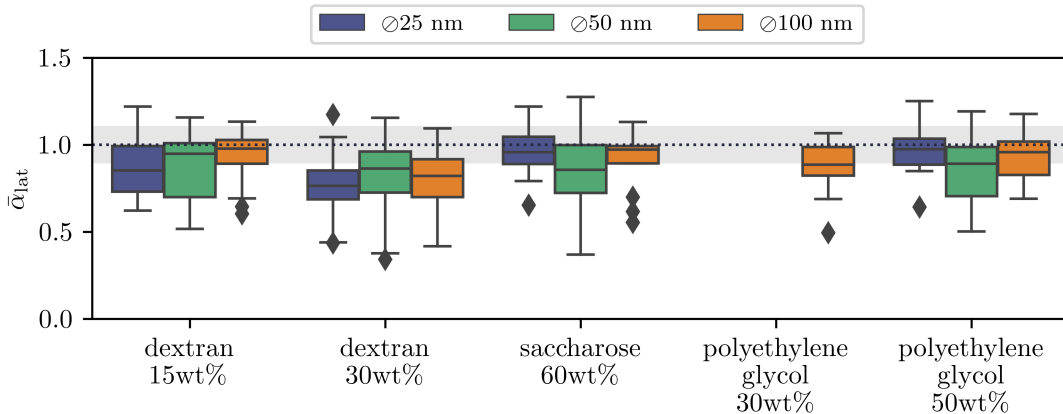


Figure 7.9.: Box-and-whiskers plots of the individual averaged anomalies extracted from the particles' one-dimensional MSDs in lateral directions. A gray-shaded area indicates a 10% interval around the normal diffusive scaling ($\bar{\alpha} = 1$, dotted black line). Whiskers corresponds to 1.5 of the interquartile range and outliers are displayed as diamonds.

These findings reproduce the results of 2D-SPOT experiments that were published by ERNST *et al.* in [133, 203]. However, the greater knowledge of the measurement errors of the experimental setup demonstrates that such conclusions should be drawn only cautiously. The selection of the parameter ranges and the applied corrections significantly influence the results. With the present implementation for axial localization, the measurements are only of limited use for the identification of anomalies in the diffusion behavior. The benefit of the third dimension of SPOT, in this respect, is simply that longer trajectories can be obtained even under more difficult conditions than 2D-SPOT would allow for.

7.3 | CONCLUSIONS FROM THE REFERENCE EXPERIMENTS

Concluding this section, 3D-SPOT can be successfully used to measure dynamic viscosities of aqueous fluids. By choosing an appropriate particle size, there is some flexibility regarding the range of viscosities that are able to be determined, but high viscosities are beneficial. While an increased number of measurements and an elongated acquisition time per trajectory can increase the accuracy, the precision in the determination of absolute values of SPOT is not outstanding. The reason for this is the high sensitivity regarding the exact measurement and evaluation conditions, e.g., the particle size or the analyzed time interval. Therefore, series of measurements should always be carried out with systematic parameter variation to eliminate a misleading parameter choice. Furthermore, only well-defined materials like particle with a sharply peaking size-distribution should be used.

Nevertheless, 3D-SPOT is recommended for the use in viscosimetry when other measurement methods fail. For example, if the total sample volume is very small ($\sim 10 \mu\text{L}$) or only a few probe particles are present or allowed to be inserted. Very specific problems, such as the determination of local viscosities in volumes down to one picoliter or changes over time, can also be addressed.

The abundance of data points measured by 3D-SPOT tempts to the evaluation of diffusion anomalies. This is quite justified, but should only be evaluated very prudently. Active particle tracking with mechanical systems has an intrinsic predisposition to oscillate, resulting in residues in the particle trajectories that cannot be easily filtered out. However, verified parameter selection allows for qualitative comparisons in particular, which produce clear results. Unfortunately, the accuracy along the z -axis is currently still too low to serve the evaluation of diffusion anomalies.

8 | DIFFUSION BEHAVIOR OF NANOPARTICLES IN COMPLEX FILTRATION MEDIA

In the previous sections, the method and implementation of 3D-SPOT, its pitfalls and shortcomings, and its application to samples of known properties was described. In this section, however, the focus is shifted to its application on a new system. The diffusion behavior of nanometer-sized colloidal particles will now be investigated in a nanoporous polymer membrane following the motivation given in the introductory section 1.3.

To put it in a nutshell, this part of the thesis will first consist of a characterization of the membrane material. Therefore, its morphology is studied with *environmental scanning microscopy* (eSEM) and collated with the expectation generated from the formation process. After that, 3D-SPOT is used to measure the confined diffusion of nanoparticles inside the membrane's porous network. Tracking results are processed to obtain the void volume that is accessible to the particle's motion, which can be compared to the electron microscopy outcome. Finally, the measured motion is inspected in more detail and related to theoretical models describing the diffusion behavior of the particle best.

Parts of the results presented in this chapter are published in [204]. Moreover, this chapter is connected to studies reported in my master's thesis. For this reason, a review of the preliminary work on which this study is based will be given in the following.

8.1 | PRELIMINARY WORK

Porous membranes derived from block copolymers are promising materials for controlled separation and there are many preparation pathways available.[97, 205] Our cooperation partner, the group of FELIX H. SCHACHER at the Friedrich-Schiller-University of Jena, used the method of *self-assembly and non-solvent induced phase separation* (SNIPS [181], see section 5.2) to obtain membranes from block copolymers like polystyrene-*block*-poly(N,N-dimethylaminoethyl methacrylate) (PS₈₁-*b*-PDMAEMA₁₉, subscripts denote the weight fractions of the corresponding segments, see fig. 8.1(a) for the chemical structure).[206, 207]

They characterized the polymer and the finally created membranes with established methods. In particular, they showed that the prepared membranes exhibited a defect-free surface over several 100 μm^2 of a porous polystyrene matrix.[206] The morphology appeared asymmetric in the membranes cross section according to SEM micrographs and in agreement with the expectations generated from the preparation method. It was shown by *water flux* and *silica particle filtration* measurements that the *pH* and the temperature responsive minority block, PDMAEMA, is capable of changing the permeability of the entire mem-

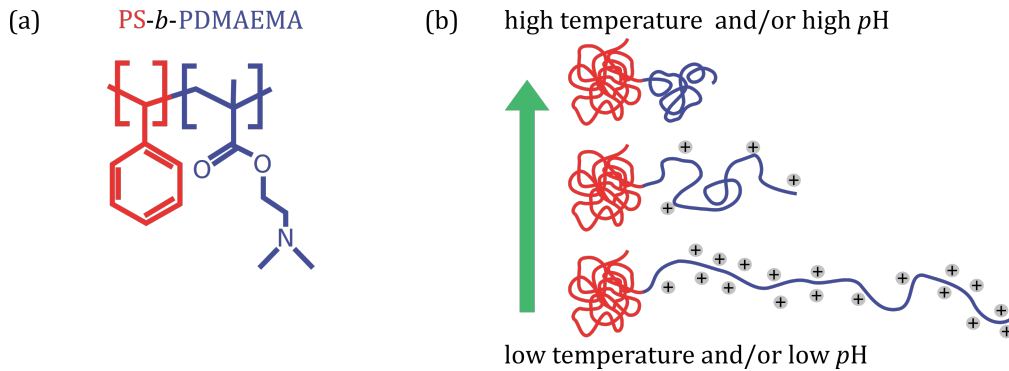


Figure 8.1.: (a) Chemical structure of polystyrene-*block*-poly(*N,N*-dimethylaminoethyl methacrylate).[206] (b) Illustration of the conformational changes PS-*b*-PDMAEMA undergoes for changing environmental conditions. In the low temperature and/or *pH* range, the PDMAEMA-chain (blue line) charges positively and stretches due to intra-molecular repulsion. By increasing the ambient temperature or *pH* the chain loses its charges and relaxes to a random coil. The PS-block (red line) remains unaltered.

brane. It was assumed that the PDMAEMA block covers the surface of the polystyrene scaffold in the nanoporous separation layer and that the switching of permeability was due to a swelling of this block (Similar to the illustration given in fig. 5.5(b)). The PDMAEMA chains collapse for high *pH* and/or temperature and enlarge for low *pH* and/or temperature (see fig. 8.1(b)). The conformational changes of the macromolecule causing the stretching result from an electrostatic charging of the chains for decreasing *pH* value. As those chains become charged, the macromolecules repels themselves and expand. For higher temperatures, more charges are necessary to reach the same intramolecular repulsion. While one can be relatively sure about the structure and surface properties of the skin layer, no reliable information on the detailed structure of the macroporous bulk material is available. However, it seems likely that the minority block is partly incorporated into the membrane scaffold and that there is no well defined surface composition.[206]

This is the point where SPOT attempts to extract information about the membrane morphology. In my master thesis, I tried to reproduce the work of HARAMAGATTI *et al.* using 2D-SPOT instead of camera-based SPT to track fluorescently labeled polystyrene beads in PS₈₁-*b*-PDMAEMA₁₉ membranes.[208] Due to slightly different preparation parameters, the more recently used membranes, exhibit significantly bigger pore sizes as those discussed in [206] and [208]. The pore diameter was extracted from scanning electron micrographs of the skin layer and amounted to about 3 μm compared to 20–80 nm in the aforementioned references.

It turned out that there are two major problems with SPOT measurements in this system. The first one is an unfavorable autofluorescence of the polymer combined with a strong light scattering at the membrane scaffold. This leads to a very inhomogeneous background signal that hampers the particle localization significantly. By using polystyrene spheres with a large stokes shift (TransFluoSpheres, see table 5.1 and fig. 5.4 for the spectrum), a suitable spectral design of the experiment was achieved, in which the particles emit at longer wavelengths than those where the membrane's autofluorescence occurs. The second major problem with the PS₈₁-*b*-PDMAEMA₁₉ system was strong electrostatic interaction between the tracked particles and the membrane wall. In contrast to [208], a saturation of adsorption sites was not achieved by immersing the membrane in a diluted silica nanoparticle solution. This approach fails for SPOT, because pure water is here an unfeasible solution medium due to its low viscosity. The changed environmental conditions

compared with HARAMAGATTI's SPT experiments may either lead to a release of the silica nanoparticles from the membrane or an increase of the number of adsorption sites for the probe particle. The key to reduce this problem was the neutralization of either the tracer particle or the membrane wall. Therefore, the pH was adjusted via the buffer composition and detergent was added to increase the particle stability. Nevertheless, the tracer particle adsorption was very severe due to the PDMAEMA block. For the experiments to be presented in this thesis, the severe tracer particle adsorption problem was avoided by exchanging the polymer. Here, the nanoporous membranes were formed from the triblock terpolymer $PS_{43}\text{-}b\text{-}PI_{40}\text{-}b\text{-}PNIPAAm_{17}$. In the material section (see section 5.2 and section 5.3.2), those membranes and their preparation are described in detail.

8.2 | MORPHOLOGY INSPECTION BY ENVIRONMENTAL SCANNING ELECTRON MICROSCOPY

For reference purposes, the membranes have been investigated by *environmental scanning electron microscopy* (eSEM). Resulting micrographs are analyzed with a digital image processing technique, called *chord length analysis* (CLA), to characterize the length scales of the occurring voids.

Water inflated and cooled pieces of the membrane were placed in the sample chamber of an electron microscope (FEI Quanta FEG 250, Thermo Fisher Scientific) that was operated in the *environmental scanning electron microscopy* (eSEM) mode. The chamber was chilled to 2°C for 20 min and flushed twice with water vapour. After that, it was stabilized at a pressure of 715 Pa corresponding to a humidity of about 100 %. Under these conditions, the membrane pores are completely filled with water and therefore, cannot be imaged by the electron microscope. In order to reveal the pores and to ensure that the drying process itself does not alter the structure, the moisture was gradually reduced by lowering the pressure within the sample chamber. An example of an eSEM micrograph of the membrane surface is shown as a function of the humidity in fig. 8.2.

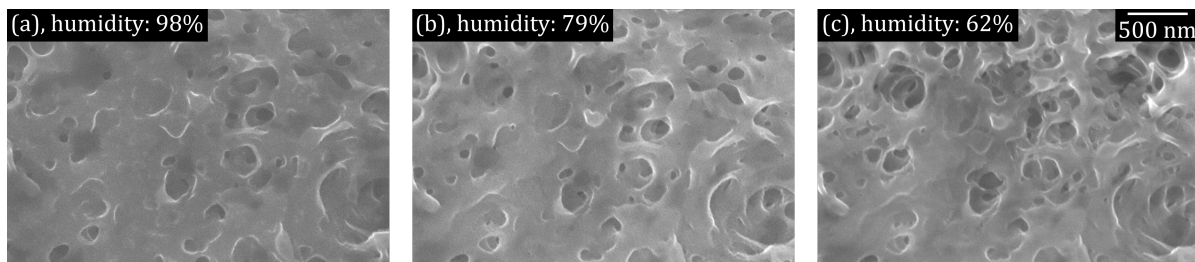


Figure 8.2.: eSEM micrograph of the membrane surface for the ambient humidity decreasing from 98 % to 62 % (left to right). The humidity was controlled by reducing the pressure from (a) 697 Pa via (b) 560 Pa to (c) 437 Pa at a constant temperature of 2°C . (Voltage: 10 kV, Magnification: $40\,000\times$)

The contrast and richness of the surface details were sufficiently enhanced at a humidity of 62 %, while the membrane's structure remains unaltered. This ensured sample conditions that are, although not fully identical, but at least comparable to those prevailing during SPOT experiments. The morphology of the membranes was inspected under these conditions at different locations. An example for a side view, a top view, and a bottom view of a membrane are shown in fig. 8.3. The thickness varies in the range of $20\ \mu\text{m}$ to $35\ \mu\text{m}$ (here: $(33 \pm 2)\ \mu\text{m}$, but see also fig. E.5(a) and (b)), and it consists of a sponge-like bulk

structure capped with a thin, a few hundred nanometres wide top layer. This observed structure fulfills the expectation generated from the SNIPS formation process. For the top layer, the top-view (fig. 8.3(b)) reveals a relatively homogeneous distribution of pores with diameters clearly smaller than $1\ \mu\text{m}$. This is in contrast to the structure of the bulk material as shown in the bottom view (fig. 8.3(c)). Further eSEM micrographs showing cross sectional views (see fig. E.5), high magnifications (see fig. E.6) or membrane areas with defects (see fig. E.7) can be found in the appendix E.3.

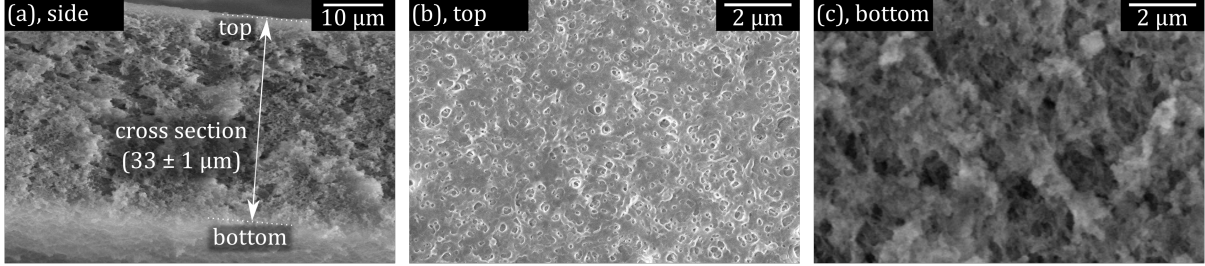


Figure 8.3.: Environmental scanning electron micrograph of a (a) side (b) top and (c) bottom view of the $\text{PS}_{43}\text{-}b\text{-PI}_{40}\text{-}b\text{-PNIPAAm}_{17}$ triblock terpolymer membrane.

In order to quantify the pore sizes from the eSEM images, CLA was applied, a digital image processing technique for characterizing the length scales occurring within an inhomogeneous structure. It is based on a binarized image, where black areas represent the membrane wall and white areas indicate void spaces. Within the void space a given number (actually some hundreds or thousands) of points are randomly selected. From these starting points, straight lines are expanded pixel by pixel in different directions until they hit the membrane wall. Lines leading in opposite directions are merged into one single, so-called, *chord*. A histogram over the length L of this chords is interpreted as the membrane's morphological pore size distribution $P_{\text{CLA}}(L)$.

The benefit of this fully automatized evaluation is often hampered by the difficulty of correctly binarizing the image. After enhancing the contrast of the images, binarization is usually done by thresholding. Several algorithms like the Otsu method are available for determining a suitable greyscale level.[209] Best results have been obtained by choosing the threshold as the midpoint between the maximum of the gray scale histogram and its steepest descent. This value is feed into the adaptive binarization method of the used MATLAB (The Mathworks, Inc., Version R2016a) scripts. After that, all void areas that touch the boundary of the micrograph region are removed because their areas are artificially cropped. Then the method still might lead to misinterpretations concerning what is recognized as a wall or a void. Therefore, for each region assigned as a void, the area A_{void} and the perimeter u_{void} are determined from the pixelated image and the parameter $m_{\text{void}} = 4\pi A_{\text{void}}/u_{\text{void}}^2$ is calculated. Given the membrane formation process, it is expected to deal with round pores. Structures with irregular contours featuring $m_{\text{void}} \leq 0.5$ are rejected from the analysis. For a perfect circular void the circularity parameter m_{void} becomes 1. Note that that this criterion is independent of the size of the pores which are discriminated exclusively according to their shapes.

The so-called *k-Gamma distribution* $P_{k\Gamma}(L)$ describes the void size distribution in disordered pores spaces and is given as

$$P_{k\Gamma}(L) = \frac{k^k}{\Gamma(k)} L^{k-\mu_c} \mu_c^{-k} \exp\left(-\frac{kL}{\mu_c}\right), \quad (8.1)$$

where μ_c denotes the first statistical moment and k is used for the definition of the second moment σ_c via $\sigma_c^2 = \mu_c^2/k$. [210] The symbol $\Gamma(x)$ represents the gamma function with argument x . Fitting this model to chord size distributions was already successfully applied to inspect disordered macroporous-mesoporous silica monoliths [211], porous polymer films [180] and packed glass bead beds [212]. The CLA results for the membrane at hand are shown in fig. 8.4 and described well by the k -Gamma distribution with $\mu_{c,\text{bulk}} = (360 \pm 10)$ nm and $\sigma_{c,\text{bulk}} = (212 \pm 7)$ nm for the bottom-view micrograph, and $\mu_{c,\text{top}} = (81.0 \pm 1.3)$ nm and $\sigma_{c,\text{top}} = (44.0 \pm 0.7)$ nm for the top-view micrograph.

This analysis testifies that a significant fraction of the pores would not be accessible by conventional optical microscopy because they feature sizes that are in the order or smaller than the classical diffraction limit of light.

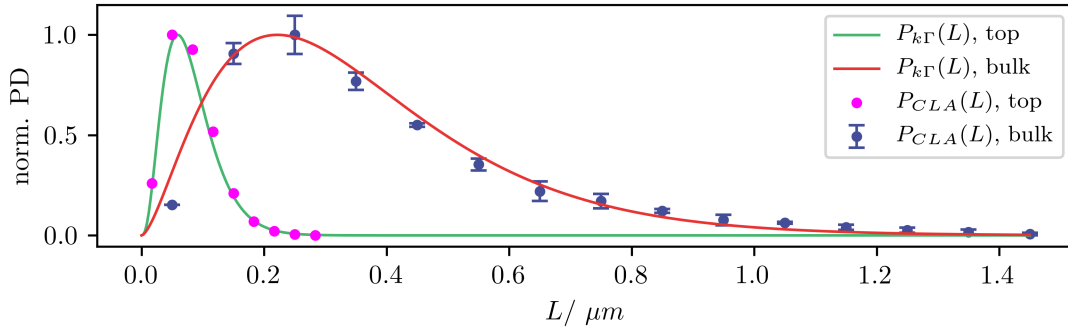


Figure 8.4.: Distribution of chord length $P_{CLA,\text{top}}(L)$ (magenta colored dots) and $P_{CLA,\text{bulk}}(L)$ (blue dots) extracted via CLA from eSEM micrographs with top-view or bottom-view, respectively, and the corresponding fits $P_{k\Gamma,\text{top}}(L)$ (green line) and $P_{k\Gamma,\text{CLA,bulk}}(L)$ (red line) with the k -Gamma distribution.

8.3 | 3D-SPOT WITHIN THE POROUS BULK STRUCTURE OF THE POLYMER MEMBRANES

With the help of 3D-SPOT, the behavior of fluorescent nanospheres within the porous bulk structure of the introduced membranes is inspected. Having prepared the nanoparticle suspensions of polystyrene spheres that are (25 ± 4) nm, (50 ± 18) nm and (100 ± 20) nm in nominal diameter (see section 5.3.2 for details), each of them was used separately to conduct 3D-SPOT experiments.

In contrast to the approach taken in the preliminary works described in section 8.1, the signal-to-noise ratio of the fluorescence recordings was enhanced by the reduction of the laser light back-scattering via refractive index matching and not by suppression of the autofluorescence detection as it turned out to be more effective. The refractive index of the membrane material is approximately that of polystyrene ($\tilde{n}_{\text{membrane}} \approx \tilde{n}_{\text{PS}} \approx 1.62$) [213] and must be compared with that of the solution medium ($\tilde{n}_{\text{buffer}} = 1.43$) which was increased with the help of 2,2'-tiodiethanol (TDE, $\tilde{n}_{\text{TDE}} = 1.52$). This is not a perfect match, but sufficient to increase the transparency of the membrane to a useful level (see fig. E.4 in the appendix E.2). Refractive indices were checked by a refractometer (Abbemat, Anton Paar GmbH) at several wavelengths (see fig. E.3 in the appendix E.2). The amount of TDE was kept as low as possible to conduct the experiments under conditions that are close to pure

water applications. TDE was used, because it is polar, miscible with water and already successfully applied in similar situations.[180]

Trajectories are recorded with 3D-SPOT from multiple micrometers inside the membrane material and as long as none of several predefined measurement termination criteria are met. Those termination criteria are the loss of the particle, unexpected changes in the photon detection rate or a stage scanner target position out of range. Trajectories that are too short are excluded from further processing. Finally, 32 trajectories of the 25 nm, 17 trajectories of the 50 nm, and 28 trajectories of the 100 nm particles are left for further analysis. Unfortunately, experiments suffered from drift as was double checked via the microscope's wide-field mode. Therefore, drift-correction has been applied.

Five trajectories of the 25 nm nanobeads are displayed as an example in fig. 8.5. Alongside the diffusive pathways, a 3D-SPOT record of a particle that was immobilized on a glass surface is shown that features variations in the spatial positions along all three dimensions that are consistent with Gaussian distributions with standard deviations of $\hat{\sigma}_t \approx (8 \text{ nm}, 8 \text{ nm}, 12 \text{ nm})$. This provides a measure for the localization accuracy with the used setup settings. The other diffusive particle traces feature a great variety in their shapes but differences from free diffusion (see e.g., fig. 7.1) or the static case (fig. 8.5 (f)) are already visible by eye.

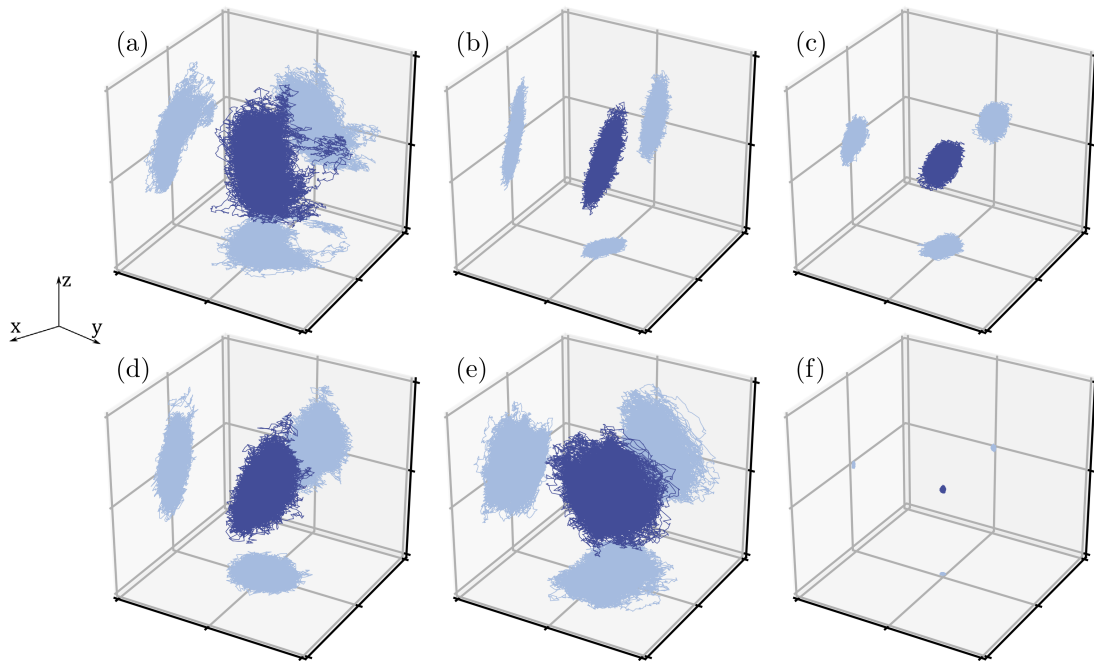


Figure 8.5.: (a–e) Examples of five different 3D-trajectories (dark blue) and their plane projections (light blue) from fluorescent nanoparticles of 25 nm in diameter recorded with 3D-SPOT. (f) A trajectory recorded from a fluorescent nanoparticle that was immobilized on a glass surface for reference. All trajectories are shown within a cube of $2 \mu\text{m}$ edge length.

8.4 | ACCESSIBLE VOID SPACE DISTRIBUTION

After those qualitative observations, quantitative results will be extracted from the recorded particle trajectories. In the last section, it became clear that the trajectories recorded with 3D-SPOT show very inhomogeneous results that are not unexpected considering the electron microscopic elucidation of the membrane morphology in section 8.2.

In the following, the membrane's porous space that is accessible for diffusion will be determined and compared with the findings from the electron microscopic morphology analysis. Therefore, the void space accessible for diffusion is derived for each particle size utilizing the MSD without any model assumptions about the underlying diffusion dynamics. In accordance with literature, the accessible void space should shrink with increasing particle size[180] and it should be smaller than what is known from the eSEM. Figure 8.6 illustrates the differences in accessible void space for particle with different diameters.

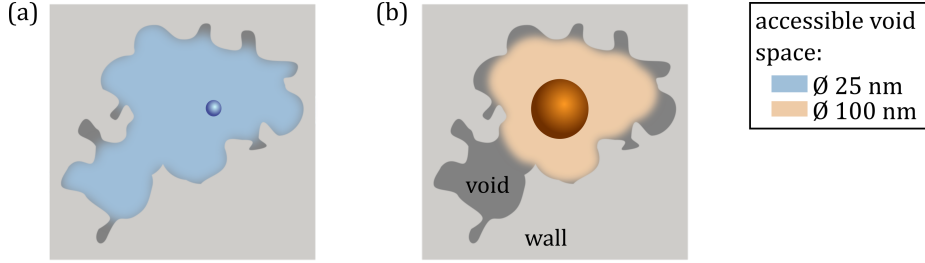


Figure 8.6.: Illustration of the void space accessible for particles that differ in diameter. The orange particle (b) is four times larger than the blue (a), and, therefore, it is closer confined in its motion.

The measured trajectories are given again as time series of estimated positions $\hat{\mathbf{r}}[k] = (\hat{r}_x[k], \hat{r}_y[k], \hat{r}_z[k])$ and used to compute the time-averaged MSDs for each spatial dimension separately. The typical curves of MSDs for confined motion is observed for all three particle sizes as can be seen in fig. 8.7, starting with a steady growth that levels-off and ends in a plateau. The initial rise appears approximately linear in τ . The plateaus are not perfectly flat and decrease on average with increasing particle diameter. Since the level of the plateau scales with the squared size of the confining void (see section 2.5), the MSD can be used to determine an estimate of the pore size distribution within the bulk structure of the triblock terpolymer membrane. The MSD values are averaged over the range $\tau \in [1 \text{ s}; 4 \text{ s}]$ indicated by the gray shaded area in fig. 8.7.

These plateau levels are associated with the confinement lengths $\hat{\mathcal{L}}$ by the arithmetic average of N_τ MSD-points in the lag time interval $\tau_i \in [1 \text{ s}; 4 \text{ s}]$ given by

$$\hat{\mathcal{L}} = \frac{2}{N_\tau} \sum_{\tau_i \in [1 \text{ s}; 4 \text{ s}]}^{N_\tau} \sqrt{\text{MSD}[i]}, \quad (8.2)$$

and $\tau_i = i\delta t$. Hence, each trajectory results in three confinement lengths $\hat{\mathcal{L}}$ in analogy to the CLA, where a void space's size is also probed along different directions simultaneously. Since the particle diameter is not of negligible size compared with the expected void sizes, the apparent confinement lengths $\hat{\mathcal{L}}$ must be corrected by the particle diameter a . The actual estimated confinement length is given as

$$\hat{L} = \hat{\mathcal{L}} + a. \quad (8.3)$$

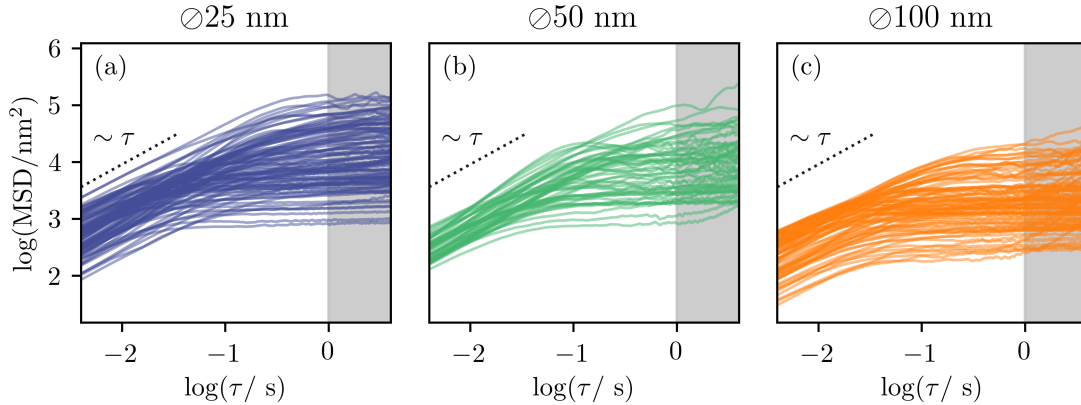


Figure 8.7.: Single-coordinate MSD curves from fluorescent nanoparticles of (a) 25 nm, (b) 50 nm, or (c) 100 nm in diameter. As a guide for the eye, the dotted black line indicates a linear scaling of the lag time τ . The shaded area corresponds to the range from which the confinement lengths are calculated. .

For each particle size, a histogram is constructed from the set of estimated confinement length and compared with the results from the CLA of the eSEM experiments in terms of the distributions first and second moment provided in table 8.1. The comparison is depicted in fig. 8.8.

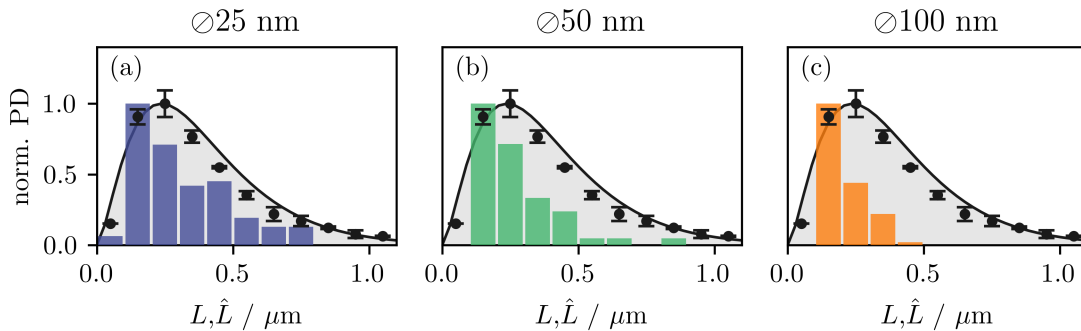


Figure 8.8.: Normalized histograms of the confinement lengths \hat{L} obtained from the MSDs for particles of (a) 25 nm, (b) 50 nm, and (c) 100 nm in diameter, respectively. The black dots refer to the normalized probability density of the pore sizes L obtained from the CLA for the bottom-view eSEM micrograph and the corresponding fitted k -Gamma distribution (solid black line), which already had been shown in fig. 8.4.

The SPOT results for the 25 nm and 50 nm sized particles are about similar, and in reasonable agreement with the results from the CLA, whereas the results obtained for the particles of 100 nm in diameter show larger deviations. This might reflect that the non-accessible void space increases with increasing particle size, which misleadingly leads to an underestimation of the total available pore sizes. Comparing the results obtained with particles of different sizes, a rule of thumb can be stated that the ratio of the size of the tracers and the pore diameters should be about 1 : 10 for reliably mapping out the void spaces in the membrane. Continuing this train of thought, the filtration features of this membrane should show increased separation capabilities for particles larger and smaller than a threshold in between 50 nm and 100 nm.

Table 8.1.: Comparison of the (bottom-view) pore size distributions obtained from eSEM and 3D-SPOT for the different particle sizes. The mean values and distribution widths are measured in terms of the moments of the k -Gamma distribution.

	CLA (bottom)	∅25 nm	∅50 nm	∅100 nm
Mean pore size / nm	360	300	270	200
Width of the distribution / nm	212	170	130	60

8.5 | DIFFUSION CHARACTERISTICS

Having characterized the porous void space that is available for the particle motion in a model-free manner just by looking at the saturation level of the MSDs, a closer look at the particle's motion will be presented in this section. Since the database is not large enough considering the complex system observed, it is not possible to point out the underlying theoretical diffusion model for sure. Instead, it should be described which statistical properties are observed and which models may be at least candidates to describe the particles diffusion characteristics.

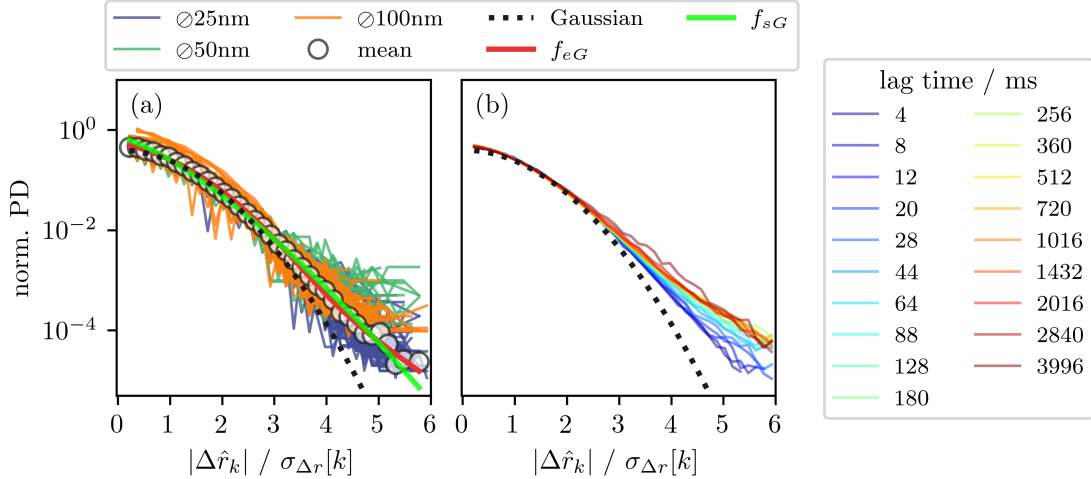


Figure 8.9.: Van Hove function of the absolute value of particle displacements normalized by the trajectories individual standard deviation. (a) Distributions calculated for a lag time of $\tau = 12$ ms. Results of single trajectories of the 25 nm, the 50 nm and the 100 nm are displayed as blue, green and orange lines, respectively. As all curves fall nicely together, they are used independent of the particle size to compute their common average (circles), which is fitted with the model of a Gaussian with an exponential tail (f_{eG} , solid red line) and a stretched Gaussian (f_{sG} , solid light green line). (b) Averages over all (size-independent) Van Hove functions calculated for different lag times (color-coded). A black dotted line in both plots is not a fitted function, but a standard Gaussian distribution.

The first quantity to look at is the particle's step size distribution calculated from the increment vectors eq. (3.33) and also known as the self-part of the Van Hove correlation (see section 2.2). While the distribution's width measures the average velocity of the particle motion, the shape helps to identify the diffusion model. Similar to the MSD analysis, each spatial dimension of the increment vector is analyzed individually, which is expressed by using the scalar notation $\Delta \hat{r}_k[i]$. A broad scattering of diffusion coefficient and therefore step size distribution widths are expected by looking at differences in the MSDs initial slopes. In order to compare the individual shapes of the Van Hove correlations, all

trajectories are normalized by their standard deviation

$$\sigma_{\Delta r}[k] = \sigma_{\Delta r}(\tau = k\Delta t) = \sqrt{\frac{1}{N_{\text{pos}} - k - 1} \sum_{i=0}^{N_{\text{pos}}-k-1} [\Delta \hat{r}_k[i] - \mathcal{E}(\Delta \hat{r}_k[i])]^2}, \quad (8.4)$$

before computing the step size distribution for a lag time of $\tau = k\Delta t = 12$ ms. This lag time is chosen to reduce the influence of measurement artifact as it corresponds to three stage position update cycles, but at the same time staying in a regime where the void boundaries do not hinder the particle's movement significantly. Remarkably, the individual particle displacement distributions collapse to a single unique curve as can be seen in fig. 8.9 (a).

The average of all Van Hove correlation functions is compared with a Gaussian standard distribution (see black dotted line in fig. 8.9). Indeed, the Gaussian distribution is in good agreement with the experimental data for displacements as large as about $3\sigma_{\Delta r}$. However, the discrepancy for larger particle displacements is also clearly visible. Similar results are observed for other systems, e.g., non-Gaussian behavior of nanoparticles in polyethylene oxide solutions[214], semidilute hydrolyzed polyacrylamide solutions in bed structures created by large glass beads[212], or of micron-sized tracers in hydrogels of mucin polymers[215]. Inspired from the mentioned references, the model functions $f_{eG}(|\Delta \hat{r}_k|/\sigma_{\Delta r}[k])$, a Gaussian with an exponential tail, and $f_{sG}(|\Delta \hat{r}_k|/\sigma_{\Delta r}[k])$, a stretched Gaussian curve, are fitted to the SPOT data. The models are written as

$$f_{eG}(x) = a_1 \exp\left(-\frac{x^2}{b_1^2}\right) + a_2 \exp\left(-\frac{|x|}{b_2}\right) \quad \text{and} \quad (8.5)$$

$$f_{sG}(x) = a_1 \exp\left(-\frac{x^{c_1}}{b_1^{c_1}}\right) \quad (8.6)$$

and parametrized according to table 8.2.

Table 8.2.: Overview about the fitting results of the Gaussian with exponential tail f_{eG} and stretched Gaussian model f_{sG} .

Model	a_1	b_1	c_1	a_2	b_2	b_3	adj. R ² / %
f_{eG}	0.319 ± 0.056	1.471 ± 0.032	-	0.292 ± 0.179	0.586 ± 0.047	-	99.83
f_{sG}	0.709 ± 0.184	0.977 ± 0.121	1.374 ± 0.093	-	-	-	99.52

Both models describe the data equally well as indicated by the coefficient of determination (adjusted R² values). Fitting by means of an ordinary Gaussian was waived, since it would require the restriction of the data range for fitting the distribution of small displacements properly. In this case a direct comparison of adjusted R² values would be misleading. In fig. 8.9 (b), the Van Hove function is also computed for varying lag times. With increasing τ , the exponential tail sets in earlier and decays slower.

The analysis leads to the conclusion that for short time scales a Gaussian distribution of displacements is dominant. Only exceptional large steps ($|\Delta \hat{r}_k| > 3\sigma_{\Delta r}[k]$) occur with up to about 100 times higher probability than would be predicted by a plain Gaussian distribution of steps. The non-Gaussianity increasing with time indicates that the confinement's influence is reasoning the exponential tails.

The standard deviation $\sigma_{\Delta r}(12$ ms) used to normalize the particle trajectory can be converted to a diffusion coefficient estimate by

$$\hat{D} = \frac{\sigma_{\Delta r}(\tau)}{2\tau}. \quad (8.7)$$

Results are shown as box-and-whisker plots in fig. 8.10 and listed in table 8.3 for the different nominal particle diameter.

Table 8.3.: Overview about the measured diffusion coefficients \hat{D} for particles of different diameters confined in the membranes porous structure.

diameter / nm	$D_{\text{free}} / \text{nm}^2 \text{ms}^{-1}$	axial $\hat{D} / \text{nm}^2 \text{ms}^{-1}$	lateral $\hat{D} / \text{nm}^2 \text{ms}^{-1}$
25	3516	46 ± 28	88 ± 53
50	1758	41 ± 18	39 ± 19
100	879	29 ± 17	31 ± 17

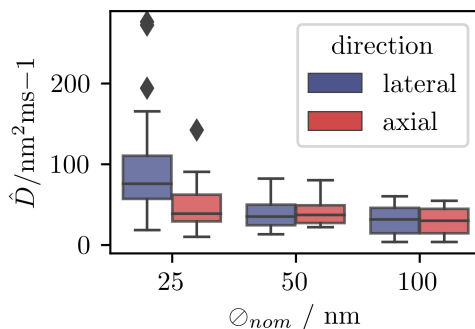


Figure 8.10.: Box-and-whisker plot illustrating the distribution of diffusion coefficients categorized by particle size and diffusion direction. Whiskers corresponds to 1.5 of the interquartile range and outliers are displayed as diamonds.

The data are further grouped by their spatial direction resolving anisotropies induced by the membrane's structural asymmetry. Apparently, diffusion coefficients decrease with increasing particle diameter as expected by the ordinary Stokes-Einstein relation eq. (2.16). In fact, the measured diffusion coefficient is about two orders of magnitude smaller compared to the free-diffusion expectation D_{free} . For the 25 nm sized particles, lateral motion is almost twice that fast as the axial movement. The two larger particle categories show similar diffusion coefficients for lateral and axial trajectory coordinates.

The reason for the drastic slow-down is not included in the data and mere conjectures are left. SKAUG *et al.* discovers in a similar system a larger than expected slow-down of particle motion due to hydrodynamic forces.[180] In their study, the reduction was less than one order of magnitude, but the accessible space was less restricted and the porous medium had no "hairy" surface. Here, an additional contribution to the particle-wall friction may be introduced by the PNIPAAm polymer chains covering the membrane scaffolds surface. Simulation of such a system could confirm or refute this idea, but exceeds the frame of this thesis.

The Van Hove correlation does not consider temporal dependencies of the particle displacements, which play an important role in several anomalous diffusion models. Such temporal correlations can be inferred from the normalized velocity autocorrelation $nVACF_{\tau}(\Delta\tau)$ (see eq. (3.34)). Figure 8.11 shows that there is no such increment correlation for short time scales but an increasing anti-correlation for increasing τ with the deepest point of the curves located at $\Delta\tau = \tau$. For $\tau = 80 \text{ ms}$, a strong anti-correlation is present and likely caused by the confinement of the motion since the MSD has already shown significant flattening in this time range. The behavior is similar for all three particle diameters with no clear trend for different particle sizes. Unfortunately, the $nVACF$ is not a good

diagnostic tool to differentiate between the anomalous confined diffusion models considered in this thesis, namely the FBM and subdiffusive CTRW.[216] Indeed, even confined Brownian motion shows anti-correlation of steps as demonstrated in a simple simulation in the appendix C.6. Thus, no useful information is gained by this analysis.

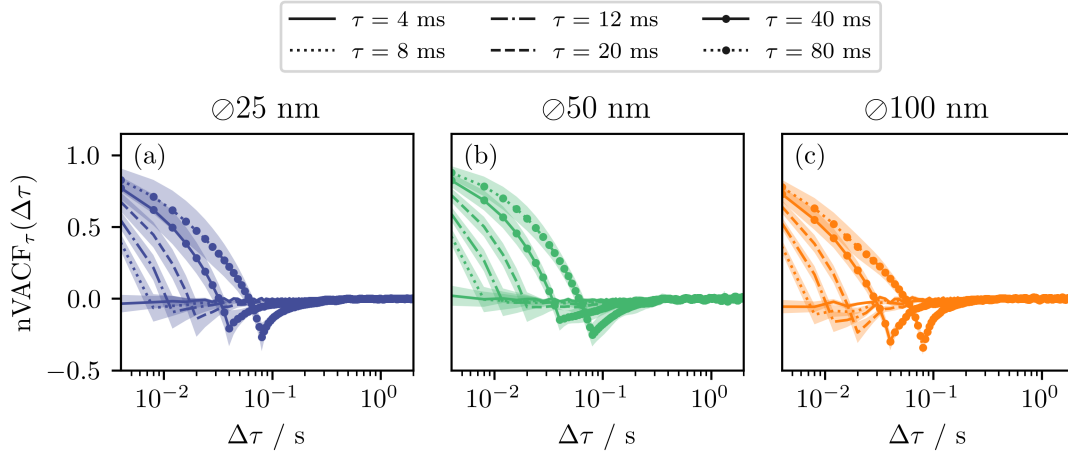


Figure 8.11.: Normalized velocity autocorrelation function $nVACF_{\tau}(\Delta\tau)$ calculated for different lag times τ and averaged for particles with a nominal diameter of (a) 25 nm, (b) 50 nm, and (c) 100 nm. The shaded area indicate the respective standard deviation.

More information is sought by inspecting the shape of the MSD. In section 8.4, the MSD was used to extract the distribution of accessible void space in a model-free manner. But the same question can be tackled by using model predictions for diffusion in confined space as worked out in section 2.5. Essentially, there are three general scaling laws to test, namely an exponential law

$$f_{\text{exp}}(\tau) = \frac{\hat{\mathcal{L}}^2}{2} \left[1 - b \exp\left(-\frac{a\tau}{\hat{\mathcal{L}}^2}\right) \right], \quad (8.8)$$

a scaling law described by the Mittag-Leffler function

$$f_{\text{ml}}(\tau) = \frac{\hat{\mathcal{L}}^2}{2} \left[1 - E_{2-\alpha} \left(-\frac{a}{\Gamma(\alpha-1)} \tau^{2-\alpha} \right) \right] \quad (8.9)$$

and a power-law

$$f_{\text{pl}}(\tau) = \frac{\hat{\mathcal{L}}^2}{2} \left[1 - \frac{a}{\tau^{\tilde{\alpha}}} \right]. \quad (8.10)$$

The exponential law would correspond to a confined Brownian walk without defining the exact geometry of the confining potential. The parameters a and b will adjust their values accordingly (see section 2.5). The exponents α and $\tilde{\alpha}$ are the anomaly parameter (Note the different ranges for sub- and superdiffusion in the models). The power-law may represent a CTRW walk in a harmonic potential eq. (2.31) and the Mittag-Leffler model is the result for fractional Langevin equation motion in a harmonic potential eq. (2.38).

The models are fitted one after the other to the single-coordinate MSDs of the individual SPOT measurements. The fitting results are grouped by particle diameter and the corresponding spatial direction (lateral or axial) to take track not only of size effects but also to consider the membranes inherent asymmetry. First of all, the adjusted R^2 values of the fitting process are shown in fig. 8.12 to check which model is the most adequate. Apparently,

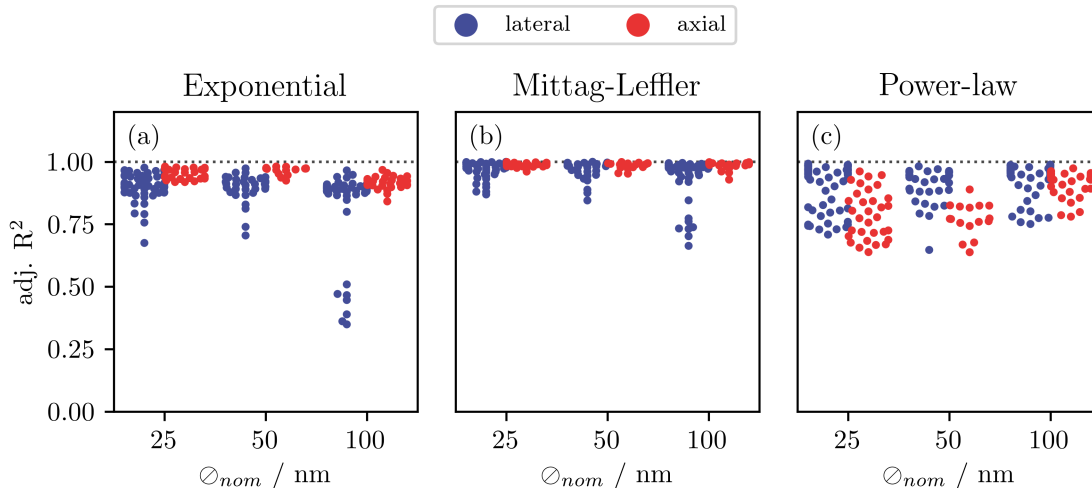


Figure 8.12.: Swarmplots of the adjusted R^2 values of the fitting process with different models. Each dot represents the result of a single coordinate of an individual particle trajectory. Individual analysis results are grouped according to the direction (lateral in blue, axial in red) and the particle diameter. Thus, there are twice as many blue dots then red. A dotted black line indicates a perfect model.

the Mittag-Leffler function $f_{\text{ml}}(\tau)$ yields the highest coefficient of determination, which is not surprising as the function has the highest degree of flexibility for adapting to the data. Because the Mittag-Leffler function interpolates between a power-law and an exponential law, it will be able to generate high adjusted R^2 values for measurements, where only one of the other models would fit well. The exponential model $f_{\text{exp}}(\tau)$ represents the data slightly worse. Both models are suited better for the axial than the lateral direction. This is not the case for the coefficients of determination of the power-law, which are distributed a lot broader and where it is not clear if the MSD in lateral or axial directions is approximated better by $f_{\text{pl}}(\tau)$. There is a group of lateral MSDs for the 100 nm particles that are very badly fitted by the exponential model. A similar cluster of data points appears for the $f_{\text{ml}}(\tau)$ but with improved coefficients of determination, and there are no such outliers for the power-law model.

In a second step, the distributions of the resulting confinement lengths \hat{L} are compared. To do so, the parameter $\hat{\mathcal{L}}$ is converted to \hat{L} with the help of eq. (8.3). Box-and-whisker plots in fig. 8.13 illustrate the distribution with the whiskers set to 1.5 of the interquartile range. Additionally to the fitting results, the confinement length distributions that were determined model-free in section 8.4 are plotted alongside. In contrast to fig. 8.8, the differences between lateral and axial coordinate traces are shown separately. Table 8.4 lists mean values and standard deviations for direct comparison.

Apparently, the estimated confinement length in z -direction is distributed around larger values. This is not only true for the model-free results independent of the particle size, but also for all other methods. For the 25 nm and 50 nm particles, the distributions and standard deviations of the specific methods are in great accordance. But the MSDs of the 100 nm particles yield confinements that are distributed sharper around smaller \hat{L}_k . This finding is even more pronounced along the axial direction. Comparison of the different methods reveals an increased broadening and shifting to larger void sizes from the exponential model to the Mittag-Leffler model, further to the model-free method, and to the power-law. Because the power-law model fits the data not with high precision, the resulting distributions are not very trustworthy. The fits with $f_{\text{exp}}(\tau)$ and $f_{\text{ml}}(\tau)$ are determined

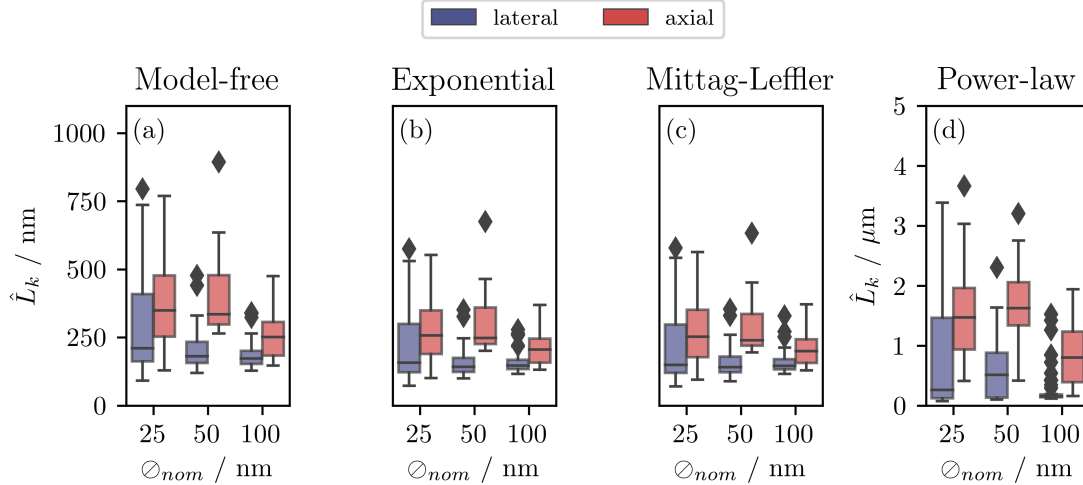


Figure 8.13.: Box-and-whisker plots of the pore sizes \hat{L} for different particle diameters determined with different methods from the same SPOT data set. Whiskers corresponds to 1.5 of the interquartile range and outliers are displayed as diamonds. Lateral and axial coordinates are grouped and displayed in blue and red, respectively. (a) Results from the model-free approach that considers the MSD plateau values in the range $\tau \in]1\text{ s}; 4\text{ s}[$ and that was already shown in fig. 8.8. Results from (b) the exponential model, (c) the Mittag-Leffler model and (d) the power-law fitted to the MSD data. Void sizes are corrected for the actual particle diameter.

Table 8.4.: Mean and standard deviation of the estimated confinement length \hat{L} for the different models and the MSD plateau-value based method.

nom. diameter/ nm	direction	Model-free \hat{L} / nm	Exponential \hat{L} / nm	Mittag-Leffler \hat{L} / nm	Power-law \hat{L} / nm
25	axial	379 ± 168	120 ± 42	274 ± 124	800 ± 368
	lateral	280 ± 166	94 ± 42	203 ± 119	435 ± 483
50	axial	407 ± 163	138 ± 43	291 ± 113	887 ± 329
	lateral	206 ± 82	86 ± 21	160 ± 62	315 ± 265
100	axial	257 ± 82	135 ± 21	206 ± 58	456 ± 240
	lateral	185 ± 49	116 ± 13	158 ± 41	184 ± 16

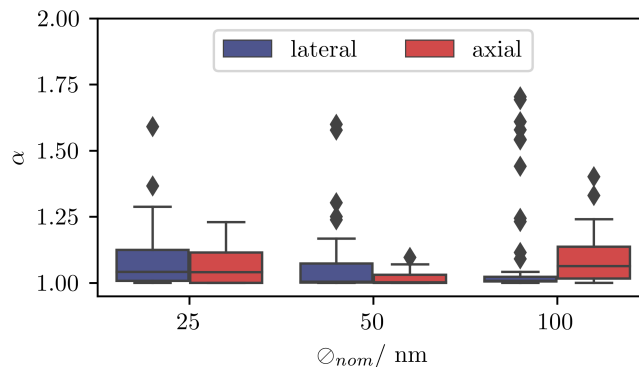


Figure 8.14.: Box-and-whisker plot of the anomaly parameter α for different particle diameters resulting from the Mittag-Leffler model. Lateral and axial coordinate data are grouped and displayed in blue and red, respectively. Whiskers corresponds to 1.5 of the interquartile range and outliers are displayed as diamonds. According to the definition of α in the model eq. (8.9), subdiffusive motion is indicated by $\alpha \in]1; 2[$.

with higher confidence and yield results comparable to the model-free method. The broad parameter distributions of the model-free method are not surprising as this approach lacks any numerical stiffness. Due to the high agreement between the Mittag-Leffler model and the measured data, this description is preferred.

Analysis of the anomaly parameter α extracted from the Mittag-Leffler model yields no significant deviations from normal diffusion (see fig. 8.14 and table 8.5).

Table 8.5.: Anomaly parameter determined by fitting the Mittag-Leffler model to the single-coordinate MSD data. Results are grouped by particle diameter and direction

nom. diameter / nm	Anomaly parameter α	
	lateral	axial
25	1.08 ± 0.11	1.06 ± 0.07
50	1.08 ± 0.15	1.02 ± 0.03
100	1.09 ± 0.20	1.09 ± 0.10

The detected anomaly is about 10% higher than 1, which is a value that was counted as normal diffusion in section 7.2. Considering that the model eq. (8.9) is inspired by the MSD for FLE motion inside a harmonic potential eq. (2.38), an α between 1 and 2 indicates subdiffusion. Summarizing, small adjustments of the anomaly parameter are sufficient to obtain almost perfect coincidence with the MSD data. To emphasize this, averages of the MSDs in lateral and axial direction are shown for the three particle sizes in fig. 8.15. The diffusion of the nanoparticles inside the membrane's void structure shows mainly Brownian characteristics with minor indications of the motion described by the subdiffusive FLE.

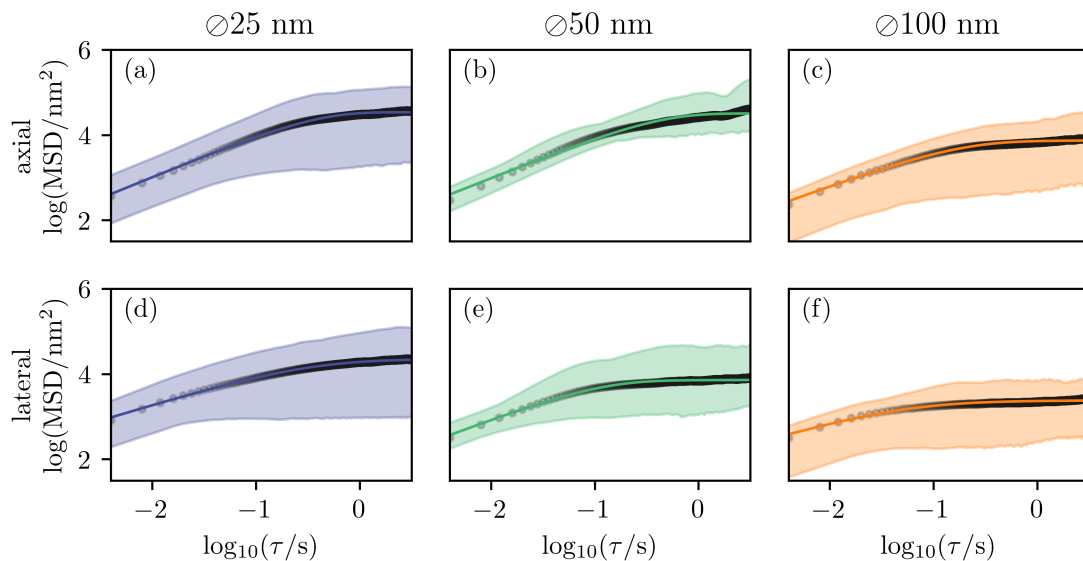


Figure 8.15.: Averages (dots) of the single-coordinate MSDs taken from fig. 8.7 for the axial (top row) and lateral (bottom row) direction and a corresponding fit of the Mittag-Leffler model f_{ml} . Shaded areas indicate the minimum-to-maximum range of the MSDs that build-up the data basis for the averaging.

8.6 | DISSCUSION OF THE 3D-SPOT EXPERIMENTS ON COMPLEX FILTRATION MATERIALS

Tracking nanoparticles within nanoporous filtration material like triblock terpolymers is a challenging task, where many problems have to be solved even before the first trajectory can be recorded. Lacking material transparency and particle adsorption are accompanied by the difficulty of infusing the porous structure with the nanobead suspensions avoiding air pockets. With the presented preparation method and used materials, light scattering has been reduced significantly and the particle mobility ensured.

Using eSEM and appropriate analysis of the associated micrographs, the intricate morphology of the membrane and its void size distribution were determined. These prior studies helped to interpret the consecutive 3D-SPOT measurements correctly.

Here, not only the results from electron microscopy could be reproduced, but the variation of the particle size revealed the difference between the actual and the accessible void space. This proves that even if a special type of electron microscopy capable of handling wet materials was used, particle-tracking based structure elucidation provides valuable complementary results. In this context, the advantage of 3D-SPOT, is not only its non-invasive approach but also its high three-dimensional spatial resolution and the chance to inspect the material in a liquid-filled state. Moreover, microscopic data about material transport within the nanoporous system is supplied.

These transport data have been evaluated in the preceding chapter. Despite a detailed analysis and the complexity of the system, no dominant diffusion anomalies have been detected. However, minor traces of motion described by the (subdiffusive) FLE were found, but its origin is still obscured. One speculative explanation might involve particle-wall interactions arising from a memory effect in the ambient viscosity mediated by the polymer chains. But for further clarification, more experiments need to be performed with, for example, a PNIPAAm block that has either been extended during synthesis or stretched by sample heating.

9 | EXTENSIONS OF SPOT: PROOF-OF-CONCEPT EXPERIMENTS

While the complexity of SPOT data is rather high and only small ensembles of particles are possible to investigate, there are strong arguments needed not to use an alternative approach instead. Especially, the very straightforward method of camera-based SPT is often sufficient as it is easily able to record tens to hundreds of trajectories simultaneously and without great concerns about measurement artifacts. Nevertheless, the 3D-SPOT setup offers a bunch of possibilities to modify or extend the resulting information. Some raw ideas that came across, will be introduced in the following.

9.1 | CONFINED-SPACE IMAGING WITH SPOT

Trajectories within confined spaces can be used to create binary images (images consisting of only two color values) of the surrounding structure. Therefore, one can divide the three-dimensional space where the motion takes place into a regular grid. The boxes limited by the grid points, so-called *voxels*, are identified as void spaces, if they are visited at least once by the particle. Voxels that are not visited at any time may belong to the constraining structure, but not necessarily have to. Likewise localization errors may yield to false identification of void voxels. Thus, the duration of trajectory acquisition must be sufficiently long and the voxel size sufficiently large. Stricter requirements for the void identification like a repetitive visiting or a correlated high photon count rate may help preventing identification errors. Previous knowledge about the confining structure can also be incorporated into the data analysis.

A trial run of this type of data analysis was done on particle trajectories recorded in the triblock terpolymer membrane in the context of the experiments discussed in section 8.3. Voxels with 20 nm edge length are created and identified as voids by the described procedure. A penetration of the nanoparticles into the membranes scaffold structure is not anticipated and localization errors are disregarded. By 3D-rendering with the ImageJ software, images of the particles accessible void space like those shown in fig. 9.1 are generated and provide a three-dimensional structure resolved with a spatial accuracy below the diffraction limit of light.

Having mapped the accessible void space that way, the motion of the particle can be set into spatial reference. Since the full trajectories contain too much information to discover particle dynamics by eye, an different visualization technique is more insightful. An image time series of z -slices overlaid by 250 ms long sub-trajectories constitute a flip book-like clip of the particle movement with respect to the pore walls. An example of such a trajectory clip is visualized in fig. 9.2. Here, the membrane wall structure is displayed in the background in a symmetric 80 nm slice around the central z -position of the sub-

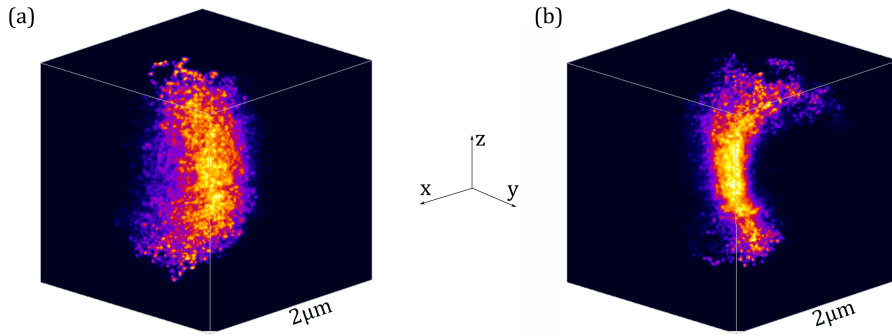


Figure 9.1.: Three-dimensional rendering of single nanopores of the triblock terpolymer membrane. Data basis are two 3D-SPOT measurements of particles of 25 nm in diameter that are processed in z -slices. For each slice the outer boundary of the places visited by the particles diffusive walk are used to compute the voids surface. The depicted pore volume is not corrected by the particle diameter and, therefore, represents the are the void space accessible for the particle’s center of mass.

trajectory. Furthermore, the void area was convolved by an Gaussian kernel to smooth the volume projection to a more realistic shape.

This very detailed representation of the SPOT data may help to investigate single event-based effects in future experiments, but it is, of course, not suited for a statistical analysis of the particle dynamics.

9.2 | DUAL-COLOR 3D-SPOT

A big drawback of SPOT is that the technique focuses just on the inspected detection volume and is unaware of the surrounding conditions in the first place. One way to circumvent this is to insert an independent wide-field channel.[66] But in a scenario where the interaction of two particles should be studied with high spatial resolution, this method is not always gainful. Some research groups implemented measurement routines that record multiple particle trajectories with a SPOT-like technique with interparticle-distances significantly larger than the detection volume.[217, 218] They scan the laser light focus sequentially on different places within the sample and remember the last known particle position for the following scan cycle before proceeding to the next tracking location. Hence, the time between two position estimations of the same particle increases linear with the number of particles to be tracked in parallel and so does the escape probability. This restricts SPOT to studies of very slow dynamical processes and clearly separated particles. Moreover, the particle identification becomes ambiguous if particle approach each other.

The here introduced attempt addresses exactly the situation, where the particles are in a proximity that is closer than the detection volume. SPOT with only one detection channel registers such interaction events only indirectly via changes in the particle’s mobility or fluorescence rate.

Detection of two photon counting channels in a SPOT experiment provides the possibility to acquire two independent position measurements per estimation cycle simultaneously, even though only one at a time can be followed. Pictorially speaking, a dual-detection-channel-SPOT method sits on the back of a single particle and experience its ride through a foggy area. Once a second particle approaches the limited field of view, its behavior, and

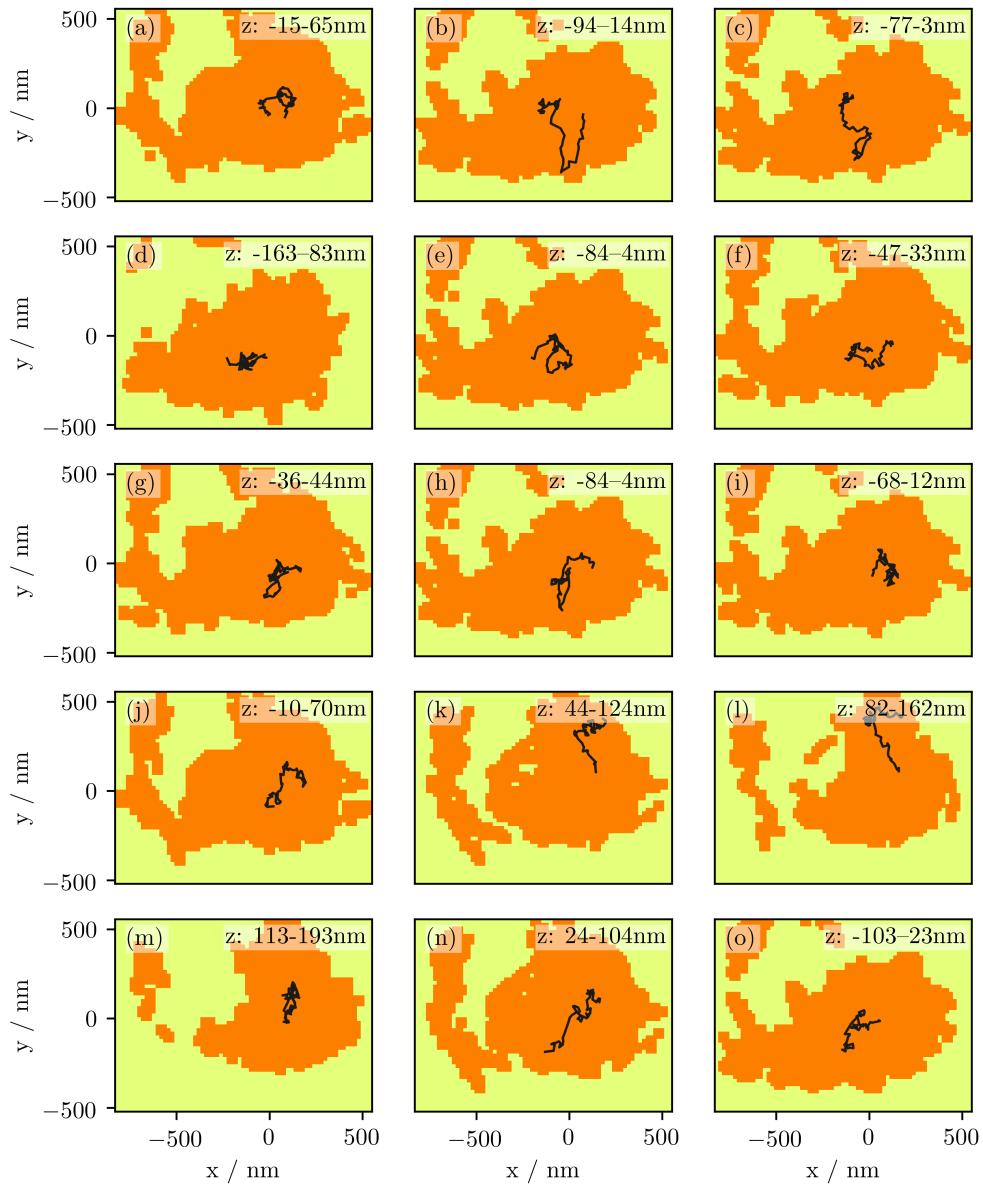


Figure 9.2.: Sequence of sub-trajectories of a single particle ($\varnothing 25$ nm) diffusing in the triblock terpolymer membrane reading from left to right and top to bottom (a) \rightarrow (o). Each frame corresponds to a 250 ms time gate. Boundaries of the accessible void space (void: orange, not-visited/wall: yellow) are generated for a 80 nm z -slice around the sub-trajectories mean z -position from the entire particle trace.

interaction with the tracked particle become visible. Technically, the two simultaneously recorded detection channels are demodulated separately, and the operator has to specify which channel should be used for feedback. The limitation is that both particles must be excited with the same wavelength, possibly yielding in large crosstalk between the detection channels. In time-correlated single-photon counting experiments, the method of *pulsed interleaved excitation* is a common way to get rid of that crosstalk.[219, 220]

In the style of pulsed interleaved excitation, therefore, the technique of *dual-color three-dimensional single-particle orbit tracking* (2C3D-SPOT) with two distinct excitation colors and detection channels was developed in the context of this thesis. It was a by-product resulting from the improved way of storing the scan path and the demodulation pattern within the memory of the ADwin system (see appendix C.3). Both functions are pre-calculated on the PC and transmitted to the ADwin memory via QtSPOT. Therefore, complex functional relations can be implemented without an increase in the ADwins workload.

The concept of 2C3D-SPOT is illustrated in fig. 9.3. The scan path used for 3D-SPOT is maintained, but now each of the two parallel orbits is sequentially created by one of two different laser wavelengths. For instance, assuming a red and a green excitation laser wavelength, first, the lower orbit is created in red and then in green, followed by the creation of the upper orbit in red and in green. For each laser scan position, photons from two detectors (detector 1 and 2, recording different spectral ranges of the emission light) are registered and multiplied by the corresponding value in the demodulation matrix (see eq. (C.60)). Using one demodulation matrix per physical detector enables the independent acquisition of two independent detection channels, one for the red excitation and detection from detector 1 and one for the green excitation and detection from detector 2. In fact, this approach makes it possible to create even more complicated detection schemes, with, for example, a total channel that contains all detected photons (detector 1 and 2 and excitation in red and green) and a second channel filtering only those photons detected from detector 2 and for the time interval of the green excitation.

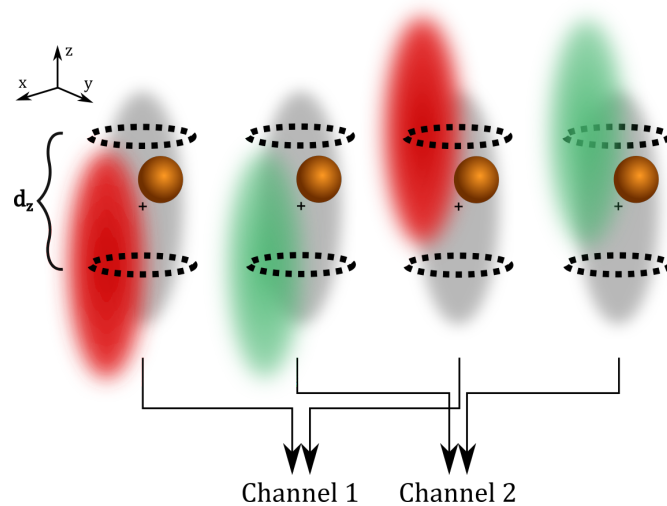


Figure 9.3.: Sketch of the localization procedure used for 2C3D-SPOT. Nested scanning of laser foci of different wavelength yields in the temporally separated excitation with two distinct wavelengths and recording with two physical detector enables the assembly of two (virtual) detection channels that may contain the positions of two types of particles.

The two detectors do not necessarily have to map spectral intervals but also polarization

axes. In this case, two excitation color channels can be recorded polarization-resolved with only two physical detectors. The concept can be generalized to three or more excitations and an increased number of detectors. But already by using two colors, many interesting experiments are possible. FRET may be measured and correlated with the position of two types of particles that may be stitched together with a linker like a polymer chain or a big aggregate.

Implementation and excessive testing of 2C3D-SPOT was not a focus of this work, so only some proof-of-concept experiments have been performed.

The creation of the differently colored orbits is very straightforward to be integrated into the setup at hand. As described in section 4.1 and D.1, two laser sources are combined and coupled into a fiber to generate a light beam consisting of two distinct wavelengths. Beam scanning is performed with AODs that show wavelength-dependent deflection characteristics (see fig. D.1). Therefore, the first AOD and the iris placed behind it (see fig. 4.1) are used as an AOD/AOTF (AOTF: *acusto optical tunable filter*) combination deflecting and filtering spectrally, provides that the used wavelengths are clearly separated in space within the occurring distances.

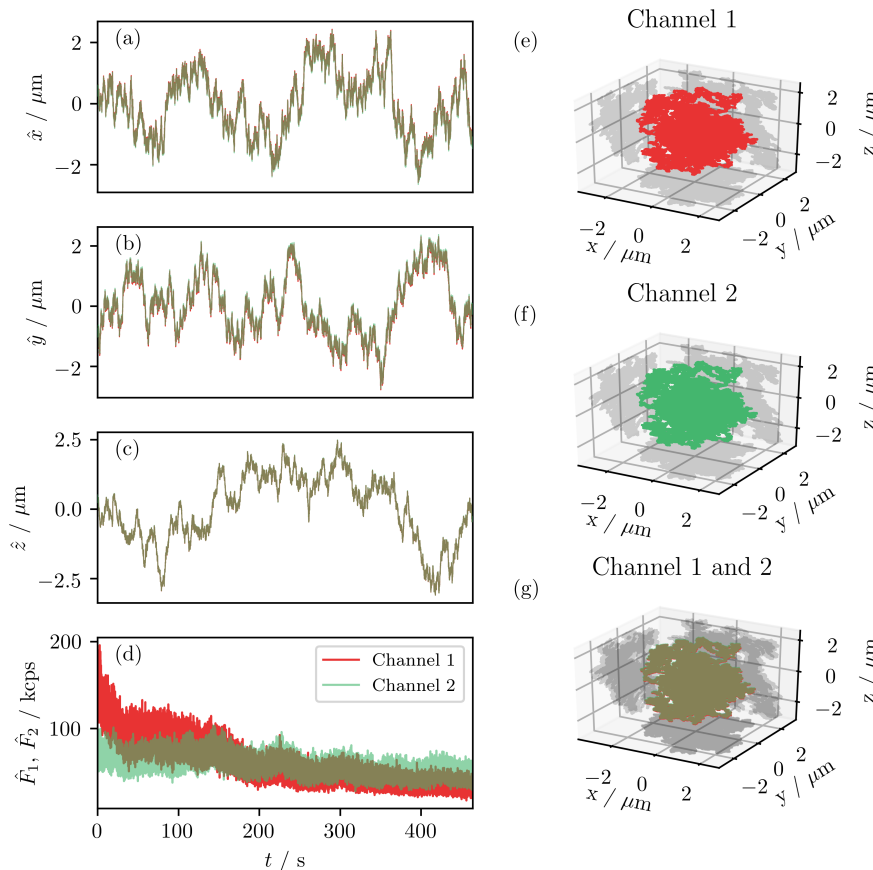


Figure 9.4.: Example of the measurement results of a 2C3D-SPOT measurement. (a-c) x-, y- and z-coordinate of the estimated particle position for channel 1 (solid red line) and channel 2 (solid green line). (d) Detected fluorescence rates for channel 1 and 2. (e-f) 3D-trajectory reconstructed from channel 1 or 2, respectively. (g) Overlapped 3D trajectories for channel 1 (red line) and channel 2 (green line) yielding a mixed color impression. Light gray lines are the 2D projections of the 3D trajectories on the corresponding planes in graphs (e) to (g).

The ability to track two positions per position estimation cycle was tested with a fluorescent

polystyrene particle, called TransFluoSpheres, that allows for very broadband excitation (see table 5.1). The demodulation functions are modified so that both APD signals are fused, and the channels are just separated by the time intervals corresponding to the different excitation wavelengths. Excitation color 1 was created with $\lambda_{\text{exc},1} = 635 \text{ nm}$ (Radius 635-25, Coherent Inc.) and excitation color 2 with $\lambda_{\text{exc},2} = 532 \text{ nm}$ (Monopower-532, ALPHALAS GmbH). As the dichroic beam splitter (see DBS in fig. 4.1), a single band longpass filter was used (zt633rdc, Chroma Technology Corp.) accepting some losses of intensity for the second excitation color, which was no problem since this laser was able to emit with higher power. Clean detection signals are achieved with a single longpass detection filter (z633 RDC, AHF analysentechnik AG). The emission spectrum of the TransFluoSpheres is centered around 645 nm and independent of the laser wavelength (see fig. 5.4). Detection channel 1, which is the overall photon detection during excitation with $\lambda_{\text{exc},1}$, is used for feedback. The second channel is the signal acquired with both detectors during excitation with $\lambda_{\text{exc},2}$. Ten trajectories of different particles and varying measurement times are recorded. An example of a 2C3D-SPOT measurement is depicted in fig. 9.4, more are shown in the appendix E.4.

At first glance, the two trajectories resulting from a single measurement coincide very well. This is expected as the same particle is recorded in both detection channels. A quantitative analysis of all trajectories yields a constant mean displacement of the channel 2 trajectory with respect to channel 1 of $\delta x = (-34.45 \pm 15.81) \text{ nm}$, $\delta y = (49.52 \pm 15.03) \text{ nm}$ and $\delta z = (4.39 \pm 9.01) \text{ nm}$ (see fig. 9.5 (a)). As the displacement is independent of the particle or time, it is attributed to a small shift of the two differently colored orbit scan path. This may be reduced by improved alignment and calibration or simply be subtracted from the data.

For the sake of completeness, the two fluorescence rate channels are plotted in fig. 9.4 (d) as well and relate to each other in fig. 9.5 (b).

Concluding this chapter, 2C3D-SPOT is already possible with the existing soft- and hardware tools and tested experimentally. While in practice, the calibration procedure of the beam width and orbit diameter is twice that laborious as in single-color 3D-SPOT, a stable setup will maintain the settings over weeks up to months. The approach makes use of the advantages of AOD-based beam scanning compared to mirror-based devices and may be further expanded to three or even more colors. Consequently, 2C3D-SPOT expands the field of applications for an orbital tracking setup dramatically without interfering with the existing one-color method.

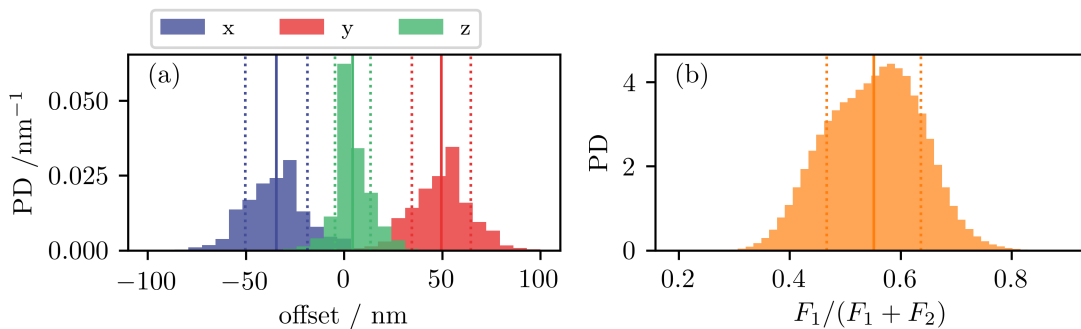


Figure 9.5.: Histogram of the shift between the trajectory from channel 2 compared to that from channel 1 for all ten trajectories shown in fig. 9.4 and fig. E.9. $\delta x = (-34.45 \pm 15.81) \text{ nm}$, $\delta y = (49.52 \pm 15.03) \text{ nm}$ and $\delta z = (4.39 \pm 9.01) \text{ nm}$

9.3 | FLUORESCENCE LIFETIME 3D-SPOT

Another extension of 3D-SPOT arises by using a pulsed laser source and photon detection with picosecond accuracy. Correlating the detection time of a photon to the point in time of the excitation of the corresponding chromophore yields the fluorescence lifetime, a sensitive measure for changes in the electrostatic environment of the probe particle. Laser pulse repetition rates higher than 1 MHz are a lot faster than the fluorescence modulation rate used for 3D-SPOT, which is in the kHz regime. That means that both processes, particle localization, and fluorescence decay measurement, are clearly distinguished by their characteristic time constants and measurements can be executed simultaneously. Hence, the information of a measured particle trajectory and the corresponding level of the fluorescent rate can be extended by the lifetime of the fluorophore's excited electronic state. This technique will be called *fluorescence lifetime three-dimensional single-particle orbit tracking* (FL3D-SPOT) and proof-of-concept experiments have been conducted leaving the detailed implementation of this technically and financially very demanding method to future use cases.

While 2C3D-SPOT is seamlessly integrated into the existing soft- and hardware architecture of the setup, FL3D-SPOT needs several modifications. First, a pulsed laser source must be used (here: SC400, Fianium Ltd.), and second, the electronic pulse(s) generated by the detector(s) and indicating the detection of a photon must be split and transmitted to a *time-correlated single-photon counting*-card (TCSPC-card, here: TimeHarp 200, PicoQuant GmbH) which gets its synchronization pulses by a wired connection to the pulsed laser source. Via splitting of the electronic signals, the photon counting executed by the ADwin is left unaffected by the ps-accurate single-photon counting which is conducted independently from SPOT by an additional PC with a TCSPC-card plugged in. In the proof-of-concept experiment, measurements were started and stopped on the second PC manually. Consequently, there is no exact assignment between position and lifetime. Lifetime measurements took place over time spans of seconds. In a systematic implementation of this method, the ADwin should send start and stop pulses to the TCSPC-card, triggering short fluorescence decay recordings that are synchronized with the trajectory positions yielding time series of fluorescence lifetimes.

Results of the experiments on fluorescent microspheres (CAF-100NM, Red Fluorescent Particles, Magsphere Inc., $\varnothing_{\text{nom.}} = 100 \text{ nm}$) tracked while diffusing in a glycerol/water mixture are shown in fig. 9.6.

Even though there is still a lot to be done to implement this technique, some basic questions have already been answered. Tracking is possible with a pulsed laser source and no severe dispersive influence of the acusto-optical crystals on the pulse width was observed. Moreover, the splitting of the electronic signals stemming from the APDs does not influence the low time resolution photon counting of SPOT and an independent TCSPC experiment can be conducted, simultaneously. The detectors and electrical signals are yet not optimized for fast timing behavior and the performance margins are not discernible. Unfortunately, the synchronization necessary to correlate particle position and lifetime measurements is currently lacking, but a straightforward way to implement is was suggested. The advantage of FL3D-SPOT is that fluorescence decays of a single particle in solution are accessible with high signal-to-noise ratios due to the long measurement time or that the temporal variation of the fluorescence lifetime may be recorded and correlated with the particles diffusing characteristics.

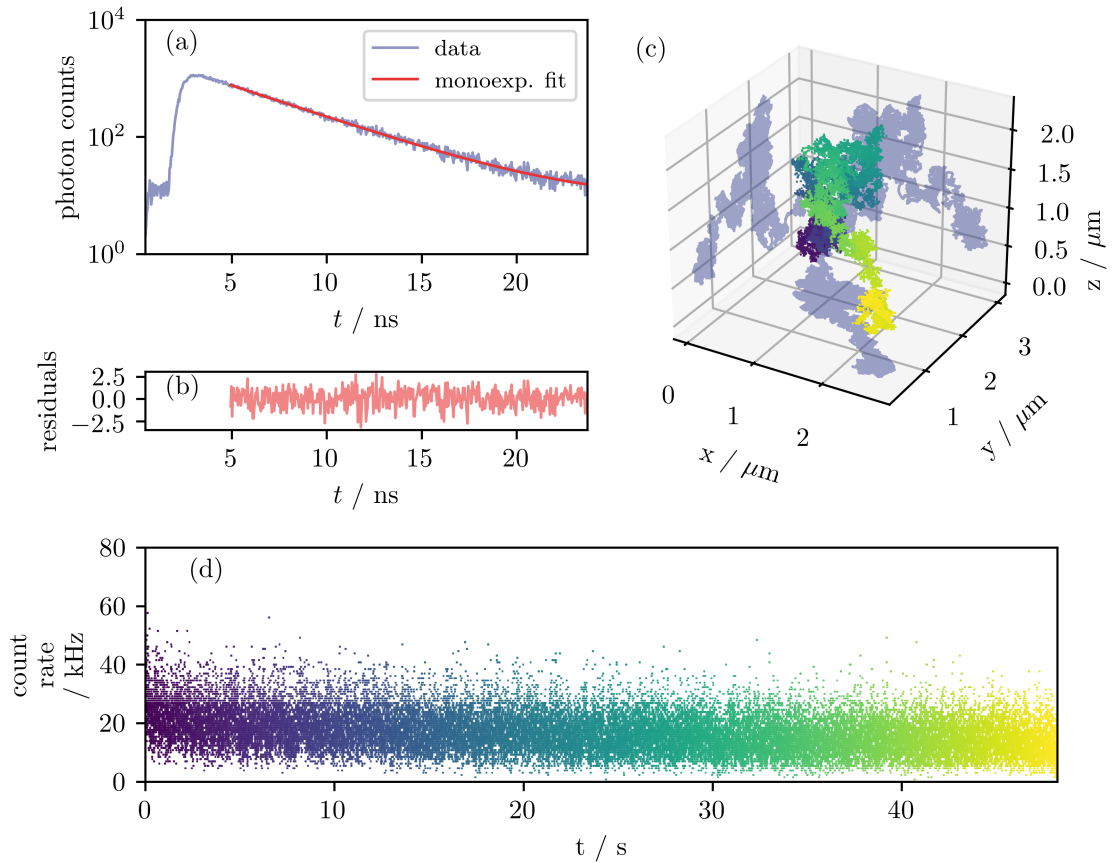


Figure 9.6.: (a) Fluorescence decay and mono-exponential tail fit of an FL3D-SPOT experiment on a single fluorescent microsphere diffusing in a glycerol/water mixture and captured with 3D-SPOT. The particle was excited at 519 nm with a repetition rate of about 40 MHz. (b) Residuals of the mono-exponential model function. (c) Synchronously measured trajectory of the tracked particle (time is color-coded according to (d)). (d) Photon count rate measured with the coarser time resolution of the SPOT electronics and using the same color-code as in (c).

10 | SUMMARY AND OUTLOOK

This work dealt with active single-particle tracking in three dimensions. For this purpose, not only comprehensive theoretical modeling of the method was presented, but also a better understanding of the measurement results was created by means of simulations. Furthermore, the technique was validated on reference systems and applied to a new research topic.

The technical and methodological improvements, especially the addition of the third dimension to the tracking data, have increased the method's complexity significantly. But on the other hand, it has also enhanced its stability and performance range yielding longer trajectories even under more unfavorable conditions. The technical novelties with reference to the nanopositioning stage and its controller rendered the method more understandable, reproducible and accurate.

While the temporal resolution of the setup was enhanced from 4 ms to 1.33 ms, the 3D-spatial resolution was only achievable at the expense of the accuracy in the lateral direction. Because the spatial resolution is highly case-dependent (fluorescence rate, particle speed, background signal, laser wavelength) no particular value can be fixated for that, but a range of 10 nm to 50 nm is realistic for normal experimental conditions. The developed user interface and control software work stable, high-performing, and was designed for flexible extensions. Some of such conceivable extensions have already been unveiled and tested. In particular, the technique of 2C3D-SPOT is a promising add-on. Already being seamlessly integrated into the existing setup, the options for further experiments are dramatically increased.

Looking back at the presented results, a variety of options appear interesting for future research projects.

For example, now that 2C3D-SPOT has been tested on broadband excitable particles, further attempts should be made to track two particles that are labeled with different dyes and connected via a linker molecule. The diffusive motion of such a particle tandem could reveal interesting dynamics, especially if the environment is patterned or anisotropic.

Future research could also repeat the presented 3D-SPOT experiments on nanoparticle diffusion inside the filtration membrane from chapter 8 but switching the stimuli-responsive polymer block by a change of the environmental temperature. Initial experiments in this direction revealed problems with the mechanical temperature stability of the sample holder. These difficulties are technical, not conceptual, and should be able to be overcome for example by using a sample holder material with a negligible coefficient of thermal expansion or by heating only very locally.

Not only switchable environments are interesting sample systems, but also nanoparticles with thermoresponsive coatings. Quantum dots or gold particles covered with PNIPAAm[221, 222] are attractive objects to be studied with 3D-SPOT as they are potential drug delivery systems.[223] One would try to heat the sample while tracking a single particle and watch a drug, e.g., represented by a dye, be released. Here, the second detection

and/or excitation color-channel may become useful.

Precisely fabricated micro- or nanostructured environments, such as inverse opals[103, 105] or microfluidic devices[123] are very instructive sample systems. The strictly specified geometry would remove some uncertainties introduced by the characterization of inhomogeneous materials like nanoporous polymer membranes and allow experiments with a well-defined horizon of expectation. Consequently, more subtle differences in diffusion modes could be extracted from nanoparticle trajectories within these kinds of environments.

The tracking of self-propelled nanoparticles, like so-called *Janus particles*[224], poses an ambitious project. One half of the surface of Janus particles consists of a material different from the other half and that, e.g., catalyzes a chemical reaction in the surrounding medium. This chemical reaction drives the particle forward and creates complicated dynamics[225, 226] that may be measured with 3D-SPOT on the nanoscale. However, their high mobility and the need for fluorescence labeling could constitute practical hurdles.

The transition to increasingly complex sample systems also requires increasingly sophisticated evaluation methods. The use of numerical simulations and modeling with the tools of system theory are certainly still promising approaches. But also more recent trends in data analysis should be kept in mind: there are already first studies on the use of *machine learning* algorithms, in particular (*convolutional*) *neural networks* and *deep learning*, for the evaluation of particle trajectories.[227–230] To utilize a machine learning model, one would simulate realizations of the theoretical particle motion with the help of the underlying statistical laws. Then, those simulation results would be used as the input of a simulation of the SPOT method to obtain the corresponding measured trajectory. Having done so for several different theoretical particle motion frameworks, the machine learning model could be trained with those data. The finally educated analysis model could then be applied to real-world measurements to differentiate between the learned theoretical laws. Perhaps another promising approach is to train the computer algorithm not with simulation data but from measurement results in reference systems.

In summary, already this incomplete list of possible research projects is long and aspirational, but 3D-SPOT and its extensions are technically and experimentally demanding and require diligent data analysis. However, no matter what projects are tackled, what particles are used, or what analysis is applied, I am sure that there are plenty of situations where fluorescence-based high-resolution tracking of nanoparticles is beneficial and may help to solve future scientific questions.

PART II | APPENDIX

A | SYSTEM THEORY AND CONTROL SYSTEMS

System theory is an abstract, general, and mathematical approach to describe and calculate the behavior of physical systems in time. In control engineering, physical systems are frequently described in the formalism of *state-space models* and/or with *transfer function (matrices)*. Both methods are suitable for different purposes and have their respective limitations regarding validity and applicability. Especially in linear time-invariant systems, both formalisms are reduced to a fundamental framework that can be easily applied to various applications. In addition, there are algebraic expressions on how to calculate transfer functions from state-space models and vice versa. In this thesis, tools and concepts from system theory are used frequently and for different purposes. They can describe the vibrational behavior of a nanopositioning stage, create simulations that imitate the results of the SPOT method or help solving the Langevin equation in diffusion theory. Because of its importance for this work, basic elements of system theory will be outlined in this section. The entire chapter is mainly based on [231], where more detailed derivations and explanations can be found.

A.1 | STATE-SPACE FORMALISM

In the formalism of the state-space models, a state of the system at time t is summarized in the elements of a vector $\mathbf{x}(t) \in \mathbb{R}^n$. The most fundamental state-space model describes the system with a set of dynamic equations:

$$\dot{\mathbf{x}}(t) = \mathbf{f}(\mathbf{x}(t), \mathbf{u}(t)), \quad (\text{A.1})$$

$$\mathbf{y}(t) = \mathbf{g}(\mathbf{x}(t), \mathbf{u}(t)) . \quad (\text{A.2})$$

Eq. (A.1) is called the *state equation* because it describes the temporal evolution of the system state itself in dependency of the current state $\mathbf{x}(t)$ and of an *input vector* $\mathbf{u}(t) \in \mathbb{R}^m$. Examples for system inputs are external forces, light irradiation or applied voltages. Eq. (A.2) is the *output equation*, relating the input and system state to an *output vector* $\mathbf{y}(t) \in \mathbb{R}^r$. The system output can be understood, for instance, as a measurement of a system property. In general, the vector functions

$$\mathbf{f}(\mathbf{x}(t), \mathbf{u}(t)) = (f_1(\mathbf{x}(t), \mathbf{u}(t)), f_2(\mathbf{x}(t), \mathbf{u}(t)), \dots, f_n(\mathbf{x}(t), \mathbf{u}(t))) \quad \text{and} \quad (\text{A.3})$$

$$\mathbf{g}(\mathbf{x}(t), \mathbf{u}(t)) = (g_1(\mathbf{x}(t), \mathbf{u}(t)), g_2(\mathbf{x}(t), \mathbf{u}(t)), \dots, g_r(\mathbf{x}(t), \mathbf{u}(t))) \quad (\text{A.4})$$

are nonlinear functions, with f_i and g_j being scalar functions. If \mathbf{f} and \mathbf{g} are linear, the eqns. (A.1)–(A.2) reduce to

$$\dot{\mathbf{x}}(t) = \mathbf{A}(t)\mathbf{x}(t) + \mathbf{B}(t)\mathbf{u}(t) \quad \text{and} \quad (\text{A.5})$$

$$\mathbf{y}(t) = \mathbf{C}(t)\mathbf{x}(t) + \mathbf{D}(t)\mathbf{u}(t). \quad (\text{A.6})$$

Note that any linear ordinary differential equation of arbitrary order can be converted into a system of coupled first order differential equations like eq. (A.5). The occurring matrices are called the *system* or *dynamic matrix* $\mathbf{A}(t) \in \mathbb{R}^{n \times n}$, the *input matrix* $\mathbf{B}(t) \in \mathbb{R}^{n \times m}$, the *output matrix* $\mathbf{C}(t) \in \mathbb{R}^{r \times n}$ and the *direct transfer* or *feed forward matrix* $\mathbf{D}(t) \in \mathbb{R}^{r \times m}$.

If all these matrices are constant in time, the system is called a *linear and time invariant* (LTI) continuous-time system that is written as

$$\dot{\mathbf{x}}(t) = \mathbf{A}\mathbf{x}(t) + \mathbf{B}\mathbf{u}(t) \quad \text{and} \quad (\text{A.7})$$

$$\mathbf{y}(t) = \mathbf{C}\mathbf{x}(t) + \mathbf{D}\mathbf{u}(t). \quad (\text{A.8})$$

The state variables $\mathbf{x}(t)$ are a (minimum) set of variables that fully describe the system at a given time, \mathbf{A} is a representation of the system's intrinsic dynamics, and \mathbf{B} defines how external energy is added into the system. The outputs $\mathbf{y}(t)$ of the system are not necessarily the system's state vector, but a linear combination of the states and the inputs. The matrix \mathbf{D} allows the inputs to bypass the system dynamics and feed-forward to the output.

Once a system is modeled in state-space, its dynamics can be calculated from equations with general validity. First, the solution of the system dynamics needs the definition of the initial state $\mathbf{x}(t_0 = 0) = \mathbf{x}_0$. Then eq. (A.7) can be solved via Laplace transformation in s -space as

$$\mathbf{X}(s) = (s\mathbf{1} - \mathbf{A})^{-1} \mathbf{x}_0 + (s\mathbf{1} - \mathbf{A})^{-1} \mathbf{B}\mathbf{U}(s) \quad \text{and} \quad (\text{A.9})$$

$$\mathbf{Y}(s) = \mathbf{C}(s\mathbf{1} - \mathbf{A})^{-1} \mathbf{x}_0 + \mathbf{C}(s\mathbf{1} - \mathbf{A})^{-1} \mathbf{B}\mathbf{U}(s) + \mathbf{D}\mathbf{U}(s). \quad (\text{A.10})$$

Here, $\mathbf{1}$ is the *identity matrix*. The occurring term $(s\mathbf{1} - \mathbf{A})^{-1}$ is called the *resolvent matrix* and can also be calculated as

$$(s\mathbf{1} - \mathbf{A})^{-1} = \frac{\text{adj}(s\mathbf{1} - \mathbf{A})}{\det(s\mathbf{1} - \mathbf{A})} \quad (\text{A.11})$$

The inverse Laplace transformation of the resolvent matrix is called the *state transition matrix*

$$\mathcal{L} \left\{ (s\mathbf{1} - \mathbf{A})^{-1} \right\}^{-1} = e^{\mathbf{A}t}. \quad (\text{A.12})$$

and it makes use of the matrix exponential $e^{\mathbf{X}t}$ that is defined by its series expansion

$$e^{\mathbf{X}t} = \sum_{k=0}^{\infty} \frac{\mathbf{X}^k t^k}{k!}. \quad (\text{A.13})$$

Consequently, the solution of the state and output equation can be written in the time-

domain as

$$\mathbf{x}(t) = e^{At} \mathbf{x}_0 + \int_0^t e^{A(t-\tau)} \mathbf{B} \mathbf{u}(\tau) d\tau \quad \text{and} \quad (\text{A.14})$$

$$\mathbf{y}(t) = \mathbf{C} e^{At} \mathbf{x}_0 + \mathbf{C} \int_0^t e^{A(t-\tau)} \mathbf{B} \mathbf{u}(\tau) d\tau + \mathbf{D} \mathbf{u}(t) . \quad (\text{A.15})$$

A.2 | TRANSFER FUNCTION MATRIX FORMALISM

For a system at rest, in particular if the initial state is the zero state $\mathbf{x}_0 = \mathbf{0}$, eq. (A.10) shrinks to the form

$$\mathbf{Y}(s) = \mathbf{G}(s) \mathbf{U}(s) \quad (\text{A.16})$$

with the *transfer function matrix*

$$\mathbf{G}(s) = \mathbf{C} (s\mathbb{1} - \mathbf{A})^{-1} \mathbf{B} + \mathbf{D} . \quad (\text{A.17})$$

Provided that the transfer function matrix is known, the system's response to an arbitrary input signal is easily calculated by eq. (A.16). For systems consisting of a *single input and a single output* (SISO), the transfer function matrix collapses to a scalar, called the *transfer function*. Thus the transfer function matrix is a generalization of the scalar transfer function for *multi-input/multi-output* (MIMO) systems and bridges the formalism of transfer functions with state-space models. This theoretical framework was first proposed by HOWARD H. ROSENBROCK in 1966 [232] and is especially useful in computer-aided applications such as simulations or electronically controlled plants. While for systems, where only the relation between the input and the output of the system should be described efficiently, transfer functions are the right choice. System modeling via state equations is superior to the transfer function matrix formalism in that it allows insights into the internal state variables. One of the advantages of the transfer functions formalism is that simple multiplications of transfer functions describe sequences of LTI systems. For instance, if the output of system (I), denoted as $\mathbf{Y}_{(I)}(s)$, serves as the input of system (II), written as $\mathbf{U}_{(II)}(s)$, the total transfer function is that of (II) times that of (I) or short $\mathbf{G}_{(I),(II)}(s) = \mathbf{G}_{(II)}(s) \mathbf{G}_{(I)}(s)$ and the final output is

$$\mathbf{Y}_{(II)}(s) = \mathbf{G}_{(II)}(s) \mathbf{U}_{(II)}(s) = \mathbf{G}_{(II)}(s) \mathbf{G}_{(I)}(s) \mathbf{U}_{(I)}(s) = \mathbf{G}_{(I),(II)} \mathbf{U}_{(I)}(s) . \quad (\text{A.18})$$

If a m th order differential equation represents a linear and time-invariant SISO system, it is easy to represent it in transfer function form. Consider the differential equation with $u(t)$ as input and $y(t)$ as output

$$a_0 y(t) + a_1 \frac{d}{dt} y(t) + \cdots + a_{n-1} \frac{d^{n-1}}{dt^{n-1}} y(t) + \frac{d^n}{dt^n} y(t) = b_0 u(t) + b_1 \frac{d}{dt} u(t) + \cdots + b_m \frac{d^m}{dt^m} u(t) . \quad (\text{A.19})$$

Assuming that the system is in rest for $t = 0$. After taking the Laplace transform, each differentiation in the time domain can be replaced by multiplication with the complex frequency s in the Laplace domain, and the differential equation transforms to

$$(a_0 + a_1 s + \cdots + a_{n-1} s^{n-1} + s^n) Y(s) = (b_0 + b_1 s + \cdots + b_m s^m) U(s) . \quad (\text{A.20})$$

Making use of eq. (A.16), the transfer function is easily seen to be

$$G(s) = \frac{Y(s)}{U(s)} = \frac{b_0 + b_1s + b_2s^2 + \cdots + b_ms^m}{a_0 + a_1s + a_2s^2 + \cdots + a_{n-1}s^{n-1} + s^n} . \quad (\text{A.21})$$

For $n \geq m \geq 1$, the system is *proper* and non-trivial. A proper transfer function will never grow unbounded as the frequency approaches infinity:

$$|G(\pm i\infty)| < \infty \quad (\text{A.22})$$

A.3 | SYSTEM MODELING OF A DRIVEN OSCILLATOR

As an example for a SISO system, a damped and driven oscillatory system is modeled in state-space first and then transformed to the transfer function formalism with the help of eq. (A.17).

Consider an object of mass m that oscillates along the coordinate q . The movement of the mass is damped with λ . The natural frequency of the system is ω_n . For an external driving force F_{ext} that acts on the and damped oscillator, Newtons second law takes the form

$$\ddot{q}(t) + 2\lambda\omega_n\dot{q}(t) + \omega_n^2q = F_{\text{ext}}(t)/m . \quad (\text{A.23})$$

This second-order differential equation can be rewritten to maintain the matrix notation as a system of two coupled first order differential equations

$$\frac{d}{dt} \begin{pmatrix} q \\ \dot{q} \end{pmatrix} = \begin{pmatrix} 0 & 1 \\ -\omega_n^2 & -2\lambda\omega_n \end{pmatrix} \cdot \begin{pmatrix} q \\ \dot{q} \end{pmatrix} + \begin{pmatrix} 0 \\ 1/m \end{pmatrix} \cdot F_{\text{ext}} . \quad (\text{A.24})$$

Using the previous notation, this equation can be identified as the state equation of the system with the state $\mathbf{x}(t) = \begin{pmatrix} q & \dot{q} \end{pmatrix}^T$ as the position and speed of the moving mass, and the input vector as the applied acceleration affects only the speed $\mathbf{u}(t) = u(t) = F_{\text{ext}}/m$. The system and input matrices are

$$\mathbf{A} = \begin{pmatrix} 0 & 1 \\ -\omega_n^2 & -2\lambda\omega_n \end{pmatrix} \quad \text{and} \quad \mathbf{B} = \begin{pmatrix} 0 \\ 1/m \end{pmatrix} \quad (\text{A.25})$$

respectively. In this example, the output should be a direct measurement of the position of the oscillator. Thus, the output equations are

$$y = \begin{pmatrix} 1 & 0 \end{pmatrix} \begin{pmatrix} q \\ \dot{q} \end{pmatrix} , \quad (\text{A.26})$$

and a comparison with the previous notation yields in $\mathbf{C} = \begin{pmatrix} 1 & 0 \end{pmatrix}$ and $\mathbf{D} = 0$. The resolvent matrix can be calculated as

$$(s\mathbf{1} - \mathbf{A})^{-1} = \frac{\text{adj}(s\mathbf{1} - \mathbf{A})}{\det(s\mathbf{1} - \mathbf{A})} = \frac{\begin{pmatrix} s + 2\lambda\omega_n & 1 \\ -\omega_n^2 & s \end{pmatrix}}{s(s + 2\lambda\omega_n) + \omega_n^2} , \quad (\text{A.27})$$

and the transfer function matrix reduced to a scalar

$$G_{\text{forced osci.}}(s) = \mathbf{C}(s\mathbf{1} - \mathbf{A})^{-1}\mathbf{B} + \mathbf{D} = \frac{1}{(s^2 + 2\omega_n\lambda s + \omega_n^2)m} \quad (\text{A.28})$$

Sometimes it is more convenient to express this transfer function with the so-called DC gain k_{dc} , which is the ratio of the magnitude of the steady-state step response to the magnitude of the step input. For the second-order system, the DC gain is $k_{dc} = (m\omega_n^2)^{-1}$, and the transfer function can be written as

$$G_{\text{forced osci.}}(s) = \frac{k_{dc}\omega_n^2}{s^2 + 2\omega_n\lambda s + \omega_n^2} \quad (\text{A.29})$$

Alternatively, the transfer function $G_{\text{forced osci.}}(s)$ could be obtained from eq. (A.23) directly, by using eq. (A.19) and eq. (A.21).

A.4 | SYSTEM IDENTIFICATION

Assume a complicated physical or technical system that should be modeled mathematically, but it is not possible to obtain a model on first principles (*white-box model*) for some reason. In this case, a standard method to handle such *black-box* systems is to measure its behavior $\mathbf{y}(t)$ on applying an external stimulus $\mathbf{u}(t)$. Black-box modeling is very challenging, but sometimes there are some insights into the system dynamics that allow for a sophisticated guess of the model equation containing free parameters that have to be identified. In this case, one speaks of a *grey-box model*. There are elaborated tools like *Volterra series* models, *NARMAX* models (*nonlinear autoregressive moving average model with exogenous inputs*), or *neural network* models for nonlinear systems.[233]

For linear or/and SISO systems, there is a more straightforward way for system identification. Therefore, specifically shaped input signals are applied to the system, and the system response is measured and identified with a characteristic function. Typical input signals are rapid impulses, steps, or sinusoidal excitations, yielding in the so-called *unit impulse response (matrix)*, the *unit step response (matrix)*, and the *frequency response (matrix)*, respectively. Each of them is closely related to the transfer function (matrix) and has its merits describing a system or in the simplicity with which it can be measured. Since this assessment varies depending on the respective question's focus, all these functions appear in practical applications. Therefore, they and their relation to the transfer function are enumerated in the following section.

A.4.1 | UNIT IMPULSE RESPONSE (MATRIX)

If the input $\mathbf{u}(t)$ is a Dirac delta impulse $\delta(t)$ and the initial state is the zero state $\mathbf{x}_0 = \mathbf{0}$, the output of the system is given as

$$\tilde{\mathbf{y}}(t) = \mathbf{C}e^{At}\mathbf{B} + \mathbf{D}\delta(t) . \quad (\text{A.30})$$

Transforming this into s -space and using that the Laplace transform of the Dirac delta distribution is $\mathcal{L}\{\delta(t)\} = \mathbf{1}$, one obtains that $\tilde{\mathbf{y}}(t)$ is the inverse Laplace transform of the transfer function matrix,

$$\tilde{\mathbf{Y}}(s) = \mathbf{C}(s\mathbf{1} - \mathbf{A})^{-1}\mathbf{B} + \mathbf{D} = \mathbf{G}(s) . \quad (\text{A.31})$$

Following the literature convention, $\tilde{\mathbf{y}}(t)$ will be written as $\mathbf{g}(t) = \mathcal{L}\{\mathbf{G}(s)\}^{-1}$ and called *unit impulse response (matrix)* (UIR). The UIR is the time-domain equivalent to the transfer function providing a vivid picture of the functioning of LTIs. Using that multiplication in the s domain is a convolution in the time domain, (A.16) can be rewritten as

$$\mathbf{y}(t) = \int_0^t \mathbf{g}(t - \tau) \mathbf{u}(\tau) d\tau. \quad (\text{A.32})$$

Therefore, the picture conveyed by the convolution integral is a good illustration of the mathematical properties of linear systems. The system's response to an arbitrary input $\mathbf{u}(t)$ can be calculated with the help of the UIR by segmenting the input $\mathbf{u}(t)$ into an infinite number of delta pulses of given amplitudes. The system responds to each of those delta pulses with its UIR but scaled by the corresponding amplitude. Consequently, the actual system response is the superposition of all individual scaled UIRs.

A.4.2 | UNIT STEP RESPONSE (MATRIX)

One crucial point is that a delta impulse is impossible to realize in real-world systems. A real physical pulse is only a valid approximation if its pulse width is significantly smaller than the smallest typical timescale of the system to be described. Instead of applying a delta-like impulse to the system, sometimes it is technically more convenient to change the input signal "instantaneously" from one constant level to another. The system's reaction to a stepped shaped input of step size 1 is the *unit step response (matrix)* (USR), denoted as $\mathbf{y}_{\text{USR}}(t)$ and mathematically related to the UIR by integration:

$$\mathbf{y}_{\text{USR}}(t) = \int_0^t \mathbf{g}(\tau) d\tau \iff \mathbf{g}(t) = \frac{d}{dt} \mathbf{y}_{\text{USR}}(t). \quad (\text{A.33})$$

With this relationship, the USR is quickly converted to a transfer function using $\mathbf{G}(s) = \mathcal{L}\{\mathbf{g}(t)\} = s\mathcal{L}\{\mathbf{y}_{\text{USR}}(t)\}$.

A.4.3 | FREQUENCY RESPONSE (MATRIX)

If an LTI is excited with a sinusoidal shaped input, the steady-state solution is sinusoidal again, but depending on the input frequency, the amplitude and phase of the output are modified. The *frequency response (matrix)* describes this behavior. Its relation to the other characteristic responses becomes apparent by inserting a sinusoidal wave as an input $u(t) = e^{j\omega t}$ into eq. (A.32):

$$\begin{aligned} y(t) &= \int_0^\infty g(\tau) e^{j\omega(t-\tau)} d\tau = e^{j\omega t} \int_0^\infty g(\tau) e^{-j\omega\tau} d\tau = e^{j\omega t} \mathcal{F}\{g(t)\} \\ &= e^{j\omega t} G(\omega) = u(t)G(\omega). \end{aligned} \quad (\text{A.34})$$

Now it is obvious that $G(\omega)$ is the Fourier transform of the impulse response and a complex scaling factor for the reproduced input signal. This means the amplitude and phase of the input exponential are modified while the remaining shape is retained. The frequency response is the sub-set of transfer function for purely imaginary arguments,

$$G(\omega) = G(s)|_{s=j\omega}. \quad (\text{A.35})$$

One can write the frequency response as a complex number in amplitude/phase notation $G(\omega) = |G(\omega)| \exp(j\angle G(\omega))$. A *Bode plot* displays the amplitude gain $|G(\omega)|$ and the phase $\angle G(\omega)$ against a logarithmic frequency scale in two separate plots that are called the *Bode magnitude* and *Bode phase plot*, respectively. It is therefore, an intuitive representation of the dynamical behavior of the system under periodic excitation.

A.5 | CONTROLLER CANONICAL FORM

When a system is defined by a transfer function of shape eq. (A.21), it can be transformed into a state-space representation. The problem with this conversion is that the state variables do not appear in the transfer function formalism, and one does not intrinsically know which quantities should be used for this purpose.

The following systematic strategy is one way to solve this problem. First, the procedure to obtain a transfer function from a single differential equation of m th order in appendix A.2 is reversed. Once a single differential equation is found, it can be dissected into a set of coupled first-order differential equations. In the next step, the state variables must be defined. A suitable selection of $\mathbf{x}(t)$ helps to transform the set of first-order differential equations into a standard form of the state-space formalism.[231] For $G(s)$ defined by eq. (A.21), the so-called *controller canonical form* of the state-space model can be constructed by selecting the state variables as

$$\begin{aligned}
\dot{x}_1(t) &= x_2(t), \\
\dot{x}_2(t) &= x_3(t), \\
\dot{x}_3(t) &= x_4(t), \\
&\vdots \\
\dot{x}_{n-2}(t) &= x_{n-1}(t), \\
\dot{x}_{n-1}(t) &= x_n(t), \\
\dot{x}_n(t) &= -a_0x_1(t) - a_1x_2(t) - \cdots - a_{n-2}x_{n-1}(t) - a_{n-1}x_n(t) + u(t).
\end{aligned} \tag{A.36}$$

These selected states are often called the *phase variables* of the system. The state-space representation of the system is now written as

$$\dot{\mathbf{x}} = \begin{pmatrix} 0 & 1 & 0 & \cdots & 0 \\ 0 & 0 & 1 & \cdots & 0 \\ \vdots & \vdots & \vdots & \ddots & \vdots \\ 0 & 0 & 0 & \cdots & 1 \\ -a_0 & -a_1 & -a_2 & \cdots & a_{n-1} \end{pmatrix} \mathbf{x} + \begin{pmatrix} 0 \\ 0 \\ \vdots \\ 0 \\ 1 \end{pmatrix} u \quad \text{and} \tag{A.37}$$

$$y = (b_0 - a_0b_n \quad b_1 - a_1b_n \quad \cdots \quad b_{n-2} - a_{n-2}b_n \quad b_{n-1} - a_{n-1}b_n) \mathbf{x} + b_n u \tag{A.38}$$

A.6 | LINEAR TIME-INVARIANT DISCRETE-TIME SYSTEMS

Nowadays almost all measurement and control tasks are performed by computers, and system modeling must be performed on a discrete-time scale. With the help of the solution of the continuous-time LTI system eqns. (A.14)–(A.15), and the assumption that all signals are constant between sample instants, it is possible to derive the discrete-time state and output equations as

$$\mathbf{x}[k+1] = \mathbf{A}_d \mathbf{x}[k] + \mathbf{B}_d \mathbf{u}[k] \quad (\text{A.39})$$

$$\mathbf{y}[k] = \mathbf{C} \mathbf{x}[k] + \mathbf{D} \mathbf{u}[k] \quad (\text{A.40})$$

with $\mathbf{A}_d = e^{\mathbf{A}\Delta t}$ and $\mathbf{B}_d = \int_0^{\Delta t} e^{\mathbf{A}t} dt$. This transformation is called *step-invariant transformation*. Here, the frequently used notation applies that uses square brackets for quantities that are given on equidistant and discrete points in time [...] and round brackets (...) for continuous-time measures. For instance, the discrete-time state vector $\mathbf{x}[k]$ corresponds to the continuous-time vector $\mathbf{x}(k\Delta t)$, with k being a positive integer. In this notation, the solution of the discrete-time system is

$$\mathbf{x}[k] = \mathbf{A}_d^k \mathbf{x}_0 + \sum_{i=0}^{k-1} \mathbf{A}_d^{k-1-i} \mathbf{B}_d \mathbf{u}[i] \quad (\text{A.41})$$

$$\mathbf{y}[k] = \mathbf{C} \mathbf{A}_d^k \mathbf{x}_0 + \sum_{i=0}^{k-1} \mathbf{C} \mathbf{A}_d^{k-1-i} \mathbf{B}_d \mathbf{u}[i] + \mathbf{D} \mathbf{u}[k] \quad (\text{A.42})$$

For time-discrete signals the role of the Laplace transformation is played by the z -transformation, which is defined for the discretely sampled function $f[k]$ as

$$F[z] = \sum_{k=-\infty}^{\infty} f[k] z^{-k} \quad (\text{A.43})$$

with $z \in \mathbb{C}$. The inverse z -Transformation is given as

$$f[k] = \frac{1}{2\pi i} \oint_{\mathbb{C}} F[z] z^{k-1} dz . \quad (\text{A.44})$$

Consistent notation requires the z -transformed of a quantity to be expressed with capital letters and squared brackets.

Using the z -transformation, the solution of the discrete-time LTI system can be written in z -domain as

$$\mathbf{X}[z] = (z\mathbb{1} - \mathbf{A}_d)^{-1} z \mathbf{x}_0 + (z\mathbb{1} - \mathbf{A}_d)^{-1} \mathbf{B}_d \mathbf{U}[z] \quad (\text{A.45})$$

$$\mathbf{Y}[z] = \mathbf{C} (z\mathbb{1} - \mathbf{A}_d)^{-1} z \mathbf{x}_0 + \mathbf{C} (z\mathbb{1} - \mathbf{A}_d)^{-1} \mathbf{B}_d \mathbf{U}[z] \quad (\text{A.46})$$

$$(\text{A.47})$$

For the particular case of a system at rest $\mathbf{x}_0 = \mathbf{0}$, the system's output is

$$\mathbf{Y}[z] = \mathbf{G}[z] \mathbf{U}[z] \quad (\text{A.48})$$

with the *discrete transfer function matrix*, defined as

$$\mathbf{G}[z] = \mathbf{C} (z\mathbf{1} - \mathbf{A}_d)^{-1} \mathbf{B}_d + \mathbf{D} . \quad (\text{A.49})$$

Eq. (A.48) can be rewritten in the time domain as the discrete convolution of the discrete UIR with the input function

$$\mathbf{y}[k] = \sum_{i=0}^k \mathbf{g}[k-i] \mathbf{u}[i] . \quad (\text{A.50})$$

The discrete UIR is

$$\mathbf{g}[k] = \begin{cases} \mathbf{D} & \text{for } k = 0 \\ \mathbf{C} \mathbf{A}_d^{k-1} \mathbf{B}_d & \text{for } k \geq 1 \end{cases} \quad (\text{A.51})$$

A.7 | CONTROL SYSTEMS

Proceeding now with the continuous-time systems, it should be considered that a transformation to a discretized time scale is possible, yielding analog equations. Often, there is the desire to prescribe the manner of the system's response in the presence of disturbances. The central element to achieve this is feedback. A system with feedback is called a *closed-loop* system, while a system without feedback is an *open-loop* system. A control system can be both, but in a closed-loop system, the system state or output is able to compensate for errors due to external disturbances. While the field of control systems is vast, this section will be limited to a few basic control schemata.

A.7.1 | FULL STATE FEEDBACK

If an accurate linear state-space model of the system is available, it is possible to design a closed-loop control system that stabilizes it with respect to a reference $\mathbf{u}_{\text{tar}}(t)$. Therefore, the state itself feeds back to the input and compares with a reference signal, $\mathbf{u}_{\text{tar}}(t)$. The feed-forward term is not present, so that the system's output is just a measurement of the states themselves or linear combinations of them.

Therefore, eqns. (A.7)–(A.8) are redefined as

$$\dot{\mathbf{x}}(t) = \mathbf{A} \mathbf{x}(t) + \mathbf{B} \mathbf{u}(t) \quad \text{and} \quad (\text{A.52})$$

$$\mathbf{y}(t) = \mathbf{C} \mathbf{x}(t). \quad (\text{A.53})$$

Now a linear feedback law around the system is established as

$$\mathbf{u}(t) = -\mathbf{K} \mathbf{x}(t) + \mathbf{u}_{\text{tar}}(t) , \quad (\text{A.54})$$

with the *feedback matrix* (or *gain matrix*) $\mathbf{K} \in \mathbb{R}^{n \times m}$ and the reference input $\mathbf{u}_{\text{tar}}(t)$ of the same dimension as $\mathbf{u}(t)$. Inserting the feedback law (A.54) into (A.52) yields the closed-loop system with full state feedback

$$\dot{\mathbf{x}}(t) = \mathbf{A}_k \mathbf{x}(t) + \mathbf{B} \mathbf{u}_{\text{tar}}(t), \quad (\text{A.55})$$

with $\mathbf{A}_k = (\mathbf{A} - \mathbf{B} \mathbf{K})$. To reach stability, the eigenvalues of \mathbf{A}_k must be located in the left half-plane. Placing the eigenvalues in the desired position yields the values of the elements in the gain matrix \mathbf{K} . This procedure is called *pole placement* and requires sufficient knowledge about the system dynamics.

A.7.2 | FEEDBACK BASED ON THE SYSTEMS OUTPUT

Similar to full state feedback, a control loop can be constructed based on the output of the system and comparing it with a reference $\mathbf{u}_{\text{tar}}(t)$. The feedback law is simply given by

$$\mathbf{u}(t) = -\mathbf{K}\mathbf{y}(t) + \mathbf{u}_{\text{tar}}(t) . \quad (\text{A.56})$$

Inserting this into a state-space model like eqns. (A.52)–(A.53), yields

$$\dot{\mathbf{x}}(t) = \mathbf{A}\mathbf{x}(t) - \mathbf{B}\mathbf{K}\mathbf{y}(t) + \mathbf{B}\mathbf{u}_{\text{tar}}(t) \quad \text{and} \quad (\text{A.57})$$

$$\mathbf{y}(t) = \mathbf{C}\mathbf{x}(t) - \mathbf{D}\mathbf{K}\mathbf{y}(t) + \mathbf{D}\mathbf{u}_{\text{tar}}(t) . \quad (\text{A.58})$$

By solving the output equation for \mathbf{y} , this system becomes

$$\dot{\mathbf{x}}(t) = [\mathbf{A} - \mathbf{B}\mathbf{K}(\mathbf{1} + \mathbf{D}\mathbf{K})^{-1}\mathbf{C}] \mathbf{x}(t) + \mathbf{B} [\mathbf{1} - \mathbf{K}(\mathbf{1} + \mathbf{D}\mathbf{K})^{-1}\mathbf{D}] \mathbf{u}_{\text{tar}}(t) \quad \text{and} \quad (\text{A.59})$$

$$\mathbf{y}(t) = (\mathbf{1} + \mathbf{D}\mathbf{K})^{-1}\mathbf{C}\mathbf{x}(t) + (\mathbf{1} + \mathbf{D}\mathbf{K})^{-1}\mathbf{D}\mathbf{K}\mathbf{y}(t) + \mathbf{D}\mathbf{u}_{\text{tar}}(t) . \quad (\text{A.60})$$

For $\mathbf{D} = \mathbf{0}$, this simplifies to

$$\dot{\mathbf{x}}(t) = [\mathbf{A} - \mathbf{B}\mathbf{K}\mathbf{C}] \mathbf{x}(t) + \mathbf{B}\mathbf{u}_{\text{tar}}(t) \quad \text{and} \quad (\text{A.61})$$

$$\mathbf{y}(t) = \mathbf{C}\mathbf{x}(t) , \quad (\text{A.62})$$

which is very similar to the full state feedback system, despite the appearance of the matrix \mathbf{C} in the state equation. A block diagram of such a controlled system is given in fig. A.1.

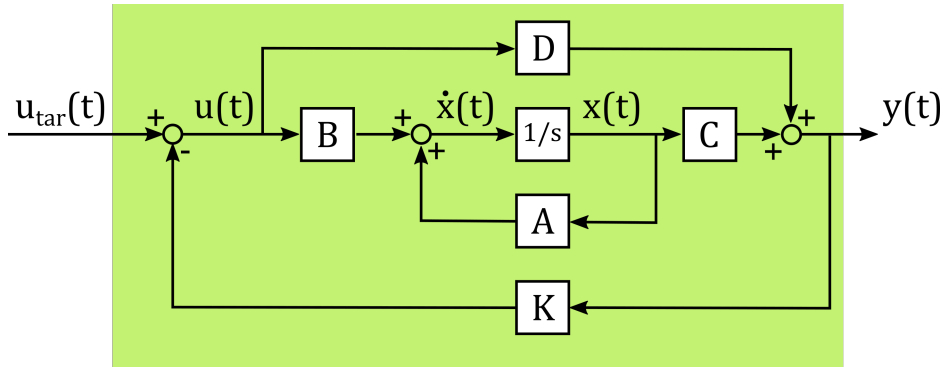


Figure A.1.: Block diagram of a control loop in state-space that feeds back the system’s output. A reference signal $\mathbf{u}_{\text{tar}}(t)$ enters the system, where it is balanced with the output $\mathbf{y}(t)$ to generate the control input $\mathbf{u}(t)$. The integration of the system state changes $\dot{\mathbf{x}}(t)$ to $\mathbf{x}(t)$ is represented by the box labeled by $1/s$. The boxes labeled by \mathbf{A} , \mathbf{B} , \mathbf{C} , \mathbf{D} , and \mathbf{K} are the matrices that act on the variables. The green box represents the complete closed-loop system.

A.7.3 | PID CONTROLLER

A ubiquitous controller is the *proportional–integral–derivative controller* (PID Controller) as it lacks the necessity of insights into the system dynamics. Instead, it operates just on the system’s output compared with a reference signal $u_{\text{tar}}(t)$. $u(t)$ is the control voltage that drives the plant, which can be described by the transfer function $P(s)$. The plant has the response $y(t)$, which is fed back to be compared with the reference/target signal $u_{\text{tar}}(t)$. The difference between the target and the plant’s response is the tracking error

$e(t) = -y(t) + u_{\text{tar}}(t)$. The PID controller tries to minimize this error by generating the control voltage of the plant $u(t)$ scaled by the error itself (P), the integral over it (I), and sensitive to the amount by which the error changes (D). Each part of the control voltage has its own proportionality constant K_p , K_i , and K_d respectively. Thus, the input of the system $P(s)$ is constructed from the corresponding mathematical operation on the error signal or written as

$$u(t) = K_p e(t) + K_i \int e(t) dt + K_d \dot{e}(t) . \quad (\text{A.63})$$

The transfer function $C_{\text{ctrl}}(s)$ of the PID controller can be obtained via the Laplace transform of eq. (A.63) to

$$C_{\text{ctrl}}(s) = \frac{U(s)}{E(s)} = \frac{K_d s^2 + K_p s + K_i}{s} . \quad (\text{A.64})$$

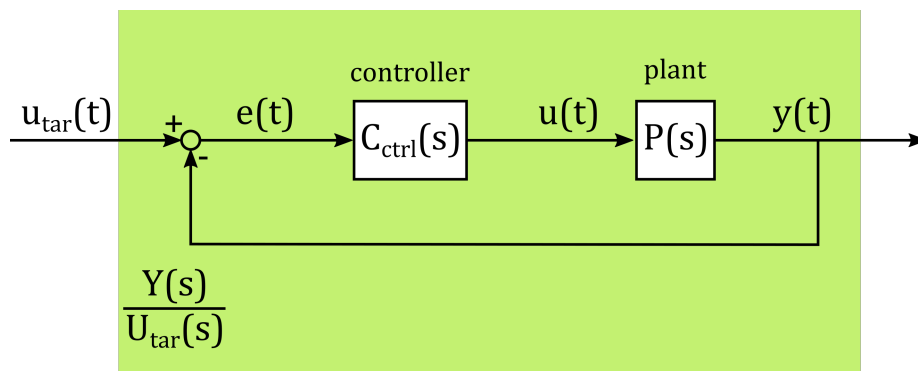


Figure A.2.: Block diagram of a feedback loop like it appears in a PID controller. A reference signal $u_{\text{tar}}(t)$ enters the system, where it is balanced with the plant's output $y(t)$ to obtain the tracking error $e(t)$. A controller with transfer function $C_{\text{ctrl}}(s)$ converts the tracking error into a control signal $u(t)$ for a plant with transfer function $P(s)$. The green box represents the system that is described by the transfer function $Y(s)/U_{\text{tar}}(s)$.

A simple feedback loop is presented in fig. A.2, where a controller with transfer function $C_{\text{ctrl}}(s)$ evaluates the tracking error $e(t) = u_{\text{tar}}(t) - y(t)$ to generate a control signal $u(t)$ that is the input of a plant with transfer function $P(s)$, the controlled system response is given in s -space as

$$\left. \frac{Y(s)}{U_{\text{tar}}(s)} \right|_{\text{feedback}} = \frac{P(s)C_{\text{ctrl}}(s)}{1 + P(s)C_{\text{ctrl}}(s)} . \quad (\text{A.65})$$

For example, an oscillatory system with the plant's transfer function given by eq. (A.29) that is controlled by a PID controller has the control system transfer function

$$G_{\text{PID, osci}}(s) = \frac{(K_d s^2 + K_p s + K_i) k_{dc} \omega_n^2}{s^3 + (2\lambda \omega_n + K_d k_{dc} \omega_n^2) s^2 + (\omega_n^2 + K_p k_{dc} \omega_n^2) s + K_i k_{dc} \omega_n^2} . \quad (\text{A.66})$$

In fig. A.3, the frequency and step response of a driven and damped oscillator system given by eq. (A.29) and its PID controlled version defined by eq. (A.66) is presented as an example for the influence of the controller on the systems dynamical behavior. With the selected control parameter, the large amplitude gain around the resonance frequency and the phase lagging is flattened. In total, the controlled system appears to respond a lot faster and less prone to oscillate.

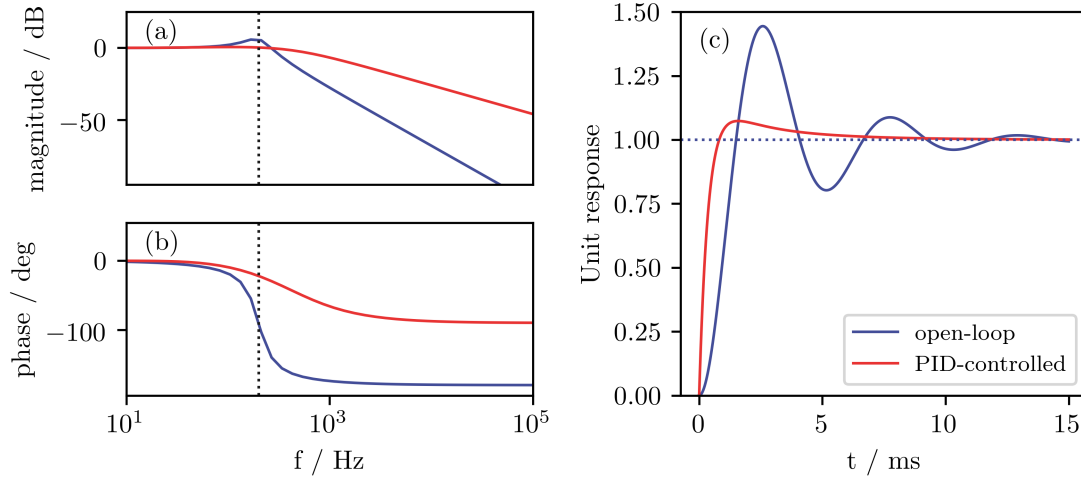


Figure A.3.: (a) Bode magnitude and (b) Bode phase plot of an open-loop (solid blue line) system of a driven and damped oscillatory system and a PID-controlled one (solid red line). The oscillator's natural frequency $\omega_n/(2\pi) = 200$ Hz is indicated as a black dotted line. (c) Step response of the same open-loop and PID-controlled system. The black dotted line marks the target position. The damping coefficient was $\lambda = 0.25$ in both systems and the control parameter are set arbitrarily to $K_d = 0.02$, $K_p = 2$, $K_i = 400$.

A.8 | WHITE NOISE IN DYNAMICAL SYSTEMS

One can ask the question, what happens to a random process if it transmits a dynamical system or more specific, what happens to its statistical measures like the expectation values and variances? An answer to the properties of white noise propagating through a time-dependent linear system is found by the *Lyapunov equation*, which should be motivated in this section. Consider the linear but time-dependent system of the form

$$\dot{\mathbf{x}}(t) = \mathbf{A}(t)\mathbf{x}(t) + \mathbf{B}_\nu(t)\boldsymbol{\nu}(t) . \quad (\text{A.67})$$

Here, the driving term of the system is $\boldsymbol{\nu}(t)$, a wide sense stationary, white noise with zero mean and covariance $\mathbf{R}_\nu(\tau) = \mathbf{V}(\tau)\delta(\tau)$. $\mathbf{V}(\tau)$ is called *covariance amplitude*. The time-dependent process variance matrix is written as

$$\mathbf{Q}(t) = \mathcal{E}(\mathbf{x}(t)\mathbf{x}^T(t)) , \quad (\text{A.68})$$

and the initial conditions are given by a finite expectation value and covariance,

$$\mathcal{E}(\mathbf{x}(t_0)) = \mathbf{m}_0 \quad \text{and} \quad (\text{A.69})$$

$$\mathcal{E}(\mathbf{x}(t_0)\mathbf{x}^T(t_0)) = \mathbf{Q}(t_0) . \quad (\text{A.70})$$

For a time-dependent linear process, the solution is

$$\mathbf{x}(t) = \phi(t_1, t_0)\mathbf{x}(t_0) + \int_{t_0}^t \phi(t, \tau)\mathbf{B}_\nu(\tau)\boldsymbol{\nu}(\tau)d\tau , \quad (\text{A.71})$$

with the *state transition matrix* $\phi(t, \tau) = e^{\mathbf{A}(t-\tau)}$. [231] Using eq. (A.71) the following product can be calculated

$$\begin{aligned} \mathbf{x}(t_1)\mathbf{x}^T(t_2) &= \phi(t_1, t_0)\mathbf{x}(t_0)\mathbf{x}^T(t_0)\phi(t_2, t_0) + \phi(t_1, t_0)\mathbf{x}(t_0) \left[\int_{t_0}^{t_2} \phi(t_2, \tau)\mathbf{B}_\nu(\tau)\boldsymbol{\nu}(\tau)d\tau \right]^T \\ &\quad + \left[\int_{t_0}^{t_1} \phi(t_1, \tau)\mathbf{B}_\nu(\tau)\boldsymbol{\nu}(\tau)d\tau \right] \mathbf{x}^T(t_0)\phi^T(t_1, t_0) \\ &\quad + \left[\int_{t_0}^{t_1} \phi(t_1, \tau)\mathbf{B}_\nu(\tau)\boldsymbol{\nu}(\tau)d\tau \right] \left[\int_{t_0}^{t_2} \phi(t_2, \tau)\mathbf{B}_\nu(\tau)\boldsymbol{\nu}(\tau)d\tau \right]^T . \end{aligned} \quad (\text{A.72})$$

Taking the expectation value and making use of the delta function in the noise term, the process variance matrix is

$$\begin{aligned} \mathbf{Q}(t) &= \mathcal{E}(\mathbf{x}(t)\mathbf{x}^T(t)) \\ &= \phi(t, t_0)\mathbf{Q}(t_0)\phi^T(t, t_0) + \int_{t_0}^t \phi(t, \tau)\mathbf{B}_\nu(\tau)\mathbf{V}(\tau)\mathbf{B}_\nu^T(\tau)\phi^T(t, \tau)d\tau . \end{aligned} \quad (\text{A.73})$$

This can be converted to a differential equation, called the *time-dependent Lyapunov equation*, by differentiation with respect to time as

$$\dot{\mathbf{Q}}(t) = \mathbf{A}(t)\mathbf{Q}(t) + \mathbf{Q}(t)\mathbf{A}^T(t) + \mathbf{B}_\nu(t)\mathbf{V}(t)\mathbf{B}_\nu^T(t) . \quad (\text{A.74})$$

The time-dependent Lyapunov equation describes the propagation of white noise through a dynamic system. However, non-white noise processes may behave differently. For time-invariant, stable systems, eq. (A.74) reduces to the *Lyapunov (matrix) equation*

$$\mathbf{A}\mathbf{Q}_\infty + \mathbf{Q}_\infty\mathbf{A}^T + \mathbf{B}_\nu\mathbf{V}\mathbf{B}_\nu^T = 0 . \quad (\text{A.75})$$

The solution \mathbf{Q}_∞ of eq. (A.75) is the steady-state value of the process variance, and it is equal to the long time limit of $\mathbf{Q}(t)$ written as

$$\mathbf{Q}_\infty = \lim_{t \rightarrow \infty} \mathbf{Q}(t) = \int_0^\infty e^{\mathbf{A}\tau}\mathbf{B}_\nu\mathbf{V}\mathbf{B}_\nu^T e^{\mathbf{A}^T\tau}d\tau . \quad (\text{A.76})$$

B | ANOMALOUS DIFFUSION MODELS

B.1 | CONTINUOUS-TIME RANDOM WALK

The *continuous-time random walk* (CTRW) model is a direct generalization of the standard random walk. It was initially developed in the field of amorphous semiconductors to describe the motion of charge carriers.[234, 235] Today, CTRW is frequently used to describe phenomena in very different scientific fields, e.g., microscopic particle motion in actin networks[236], (macroscopic) tracer motion in hydrogeological formations[237, 238], or single share prices in high-frequency trading[239]. Like the ordinary random walk, steps Δr in a CTRW are independent and identically distributed with the probability density function $\lambda_{\text{ctrw}}(\Delta r)$. The extension to Brownian motion lies in the introduction of an additional random variable, which is a waiting time τ between consecutive steps drawn from the waiting time distribution $\psi_{\text{ctrw}}(\tau)$. One can define a characteristic waiting time as

$$\tilde{\tau} = \mathcal{E}(\tau) = \int_0^\infty \tau \psi_{\text{ctrw}}(\tau) d\tau, \quad (\text{B.1})$$

which diverges for an underlying asymptotic power-law distribution $\psi_{\text{ctrw}}(\tau) \sim 1/\tau^{1+\alpha}$ with $\alpha \in]0; 1[$. [110] Free motion obeying these statistics appears subdiffusive in the ensemble average indicated by an ensemble-averaged MSD scaling with $\sim \tau^\alpha$. This can be viewed from that point that as time passes, more and more long waiting times accumulate, and the particles under investigation freeze in their movement. Due to this aging effect, the prerequisites for ergodicity are violated, and time-averages may differ. In fact, the time-averaged MSD of particles undergoing CTRW in free space scales linearly in lag time τ . CTRW obeys the diffusion equation written as

$$\frac{\partial}{\partial t} \mathcal{P}_{\text{ctrw}}(r, t) = D_\alpha \frac{\partial^{1-\alpha}}{\partial t^{1-\alpha}} \frac{\partial^2}{\partial r^2} \mathcal{P}_{\text{ctrw}}(r, t), \quad (\text{B.2})$$

This is a fractional partial differential equation, called *fractional diffusion equation*, using the *Riemann-Liouville fractional operator*, which is defined by its influence on a time-dependent function $f(t)$ as

$$\frac{\partial^{-\lambda}}{\partial t^{-\lambda}} f(t) = \frac{1}{\Gamma(\lambda)} \int_0^t \frac{f(t')}{(t-t')^{1-\lambda}} dt' \quad (\text{B.3})$$

with the real number $\lambda \in]0; 1[$. Note the validity of the property $\frac{\partial^{1-\lambda}}{\partial t^{1-\lambda}} f(t) = \frac{\partial}{\partial t} \frac{\partial^{-\lambda}}{\partial t^{-\lambda}} f(t)$. [240] As eq. (B.2) contains a memory kernel, its solution $\mathcal{P}_{\text{ctrw}}(x, t)$ is non-Gaussian. The exact result was expressed in terms of a *Fox H-function* or a *one-sided Lévy stable distribution*. [241, 242] However, it's easier to write down the transformation into s -space, where the propagator appears as a stretched Gaussian with the distinct features of a cusp at

$r = 0$, noted as[243]

$$\mathcal{P}_{\text{ctrw}}(x, s) = \frac{s^{\alpha/2-1}}{\sqrt{4D_\alpha}} \exp\left\{-\frac{|r|s^{\alpha/2}}{\sqrt{D_\alpha}}\right\}. \quad (\text{B.4})$$

The connection between the waiting-time $\psi_{\text{ctrw}}(\tau)$, the jump length distribution $\lambda_{\text{ctrw}}(\Delta x)$, and the particle's joint probability density function satisfying eq. (B.2) can be found in [244].

In fig. B.1, an example of a single CTRW realization is depicted. Data are simulated according to the algorithm proposed in [245], yielding a trace with periods of no motion and sudden large steps. Those long, fully immobilized time periods that appear in an ideal CTRW are not observed in all experimental scenarios. For example, in SPT data, localization uncertainties overlay the stalled particle motion. In theoretical models or simulations, Ornstein-Uhlenbeck noise may be added to a native subdiffusive CTRW process to attribute to that localization noise. The associated expectation of the time-averaged MSD becomes

$$\text{MSD}_{\text{noisy-ctrw}}(\tau) \approx \frac{2D_\alpha}{\Gamma(1+\alpha)} \frac{\tau}{T^{1-\alpha}} + \frac{2\nu_{\text{ou}}^2 D}{k_{\text{ou}}} (1 - e^{-k_{\text{ou}}\tau}) \quad (\text{B.5})$$

with noise amplitude ν_{ou} and the inverse noise relaxation time-scale k_{ou} . [246]

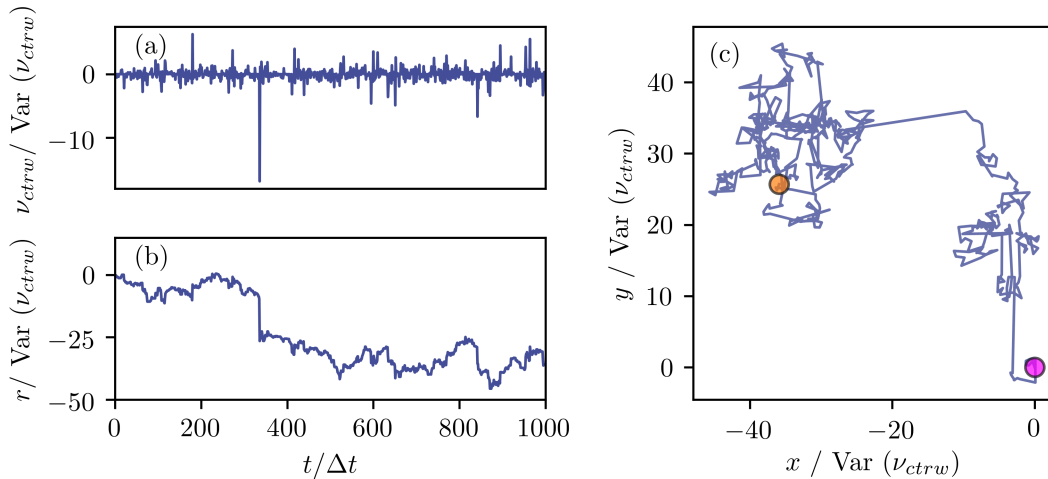


Figure B.1.: Normalized example of a continuous-time random walk. (a) Noise term $\nu_{\text{ctrw}} = \partial r / \partial t$ that drives the particle's motion. (b) Time series of the particle position following subdiffusive CTRW. (c) Two-dimensional (normalized) trajectory resulting in the typical random pathway with large steps. A violet and orange sphere mark the first and the last position of the trajectory, respectively.

B.2 | FRACTIONAL BROWNIAN MOTION

Long-term memory of time series is often measured with the *Hurst exponent* $H = \alpha/2$ going back to the British physicist HAROLD EDWIN HURST. His study on measuring the long-term storage capacity of water reservoirs, particularly the River Nile, inspired MANDELBROT and VAN NESS to their pioneering work on *fractional Brownian motion* (FBM).[247] The usage of FBM is not only restricted to hydrology, but also for the description of data traffic in local area networks[248–250] or for particle motion in viscoelastic or crowded environments[133, 251]. However, the suitability of FBM for economic modeling is still discussed.[252, 253] Originally, FBM was defined in terms of a stochastic integral

$$r(t) = \frac{1}{\Gamma\left(\frac{1+\alpha}{2}\right)} \left\{ \int_0^t (t-t')^{(\alpha-1)/2} d\mathcal{B}(t') + \int_{-\infty}^0 \left[(t-t')^{(\alpha-1)/2} - (-t')^{(\alpha-1)/2} d\mathcal{B}(t') \right] \right\}, \quad (\text{B.6})$$

with the ordinary Brownian motion process $\mathcal{B}(t)$. As it is difficult to interpret an integral with a random integrator, a more intuitive representation is given by a Langevin equation for the overdamped case,

$$\dot{r}(t) = \nu_{\text{fgn}}(t). \quad (\text{B.7})$$

Here, *fractional Gaussian noise* $\nu_{\text{fgn}}(t)$ is introduced that is normally distributed, but power-law correlated in time[110] written as

$$\mathcal{E}(\nu_{\text{fgn}}(t)) = 0 \quad \text{and} \quad (\text{B.8})$$

$$\mathcal{E}(\nu_{\text{fgn}}(t)\nu_{\text{fgn}}(t')) = \alpha\tilde{D}_\alpha |t-t'|^{\alpha-2} + 2\alpha\tilde{D}_\alpha |t-t'|^{\alpha-1} \delta(t-t'). \quad (\text{B.9})$$

For $\alpha \in]1, 2[$, the noise is positively correlated or called *persistent* and for the opposite case, $\alpha \in]0, 1[$, it is negatively correlated or called *antipersistent*. Thus, FBM is subdiffusive if the noise is antipersistent.[254] From eq. (B.9), the position autocorrelation can be derived as

$$\mathcal{E}(r(t)r(t')) = \tilde{D}_\alpha \left(t^\alpha + t'^\alpha - |t-t'|^\alpha \right). \quad (\text{B.10})$$

The diffusion equation for FBM is given as

$$\frac{\partial}{\partial t} \mathcal{P}_{\text{fbm}}(r, t) = \alpha\tilde{D}_\alpha t^{\alpha-1} \frac{\partial^2}{\partial x^2} \mathcal{P}_{\text{fbm}}(x, t). \quad (\text{B.11})$$

This equation is, in fact, local in time containing no memory kernel. Instead, a time-dependent diffusion coefficient $\tilde{D}(t) = \alpha\tilde{D}_\alpha t^{\alpha-1}$ creates non-Markovian behavior. It turns out that the probability density function of FBM is of Gaussian shape

$$\mathcal{P}_{\text{fbm}}(r, t) = \frac{1}{\sqrt{4\pi\tilde{D}_\alpha t^\alpha}} \exp\left(-\frac{r^2}{4\tilde{D}_\alpha t^\alpha}\right). \quad (\text{B.12})$$

Using eq. (B.12) and eq. (B.10), the time- and ensemble-averaged MSD can be calculated and compared. Both scales according to eq. (2.26) and ergodicity is fulfilled. In fig. B.2, a realization of a subdiffusive FBM pathway is generated with the simulation method proposed by HOSKING.[255] Due to the antipersistent noise, the motion appears a lot more correlated than Brownian motion.

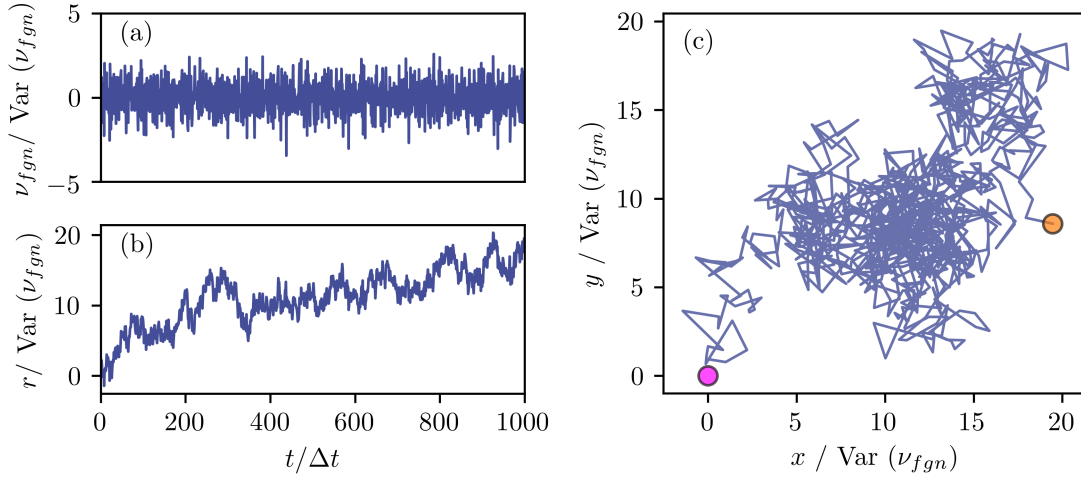


Figure B.2.: Normalized example of a fractional Brownian motion walk. (a) Normalized fractional Gaussian noise ν_{fgn} that drives the particles motion. Hurst exponent H was set to 0.3, corresponding to antipersistent noise ($\alpha = 0.6$) (b) Time series of the particle position following subdiffusive FBM. (c) Two-dimensional (normalized) trajectory resulting in the typical random pathway with large steps. A violet and orange sphere mark the first and the last position of the trajectory, respectively.

B.3 | FRACTIONAL LANGEVIN EQUATION

For FBM, the fractional Gaussian noise is considered external, and thus, the fluctuation-dissipation theorem breaks down. In the work by LUTZ, a *fractional Langevin equation* (FLE) is introduced that describes similar non-Markovian behavior, but obeys a generalized version of the fluctuation-dissipation theorem.[256] Starting with a random-matrix Hamiltonian approach, LUTZ *et al.* derived a *generalized Langevin equation* for a particle of mass m exposed to correlated noise $\tilde{\nu}(t)$

$$m\ddot{r}(t) = -\xi_\alpha \int_0^t \mathcal{K}(t-t')\dot{r}(t')dt' + \tilde{\nu}(t) . \quad (\text{B.13})$$

Here, the *generalized friction coefficient* ξ_α of physical dimension $\text{kg s}^{-\alpha}$ was introduced. The memory kernel $\mathcal{K}(t-t')$ satisfies the *second fluctuation-dissipation theorem*

$$\mathcal{E}(\tilde{\nu}(t)\tilde{\nu}(t')) = k_B \mathcal{F}\tilde{\xi}\mathcal{K}(t-t') , \quad (\text{B.14})$$

connecting the friction and memory kernel with the correlation of the noise. For fractional Gaussian noise, the memory kernel becomes $\mathcal{K}_{fgn}(t-t') = (t-t')^{\alpha-2}$, and the generalized Langevin equation can be written as a *fractional Langevin equation*

$$m\ddot{r}(t) = -\xi_\alpha \frac{\partial^{\alpha-1}}{\partial t^{\alpha-1}} \dot{r}(t) + \tilde{\eta}\nu_{fgn}(t) . \quad (\text{B.15})$$

For the sake of consistency, the Riemann-Liouville fractional operator (see eq. (B.3)) was used, instead of the Caputo fractional derivative definition that appears favored by many

other authors.[110, 254, 257] The coupling constant $\tilde{\eta}$ imposed by eq. (B.14) is

$$\tilde{\eta} = \sqrt{\frac{k_B \mathcal{T} \xi_\alpha}{\tilde{D}_\alpha \alpha (\alpha - 1)}} \quad (\text{B.16})$$

with the physical dimension kg s^{-1} . Utilizing the FLE to calculate a particle's MSD in free space, ergodic behavior is obtained, and the MSD arises as

$$\text{MSD}_{\text{FLE}} = \frac{2k_B \mathcal{T}}{m} \tau^2 E_{\alpha,3} \left(-\Gamma(\alpha - 1) \frac{\xi_\alpha}{m} \tau^\alpha \right). \quad (\text{B.17})$$

The appearing *generalized Mittag-Leffler function* $E_{a,b}(x)$ is defined by

$$E_{a,b}(x) = \sum_{n=0}^{\infty} \frac{x^n}{\Gamma(an + b)}. \quad (\text{B.18})$$

On short time scales $\tau \ll (m/\xi_\alpha)^{1/\alpha}$, the MSD scales ballistically with τ^2 and proportional to $\tau^{2-\alpha}$ for longer lag times $\tau \gg (m/\xi_\alpha)^{1/\alpha}$. In contrast to FBM, subdiffusive behavior is obtained for persistent noise $\alpha \in]1; 2[$.

C | METHODOLOGICAL DETAILS

C.1 | MOLECULE DETECTION EFFICIENCY FUNCTION

In section 3.1, a representation of the molecule detection efficiency function (MDF) as a modified Gaussian-Lorentzian profile was introduced and used to model the detected particle emission rate within the SPOT setup . Here, its emerge in the description of fluorescence signals will be motivated.

The intensity profile of a laser beam focused to position \mathbf{r}_L is given as $I_{\text{exc}}(\mathbf{r}_L, \mathbf{r})$ and moderately excites a distribution of chromophores described by the concentration profile $c(t, \mathbf{r})$ to emit fluorescence with the rate distribution

$$\mathfrak{F}(\mathbf{r}_L, \mathbf{r}, t) = \eta_Q I_{\text{exc}}(\mathbf{r}_L, \mathbf{r}) c(t, \mathbf{r}). \quad (\text{C.1})$$

Here, the symbol η_Q accounts for absorbance and quantum yield of the chromophores. The emission signal is partially collected by the microscope optics and projected to an image plane. Those optical components can be described by the microscopes *point-spread function* $\text{PSF}(\mathbf{r} - \mathbf{r}')$, assumed to be normalized with the factor ζ_{PSF}^{-1} . The fluorescence rate distribution in the image plane is

$$\tilde{\mathfrak{F}}(\mathbf{r}_L, \mathbf{r}, t) = \zeta_{\text{PSF}}^{-1} \int \mathfrak{F}(\mathbf{r}_L, \mathbf{r}', t) \text{PSF}(\mathbf{r} - \mathbf{r}') d^3 r'. \quad (\text{C.2})$$

By placing a circular optical aperture (pinhole) in the image plane, the detectable fluorescence rate is cropped sharply, and the remaining fluorescence signal is

$$\begin{aligned} F(\mathbf{r}_L, t) &= \int \text{circ}(\mathbf{r}/a_{\odot}) \tilde{\mathfrak{F}}(\mathbf{r}_L, \mathbf{r}, t) d^3 r \\ &= \eta_Q \zeta_{\text{PSF}}^{-1} \int \text{circ}(\mathbf{r}/a_{\odot}) \int I_{\text{exc}}(\mathbf{r}_L, \mathbf{r}') c(t, \mathbf{r}') \text{PSF}(\mathbf{r} - \mathbf{r}') d^3 r' dx dy. \end{aligned} \quad (\text{C.3})$$

Here, a is the radius of the image of the aperture projected to the sample plane accounting for the microscope's magnification, and the disk function $\text{circ}(\mathbf{r})$ is defined by

$$\text{circ}(\mathbf{r}) = \begin{cases} 1 & \text{for } \sqrt{x^2 + y^2} \leq 1 \\ 0 & \text{for } \sqrt{x^2 + y^2} > 1 \end{cases}, \quad (\text{C.4})$$

using that $\mathbf{r} = (x, y, z)$. Rearranging eq. (C.3) allows to identify functions defined in the literature. QIAN *et al.*[258] and RIGLER *et al.*[259] defined the *collection efficiency amplitude* $\kappa(\mathbf{r}')$ as

$$\kappa(\mathbf{r}') = \zeta_{\text{PSF}}^{-1} \int \text{circ}(\mathbf{r}/a) \text{PSF}(\mathbf{r} - \mathbf{r}') dx dy. \quad (\text{C.5})$$

The collection efficiency amplitude can be concatenated with the laser excitation profile

to an apparent excitation profile or better-called *molecule detection efficiency function* $\text{MDF}(\mathbf{r}_L, \mathbf{r}')$ [143, 258, 259] and is written as

$$\text{MDF}(\mathbf{r}_L, \mathbf{r}') = \eta_Q \kappa(\mathbf{r}') I_{\text{exc}}(\mathbf{r}_L, \mathbf{r}') . \quad (\text{C.6})$$

Inserting this into eq. (C.3) yields a simple relation between the detected fluorescence rate and the chromophore distribution in the sample plane

$$F(t) = \int \text{MDF}(\mathbf{r}_L, \mathbf{r}') c(t, \mathbf{r}') d^3r . \quad (\text{C.7})$$

C.2 | STATISTICAL PROPERTIES OF THE POSITION ESTIMATOR

In section 3.2 the particle position estimator is introduced without a proper derivation, which should be now be made up for. Starting with the statistical properties of a measured photon trace realization, the expectation value of its sine, cosine and square wave transformed are calculated for the SPOT scenario. Those transformed quantities of the photon traces can be obtained in an experiment and relate to the particle position. Thus, they can be rearranged to constitute the desired position estimator. For the readers convenience, some expression from the main text in section 3.2 are repeated in the following section.

A photon trace $\Upsilon(t) = \sum_i \delta(t - t_i)$ (see section 3.2) is characterized by the expectation value and covariance

$$\mathcal{E}(\Upsilon(t)) = F(t) , \quad \text{and} \quad (\text{C.8})$$

$$\mathcal{E}(\Upsilon(t_1)\Upsilon(t_2)) = F(t_1)F(t_2) + F(t_1)\delta(t_1 - t_2) . \quad (\text{C.9})$$

A Fourier integral defines the signal component at angular frequency ω as

$$\Upsilon_t(\omega) = \int_{t_0}^{t_0+\tau} \Upsilon(t') e^{-j\omega t'} dt' . \quad (\text{C.10})$$

The index t indicates that the frequency component of the signal depends on the selected time interval $[t_0; t_0 + \tau]$ since $\Upsilon(t)$ is a random process. Eq. (C.8) can be used to calculate the expectation value of $\Upsilon_t(\omega)$ as

$$\mathcal{E}(\Upsilon_t(\omega)) = \int_{t_0}^{t_0+\tau} \mathcal{E}(\Upsilon(t')) e^{-j\omega t'} dt' = \int_{t_0}^{t_0+\tau} F(t') e^{-j\omega t'} dt' = F_t(\omega) . \quad (\text{C.11})$$

In practice, a small signal chunk $\Upsilon(t')$ for $t' \in [t_0; t_0 + \tau]$ is recorded, and phase-sensitive lock-in integration provides the cosine and sine transformation of the signal as the in-phase and quadrature signals for a particular frequency ω . Dissecting the Fourier transformation into cosine and sine transformation as the real and imaginary part of a complex number (imaginary unit: j) with the Euler formula,

$$e^{jz} = \cos(z) + j \sin(z) , \quad (\text{C.12})$$

helps to relate the calculated expectation value to the experimentally accessible quantities

$$\begin{aligned}\Upsilon_t(\omega) &= \int_{t_0}^{t_0+\tau} \Upsilon(t') \cos(\omega t') dt' - j \int_{t_0}^{t_0+\tau} \Upsilon(t') \sin(\omega t') dt' \\ &= \mathcal{C} \{ \Upsilon(t') \} (\omega) - i\mathcal{S} \{ \Upsilon(t') \} (\omega) .\end{aligned}\quad (\text{C.13})$$

For 3D-SPOT, the fluorescence rate of the particle fixed at \mathbf{r}_p is modulated externally and position-dependent with carrier frequencies ω_0 and $\omega_0/2$. A laser focus scanned specifically along the pathway eq. (3.8) creates the modulation. The microscopes MDF is modeled with the modified Gaussian-Lorentzian shape eq. (3.1) yielding the fluorescence-rate given by eq. (3.10). Thus, the integration time is selected to $\tau = 2Tn_{sp}$ with n_{sp} being the number of total beam scan periods of duration $2T = 4\pi/\omega_0$. One looks for a closed-form expression of

$$F_{S,t}(\omega, \mathbf{r}_p) = \int_{t_0}^{t_0+2Tn_{sp}} F_S(t', \mathbf{r}_p) e^{-j\omega t'} dt , \quad (\text{C.14})$$

for the integer numbers of the carrier frequency $\omega = k\omega_0$. Therefore, the fluorescence rate expression for 3D-SPOT (see eq. (3.10) in the main text) is converted to cylinder coordinates $\mathbf{r}_p = (x_p, y_p, z_p) = (\rho_p \cos(\varphi_p), \rho_p \sin(\varphi_p), z_p)$ with the help of an addition theorem.

$$F_S(t, \mathbf{r}_p) = \frac{F_0 w_{xy}^2 \kappa(z_p)}{w^2(z_p - \frac{d_z}{2} \text{sqw}(\frac{\omega}{2}t))} \exp \left\{ -\frac{2 \left[\rho_p^2 + 2R\rho_p \cos(\varphi_p - \omega_0 t) + R^2 \right]}{w^2(z_p - \frac{d_z}{2} \text{sqw}(\frac{\omega}{2}t))} \right\} \quad (\text{C.15})$$

The notation is easier after defining constant beam waists and amplitudes,

$$w_{1,2}(z_p) = w_{xy} \sqrt{1 + \frac{(z_p \mp \frac{d_z}{2})^2}{w_z^2}} \quad \text{and} \quad (\text{C.16})$$

$$A_l(\rho_p, z_p) = \frac{F_0 w_{xy}^2 \kappa(z_p)}{w_l^2(z_p)} \exp \left[-\frac{2(\rho_p^2 + R^2)}{w_l^2(z_p)} \right]. \quad (\text{C.17})$$

Using these four definitions, the integral over the fluorescence rate is split into time intervals, where the z -coordinate of the laser focus is constant:

$$\begin{aligned}F_{S,t}(k\omega_0, \mathbf{r}_p) &= n_{sp} \left[A_1(\rho_p, z_p) \int_{t_0}^{t_0+T} \exp \left[-\frac{4R\rho_p \cos(\varphi_p - \omega_0 t)}{w_1^2(z_p)} \right] e^{-ik\omega_0 t} dt \right. \\ &\quad \left. + A_2(\rho_p, z_p) \int_{t_0+T}^{t_0+2T} \exp \left[-\frac{4R\rho_p \cos(\varphi_p - \omega_0 t)}{w_2^2(z_p)} \right] e^{-ik\omega_0 t} dt \right].\end{aligned}\quad (\text{C.18})$$

A useful integral,

$$\frac{1}{2\pi} \int_0^{2\pi} \exp \{ p \cos(\xi) + q \sin(\xi) + jm\xi \} d\xi = \exp \{ jm \underline{\angle p + iq} \} I_m \left(\sqrt{p^2 + q^2} \right) , \quad (\text{C.19})$$

will help to evaluate eq. (C.18). Here, $I_m(x)$ is m -th order modified Bessel function of first kind and argument x . The symbol $\underline{\angle z}$ notes the phase angle of the complex number z . Substituting the integration variable with $\omega_0(t' - t_0)$ in eq. (C.18) and selecting t_0 such that $\cos(\omega_0 t_0) = 1$ and $\sin(\omega_0 t_0) = 0$, these integrals are solved with the help of eq. (C.19)

as

$$F_{S,t}(k\omega_0, \mathbf{r}_p) = Tn_{sp}e^{-ik\varphi_p} \left[A_1(\rho_p, z_p)I_{-k}\left(\frac{4R\rho_p}{w_1^2(z_p)}\right) + A_2(\rho_p, z_p)I_{-k}\left(\frac{4R\rho_p}{w_2^2(z_p)}\right) \right]. \quad (\text{C.20})$$

The two signal parts that do not depend on the particle's azimuthal angle φ_p will be defined as

$$\Omega_{l,t}^{(k)}(\rho_p, z_p) = A_l(\rho_p, z_p)I_k\left(\frac{4R\rho_p}{w_l^2(z_p)}\right), \quad (\text{C.21})$$

to shorten the notation further. Now the expectation of the cosine and sine transformation of the measured photon traces are written in a closed analytical form as

$$\mathcal{E}(\mathcal{C}\{\Upsilon(t, \mathbf{r}_p)\}(\omega_0)) = \text{Re}\{F_{S,t}(\omega_0, \mathbf{r}_p)\} = Tn_{sp}\cos(\varphi_p) \left[\Omega_{1,t}^{(1)}(\rho_p, z_p) + \Omega_{2,t}^{(1)}(\rho_p, z_p) \right], \quad (\text{C.22})$$

$$\mathcal{E}(\mathcal{S}\{\Upsilon(t, \mathbf{r}_p)\}(\omega_0)) = \text{Im}\{F_{S,t}(\omega_0, \mathbf{r}_p)\} = Tn_{sp}\sin(\varphi_p) \left[\Omega_{1,t}^{(1)}(\rho_p, z_p) + \Omega_{2,t}^{(1)}(\rho_p, z_p) \right]. \quad (\text{C.23})$$

For the localization of the particle in the z -direction, demodulation with a square wave is introduced

$$\mathcal{S}q\{\Upsilon(t, \mathbf{r}_p)\}(\omega_0) = \int_{t_0}^{t_0+2Tn_{sp}} \Upsilon(t', \mathbf{r}_p) \text{sqw}\left(\frac{\omega_0 t'}{2}\right) dt'. \quad (\text{C.24})$$

By splitting the integral into sections of duration T starting at t_0 , which is arbitrarily defined as the beginning of a square wave period, the expectation value can be calculated, and the integration becomes easy. Using eq. (C.19) with $m = 0$ on obtains

$$\begin{aligned} \mathcal{E}(\mathcal{S}q\{\Upsilon(t, \mathbf{r}_p)\}(\omega_0)) &= n_{sp} \left[\int_{t_0}^{t_0+T} \mathcal{E}(\Upsilon(t', \mathbf{r}_p)) dt' - \int_{t_0+T}^{t_0+2T} \mathcal{E}(\Upsilon(t', \mathbf{r}_p)) dt' \right] \\ &= n_{sp} \left[\int_{t_0}^{t_0+T} F_S(t', \mathbf{r}_p) dt' - \int_{t_0+T}^{t_0+2T} F_S(t', \mathbf{r}_p) dt' \right] \\ &= Tn_{sp} \left[A_1(\rho_p, z_p)I_0\left(\frac{4R\rho_p}{w_1^2(z_p)}\right) - A_2(\rho_p, z_p)I_0\left(\frac{4R\rho_p}{w_2^2(z_p)}\right) \right] \\ &= Tn_{sp} \left[\Omega_{1,t}^{(0)}(\rho_p, z_p) - \Omega_{2,t}^{(0)}(\rho_p, z_p) \right]. \end{aligned} \quad (\text{C.25})$$

The expression $\Omega_{l,t}^{(k)}(\rho_p, z_p)$ can be approximated for $k = 0$, $k = 1$, and $k = 2$ by expanding it as a multidimensional Taylor series around $(\rho_p, z_p) = \mathbf{0}$ that is aborted after the first-order terms of ρ_p and z_p .

$$\Omega_{l,t}^{(0)}(\rho_p, z_p) \approx F_0 \frac{w_{xy}^2}{w_c^2} \exp\left(-\frac{2R^2}{w_c^2}\right) \left[1 + (-1)^{l+1} \frac{d_z w_{xy}^2}{w_c^4 w_z^2} (w_c^2 - 2R^2) z_p \right], \quad (\text{C.26})$$

$$\Omega_{l,t}^{(1)}(\rho_p, z_p) \approx F_0 \frac{w_{xy}^2}{w_c^2} \exp\left(-\frac{2R^2}{w_c^2}\right) \frac{2R}{w_c^2} \rho_p, \quad \text{and} \quad (\text{C.27})$$

$$\Omega_{l,t}^{(2)}(\rho_p, z_p) \approx F_0 \frac{w_{xy}^2}{w_c^2} \exp\left(-\frac{2R^2}{w_c^2}\right) \frac{2R^2 \rho_p^2}{w_c^4} \left[1 + (-1)^{l+1} \frac{d_z w_{xy}^2}{w_c^4 w_z^2} (4w_c^2 - 6R^2) z_p \right]. \quad (\text{C.28})$$

Here, the lateral beam waist in the central plane of the detection w_c was defined as

$$w_c = w(d_z/2) = w(-d_z/2) = w_{xy} \sqrt{1 + \frac{d_z^2}{4w_z^2}} . \quad (\text{C.29})$$

Using these approximations, the cosine, sine, and square wave transformed of the fluorescence rate become linear in the radial and axial particle displacement ρ_p and z_p :

$$\mathcal{E}(\mathcal{C}\{\Upsilon(t, \mathbf{r}_p)\}(\omega_0)) \approx F_0 T n_{sp} \frac{w_{xy}^2}{w_c^2} \exp\left(-\frac{2R^2}{w_c^2}\right) \frac{4R}{w_c^2} \rho_p \cos(\varphi_p) , \quad (\text{C.30})$$

$$\mathcal{E}(\mathcal{S}\{\Upsilon(t, \mathbf{r}_p)\}(\omega_0)) \approx F_0 T n_{sp} \frac{w_{xy}^2}{w_c^2} \exp\left(-\frac{2R^2}{w_c^2}\right) \frac{4R}{w_c^2} \rho_p \sin(\varphi_p) , \quad \text{and} \quad (\text{C.31})$$

$$\mathcal{E}(\mathcal{S}q\{\Upsilon(t, \mathbf{r}_p)\}(\omega_0)) \approx 2T n_{sp} F_0 \frac{w_{xy}^2}{w_c^2} \exp\left(-\frac{2R^2}{w_c^2}\right) \frac{d_z w_{xy}^2}{w_c^4 w_z^2} (w_c^2 - 2R^2) z_p . \quad (\text{C.32})$$

The terms $\rho_p \cos(\varphi_p)$ and $\rho_p \sin(\varphi_p)$ are immediately identified as x_p and y_p . Because the approximations are only valid for $\rho_p/w_{xy} \ll 1$ and $R \approx w_{xy}$, wrong estimates of the particle's radial and axial coordinate are obtained on violation of this condition. Nevertheless, the particle's azimuthal angle φ_p is not affected by the linearization.

Some of the prefactors in eqns. (C.30)–(C.32) can be summarized to a quantity that is easy to interpret. Defining

$$N_{ph} = 2T n_{sp} F_0 \frac{w_{xy}^2}{w_c^2} \exp\left(-\frac{2R^2}{w_c^2}\right) , \quad (\text{C.33})$$

and calculating the integral over the entire fluorescence rate signal in the same way as before, one obtains

$$\begin{aligned} \int_{t_0}^{t_0+2Tn_{sp}} F_S(t, \mathbf{r}_p) dt' &= T n_{sp} \left[\Omega_{1,t}^{(0)}(\rho_p, z_p) + \Omega_{2,t}^{(0)}(\rho_p, z_p) \right] \\ &\approx 2T n_{sp} F_0 \frac{w_{xy}^2}{w_c^2} \exp\left(-\frac{2R^2}{w_c^2}\right) \\ &= N_{ph} . \end{aligned} \quad (\text{C.34})$$

Here, the linear approximation of $\Omega_{l,t}^{(0)}(\rho_p, z_p)$ was used again. The meaning of N_{ph} as the total number of photons if the particle would stay fixed within the origin for the entire acquisition period, is clear now. A similar definition is applied for the integral over the recorded photon trace

$$N_{ph}(t) = \int_t^{t+2Tn_{sp}} \Upsilon(t, \mathbf{r}_p) dt' . \quad (\text{C.35})$$

The expectation value of the detected number of photons is $\mathcal{E}(N_{ph}(t)) = N_{ph}$. This is very useful because N_{ph} is a quantity that is experimental accessible than F_0 and can be used to substitute some of the prefactors in eqns. (C.30)–(C.32). One obtains estimator equations for the particle position based on a transformed acquisition of the detected photon stream.

The estimated particle position $\hat{\mathbf{r}}_p = (\hat{x}_p, \hat{y}_p, \hat{z}_p)$ is defined as

$$\hat{x}_p(t) = \frac{w_c^2}{2RN_{ph}} \int_t^{t+2Tn_{sp}} \Upsilon(t', \mathbf{r}_p) \cos(\omega_0 t') dt' , \quad (\text{C.36})$$

$$\hat{y}_p(t) = \frac{w_c^2}{2RN_{ph}} \int_t^{t+2Tn_{sp}} \Upsilon(t', \mathbf{r}_p) \sin(\omega_0 t') dt' , \quad \text{and} \quad (\text{C.37})$$

$$\hat{z}_p(t) = \frac{w_c^4 w_z^2}{d_z w_{xy}^2 (w_c^2 - 2R^2) N_{ph}} \int_t^{t+2Tn_{sp}} \Upsilon(t', \mathbf{r}_p) \text{sqw}\left(\frac{\omega_0}{2} t'\right) dt' . \quad (\text{C.38})$$

Rearrangement yields

$$\hat{\mathbf{r}}_p(t) = \begin{pmatrix} \hat{x}_p(t) \\ \hat{y}_p(t) \\ \hat{z}_p(t) \end{pmatrix} = N_{ph}^{-1} \int_{t_0}^{t_0+\tau} \Upsilon(t', \mathbf{r}_p) \begin{pmatrix} \frac{w_c^2}{2R_y} \cos(\omega_0 t) \\ \frac{w_c^2}{2R_x} \sin(\omega_0 t) \\ \frac{w_c^4 w_z^2}{d_z w_{xy}^2 (w_c^2 - 2R^2)} \text{sqw}\left(\frac{\omega_0}{2} t\right) \end{pmatrix} \quad (\text{C.39})$$

$$= N_{ph}^{-1} \int_{t_0}^{t_0+\tau} \Upsilon(t', \mathbf{r}_p) \mathbf{demod}(t') dt' , \quad (\text{C.40})$$

by defining the *demodulation vector function* $\mathbf{demod}(t')$ as

$$\mathbf{demod}(t) = \begin{pmatrix} \frac{w_c^2}{2R_y} \cos(\omega_0 t) \\ \frac{w_c^2}{2R_x} \sin(\omega_0 t) \\ \frac{w_c^4 w_z^2}{d_z w_{xy}^2 (w_c^2 - 2R^2)} \text{sqw}\left(\frac{\omega_0}{2} t\right) \end{pmatrix} . \quad (\text{C.41})$$

In the last section, the expectation values of the estimated particle position $\hat{\mathbf{r}}_p$ are calculated from the expectation values of the transformed recorded photon traces $\Upsilon(t, \mathbf{r}_p)$. Now the photon counting statistics should be used to calculate an expression for the variance of $\hat{\mathbf{r}}_p$. Starting with the lateral coordinates, the variance of $\Upsilon_t(\omega_0, \mathbf{r}_p)$ will be calculated first

$$\begin{aligned} \text{Var}(\mathcal{C}\{\Upsilon(t, \mathbf{r}_p)\}(\omega_0)) &= \mathcal{E}\left([\mathcal{C}\{\Upsilon(t, \mathbf{r}_p)\}(\omega_0) - \mathcal{E}(\mathcal{C}\{\Upsilon(t, \mathbf{r}_p)\}(\omega_0))\right]^2) \\ &= \mathcal{E}\left([\mathcal{C}\{\Upsilon(t, \mathbf{r}_p)\}(\omega_0)]^2\right) - \mathcal{E}(\mathcal{C}\{\Upsilon(t, \mathbf{r}_p)\}(\omega_0))^2 , \end{aligned} \quad (\text{C.42})$$

$$\text{Var}(\mathcal{S}\{\Upsilon(t, \mathbf{r}_p)\}(\omega_0)) = \mathcal{E}\left([\mathcal{S}\{\Upsilon(t, \mathbf{r}_p)\}(\omega_0)]^2\right) - \mathcal{E}(\mathcal{S}\{\Upsilon(t, \mathbf{r}_p)\}(\omega_0))^2 \quad \text{and} \quad (\text{C.43})$$

$$\text{Var}(\mathcal{S}q\{\Upsilon(t, \mathbf{r}_p)\}(\omega_0)) = \mathcal{E}\left([\mathcal{S}q\{\Upsilon(t, \mathbf{r}_p)\}(\omega_0)]^2\right) - \mathcal{E}(\mathcal{S}q\{\Upsilon(t, \mathbf{r}_p)\}(\omega_0))^2 . \quad (\text{C.44})$$

The real and imaginary part of the Fourier transformed photon traces $\Upsilon_t(\omega_0, \mathbf{r}_p)$ can be expressed by its complex conjugated $\Upsilon_t^*(\omega_0, \mathbf{r}_p)$ as

$$\mathcal{C}\{\Upsilon(t, \mathbf{r}_p)\}(\omega_0) = \text{Re}\{\Upsilon_t(\omega_0, \mathbf{r}_p)\} = \left[\frac{\Upsilon_t(\omega_0, \mathbf{r}_p) + \Upsilon_t^*(\omega_0, \mathbf{r}_p)}{2} \right] , \quad \text{and} \quad (\text{C.45})$$

$$\mathcal{S}\{\Upsilon(t, \mathbf{r}_p)\}(\omega_0) = \text{Im}\{\Upsilon_t(\omega_0, \mathbf{r}_p)\} = \left[\frac{\Upsilon_t(\omega_0, \mathbf{r}_p) - \Upsilon_t^*(\omega_0, \mathbf{r}_p)}{2i} \right] . \quad (\text{C.46})$$

Because it is necessary for the following considerations to express the expectation value of the square of the transformed photon trace and the absolute squared photon trace by the transformed fluorescence rates, this calculation will be conducted first. One obtains for the

expectation value of the square of the transformed photon trace

$$\begin{aligned}
 \mathcal{E}(\Upsilon_t(\omega_0, \mathbf{r}_p)^2) &= \mathcal{E}\left(\int_{t_0}^{t_0+2Tn_{sp}} \Upsilon(t', \mathbf{r}_p) e^{-i\omega_0 t'} dt' \int_{t_0}^{t_0+2Tn_{sp}} \Upsilon(t'', \mathbf{r}_p) e^{-j\omega_0 t''} dt''\right) \\
 &= \int_{t_0}^{t_0+2Tn_{sp}} e^{-j\omega_0 t'} \int_{t_0}^{t_0+2Tn_{sp}} e^{-j\omega_0 t''} \mathcal{E}(\Upsilon(t', \mathbf{r}_p) \Upsilon(t'', \mathbf{r}_p)) dt'' dt' \\
 &= \int_{t_0}^{t_0+2Tn_{sp}} e^{-j\omega_0 t'} \int_{t_0}^{t_0+2Tn_{sp}} e^{-j\omega_0 t''} [F_S(t', \mathbf{r}_p) F_S(t'', \mathbf{r}_p) \\
 &\quad + F_S(t', \mathbf{r}_p) \delta(t' - t'')] dt'' dt' \\
 &= \int_{t_0}^{t_0+2Tn_{sp}} F_S(t', \mathbf{r}_p) e^{-j\omega_0 t'} dt' \int_{t_0}^{t_0+2Tn_{sp}} F_S(t'', \mathbf{r}_p) e^{-j\omega_0 t''} dt'' \\
 &\quad + \int_{t_0}^{t_0+2Tn_{sp}} e^{-j2\omega_0 t'} F_S(t', \mathbf{r}_p) dt' \\
 &= F_{S,t}(\omega_0, \mathbf{r}_p)^2 + F_{S,t}(2\omega_0, \mathbf{r}_p)
 \end{aligned} \tag{C.47}$$

and analogously for the absolute square

$$\begin{aligned}
 \mathcal{E}(|\Upsilon_t(\omega_0, \mathbf{r}_p)|^2) &= \mathcal{E}\left(\int_{t_0}^{t_0+2Tn_{sp}} \Upsilon(t', \mathbf{r}_p) e^{-i\omega_0 t'} dt' \int_{t_0}^{t_0+2Tn_{sp}} \Upsilon(t'', \mathbf{r}_p) e^{i\omega_0 t''} dt''\right) \\
 &= |F_{S,t}(\omega_0, \mathbf{r}_p)|^2 + F_{S,t}(0, \mathbf{r}_p) .
 \end{aligned} \tag{C.48}$$

Using eq. (C.45), eq. (C.46) and eq. (C.48) the expectation of the squared real part becomes

$$\begin{aligned}
 \mathcal{E}(\text{Re}\{\Upsilon_t(\omega_0, \mathbf{r}_p)\}^2) &= \frac{1}{4} [\mathcal{E}(\Upsilon_t(\omega_0, \mathbf{r}_p)^2) + 2\mathcal{E}(|\Upsilon_t(\omega_0, \mathbf{r}_p)|) + \mathcal{E}(\Upsilon_t^*(\omega_0, \mathbf{r}_p))^2] \\
 &= \frac{1}{4} [F_{S,t}(\omega_0, \mathbf{r}_p)^2 + F_{S,t}(2\omega_0, \mathbf{r}_p) + 2(|F_{S,t}(\omega_0, \mathbf{r}_p)| + F_{S,t}(0, \mathbf{r}_p)) \\
 &\quad + F_{S,t}^*(\omega_0, \mathbf{r}_p)^2 + F_{S,t}^*(2\omega_0, \mathbf{r}_p)] ,
 \end{aligned} \tag{C.49}$$

and an analogous equation holds true for the imaginary part. Finally, the variances for the cosine and sine transformed signal is

$$\text{Var}(\mathcal{C}\{\Upsilon(t, \mathbf{r}_p)\}(\omega_0)) = \frac{1}{4} [F_{S,t}(2\omega_0, \mathbf{r}_p) + F_{S,t}^*(2\omega_0, \mathbf{r}_p) + F_{S,t}(0, \mathbf{r}_p)] , \quad \text{and} \tag{C.50}$$

$$\text{Var}(\mathcal{S}\{\Upsilon(t, \mathbf{r}_p)\}(\omega_0)) = \frac{1}{4} [F_{S,t}(2\omega_0, \mathbf{r}_p) + F_{S,t}^*(2\omega_0, \mathbf{r}_p) - F_{S,t}(0, \mathbf{r}_p)] . \tag{C.51}$$

These equations can be used to calculate the variance of the lateral particle position estimator. The integration rule eq. (C.19) helps again for the evaluation of the occurring integrals, and eq. (C.26) and eq. (C.28) can be used to simplify the expressions for particles

close to the origin:

$$\begin{aligned}
 \text{Var}(\hat{x}_p) &= \left(\frac{w_c^2}{2RN_{ph}} \right)^2 \left[\mathcal{E} \left([C \{ \Upsilon_t(\omega_0, \mathbf{r}_p) \} (\omega_0)]^2 \right) - \mathcal{E} \left(C \{ \Upsilon_t(\omega_0, \mathbf{r}_p) \} (\omega_0) \right)^2 \right] \\
 &= \left(\frac{w_c^2}{2RN_{ph}} \right)^2 \frac{Tn_{sp}}{2} \left\{ \left[\Omega_{1,t}^{(2)}(\rho_p, z_p) + \Omega_{2,t}^{(2)}(\rho_p, z_p) \right] \cos(2\varphi_p) \right. \\
 &\quad \left. + \left[\Omega_{1,t}^{(0)}(\rho_p, z_p) + \Omega_{2,t}^{(0)}(\rho_p, z_p) \right] \right\} \\
 &\approx \left(\frac{w_c^2}{R\sqrt{8N_{ph}}} \right)^2 .
 \end{aligned} \tag{C.52}$$

Before inserting the expression for N_{ph} , two definitions are handy, first the integrated peak number of photons per scan period

$$N_{\max} = 2TF_0 , \tag{C.53}$$

and second the lateral scan path geometry function

$$\Lambda_{xy}(\xi_\rho, \xi_z) = \frac{(1 + \xi_z^2/4)^{3/2}}{\sqrt{8}\xi_\rho} \exp\left(\frac{\xi_\rho^2}{1 + \xi_z^2/4} \right) . \tag{C.54}$$

This dimensionless function only depends on the modulation distances scaled by the characteristic laser focus length scale along the corresponding axis. Inserting eqns. (C.53)–(C.54) into eq. (C.52) yields the localization variance in lateral direction

$$\text{Var}(\hat{y}_p) \approx \text{Var}(\hat{x}_p) \approx \left(\frac{w_{xy}\Lambda_{xy}(R/w_{xy}, d_z/w_z)}{\sqrt{N_{\max}n_{sp}}} \right)^2 . \tag{C.55}$$

This is an intuitive three-dimensional generalization of the results obtained in [51]. Next, the variance of the z -coordinate estimator has to be calculated. It traces back to evaluating the variance of the square wave transformed photon trace, which is again calculated by splitting the integrals into sections where the focus' axial position is constant. Several expectation values are necessary to calculate, beginning with the expected value for the squared photon trace of the first time interval:

$$\begin{aligned}
 \mathcal{E} \left(\left[\int_{t_0}^{t_0+T} \Upsilon(t', \mathbf{r}_p) dt' \right]^2 \right) &= \int_{t_0}^{t_0+T} \int_{t_0}^{t_0+T} \mathcal{E}(\Upsilon(t', \mathbf{r}_p)\Upsilon(t'', \mathbf{r}_p)) dt'' dt' \\
 &= \int_{t_0}^{t_0+T} \int_{t_0}^{t_0+T} [F_S(t', \mathbf{r}_p)F_S(t'', \mathbf{r}_p) + F_S(t', \mathbf{r}_p)\delta(t' - t'')] dt'' dt' \\
 &= \left[\int_{t_0}^{t_0+T} \Upsilon(t', \mathbf{r}_p) dt' \right]^2 \\
 &\quad + \int_{t_0}^{t_0+T} \Upsilon(t', \mathbf{r}_p)\Theta(t' - t_0)\Theta(T + t_0 - t') dt' \\
 &= [T\Omega_1^{(0)}(\rho_p, z_p)]^2 + T\Omega_1^{(0)}(\rho_p, z_p) .
 \end{aligned} \tag{C.56}$$

A similar result is obtained for the second time interval. Furthermore, the expectation

value for the product of both time intervals is calculated the same way yielding

$$\mathcal{E}\left(\int_{t_0}^{t_0+T} \Upsilon(t', \mathbf{r}_p) dt' \int_{t_0+T}^{t_0+2T} \Upsilon(t', \mathbf{r}_p) dt'\right) = T^2 \Omega_1^{(0)}(\rho_p, z_p) \Omega_2^{(0)}(\rho_p, z_p) . \quad (\text{C.57})$$

Therefore, the estimator variance in the axial direction is,

$$\begin{aligned} \text{Var}(\hat{z}_p) &= \left(\frac{w_c^4 w_z^2}{d_z w_{xy}^2 (w_c^2 - 2R^2) N_{ph}}\right)^2 T n_{sp}^2 \left(\Omega_1^{(0)}(\rho_p, z_p) + \Omega_2^{(0)}(\rho_p, z_p)\right) \\ &\approx \left(\frac{w_z \Lambda_z(R/w_{xy}, d_z/w_z)}{\sqrt{N_{\max}}}\right)^2 , \end{aligned} \quad (\text{C.58})$$

where the axial scan path geometry function was defined as

$$\Lambda_z(\xi_\rho, \xi_p) = \frac{(1 + \xi_z^2/4)^{5/2}}{\xi_z(1 + \xi_z^2/4 - 2\xi_\rho^2)} \exp\left(\frac{\xi_\rho^2}{1 + \xi_z^2/4}\right) . \quad (\text{C.59})$$

C.3 | DEMODULATION ON A DIGITAL SIGNAL PROCESSOR

The strength of the presented demodulation technique for real-time application and digital signal processing is that the transformation function $\mathbf{demod}(t)$ (see section 3.2) can be calculated in advance and stored as a matrix \mathcal{M} in the processors random access memory, saving computation time when the experiment is running. Furthermore, the integrals are converted to sums that can be added simultaneously to the signal acquisition with very few calculation operations needed. For this purpose, the modulation period $2T = 4\pi\omega_0^{-1}$ is dissected into n_s equidistant sampling points. This creates the discretized time scale $t = k\Delta t$ with the integer $k \in [0; n_s n_{sp}]$ used to sample the photon trace $n_{ph}[k] = F(t, \mathbf{r}_p)\Delta t$. With these parameter settings, the transformation matrix has shape $n_s n_{sp} \times 3$ and is defined as

$$\mathcal{M} = \begin{pmatrix} \text{demod}_x(0) & \text{demod}_x(\Delta t) & \dots & \text{demod}_x(n_s n_{sp} \Delta t) \\ \text{demod}_y(0) & \text{demod}_y(\Delta t) & \dots & \text{demod}_y(n_s n_{sp} \Delta t) \\ \text{demod}_z(0) & \text{demod}_z(\Delta t) & \dots & \text{demod}_z(n_s n_{sp} \Delta t) \end{pmatrix} . \quad (\text{C.60})$$

The matrix element in the k th column and j th row is therefore

$$\mathcal{M}[k, j] = \text{demod}_j(k\Delta t) . \quad (\text{C.61})$$

Estimated particle positions at times $t = i\Delta t$ and coordinate j are written as

$$\hat{r}_p[i, j] = N_{ph}[i]^{-1} \sum_{k=i}^{i+n_s n_{sp}} \mathcal{M}[k, j] n_{ph}[k] . \quad (\text{C.62})$$

In this notation, the number of detected photons is simply

$$N_{ph}[i] = \sum_{k=i}^{i+n_s n_{sp}} n_{ph}[k] . \quad (\text{C.63})$$

C.4 | MEAN SQUARED DISPLACEMENT COMPUTATION BASED ON FAST FOURIER TRANSFORMATION

For a measured trajectory given as discrete positions written as $\hat{\mathbf{r}}[k]$, the time-averaged MSD can be calculated as eq. (3.35) (see section 3.4). But this sum can also be split into a sum of correlation functions:

$$\begin{aligned} \text{MSD}[k] &= \frac{1}{N_{\text{pos}} - k} \sum_{i=0}^{N_{\text{pos}} - k - 1} \left(\hat{\mathbf{r}}^2[i + k] + \hat{\mathbf{r}}^2[i] \right) - \frac{2}{N_{\text{pos}} - k} \sum_{i=0}^{N_{\text{pos}} - k - 1} \left(\hat{\mathbf{r}}[i] \cdot \hat{\mathbf{r}}[i + k] \right) \\ &= P_1[k] - 2P_2[k] \end{aligned} \quad (\text{C.64})$$

Thereby, the second term $P_2[k]$ is the *autocorrelation function* of the position. By the Wiener-Khinchin theorem, the *power spectral density* is the Fourier transform of the autocorrelation function. Consequently, the power spectral density can be quickly calculated with the *fast Fourier transformation* (FFT) algorithm and then Fourier-inverted to obtain $P_2[k]$. To handle the non-periodicity of the discrete input signal, the data has to be zero-padded to twice the length of the signal. By doing this, the non-cyclic autocorrelation function is computed as required. The described procedure is mathematically expressed as

$$P_2[k] = \mathcal{F}^{-1} \{ \mathcal{F} \{ \hat{\mathbf{r}} \} \cdot \mathcal{F}^* \{ \hat{\mathbf{r}} \} \} . \quad (\text{C.65})$$

A recursive relation holds for $P_1[i]$ that is given by

$$P_1[k] = P_1[k - 1] - \hat{\mathbf{r}}^2[k - 1] - \hat{\mathbf{r}}^2[N_{\text{pos}} - k] \quad \text{and} \quad (\text{C.66})$$

$$P_1[0] = 2 \sum_{i=0}^{N_{\text{pos}} - 1} \hat{\mathbf{r}}^2[i] . \quad (\text{C.67})$$

While a straightforward computation of the MSD scales proportional to N_{pos}^2 , the FFT-based algorithm reduces the number of multiplications by using symmetries in the calculation. The FFT-based computation time, therefore, scales proportional to $N_{\text{pos}} \log_2(N_{\text{pos}})$, which is advantageous for large data sets, namely large N_{pos} .

C.5 | SIMULATION OF THE 3D-SPOT METHOD

Simulations are run on a Dell XPS 15 (2.2 GHz Intel Core i7-3632QM quad core, 8 Gbyte DDR3 RAM) with a 64-bit Windows 10 operating system. Code is written in Python 3.7.6 and makes extensive use of the Numpy 1.18.1[260], SciPi 1.4.1[261], lmfit 1.0.0[262], and Pandas 1.0.0[263] libraries. The SPOT setup simulation is strongly related to the block diagram in fig. C.1, and an overview of the occurring time scales is illustrated in fig. C.2. The time resolution of the simulation is chosen to correspond to a single photon sampling point of duration δt . The duration of four lateral and two axial laser focus cycles is dissected into $n_s = 32$ sampling points (Note that in the real world implementation of SPOT, the number of sampling points per position estimation cycle is $n_s = 64$). The general idea is to simulate all relevant measures on this high-resolution time scale in a loop, where each pass corresponds to a single particle position estimation. A particle is localized after each time interval of $\Delta t = n_s \cdot \delta t$, which defines the simulation result time scale that can be compared to real-world measurements. The generation of the trajectory is independent of the rest of

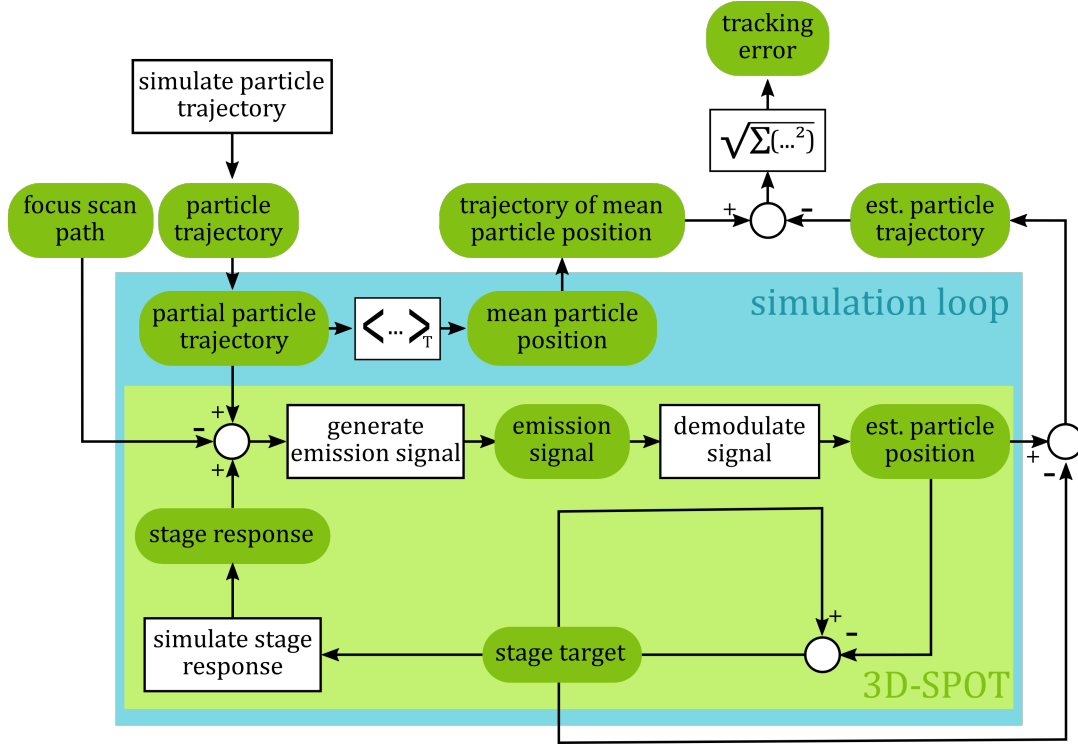


Figure C.1.: Block diagram of the simulation. For simplicity not all input and output data (e.g. the particle’s maximum photon emission rate or the beam diameter) are shown, focusing only on the main data flow.

the simulation, and therefore different scenarios can be analyzed. For the observation of a static particle, the trajectory consists of a constant position. Using the Langevin equation, the trajectory of a Brownian motion can be simulated. But also anomalous or restricted diffusion can be modeled and fed into the simulation. No matter which mode of motion should be studied, the complete trajectory is sequentially cut into subsections of n_s particle positions. The average of this partial trajectory is used to build up a trajectory of mean particle positions,

$$\bar{\mathbf{r}}[k] = \frac{1}{n_s} \sum_{i=k \cdot n_s}^{(k+1) \cdot n_s} \mathbf{r}[i]. \quad (\text{C.68})$$

Those averaged particle positions $\bar{\mathbf{r}}_p[k]$ are introduced to obtain a benchmark for the ”measured” particle position $\hat{\mathbf{r}}_p[k]$. Furthermore, the n_s particle positions are used to generate the particle’s fluorescence signal $F[i]$ during the particle position estimation cycle using eq. (3.10) assuming a Gaussian-Lorentzian laser profile. Therefore, each particle position is related to each position of the focus scan and the movement of the nanopositioning stage $\mathbf{r}_s[i]$. Thus, in eq. (3.10) the following substitution takes place:

$$\mathbf{r}_p \rightarrow \mathbf{r}_p + \mathbf{r}_s \quad (\text{C.69})$$

The actual emission signal is generated with Poisson photon counting statistics with the time-varying mean value $F[i]$. This fluorescence emission signal is demodulated with the lock-in technique eq. (3.16) using sums instead of integration, resulting in an estimate for the particle position $\hat{\mathbf{r}}_p[k]$ that is used after a given number of position estimation cycles

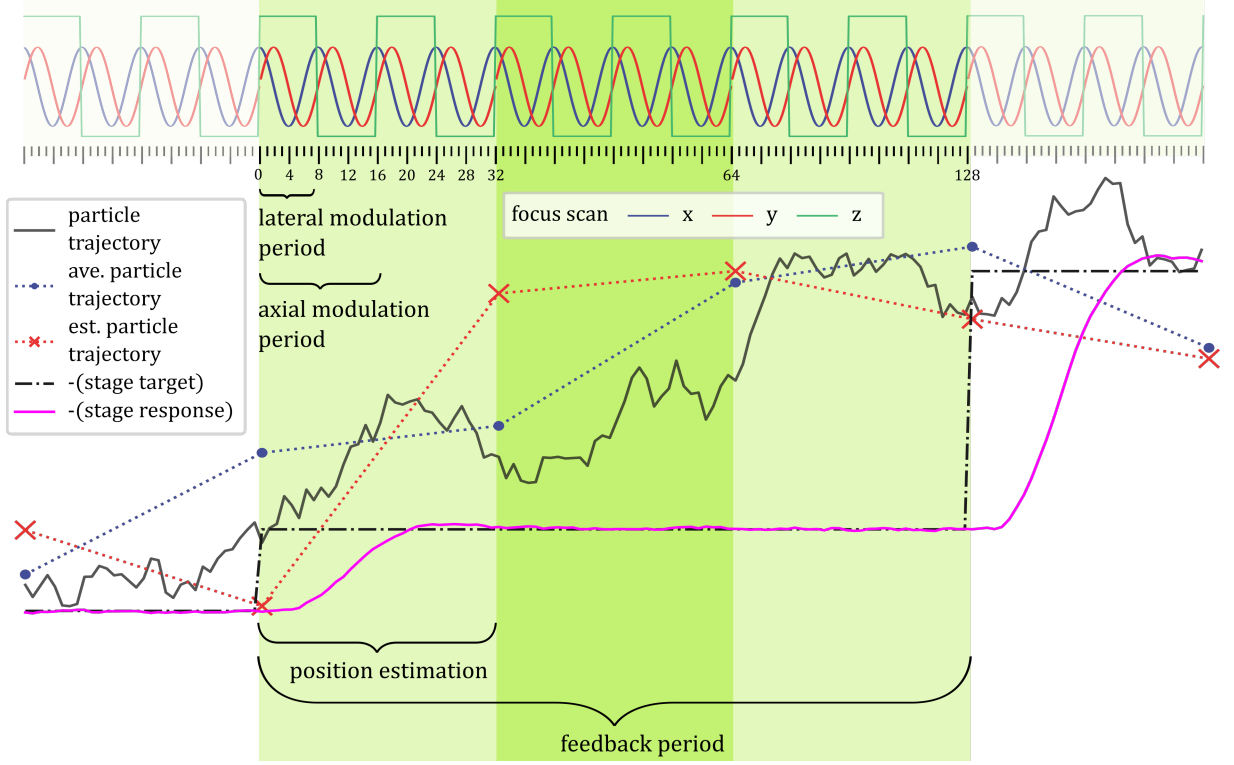


Figure C.2.: Scheme of the various time scales of the simulation. A complete position estimation period is divided into n_s equally spaced intervals (here: $n_s = 32$). Within a single position estimation period, the laser focus is scanned along the two parallel orbits twice. That means the position estimation period consists of four lateral modulation periods and two axial modulation periods. As the nanopositioning stage is slower than the desired duration of a position estimation cycle, n_{cycles} localizations are summarized to a single feedback period (here: $n_{\text{cycles}} = 3$). This defines the frequency, which is used to change the target position of the stage to a new level. Fluorescence signals, particle, and stage trajectory are simulated on the micro time scale defined by the interval δt . Since the outcome, namely the estimated trajectory, is sampled on a macro time scale defined by the position estimation period $\Delta t = n_s \delta t$, the real particle trajectory is averaged.

n_{sp} to set the feedback signal. The updated target of the stage is given as

$$\mathbf{u}_{\text{tar}}[k+1] = \mathbf{u}_{\text{tar}}[k] - \hat{\mathbf{r}}_p[k] . \quad (\text{C.70})$$

With the help of the stage-stage controller's transfer function $\mathbf{G}_{\text{sc}}[q]$, the stage target can be converted to the (deterministic) stage response $\tilde{\mathbf{r}}_s[i]$ for the next n_{cycles} loop iterations using convolution in Fourier space and taking only the real part

$$\tilde{\mathbf{r}}_s[i] = \text{Re} \left\{ \mathcal{F} \left\{ \mathbf{G}_{\text{sc}}[q] \mathbf{U}_{\text{tar}}[q] \right\}^{-1} \right\} . \quad (\text{C.71})$$

Discrete Fourier transformation is used, and the Fourier transformed of the stage target $\mathbf{U}_{\text{tar}}[q]$ is calculated from a window of the stage target positions history. The window length matches the slowest frequency in $\mathbf{G}_{\text{sc}}[q]$ and is filled with zeros if $\mathbf{u}_{\text{tar}}[i]$ is not long enough. It should be noted that also the high-frequency content must match. Consequently, $\mathbf{u}_{\text{tar}}[i]$ is generated on the δt time scale even if it varies a lot slower. As a simulation input for the stage-stage controller transfer function $\mathbf{G}_{\text{sc}}[q]$ either a model function like eq. (D.19) or eq. (D.20) can be used, or a real measurement can be inserted. Because a real stage trajectory is noisy, random numbers ϵ_s take from a Gaussian distribution with zeros mean,

and a standard deviation σ_s are added to the deterministic response, and the actual stage position is

$$\mathbf{r}_s[i] = \tilde{\mathbf{r}}_s[i] + \boldsymbol{\epsilon}_s[i] \quad \text{with } \boldsymbol{\epsilon}_s[i] \in \mathcal{N}(0, \boldsymbol{\sigma}_s) . \quad (\text{C.72})$$

The estimated particle positions are combined with the position of the sample stage to reconstruct the particle trajectory. Therefore the stage positions have to be averaged over n_s positions of the estimation cycle

$$\bar{\mathbf{r}}_s[k] = \frac{1}{n_s} \sum_{i=k \cdot n_s}^{(k+1) \cdot n_s} \mathbf{r}_s[i] . \quad (\text{C.73})$$

Hence, the reconstructed particle trajectory is calculated as

$$\hat{\mathbf{r}}[k] = \hat{\mathbf{r}}_p[k] - \bar{\mathbf{r}}_s[k] . \quad (\text{C.74})$$

C.6 | SIMULATION OF BROWNIAN MOTION INSIDE A SPHERE WITH HARD WALLS

Brownian motion is simulated inside a sphere with hard walls. Eq. (2.19) is used to calculate new positions, iteratively. The boundary effects are treated very unpretentious. Once a newly generated particle position is outside of the sphere, the simulation step is repeated until the new position is valid. Results of multiple simulations with varied diffusion coefficient are shown in fig. C.3.

All one-dimensional MSDs (see fig. C.3 (a)) approach the limit $L^2/10$ derived in [134] irrespective of the diffusion coefficient. Note that the limit of a single-coordinate MSD inside a sphere is divided by 3. Naturally, the MSD of faster particle reaches the plateau value earlier. This is intimated by two equally long trajectories of differently fast particles plotted in fig. C.3 (b) and (c). The simulated trajectory of the faster particle (fig. C.3 (c), $D\Delta t/L^2 = 40$) fills out the sphere more complete, leaving no doubts where the accessible space ends.

The nVACFs, given in fig. C.3 (d-f), reveal an increasing anti-correlation for increasing diffusion coefficient. In the simulation results with the diffusion coefficient $D\Delta t/L^2 = 100$, a slight anti-correlation is present even for $\Delta\tau/\Delta t = 1$. The restriction of possible step-directions next to the sphere's boundary hampers the cancellation of step-correlation by averaging. Faster particles inside spheres of equal size are more likely to step towards the boundary within the same period of observation. A step that theoretically moves the particle outside of the sphere is replaced by one that move it to the center. Refining the sampling rate/time resolution weakens this effect because less steps are in danger of interacting with the wall.

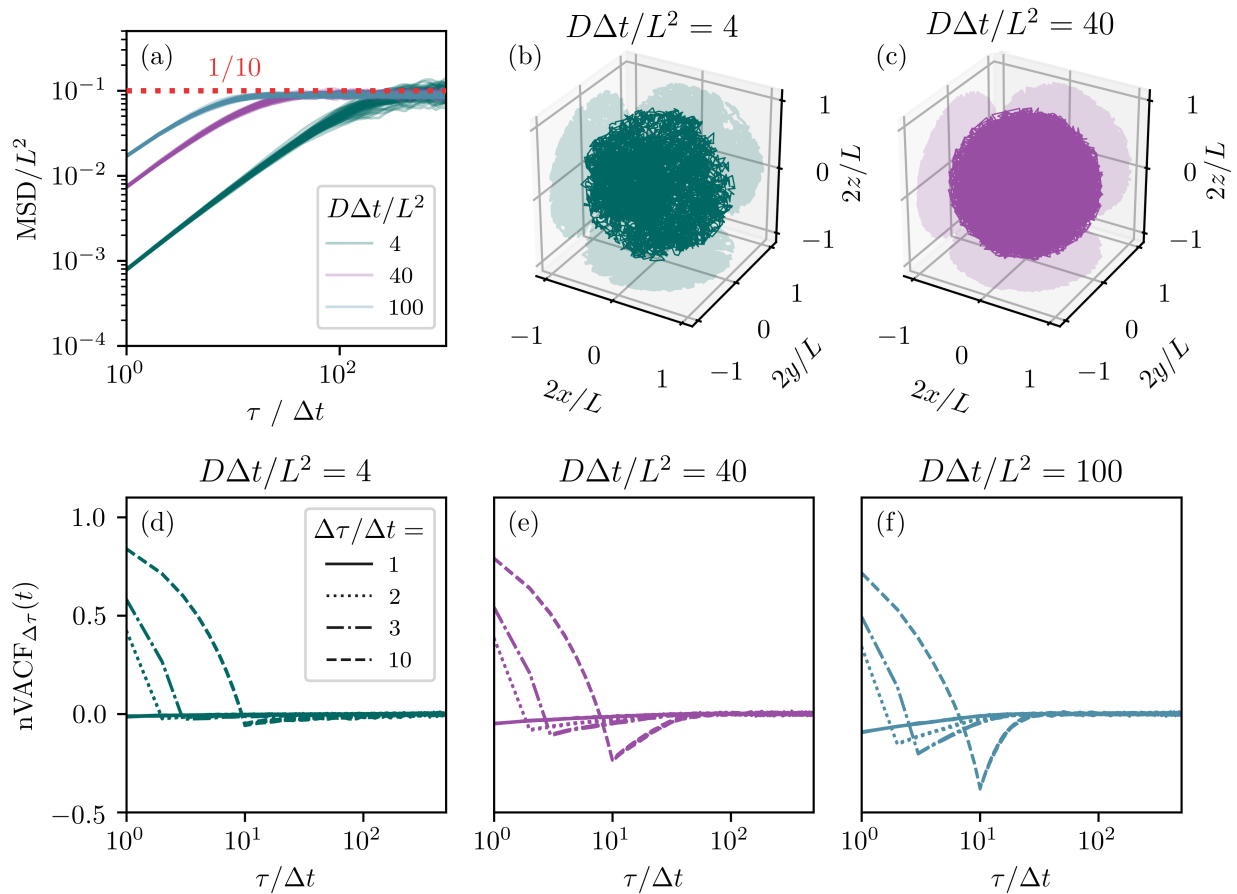


Figure C.3.: Results from simulations of Brownian motion confined in a sphere with hard walls. (a) Single-coordinate MSDs for simulation with different (normalized) diffusion coefficients and the asymptotic limit (dashed red line). (b, c) Examples of trajectories with a diffusion coefficients of $D\Delta t/L^2 = 4$ and 40. (e-f) nVACF calculated for trajectories simulated with three different diffusion coefficients and with the same period of observation.

D | TECHNICAL DETAILS

D.1 | OPTICAL SETUP

To enable easy and flexible switching between different lasers or combining multiple at the same time, the optical alignment is decoupled between the light source unit and the beam deflection path via a polarization-maintaining optical single-mode fiber (polarization-maintaining patch cable, PANDA, 405 nm, FC/PC, 2 m long, P1-405BPM-FC-2, Thorlabs Inc.). To couple the light into the fiber, an infinity-corrected objective (40x Olympus plan achromat objective, 0.65 NA, working distance 0.6 mm, RMS40X, Thorlabs Inc.) mounted on a fiber launch (fiber launch with FC-connectorized fiber holder, MBT613D/M, Thorlabs Inc.) is used. While light sources may differ depending on the conducted experiment, the setup's standard configuration is a continuous-wave green laser diode (iBeam-SMART-515-S, $\lambda_{\text{exc}} = 519$ nm, continuous-wave with pulse option, Toptica Photonics AG) that is combined via a dichroic laser beam combiner (BC, 552 nm cut-on wavelength, #86-393, Edmund Optics GmbH) with a red laser (Radius 635-25, $\lambda_{\text{ex}} = 635$ nm, continuous-wave, Coherent Inc.). Coupling efficiencies achieved with these lasers' beam profiles were about 50 %.

The laser light enters the beam deflection unit from the single-mode fiber via an achromatic collimator (protected silver reflective collimator, $\lambda_{\text{exc.}}$: 450 nm - 20 μm , RC02FC-P01, Thorlabs Inc.) that creates an output beam of 2 mm in diameter in the TEM₀₀ mode. At this position, the light power was always chosen to range between 10 and 20 mW depending on the use case. High powers are required by the microscope's wide-field imaging mode, whereas the SPOT or FCS-mode could be operated with significantly less. Furthermore, a mechanical shutter can block the light transmitted by the fiber to protect the sample from irradiation. AOD 1 deflects the light in a sinusoidal function of time and oriented vertically to the table plane. The non-adjustable diffraction order of the beam deflected from the optical axis by the AODs crystal cut is blocked by an iris. An optical relay unit (L_1 and L_2 , $f_1 = f_2 = 250$ mm, #32-919, Edmund Optics GmbH) projects the first-order diffracted light to the second and third AOD. Therefore, the light path is split into two branches by a non-polarizing 50:50 beam splitter cube (BS_2 , BS016, Thorlabs Inc.) placed behind lens L_2 . The secondary AODs are oriented perpendicular with respect to the primary one, and superimpose a deflection horizontal to the optical tabletop. Those secondary deflection patterns are phase-shifted by $\pi/2$ on the initial deflection of the light beam resulting in two laser beams that each rotate on a cone with its apex inside the second deflector crystals. In both light arms, a telecentric lens system (L_3 , L_4 and L_5 , L_6 , $f_3 = f_5 = 50$ mm, $f_4 = f_6 = 300$ mm, #32-323 and #45-215 Edmund Optics GmbH) expands the beam diameter and maps the apex of the deflection cone into a plane that corresponds to the back focal plane of the microscope objective. The necessary axial displacement of the two light orbits along the optical axis is achieved by a slight de-adjustment of each of the

second telecentric lenses (L_4 and L_6) in opposite directions. Within the focal lengths of the last telecentric lens the two beams are combined with a polarizing beam splitter cube (PBS, PBS251, Thorlabs Inc.) which requires an achromatic half-wave plate ($\lambda/2$ -WP, AHWP05M-600, Thorlabs Inc.) in one of the paths. Afterwards, the combined beams are directed through a quarter-wave plate ($\lambda/4$ -WP, #48-497, Edmund Optics GmbH) for generating circularly polarized light.

Within the first telecentric lens system (L_1 and L_2), a small percentage of the laser light intensity is reflected by a thin coverslip (BS_1) towards a photodiode (PDA55, Thorlabs Inc.) that measures the laser power for reference purposes.

For wide-field excitation, an optical lens (WFL, $f_{\text{wfl}} = 150$ mm, #L32-494, Edmund Optics GmbH) is flipped into the beam path between L_3 and L_4 , focusing the excitation light into the back focal plane of the microscope objective, and illuminating the sample with parallel light rays. The flipping mechanism of the WFL is electrically controlled (MFF101, Thorlabs Inc.) to facilitate a rapid change between imaging and SPOT mode.

The microscope body is a home-build inverted assembly with a fixed filter cube holder with the objective revolver. The sample is mounted on a nanopositioning stage that approaches the objective plane from above during focusing. The excitation light enters the input port of the filter cube holder and is deflected by a dichroic mirror (DBS, z532 RDC, AHF analysentechnik AG) to the aforementioned infinity-corrected water-immersion objective (UPLSAPO 60x, NA = 1.2, Olympus Corp.) The fluorescence from the sample is collected by the same objective, passes the dichroic, and finally reaches the detection unit.

In the detection unit, optical filters remove residual laser light. The selection of those detection filters depend on the used light sources (HQ545LP, AHF analysentechnik AG for the green laser or BLP01-633R-25, AHF analysentechnik AG for the red laser of the standard configuration). Behind the detection filters a motorized flip mirror holder (KSHM-40-LI-MDS, Owis GmbH) switches a mirror to deflect the emission light for wide-field imaging or to let it pass for the confocal detection. In the wide-field detection branch, an infinity-corrected tube lens (L_{10} , $f_{10} = 200$ mm, TTL200, Thorlabs) focuses the fluorescence collected from the sample onto a CCD camera (pixelfly usb, PCO AG). In the confocal detection mode, the emission light from the sample is focused by a lens (L_7 , $f_7 = 200$ mm, #32-917, Edmund Optics GmbH) mounted on a linear translation stage into a pinhole (P50S, Thorlabs Inc., (50 ± 3) μm pinhole diameter). In front of the pinhole, a detection shutter is able to darken a box containing the following optical components, including the two *avalanche photodiodes* (APD), completely. After the pinhole, the light is distributed by a 50:50 beam splitter cube (BS_3 , BS016, Thorlabs Inc.) via two lenses (L_8 and L_9 , $f_8 = f_9 = 50$ mm, #49-356 and #32-323, Edmund Optics GmbH) on the chips of two avalanche photodiode based single-photon counting modules (APD 1: COUNT-100C, Laser Components GmbH and APD 2: SPCM-AQR-14, PerkinElmer Inc.). This 50:50 beam splitter cube can be exchanged by a dichroic or polarizing beam splitter to measure two color- or polarization-channels, respectively (see section 9.2). Both APDs emit TTL-pulses on the detection of a single photon. These TTL-pulses are transmitted separately to the counting electronics.

D.2 | ACUSTO OPTICAL DEFLECTOR

As mentioned before, the laser beam is deflected with the help of three AODs (DTSX-400-532, Pegasus Optik GmbH) that made use of an acoustic wave in shear mode. The crystal material is tellurium dioxide (TeO_2) showing an acoustic velocity of 650 m s^{-1} .

AODs are used in the so-called *Bragg configuration*. Here, only the zero and first diffraction orders are existent because all others are annihilated by destructive interference. An wedge angle between the input and output face of the crystal is used to ensure that the zero order beam is deflected from the optical axis with a fixed angle necessary to keep the scanning beam propagating co-linearly with the incident beam. For this co-linear alignment of the first-order diffraction beam, the acoustic wave is created with the so-called *central radio frequency*, enabling symmetric linear deflection in both directions. While the intensity of the first order beam depends directly on the power of the applied signal, the deflection angle θ_{defl} is connected to the frequency of the acoustic wave ν_s itself via

$$\theta_{\text{defl}} = \frac{\lambda_{\text{exc}} \nu_s}{\tilde{n}_e c_s}, \quad (\text{D.1})$$

with the laser wavelength λ_{exc} , the crystal's refractive index \tilde{n}_e (for the extraordinary ray), and the speed of sound c_s inside the crystal.

The AODs have a $7.5 \times 7.5 \text{ mm}$ aperture for beam diameters up to 6.7 mm . The duration of deflecting the beam from one arbitrary point in space to another is called *access time*, and depends on the beam diameter. For the largest input beam diameter, the access time is about $10.3 \mu\text{s}$ and decreases for narrower beams. The electrical radio frequency that drives the AOD is generated by a *voltage controlled oscillator* (VCO, DRFA10Y-B-0, Pegasus Optik GmbH) and passes an amplifier (AMPA-B-30, Pegasus Optik GmbH) first before it reaches the AOD. The combination of VCO and amplifier serves as the AOD's driver unit that is easily addressable by analog voltages.

The VCO has two inputs, the MOD IN and the FREQ IN. Applying a voltage between 0 and 5 V to the MOD IN channel, the power of the electrical radio frequency signal, and consequently, the fraction of the laser intensity of the first-order beam is controlled. This dependency is nonlinear, and calibration is necessary. The FREQ IN channel adjusts the frequency of the electrical driver signal between 57 and 107 MHz on application of voltages between 0 and 10 V. The VCO's conversion of input voltages U_{defl} to electrical radio frequencies ν_{RF} was measured and is displayed in fig. D.1(a).

A very accurate linear relation was obtained that follows

$$\nu_{\text{RF}}(U_{\text{defl}}) = 5.85 \text{ MHz V}^{-1} \cdot U_{\text{defl}} + 56.67 \text{ MHz}. \quad (\text{D.2})$$

By adjusting the radio frequency, the angle of the beam deflection is controlled. Voltages applied to the MOD IN and FREQ IN channel will be called intensity voltages $U_{\text{intensity}}$ and deflection voltages U_{defl} , respectively. The electrical radio frequency signal is constantly amplified by 33 dB before it reaches the crystal.

For orbital scanning of the laser beam, a sinusoidal deflection voltage has to be applied to the AOD driver. The offset and amplitude of this sinusoidal voltage signal depends on the laser wavelength λ_{exc} to be deflected (see eq. (D.1)). But also for the alignment of a non-moving beam co-linear with the optical axis, the laser wavelength has to be considered. Therefore, a super-continuum laser (SC400, Fianium Ltd.) was used as the light source, because its wavelength can be selected with the build-in *acusto optical tunable*

filter (AOTF). This enables measuring of the voltage used to bring the beam back to the optical axis for a defined laser wavelength λ_{exc} . The results are shown in fig. D.1(b) for all three AODs showing approximately the same relationship. A polynomial parametrizes the central deflection voltages dependency on the laser wavelength according to

$$U_{\text{def},c}(\lambda_{\text{exc}}) = -4.807 \times 10^{-4} \text{ mV nm}^{-3} \cdot \lambda_{\text{exc}}^3 + 0.9025 \text{ mV nm}^{-2} \cdot \lambda_{\text{exc}}^2 - 587.6 \text{ mV nm}^{-1} \cdot \lambda_{\text{exc}} + 134 \text{ V} . \quad (\text{D.3})$$

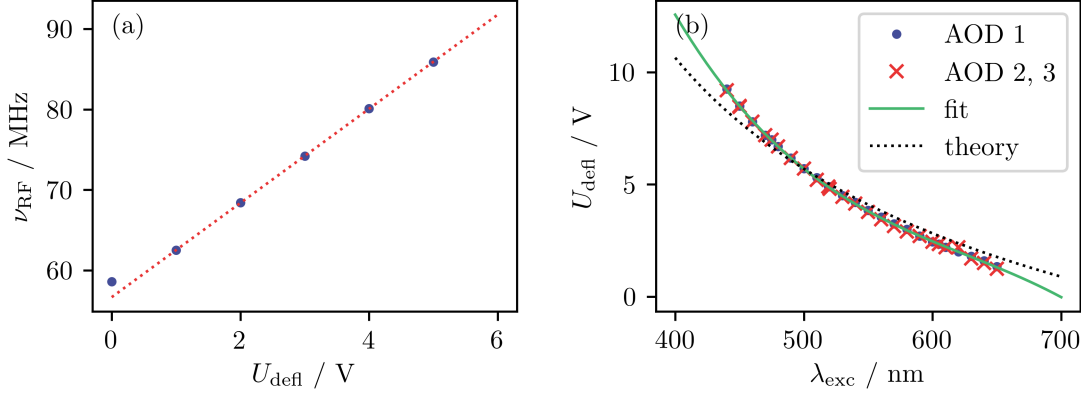


Figure D.1.: (a) The radio frequency emitted by the VCO was measured with an oscilloscope for different deflection voltages applied to the VCO. The zero voltage data point was excluded from the fit because it might be affected by a small leakage voltages of the plant. (b) The deflection voltage necessary to align the laser beam along the optical axis is plotted versus the laser wavelength. The laser wavelength was chosen by an AOTF in front of a super-continuum laser (SC400, Fianium Ltd.).

D.3 | RAY TRANSFER MATRIX ANALYSIS

In this section, a systematic formalism or ray-tracing will be used to determine important parameters of the SPOT setup. The used technique is called *ray transfer matrix analysis* (RTMA) and it is based on geometrical optics describing the propagation of light in terms of straight rays that propagates under small angles and small displacements with respect to the optical axis (*paraxial approximation*). Since the implementation of SPOT requires only minimal beam displacement and angles, the paraxial approximation is appropriate and the ray transfer matrices of the setup can be constructed.

For RTMA, the beam path is characterized by a state vector \mathbf{b} that contains its displacement b and angle φ with respect to the optical axis. Optical components and their influence on the beam path are described as 2×2 matrices. Two elementary optical matrices are the matrix of a thin lens \mathcal{L}_f with focal length f and the matrix of free space translation \mathcal{T}_d with a distance d defined by

$$\mathcal{L}_f = \begin{pmatrix} 1 & 0 \\ -1/f & 1 \end{pmatrix}, \quad \text{and} \quad \mathcal{T}_d = \begin{pmatrix} 1 & d \\ 0 & 1 \end{pmatrix}, \quad (\text{D.4})$$

respectively. Arrangements of optical components centered along the optical axis can be calculated by matrix multiplication in the correct sequence. For example, the system

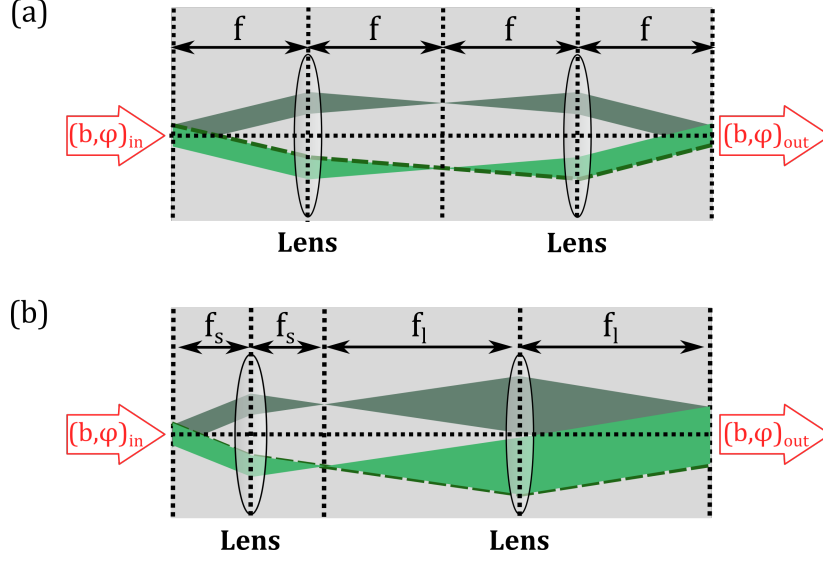


Figure D.2.: (a) Two identical lenses placed in twice the distance of their focal length constitute a relay system that inverts the image from the front to the back focal plane without magnification. (b) Group of two lenses with a short a long focal length, that are placed in a distance of the sum of their focal length. This system fulfills multiple purposes as it expands the beam diameter, scales the incoming angles, and relays the incoming beam deflection into the output plane with inverted signs.

depicted in fig. D.2(a) that consists of two identical lenses placed in twice the distance of their focal length f can be written as

$$\mathcal{R} = \mathcal{T}_f \mathcal{L}_f \mathcal{T}_{2f} \mathcal{L}_f \mathcal{T}_f = \begin{pmatrix} -1 & 0 \\ 0 & -1 \end{pmatrix} = -\mathbb{1}. \quad (\text{D.5})$$

This corresponds to an inversion of all ray directions while maintaining all other features. A deflection that leads away from the optical axis in the front focal plane will be reversed and projected in the rear focal plane. Therefore, the arrangement \mathcal{R} is an option to create a so-called *relay system*.

The system shown in fig. D.2(b) is essentially a copy of fig. D.2(a), but with lenses of two different focal length. The focal length of the first lens is f_s (short) and of the second one is f_l (long). Therefore, this composition of optical elements serves as a lever for angles and can be called *beam-expander*. The beam-expander increases the diameter of an incident light beam by a factor corresponding to the ratio of the focal lengths and simultaneously flattens the angles of propagation with the inverted factor. The ray transfer matrix of the beam-expander optics \mathcal{B}_{f_s, f_l} is written as

$$\mathcal{B}_{f_s, f_l} = \mathcal{T}_{f_l} \mathcal{L}_{f_l} \mathcal{T}_{f_s + f_l} \mathcal{L}_{f_s} \mathcal{T}_{f_s} = \begin{pmatrix} -\frac{f_l}{f_s} & 0 \\ 0 & -\frac{f_s}{f_l} \end{pmatrix}. \quad (\text{D.6})$$

In the setup for SPOT (see fig. 4.1), the output plane of the beam-expander optic is identical to the back focal plane of the objective. The y -deflection occurs in the front focal plane of the beam-expander optics (L_3 and L_4 or L_5 and L_6 in fig. 4.1), and the final matrix that describes the optical system starting from AOD 2 or 3 up to and inclusive the objective lens is called \mathcal{S}^y .

The beam deflected along the x -axis is first lead through other optical components before entering the \mathcal{S}^y system. Those additional optical components (L_1 and L_2 in fig. 4.1)

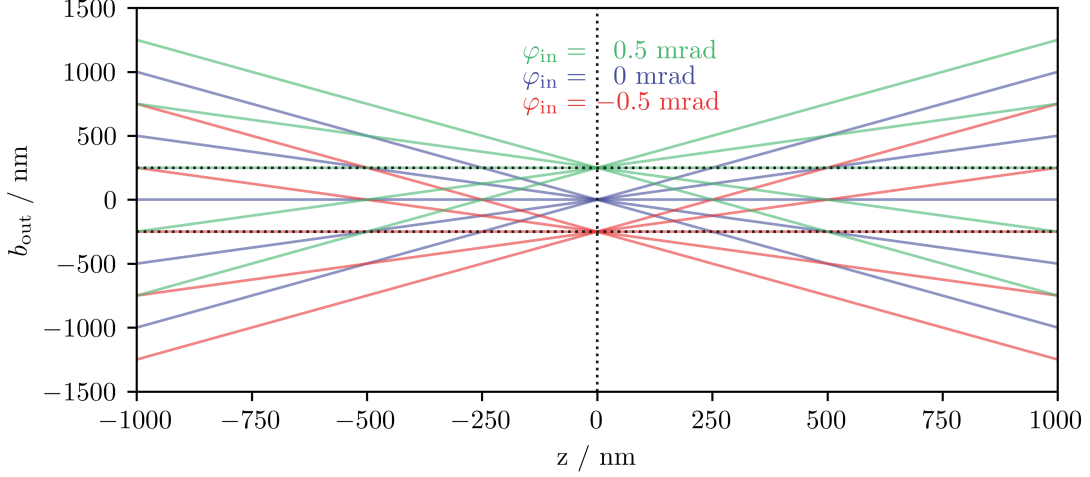


Figure D.3.: Set of rays with different deflection angles φ_{in} . Focal lengths are set according to the values of the experimental implementation. Five rays with offsets in the range between -0.5 mm and 0.5 mm are used as input. Black dotted lines indicate the plane in which the rays intersect and the orbit radius. For these deflection angles, the resulting orbit radius amounts to $R = 250$ nm.

are a relay system used to join the orthogonal deflection directions into a single point residing in AOD 2 or AOD 3, respectively. The x -deflection system starting in the center of AOD 1 up to the objective lens will be called \mathcal{S}^x . Both systems are written as

$$\mathcal{S}^y = \mathcal{L}_{f_{\text{obj}}} \mathcal{T}_{f_{\text{obj}}} \mathcal{B}_{f_s, f_l} \quad \text{and} \quad (\text{D.7})$$

$$\mathcal{S}^x = \mathcal{S}^y \mathcal{R} = -\mathcal{S}^y. \quad (\text{D.8})$$

Finally, the beam propagation behind the objective lens should be described.

The distance to the objectives focal plane is noted as z and obtained by multiplying an additional translation matrix $\mathcal{T}_{f_{\text{obj}}+z}(z)$ to the system matrices. The result is the system

$$\mathcal{M}^{x,y}(z) = \mathcal{T}_{f_{\text{obj}}+z}(z) \mathcal{S}^{x,y} = \begin{pmatrix} \mp f_l z / (f_s f_{\text{obj}}) & \pm f_{\text{obj}} f_s / f_l \\ \mp f_l / (f_s f_{\text{obj}}) & 0 \end{pmatrix}, \quad (\text{D.9})$$

The input rays are described in x - and y -direction, independently, and are given as state vectors $\mathbf{b}_{\text{in}}^{x,y} = (b_{\text{in}}^{x,y}, \varphi_{\text{in}}^{x,y}(t))$. With the help of $\mathcal{M}^{x,y}(z)$, the output rays $\mathbf{b}_{\text{out}}^{x,y}(z, t)$ can be calculated as

$$\mathbf{b}_{\text{out}}^{x,y}(z, t) = \begin{pmatrix} b_{\text{out}}^{x,y}(z, t) \\ \varphi_{\text{out}}^{x,y}(z, t) \end{pmatrix} = \mathcal{M}^{x,y}(z) \mathbf{b}_{\text{in}}^{x,y} = \begin{pmatrix} \mp \frac{f_l}{f_s} b_{\text{in}}^{x,y} z \pm \frac{f_{\text{obj}} f_s}{f_l} \varphi_{\text{in}}^{x,y}(t) \\ \mp \frac{f_l}{f_s f_{\text{obj}}} b_{\text{in}}^{x,y} \end{pmatrix}. \quad (\text{D.10})$$

In fig. D.3, the rays of three different input angles are propagated by eq. (D.10) in the range around the focal plane.

It is easy to see that for the central beam, defined by $b_{\text{in}}^{x,y} = 0$, the output beam is parallel to the optical axis but displaced by $\frac{f_{\text{obj}} f_s}{f_l} \varphi_{\text{in}}^{x,y}(t)$. Therefore, a harmonic deflection of the central beam by $\varphi_{\text{in}}^{x,y}(t) = \varphi_{\text{ampl}} \sin(\omega_0 t + \phi^{x,y})$ yields in a circular beam scan with radius

$$R(\varphi_{\text{ampl}}) = \frac{f_{\text{obj}} f_s}{f_l} \varphi_{\text{ampl}}, \quad (\text{D.11})$$

focused in the focal plane of the objective. The phase $\phi^{x,y}$ of the sinusoidal deflections influences only the starting point of the scan along the circular line. In summary, an orbit of z -independent radius can be generated in the optical system described by the ray transfer matrix $\mathcal{M}^{x,y}(z)$ by varying only the deflection angle.

The generation of a axial focus offset to the objective's focal plane is more complex to describe. The offset is created by shifting the long focal length-lens in the beam-expander unit \mathcal{B}_{f_s, f_l} towards the objective. Therefore, the beam-expander matrix becomes

$$\mathcal{B}_{f_s, f_l, p} = \mathcal{T}_{f_l - p} \mathcal{L}_{f_l} \mathcal{T}_{f_s + f_l + p} \mathcal{L}_{f_s} \mathcal{T}_{f_s} = \begin{pmatrix} -\frac{f_l^2 + p^2}{f_s f_l} & \frac{f_s p}{f_l} \\ \frac{p}{f_s f_l} & -\frac{f_s}{f_l} \end{pmatrix}. \quad (\text{D.12})$$

Hence, the new matrix of the complete system will depend parametric on the lens shift p

$$\mathcal{M}_p^{x,y}(z) = \mp \mathcal{T}_{f_{\text{obj}} + z} \mathcal{L}_{f_{\text{obj}}} \mathcal{T}_{f_{\text{obj}}} \mathcal{B}_{f_s, f_l, p} = \begin{pmatrix} \mp \frac{f_{\text{obj}}^2 p + (f_l^2 + p^2) z}{f_s f_l f_{\text{obj}}} & \pm \frac{f_s (f_{\text{obj}}^2 + p z)}{f_l f_{\text{obj}}} \\ \mp \frac{f_l^2 + p^2}{f_s f_l f_{\text{obj}}} & \pm \frac{f_s p}{f_l f_{\text{obj}}} \end{pmatrix}. \quad (\text{D.13})$$

The question arises on how to calculate the z -position of the laser beam focus in such a system. Therefore, the intersection point of two beams with the same deflection angles $\varphi_{\text{in},1} = \varphi_{\text{in},2}$ but opposite distances to the optical axis $b_{\text{in},1} = -b_{\text{in},2}$, must be searched for. Thus, this condition is expressed as

$$b_{\text{out},1}^{x,y}(z_{\text{focus}}) = b_{\text{out},2}^{x,y}(z_{\text{focus}}), \quad (\text{D.14})$$

and is true for

$$z_{\text{focus}}(p) = -\frac{f_{\text{obj}}^2 p}{f_l^2 + p^2}. \quad (\text{D.15})$$

Moving the long focal length-lens of the beam-expander unit towards the objective lens moves the laser beam focus closer to the objective lens and vice versa. This calculation also includes the case of a not modified beam-expander unit for $p = 0$, where the laser beam focus resides in the objective focal plane.

From eq. (D.15), for a symmetric and opposite displacement of the lenses by the distance p_0 , the orbital distance d_z can be determined as

$$d_z(p_0) = z_{\text{focus}}(-p_0) + z_{\text{focus}}(p_0) = \frac{2 f_{\text{obj}}^2 p_0}{f_l^2 + p_0^2}. \quad (\text{D.16})$$

The influence of the lens shift on the orbit radius can be checked. Therefore, the intersection points of rays with different b_{in} are considered in the plane $z = z_{\text{focus}}$. The beam displacement from the optical axis in this plane is independent from b_{in} by definition, but it depends on the deflection angle amplitude φ_{ampl} and (weakly) on the lens shift p :

$$R(\varphi_{\text{ampl}}, p) = \frac{f_s f_l f_{\text{obj}}}{f_l^2 + p^2} \varphi_{\text{ampl}} \underset{f_l \gg p}{\approx} \frac{f_s f_{\text{obj}}}{f_l} \varphi_{\text{ampl}}. \quad (\text{D.17})$$

For small lens shifts p compared to the focal length of the second lens in the beam-expander unit f_l , the same orbit radius as in the unshifted case is obtained. In fig. D.4, two opposed lens shifts and three deflection angles are inputted into eq. (D.13) and propagated in the range next to the focal plane ($z = 0$) to illustrate the course of the rays, the z -shift and the orbit radii.

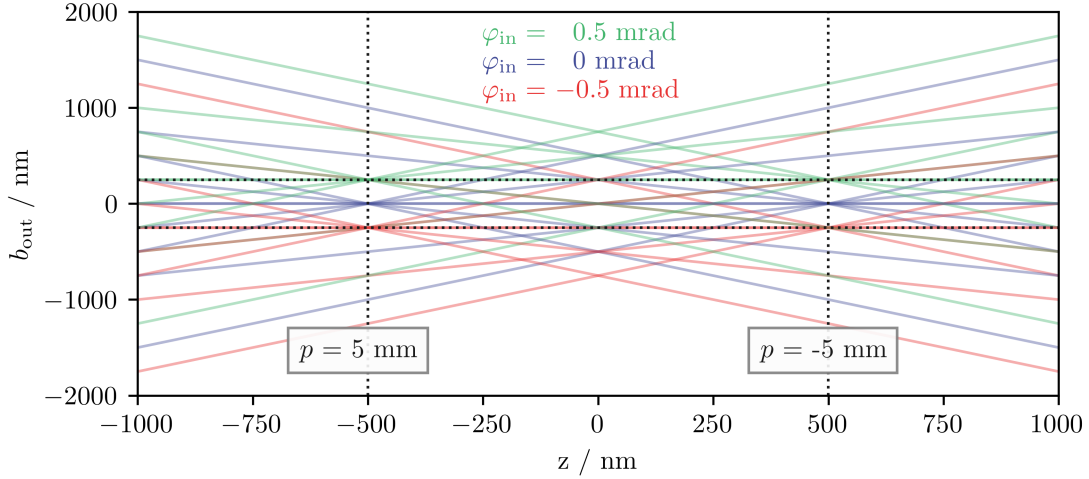


Figure D.4.: Set of rays with different deflection angles φ_{in} and with a lens shift of p . Focal lengths are set according to the values of the experimental implementation. Five rays with offsets from the optical axis in the range between -0.5 mm and 0.5 mm are used as input. Vertical black dotted lines indicate the plane in which the rays of one deflection angle intersect and horizontal black dotted lines correspond to the orbit radius created for sinusoidal deflection with 0.5 mrad as amplitude. For these deflection angles, the resulting orbit radius amounts to $R = 250$ nm, as before. The lens shift was set to $p = \pm 5$ mm, which corresponds to an orbit distance of $d_z = 1000$ nm.

Inspecting the beam deflection properties of the AODs and the connected electronics makes it possible to determine the beam scanning resolution and scanning range of the setup. According to the manufacturer datasheet, the AODs have a laser light wavelength-dependent full deflection range of about 40 - 50 mrad. This is twice the maximum deflection amplitude around the zero deflection and results in a maximum orbit radius of about 10 μm . The static resolution (ratio of the range of scan angles to the beam divergence) of the AODs themselves is given as about 400 for $\lambda_{\text{exc}} = 519$ nm. This corresponds to clearly separable ($1/e^2$ -width criterion) beam scan positions at a distance of 50 nm within the sample plane.

It is also helpful for the calibration of the setup if there is a theoretical relationship between the orbit radius and the deflection voltage. Using eqns. (D.1), (D.2) and (D.11), one obtains the scaling factor

$$\frac{dR}{dU_{\text{defl}}}(\lambda_{\text{exc}}) = \frac{dR}{d\varphi} \frac{d\varphi}{d\nu_s} \frac{d\nu_s}{dU_{\text{defl}}} = \frac{f_s f_{\text{obj}} \lambda_{\text{exc}}}{f_l \tilde{n}_e c_s} \frac{d\nu_{\text{RF}}(U_{\text{defl}})}{dU_{\text{defl}}}. \quad (\text{D.18})$$

For the laser light wavelength $\lambda_{\text{exc}} = 519$ nm, the obtained scaling factor is $dR/dU_{\text{defl}} = 0.946$ nm mV^{-1} . Moreover, it can be checked if the scan resolution is restricted due to the discretized voltage level outputted from the ADwin. While the quantization of the voltage level from the ADwin is $\Delta U_{\text{DAC}} = 305.175$ μV (see appendix D.6), the theoretical accuracy in the adjustment of the orbit radius is about 0.3 nm, and consequently not a technical limitation of the deflection capabilities.

D.4 | NANOPositionING STAGE

The P-545.3D8S stage is equipped with piezoresistive strain sensors that are read out by the internal control unit with 20 kHz. The controller consists of a PID controller with a subsequent set of two notch filters, and it converts the sensor readout and the target position to a control voltage that is applied to the actuators moving the stage. The maximum control signal slew rate was left at manufacturer settings to prevent accidental damage by large and rapid voltage changes. The notch filter must be set to the system's first resonance frequency. To determine those system resonances, the UIR (see appendix A.4.1) is measured in open-loop mode, and Fourier transformed to the frequency response (see appendix A.4.3). Because the resonances are load-dependent, a representative sample cell is mounted on top of the stage. In a Bode plot, the resonance becomes noticeable as a peak in the amplitude amplification. For the present stage, only one dominant resonance frequency at 1.7 kHz, 1.6 kHz, and 0.8 kHz were measured for the x -, y -, and z -direction, respectively (see fig. D.5 (b) and (c)).

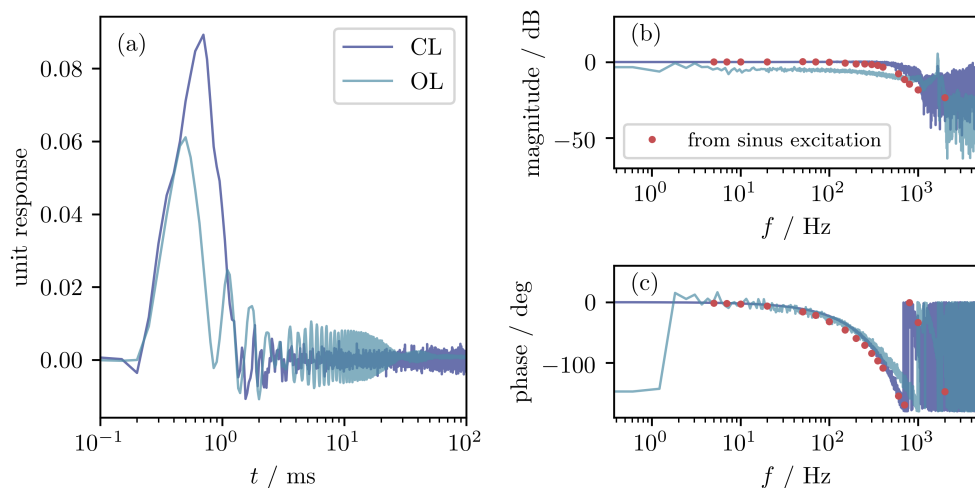


Figure D.5.: Comparison between the stages response in the closed-loop (CL, dark blue line) and open-loop (OL, marine blue line) mode. (a) Unit impulse response (UIR) and (b,c) frequency response depicted as a Bode plot with the magnitude given in (b) and phase in (c). Additionally, the magnitude amplification and the phase roll-off in the closed-loop case are shown as red dots from experiments with repetitive sinusoidal excitation.

With the notch filter frequencies set to the resonance values of the respective axis, the PID control parameters are optimized to reduce the overshoot and to shorten the rise- and settling time of the USR (see appendix A.4.2) in the closed-loop mode. Established tuning methods, such as those of Ziegler-Nichols[264] or Cohen-Coon[265], could either avoid large overshoots or generate fast response times, but not both at the same time. Manual settings are cumbersome but proven to be superior in terms of the reaction time and overshoot amplitude. Therefore, P, I, and D gains are set to 0 and changed iteratively until optimum. Once an optimum parameter set was found, the reproducibility of the step response is checked by recording the step response for steps of different height in the positive and negative direction. Relevant step sizes are smaller than about 500 nm, which corresponds to the maximum expected stage step size during a SPOT experiment, where the setup should perform best. Most of the system's unit step response functions agree well with each other when normalized and displayed in fig. D.6. But the responses to target

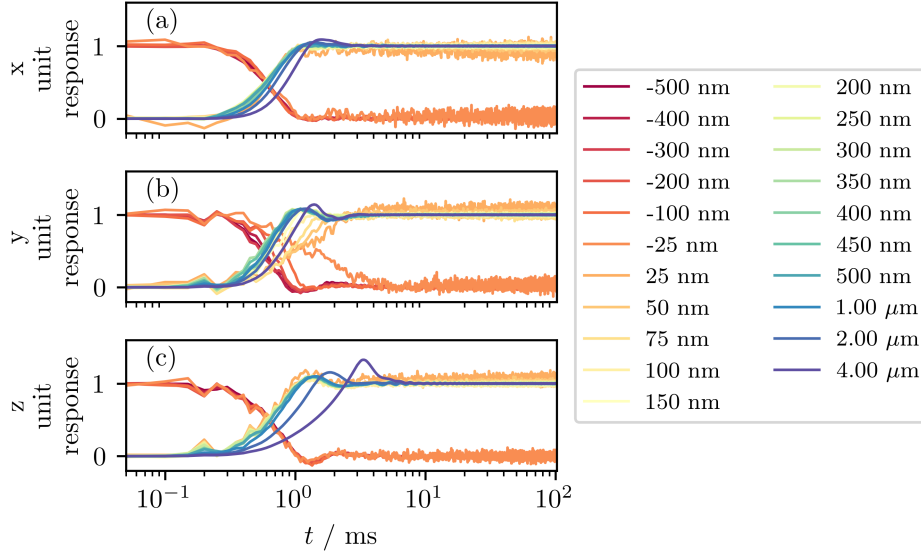


Figure D.6.: Unit step responses of the nanopositioning stage (a) x -axis, (b) y -axis, and (c) z -axis for different step heights (color-coded according to the legend indicating the step height). The responses to steps in the negative direction are subtracted from 1 for a clear representation.

steps larger than the relevant range, especially in the z -direction, do not maintain the fast rise time and small overshoot. For small steps, the noise seems to increase, but in fact, this is only due to normalization. Crucial is the slow rise time of the stage response along the y -axis for small steps and setting should be improved. Despite of these exceptions, the step response rises in less than 2 ms with an overshoot smaller than 10 % in all directions and for step responses smaller than or equal to 500 ms.

However, a characteristic of the manufacturer’s design of the nanopositioning stage becomes apparent in fig. D.6. A scan pattern often desired in confocal scan applications is to scan lines in the x -direction and vary the y -axis after each line. Once a xy -plane is completely scanned, the z -axis of the stage is adjusted. Therefore, the x -, y -, and z -axis of the stage are required to be increasingly faster. This is visible in fig. D.6 as it was possible to achieve an increasingly better quality of response of the z -axis, y -axis, and x -axis in terms of rise time and overshoot.

After the dynamic operating mode has been optimized, a characterization for static and dynamic operation can be performed. First, a long trace of the stage positions is recorded and analyzed for that reason. While the closed-loop response (fig. D.7 (a)) is stable over the entire record, the open-loop response (fig. D.7 (b)) is dominated by a strong and non-linear creeping of about $(20 \pm 10) \text{ nm s}^{-1}$. By subtracting the backbone of the drifted position trace (fig. D.7 (b), inset), a histogram can be formed that represents the short-term position noise, which is identical to the closed-loop case (fig. D.7 (c)). The backbone of the drifted stage trajectory was obtained by a moving average over a window of 201 positions. The histogram for the closed-loop mode is further broken down to show the accuracy of the individual coordinates (fig. D.7 (d)). The positional noise is given by the standard deviation of those data and amount to 1.3 nm, 1.1 nm, and 0.9 nm for the x -, y -, and z -axis, respectively. Hence, the position noise of the stage small enough to be neglected for further considerations.

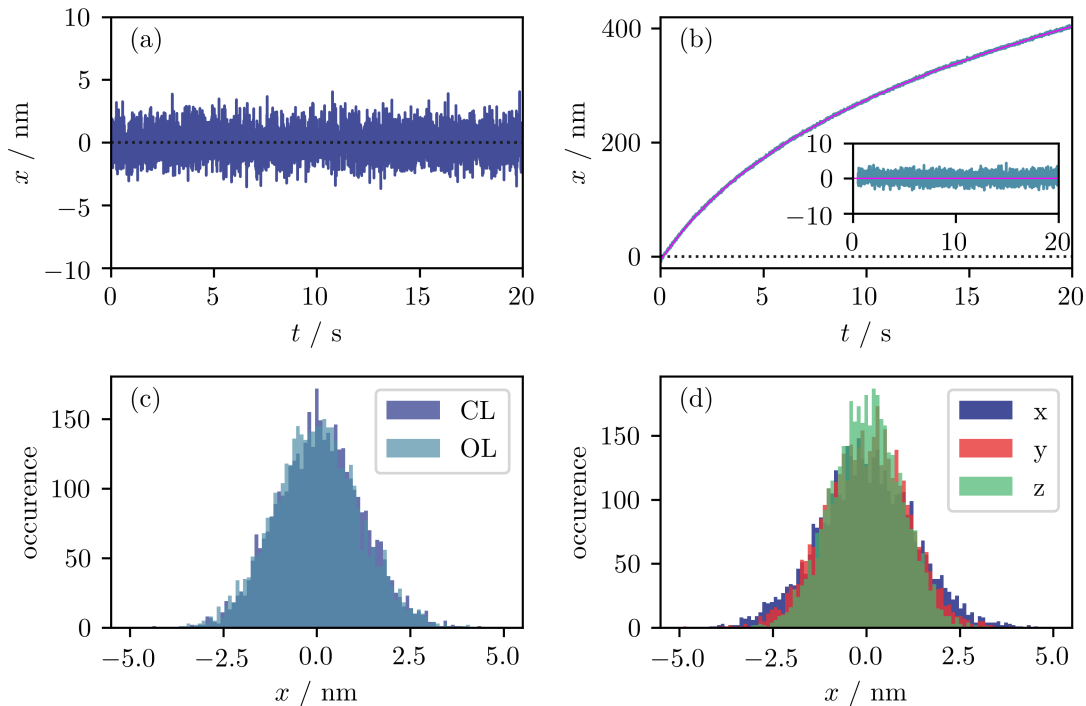


Figure D.7.: (a) Position stability of the piezo stage in the closed-loop mode. The black dotted line is the target value, which can be held well. (b) Position stability of the piezo stage in the open-loop mode. A clear drift of the position is visible. The average drift velocity is $(20 \pm 10) \text{ nm s}^{-1}$. The black dotted line is the target value, the solid magenta line the backbone of the drifted position. An inset represents the positional noise of the stage (in nm) with respect to the drift trajectory. (c) Histograms of the positions with respect to the target value for the closed-loop case and with respect to the drift trajectory for the open-loop case. (d) Histogram of the positions with respect to the target value for all three axes in the closed-loop case. The standard deviation for x -, y -, and z -direction is 1.3 nm, 1.1 nm, and 0.9 nm, respectively.

D.5 | SYSTEM IDENTIFICATION OF THE NANOPositionING STAGE-STAGE CONTROLLER

In order to characterize the performance of the SPOT setup in the dynamic mode, the transfer function of the closed-loop system must be identified. Therefore, the step response of the stage is recorded for steps of different height and direction as described before. According to eq. (A.33), those responses are normalized and averaged to obtain the unit step response, which is converted to the unit impulse response. In fig. D.5 (a) the UIR in the close-loop and open-loop mode are compared. While the closed-loop response shows only a single strong peak followed by small-amplitude oscillations, there is a slowly damped oscillation in the open-loop case that vanishes at a level that is different from the start position.

The UIR can be converted to the frequency response by Fourier transformation, as discussed before. The result is plotted as a Bode plot in fig. D.5 (b) and (c). A flat magnitude of the frequency response for an extended low-frequency regime is desired. It is reached in the close-loop case for frequencies up to about 600 Hz. In the open-loop case, this flat regime shows less magnitude, a small dip at about 1 kHz, and a strong amplitude amplification at around 1.6 kHz. The phase shift is instructive about the time that is needed to reach the target position. It shows that in the open- and close loop case, significant

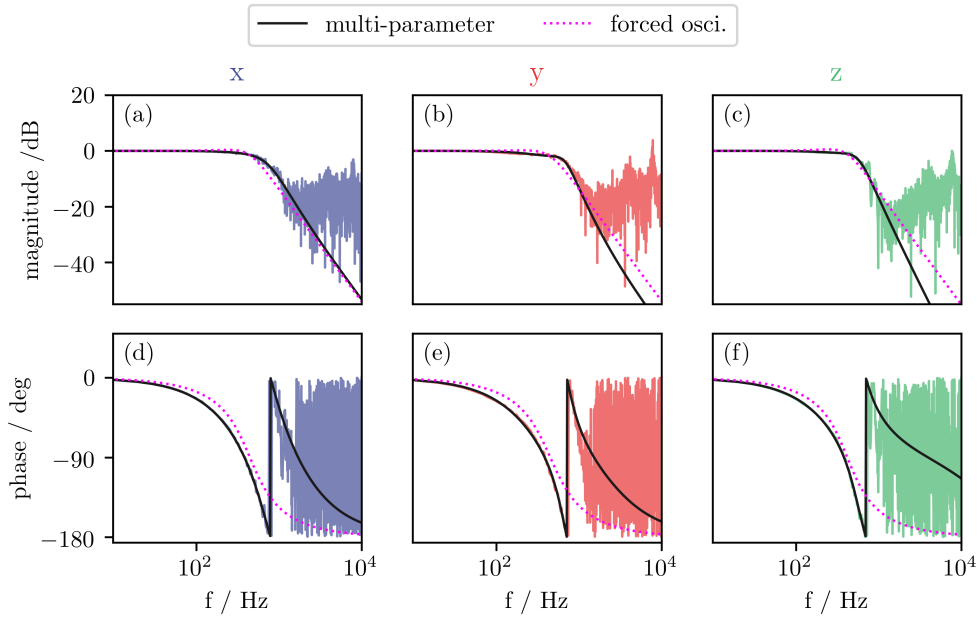


Figure D.8.: (a-c) Magnitude amplification and (d-f) phase roll-off for the closed-loop nanopositioning stage determined from the averaged unit step response. Each column corresponds to an axis of the stage. The solid black line is a multi-parameter fit designed to yield an accurate representation of the real response in the relevant frequency regime. The multi-parameter fit shows a phase wraps at about 785, 718, and 698 Hz for the x -, y -, and z -axis, respectively. Parameters of the fit are given in table D.2. The solid fuchsia line is a two-parameter fit with the model function of a driven oscillator. The parameters are listed in table D.1. The fitting range was always restricted to frequencies below 1 kHz to remove the fast phase switching influence in this regime. In addition, the data points have been logarithmically coarsened for the fitting purpose to allow uniform numerical weighting across all frequencies.

phase shifts are observed for frequencies higher than 100 Hz. Between 700 and 800 Hz, the closed-loop response phase switches signs indicating that the stage cannot be controlled that fast. The open-loop response shows a similar switching at higher frequencies in the range of 1 kHz.

To check the calculations of the conversion from a step response to a frequency response, a frequency response is recorded directly for the closed-loop case. Therefore, the stage is excited with sinusoidal signals of varying frequencies. The stages oscillatory response is fitted with a sinus function, and the amplitude gain and phase shift is extracted from the fitting parameter. The result is displayed in fig. D.5 as red dots. While the phase shift is very well reproduced, the amplitude gain decays slightly earlier. There are numerous reasons for this behavior, like errors in the amplitude fitting of the sine responses or a stronger influence of the notch filter for the data acquired with a real repetitive driving signal. Nevertheless, the different approaches to determine the frequency response deviate not much and the calculated frequency response seems reliable.

For SPOT, the nanopositioning stage is externally controlled with 250 Hz. This means that the target value can be reached, but a significant phase shift must be considered. For theoretical examinations of its influence on the SPOT process, a closed-form representation of the transfer function is a useful tool. Therefore, real measurement data are compared with a model function. A complete representation of a piezoelectric positioning system would require modeling the electrical circuit, the mechanical components of the system, and the control logic.[266] Such a comprehensive model would account not only for the

damped oscillatory behavior, but also for creeping, hysteresis and time delays. Numerous publications dedicate their efforts to this task and found clever ways to increase the controller's performance and the accuracy of the model.[267–274] Nevertheless, the main aspects of a closed-loop piezoelectric nanopositioning stage are covered by using a highly simplified model of a unity-gain, second-order low-pass system.[275] The transfer function of such a driven oscillatory system (see appendix A.3), can be written as

$$G_{\text{forced osci.}}(s) = \frac{\omega_n^2}{s^2 + 2\lambda\omega_n s + \omega_n^2}, \quad (\text{D.19})$$

But this section's main purpose is not to fully understand and optimize the chained system of positioning stage and control loop, but to find an accurate numerical representation of its response. Thus, the number of fitting parameter can be increased by using a multi-parameter transfer function given by

$$G_{\text{multi-parameter}}(s) = \frac{b_1 a_\omega^2 s + b_0 a_\omega^2}{s^3 + 2a_\lambda a_\omega s^2 + (1 - b_1) a_\omega^2 s + b_0 a_\omega^2}. \quad (\text{D.20})$$

The mathematical structure of this fit model in terms of the polynomial order of the numerator and denominator is justified by comparing it with a PI-controlled driven oscillator model (see eq. (A.65)).

In fig. D.8 each nanopositioning stage axis response is fitted with both model functions. Therefore, the transfer function is used to calculate the model's frequency response as magnitude and phase shift. The residuals between the model's output and the measurement data are calculated and used to optimize the transfer functions input parameter according to a Levenberg-Marquardt non-linear least-squares solver [276, 277]. It is necessary for computational reasons that amplitude amplification and phase shift are numerically in the same range. Therefore, the magnitude is handled in units of $\frac{1}{20}$ dB, and the phase shift in units of $\frac{1}{180}^\circ$. In addition, the data points have been logarithmically coarsened for the fitting purpose to allow uniform numerical weighting across all frequencies. Furthermore, the fitting range was restricted to frequencies below 1 kHz, removing the influence of the fast phase switching and magnitude noise in this regime. The obtained fitting parameters for the forces-oscillation and multi-parameter model are listed in table D.1 and table D.2, respectively.

Table D.1.: Fitting results of the forced-oscillation model to the frequency response of the different nanopositioning stage axes

Axis	λ	ω_n / Hz	adj. R^2
x	0.599 ± 0.017	2791 ± 62	0.9835
y	0.632 ± 0.022	2831 ± 83	0.9754
z	0.573 ± 0.016	2615 ± 55	0.9832

Table D.2.: Fitting results of the multi-parameter model to the frequency response of the different nanopositioning stage axes.

Axis	b_0 / Hz	b_1	a_λ	a_ω / Hz	adj. R^2
x	2287 ± 104	-0.259 ± 0.038	0.787 ± 0.043	5707 ± 214	0.9986
y	1702 ± 32	-0.118 ± 0.013	0.541 ± 0.010	4694 ± 40	0.9991
z	1554 ± 32	-0.013 ± 0.011	0.590 ± 0.012	4424 ± 39	0.9991

The highly simplified forced-oscillation model is only a rough approximation for the transfer function. Damping constants around 0.6 are observed and resonance frequencies of about 2.8 kHz for the lateral axes and 2.6 kHz for the z -axis. The adjusted R^2 values are higher than 0.97 and indicates the suitability of the model. Nevertheless, it underestimates the frequency at which the magnitude decays and ignores the phase switching, where it overestimates the decay constant. The multi-parameter model instead is an outstanding representation of the transfer function in the considered frequency range. It matches the magnitude and the phase shift behavior perfectly for frequencies below 700 Hz with adjusted R^2 values higher than 0.998. For higher frequencies, especially those larger than the phase switching frequency, the model's accuracy decreases.

Summarizing, the forced-oscillation model is helpful in obtaining parameters like the damping constants and resonance frequencies that approximate the behavior of the stage roughly. The multi-parameter model follows the structure of a PI-controlled oscillatory system and fits the frequency response exceptional well in the frequency regime of interest. Therefore, the multi-parameter model serves as a closed-form representation of the systems transfer function.

D.6 | ADWIN

The core component of the control logic of the SPOT setup is an ADwin system (ADwin Gold II, Jäger Computergesteuerte Messtechnik GmbH). The ADwin hardware consists of a fast digital signal processor (ADSP TS101S, 300 MHz, 31 bit TigerSHARC, Analog Devices Inc) with real-time capabilities, analog and digital inputs and outputs (18 bit analog-digital-conversion, 16 bit digital-analog-conversion) and a communicational link to a PC. The range of the analog input and output channels is -10 to 10 V corresponding to 2^{16} digits, which corresponds to a quantization of the voltage levels to $\Delta U_{\text{ADwin}} = 305.175 \mu\text{V}$. The manufacturer states the timing accuracy of the processes running on the ADwin as better than $1 \mu\text{s}$. Nevertheless, rising or falling flanks of TTL-like voltage signals at the digital input channels are registered with a temporal resolution of 10 ns , and the limitation that it is only possible to buffer 254 of these events in memory.

A schematic map of the communication and wiring network of the setup is shown in fig. D.9. It illustrates the fact, that the ADwin communicates directly via Ethernet with a separate network card installed on the PC with a maximum transfer rate of 100 Mbit s^{-1} . The communication takes place via shared memory addresses that are physically located on the ADwin but do not interfere with the timing of the ADwin processes. A code loop of fixed process time checks for values changes at specific memory addresses and triggers the execution of programmed tasks on demand. Besides the exchange of data and commands with the PC, several other communication pathways originate from the ADwin. Analog voltages are emitted to control the AOD drivers' inputs (two channels per AOD) and the three target value control voltages of the nanopositioning stage axes. Because there are in total 9 voltages necessary to generate, one of the driver voltages to AOD1 (MOD IN, see appendix D.2) is not provided by the ADwin system but by a manually adjustable power supply.

While the ADwin's analog output sockets are fully occupied, only a few of the available analog inputs are used. A resistance thermometer based on a Pt1000 sensor (TEMOD-I2C, B+B Thermo-Technik GmbH) measures the ambient temperature next to the sample cell, and a photodiode (PDA55, Thorlabs Inc.) returns the relative excitation laser power.

Furthermore, the nanopositioning stage position sensors are monitored via these analog connections.

The digital input and output channels receive TTL-pulses from both APDs and send trigger pulses to the wide-field lens flipper. The excitation and detection shutter are open and closed by switching between the low and high TTL-level of the corresponding connection. TTL-level switching changes the position of the motorized wide-field mirror. To enable this, a dedicated controller box (ELUB 5/393/9) crafted by the university's electronics workshop, is interposed.

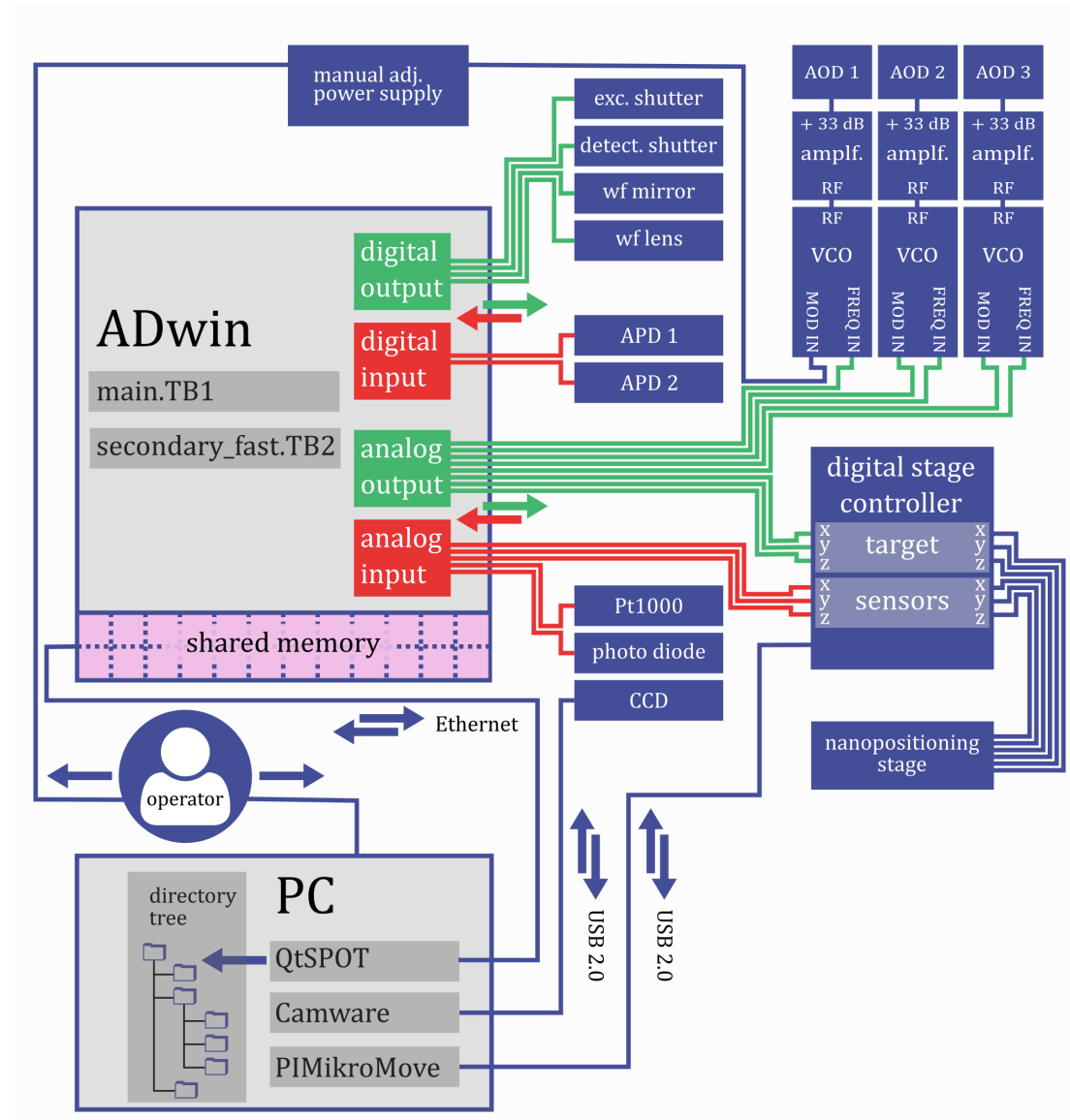


Figure D.9.: Layout of the communication pathways and the wiring of the devices.

D.7 | SOFTWARE

The SPOT setup is controlled by the ADwin system that communicates with a PC (Windows 10, 64 bit), where a graphical user interface enables the operation. That means specific programs running on the ADwin and the PC are necessary likewise.

The communication pathways are illustrated in fig. D.9. The core component that controls the current state of the setup is the main process (*main.TB1*) running on the ADwin system and supported by an additional process (*secondary_fast.TB2*) that runs faster. These two processes read and write into memory addresses that are physically located on the ADwin but also accessible from the PC without interfering with the ADwin's timing behavior. The shared memory is used for communication with a C++/Qt program and running on the PC. The PC control program is developed by myself and called "QtSPOT". It provides a *graphical user interface* (GUI) that enables the experimenter to view and adjust the setup parameters. QtSPOT serves as a platform to configure and display the setup and measurement state but also to inspect and analyze resulting data, directly. In fig. D.10, a screenshot of the QtSPOT interface while executing a FCS experiment is presented as an example. The measurement procedures are hardcoded into the software for high reproducibility, and the individual setting is written into the header of each measurement file (see appendix D.8 for a real example).

The source code is written in object-oriented C++ making extensive use of the Qt framework (Qt 5.12.6, MinGW 64-bit) not only for the creation of the GUI but also for string processing, timing, or hyper-threading. Special care was taken on performance and accuracy, especially for handling large photon arrival-time data sets, which are sometimes larger than 1 Gbyte due to the large amount of very high numbers (Minutes measured in ns). QtSPOT uses a lot of pointer arithmetic and fast algorithms taken from literature for this reason.[278]

Complex dependencies are avoided and, thus, the project depends only on the Qt framework, the ADwin driver class, and on the third-party widget "QCustomPlot" that is meant for data visualization. QCustomPlot (Version 2.0.0) is written by EMANUEL EICHHAMMER and distributed over the internet under the GNU General Public Licence (Version 3).[279] The Qt framework was used, because it is very common and freely available for non-commercial purposes. This means that support will be guaranteed for a long period of time without having to rewrite the entire project to a new framework. Since Qt runs on all platforms, the program code could also be changed to another operating system, such as Linux, in a very short amount of time. Only a few file system related functions of the existing source code are Microsoft Windows specific.

Despite QtSPOT's claim to control the complete experimental setup, additional programs are necessary for secondary tasks. The CCD camera, some aspects of the nanopositioning stage, and the communication with the TOPTICA laser are controlled by third-party software.

The CCD camera is not used for the SPOT algorithm, but only for simple time-lapse recordings or live-views of the sample. Therefore, the effort to integrate it properly into QtSPOT, maintaining all the features that are provided by the manufacturer software, was not reasonable. Currently, the camera is directly interfaced from the PC via USB 2.0 and the program Camware (V3.05, 64 bit, PCO AG).

The analog outputs of the ADwin adjust the nanopositioning stage's target, and the analog inputs read the position sensors. Therefore, all data transfer necessary for SPOT is executed by the ADwin system. However, the stage controller configuration is not

integrated into QtSPOT and the ADwin system, but a direct link from the PC via USB 2.0 and the third-party software PIMikro Move (2.20.016, Physik Instrumente (PI) GmbH & Co. KG) is utilized.

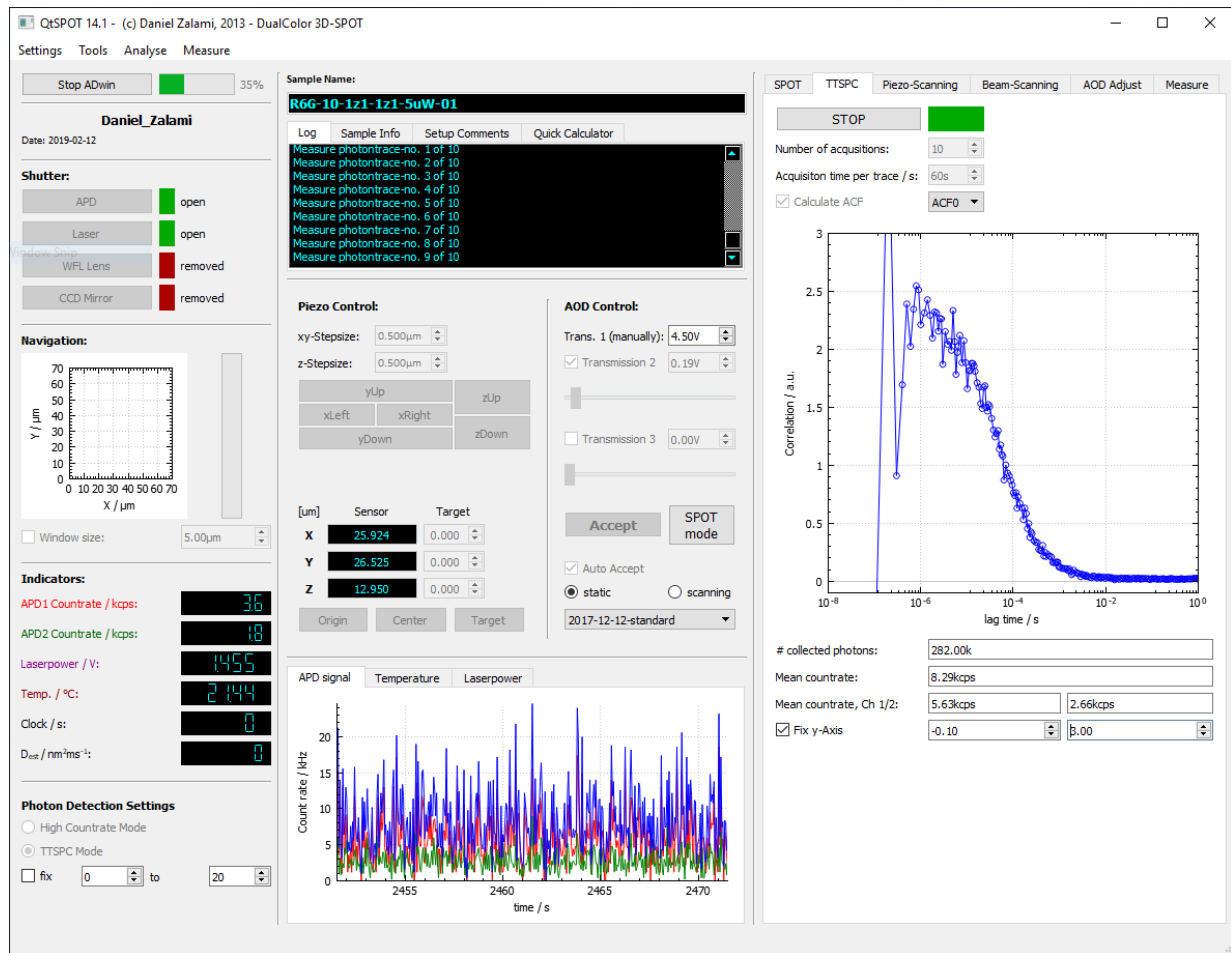


Figure D.10.: Screenshot of the main window of QtSPOT. The user interface is structured into three columns. The left and middle column are the general setup control and operator input features, presenting functionalities of universal usage. Both columns are again structured into modules serving different purposes, e.g., switching the shutter states, monitoring count rates, laser power or ambient temperature or controlling devices like the AODs. A dialog box reports on the current process status, error messages and successfully completed actions. In contrast, the right column is structured into tabs which provide control elements tailored for the specific measurement tasks. In the figure, the *time-tagged single-photon counting* (TTSPC) tab is selected yielding the control elements for a photon trace acquisition task. In the example, the operator has selected to record 10 photon traces of 60s each and to compute the fused detection channel autocorrelation function providing a FCS curve.

D.8 | EXAMPLE OF A SPOT MEASUREMENT FILE

SPOT measurements are stored on hard disc as ASCII-files consisting of a header and a tab-delimited table of the recorded data. All header lines start with a hash mark (#) and contain automatically generated information about the software and setup configuration. Additionally, manually entered notes about the sample and comments about the setup that are not recognized by the electronics are integrated as well. In the table-like tab-delimited file part, each line corresponds to a single particle localization step of the SPOT procedure starting with the earliest point in time.

```
# 3D DUAL COLOR SPOT FILE
# Tracking type: 3D, 15.0
#
#   Filename:   D:\QtSPOT\Daniel_Zalami\spot\2019-12-05\S64-I-25nm-messreihe1_0034.traj
#   Version:    15.0
#   Date:       Thu Dec 05 13:41:30 2019
#
#   Photon Counting Mode: Time Tagged Single-Photon Counting (TTSPC)
#   Temperature / C:    21.673
# =====
# LASER FOCI AND ORBITS PROPERTIES
#   Laser Wavelength / nm: 519.00      635.00
#   Waist X          / nm: 200.00      200.00
#   Waist Y          / nm: 200.00      200.00
#   Waist Z          / nm: 1000.00     1100.00
#   Radius X         / nm: 160.00      190.00
#   Radius Y         / nm: 160.00      190.00
#   Orbit distance   / nm: 1000.00     1000.00
# =====
# PIEZO STAGE SETTINGS
#   Unit of digit XYZ / nm: 1.068      1.068      0.763
#   Used piezo sensor calibration parameter settings:
#   Function: position / micrometer = p0+p1*x+p2*x^2+p3*x^3 with x in digit
#           p0, p1, p2, p3 of
#   X:      -3.02867375e+005  1.42141399e+001  -1.66563972e-004  1.33171718e-009
#   Y:      -2.57020516e+005  8.29910564e+000  4.30092914e-005  -8.48165260e-010
#   Z:      -3.95800562e+005  1.96430740e+001  -2.79246538e-004  2.26451657e-009
# =====
# AOD SETTINGS
#   Scanpattern file: D:\QtSPOT\Daniel_Zalami\aodpattern\2017-12-12-standard.orbit
#   Transmission 1 / V: 4.500 (manually set, maybe wrong)
#   Transmission 2 / V: 0.250
#   Transmission 3 / V: 0.250
#   Offset 1 / V:      4.950
#   Offset 2 / V:      4.950
#   Offset 3 / V:      4.950
#   Block 1 / V:       0.000
#   Block 2 / V:       0.000
#   Block 3 / V:       0.000
# =====
# PHOTONTRACE SETTINGS
#   Number of Photon Traces: 1
#   Acquisition time / s:    9
# =====
# SPOT SETTINGS
#   Feedback Frequency / Hz: 250.00
#   Feedback Period / ms:   4.00
#   Timeresolution / ms:   1.33
#   Scale Factor XYZ C1 / nm: 125.000      125.000      125.000
#   Scale Factor XYZ C2 / nm: -1.000      -1.000      -1.000
#   Number of orbit cycles per position: 3
#   Stop count rate threshold / Hz: 500.000000
# =====
```

```

# =====
# SETUP COMMENTS:
# >      Lichtquelle: 519 nm iBeam Smart  von TOPICA, im CW Modus
# >      10mW nach Faser
# >      Exc.: Lambda/4 Platte
# >      Objektiv: Olympus UPlanSApo 60x, NA = 1.2, Wasserimmersionsobjektiv
# >      Strahlteiler: LP 532 (Datenbank No.:778)
# >      Detect.: LP542(Datenbank No. 786); 2APDs (50:50 BS, Datenbank No. 1122)
# >      Piezo: P-545.3D8S Pinano Trak Piezo Tracking System,
# >      Physik Instrumente, mit PI(D)-Regelung:
# >      X ( Notch 0.05(at) 1700 Hz, P = 2.00, I=  60 e-5, D=2 e-4)
# >      Y ( Notch 0.05(at) 1640 Hz, P = 2.70, I=  80 e-5, D=3 e-4)
# >      Z ( Notch 0.05(at) 1700 Hz, P = 4.50, I= 120 e-5, D=3e-4)
# =====
# SAMPLE COMMENTS:
# >      keine Angaben
# =====
# Has photon arrival times file: no
# =====
# Structure of the follwing data:
#      stage position target x / digits
#      stage position target y / digits
#      stage position target z / digits
#      stage position sensor x / digits
#      stage position sensor y / digits
#      stage position sensor z / digits
#      particle positon with respect to orbits center x / digits
#      particle positon with respect to orbits center y / digits
#      particle positon with respect to orbits center z / digits
#      emitted photons channel 1/ number
#      emitted photons channel 2/ number
#      temperature next to sample / C
#      photodiode that detects laser power / V
# =====
30988 40798 26200 31016 40827 26196  8 -28 -104  9 13 21.67 0.651666
30988 40798 26200 31016 40802 26196 -34 -38 -22 58 51 21.67 0.651666
30988 40798 26200 31031 40810 26222 -26 -23 -11 46 68 21.67 0.651666
31014 40821 26211 31039 40852 26230  -6 -18 -26 55 52 21.67 0.651666
31014 40821 26211 31047 40835 26222 -22 -25 -28 68 84 21.67 0.651666
:      :      :      :      :      :      :      :      :      :      :      :
:      :      :      :      :      :      :      :      :      :      :      :
:      :      :      :      :      :      :      :      :      :      :      :

```


E | SUPPORTING MEASUREMENTS

E.1 | ROLLING-BALL VISCOMETRY

The dynamic viscosity of glycerol/water mixtures was measured in dependency of temperature and weight concentration with a rolling-ball viscometer (AMVn, Anton Paar GmbH) and density and sound velocimeter (DSA 500 M, Anton Paar, used to determine the corresponding density). The resulting parametrization is presented in fig. E.1. Similar measurements are conducted to determine the dynamic viscosity of 2,2'-thiodiethanol (TDE) and 53 vol% TDE diluted in an aqueous buffer (see fig. E.2).

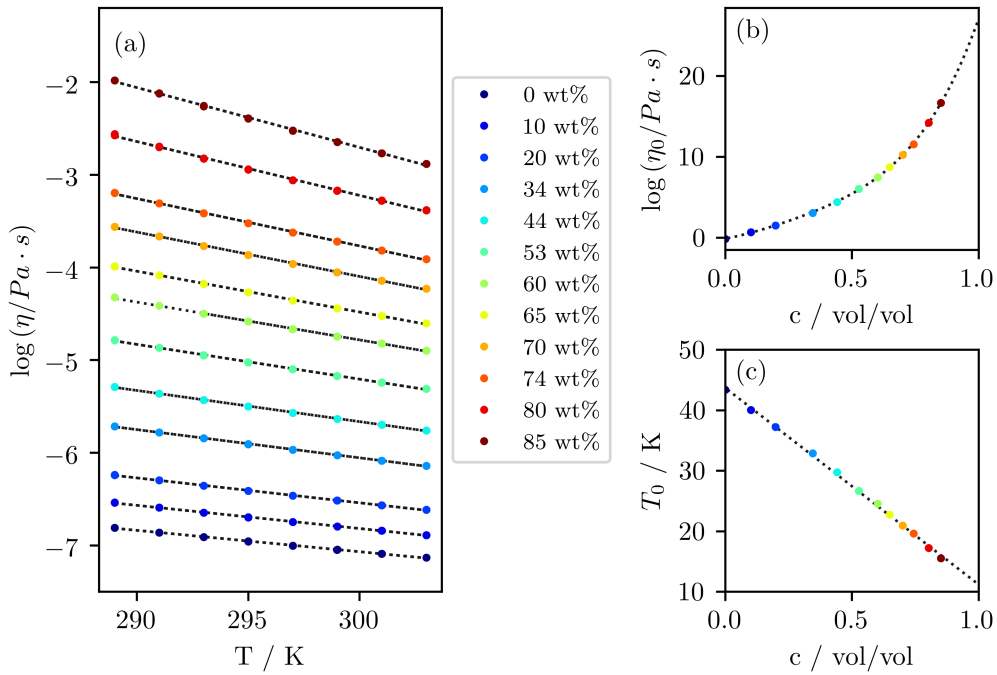


Figure E.1.: (a) Dynamic viscosity of different glycerol/water mixtures in the temperature range 16 °C to 30 °C. The measurement data are shown as colored dots, with the color code indicating the concentration in wt%. The natural logarithm of the viscosity of each mixture was fitted with a straight line, being equivalent to a monoexponential decay of the form $\eta_{\text{glycerol-water}}(c, T) = \eta_0(c) \exp\{-T/T_0(c)\}$. The concentration dependent fit-parameter, namely the amplitude $\eta_0(c)$ and temperature constant $T_0(c)$, are plotted in (b) and (c), respectively. The natural logarithm of the amplitude follows a fourth order polynomial given by $\log \eta_0(c) = 36.2860 \cdot c^4 - 33.2703 \cdot c^3 + 18.53548 \cdot c^2 + 5.6071 \cdot c - 0.1254$ and the concentration dependency of the decay temperature is represented by a straight line parametrized as $T_0(c) = -32.5154 \text{ K} \cdot c + 43.6899 \text{ K}$.

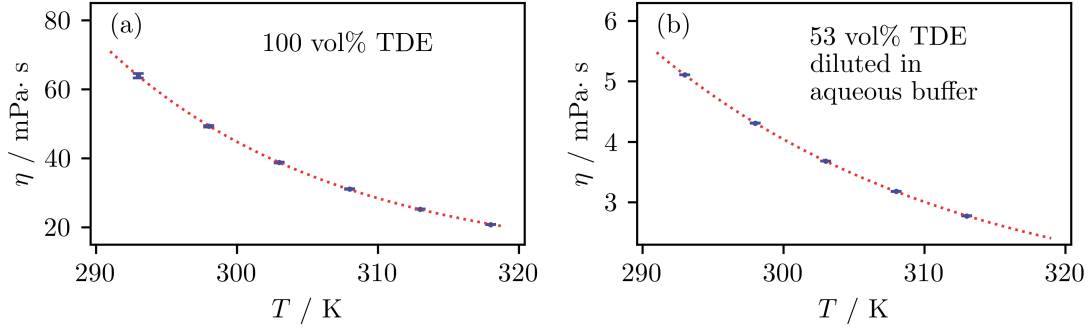


Figure E.2.: Dynamic viscosity of (a) 2,2'-thiodiethanol (TDE) and (b) TDE diluted with buffered water to 53 vol%, both solutions are measured for different temperatures with a rolling-ball viscometer (AMVn, Anton Paar GmbH). Exponential decay fit functions are drawn as red dotted lines and are given by the equations $\eta_{\text{TDE},100 \text{ vol}\%}(T) = (3.20 \pm 1.01) \times 10^9 \text{ mPa s} \cdot \exp(-T/(16.39 \pm 0.32) \text{ K}) + (8.93 \pm 0.55) \text{ mPa s}$ and $\eta_{\text{TDE},53 \text{ vol}\%}(T) = (2.610 \pm 0.431) \times 10^9 \text{ mPa s} \cdot \exp(-T/(21.28 \pm 0.28) \text{ K}) + (1.21 \pm 0.03) \text{ mPa s}$.

E.2 | REFRACTIVE INDEX MATCHING

The refractive index of 2,2'-thiodiethanol (TDE) and a respective mixture with water are characterized with a refractometer (Abbemat, Anton Paar GmbH) at multiple wavelengths (see fig. E.3). In order to visualize the mechanism of refractive index matching of the solvent with the $\text{PS}_{43}\text{-}b\text{-PI}_{40}\text{-}b\text{-PNIPAAm}_{17}$ membrane used for the experiments in chapter 8, a membrane cutting was immersed in TDE and pure water and photographed from top view (see fig. E.4).

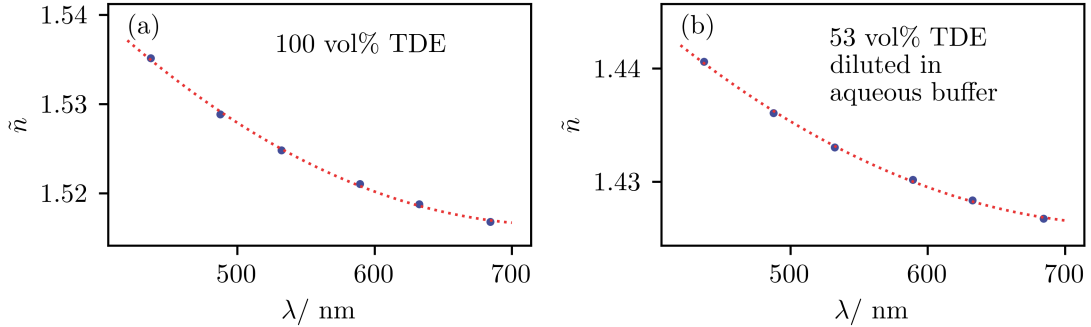


Figure E.3.: Refractive index of (a) 2,2'-thiodiethanol (TDE) and (b) TDE diluted with buffered water to 53 vol%, both solutions are measured at 20 °C with a refractometer (Abbemat, Anton Paar GmbH) at multiple wavelengths. Errorbars are too small to show. The refractive at $\lambda = 520 \text{ nm}$ is 1.53 for pure TDE and 1.43 for the diluted solution. Polynomial fit functions are drawn as red dotted lines and are given by the equations $\tilde{n}_{\text{TDE},100 \text{ vol}\%}(\lambda) = 211.3 \times 10^{-9} \text{ nm}^{-2} \cdot \lambda^2 - 309.8 \times 10^{-6} \text{ nm}^{-1} \cdot \lambda + 1.630$ and $\tilde{n}_{\text{TDE},53 \text{ vol}\%}(\lambda) = 143.5 \times 10^{-9} \text{ nm}^{-2} \cdot \lambda^2 - 216.1 \times 10^{-6} \text{ nm}^{-1} \cdot \lambda + 1.507$.

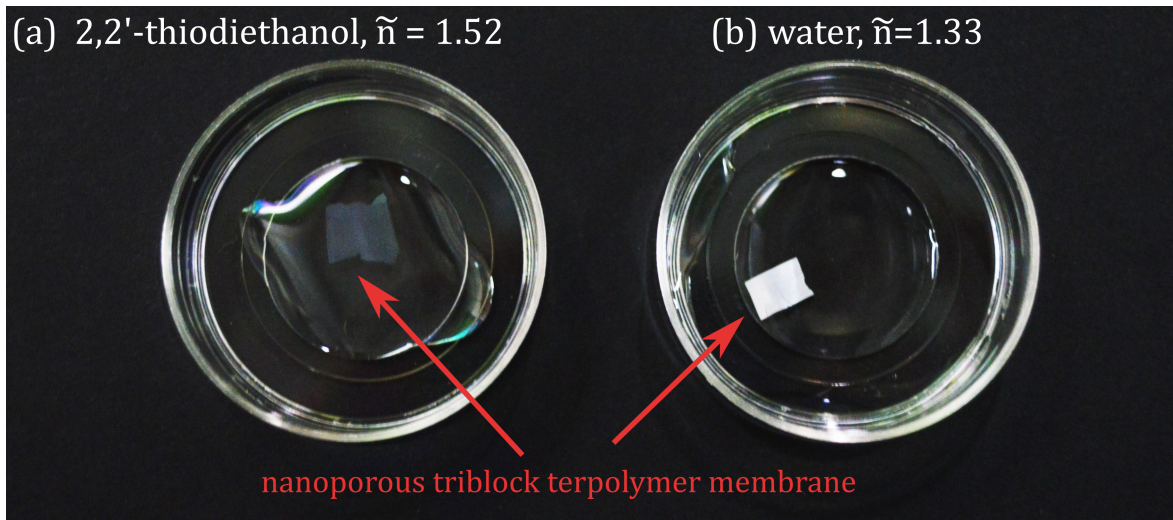


Figure E.4.: Photography to illustrate the effect of refractive index matching on the light scattering of the $\text{PS}_{43}\text{-}b\text{-PI}_{40}\text{-}b\text{-PNIPAAm}_{17}$ membrane. In (a) the membrane is immersed in 2,2'-thiodiethanol (TDE) with a refractive index of $\tilde{n}_{\text{TDE}} = 1.5$ and in (b) in pure water with a refractive index of $\tilde{n}_{\text{H}_2\text{O}} = 1.33$ in the visible wavelength range.

E.3 | ENVIRONMENTAL SCANNING ELECTRON MICROSCOPE MICROGRAPHS

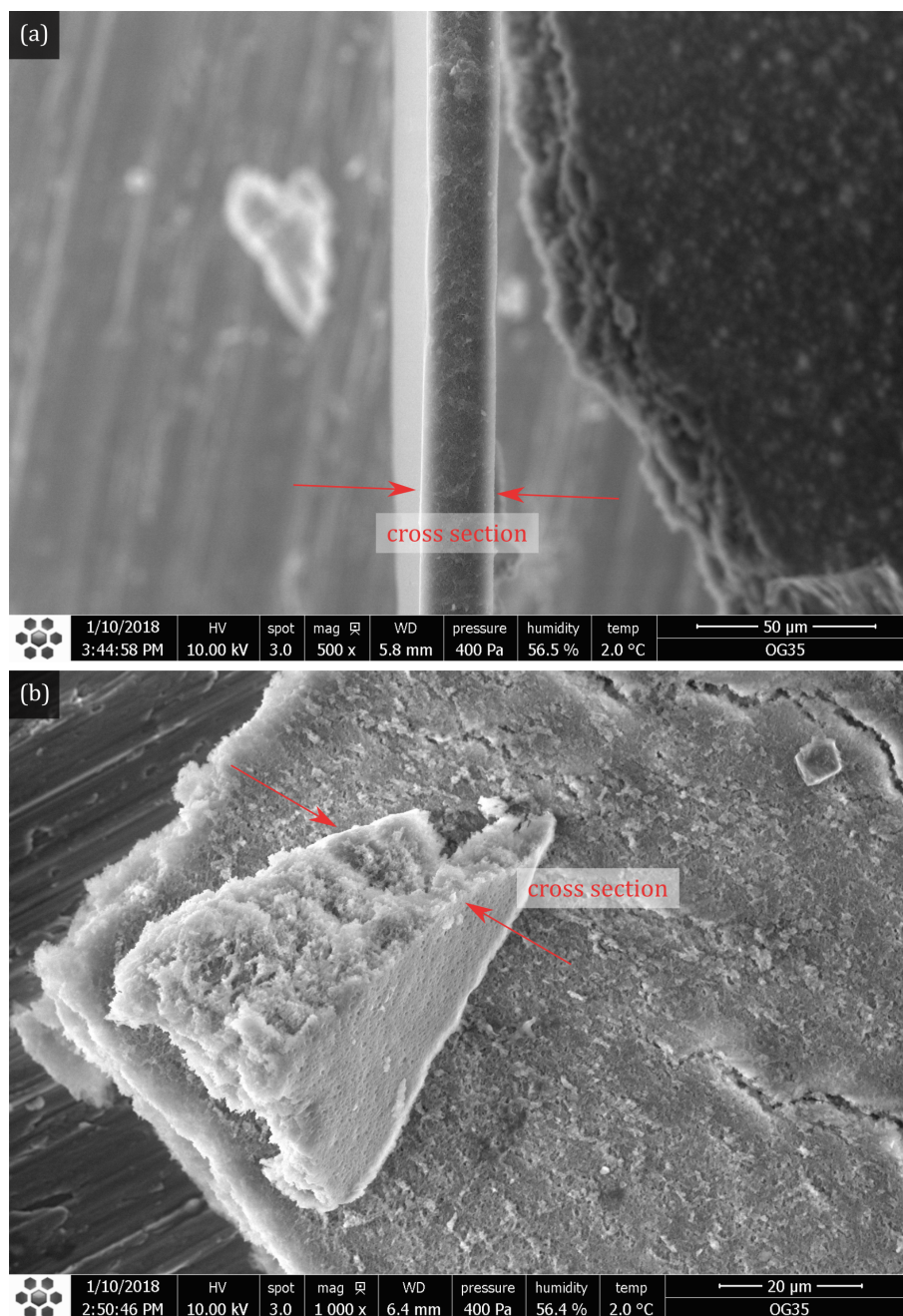


Figure E.5.: Cross sectional view of the PS₄₃-*b*-PI₄₀-*b*-PNIPAA_{m17} triblock terpolymer membrane showing a thickness of (a) $(20 \pm 1) \mu\text{m}$ and (b) $(19 \pm 5) \mu\text{m}$.

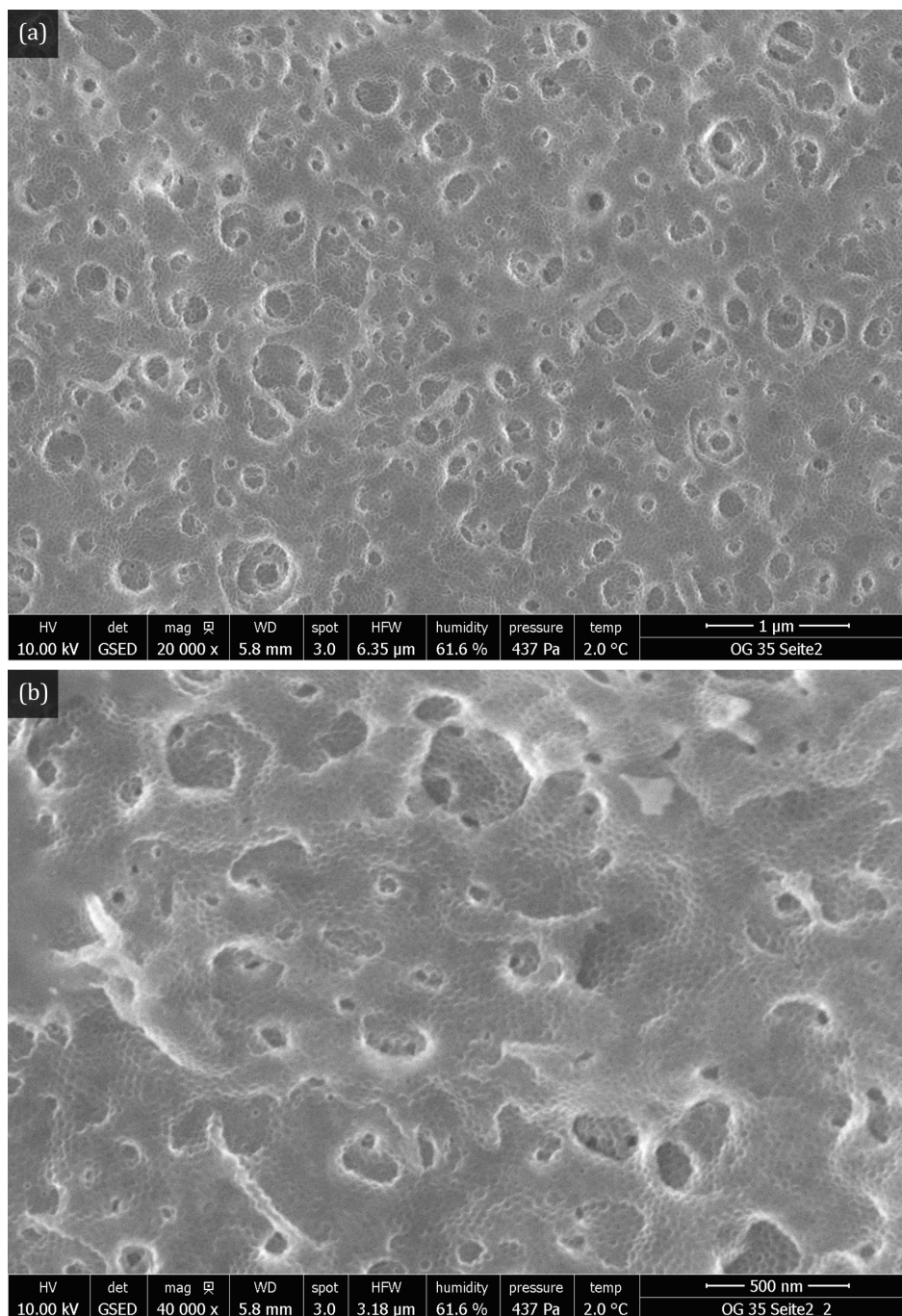


Figure E.6.: Highly magnified (top-view) sections of the $\text{PS}_{43}\text{-}b\text{-PI}_{40}\text{-}b\text{-PNIPAAm}_{17}$ triblock terpolymer membrane revealing an additional nanostructure in the 20 nm range corresponding approximately to the contour length of the used polymer.

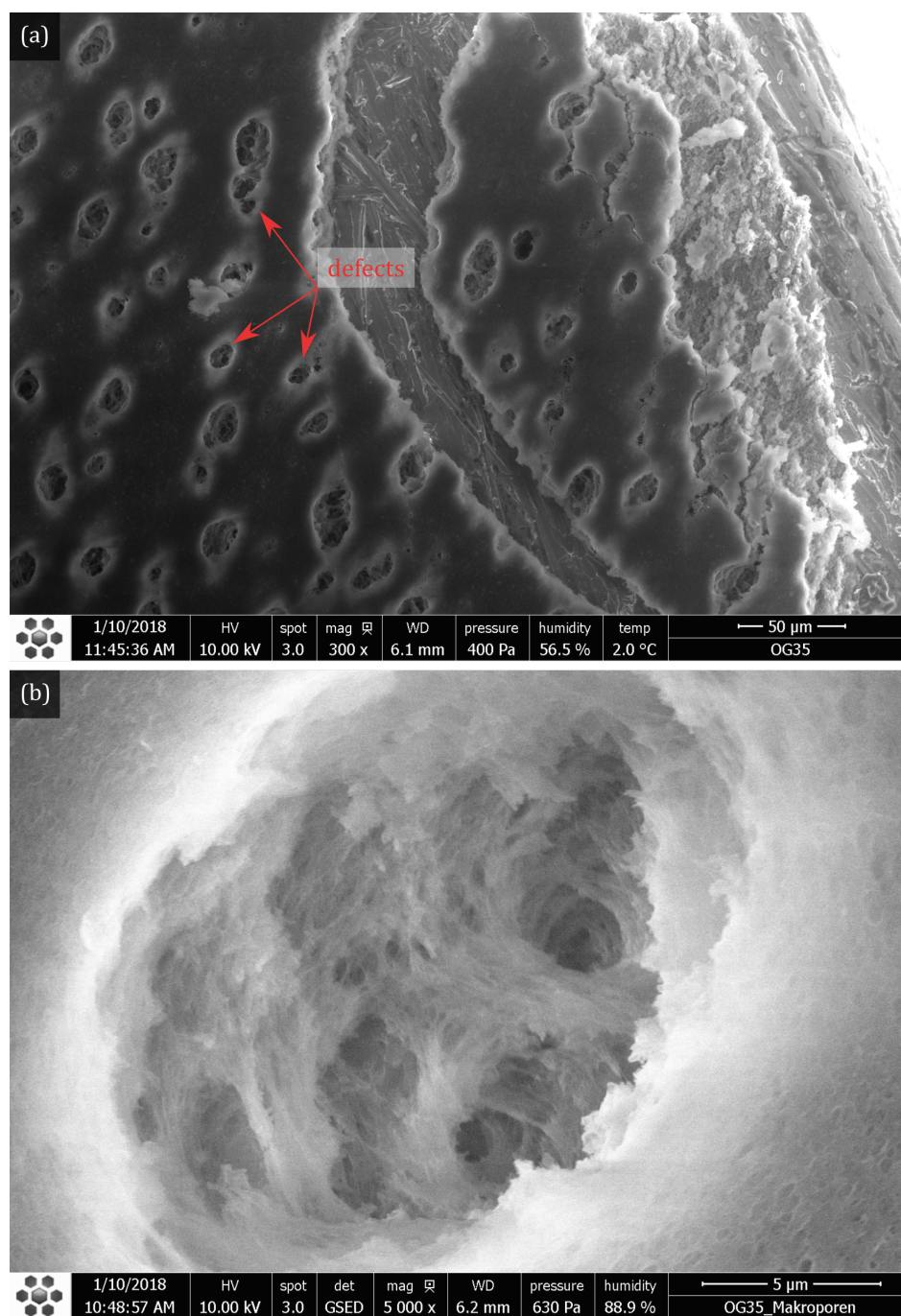


Figure E.7.: (a) Membrane cutting of the $\text{PS}_{43}\text{-}b\text{-PI}_{40}\text{-}b\text{-PNIPAAm}_{17}$ triblock terpolymer membrane with defects appearing as large macropores with sizes in the range of 10 μm to 30 μm . (b) Zoom onto a single macropore.

E.4 | 2C3D-SPOT TRAJECTORIES

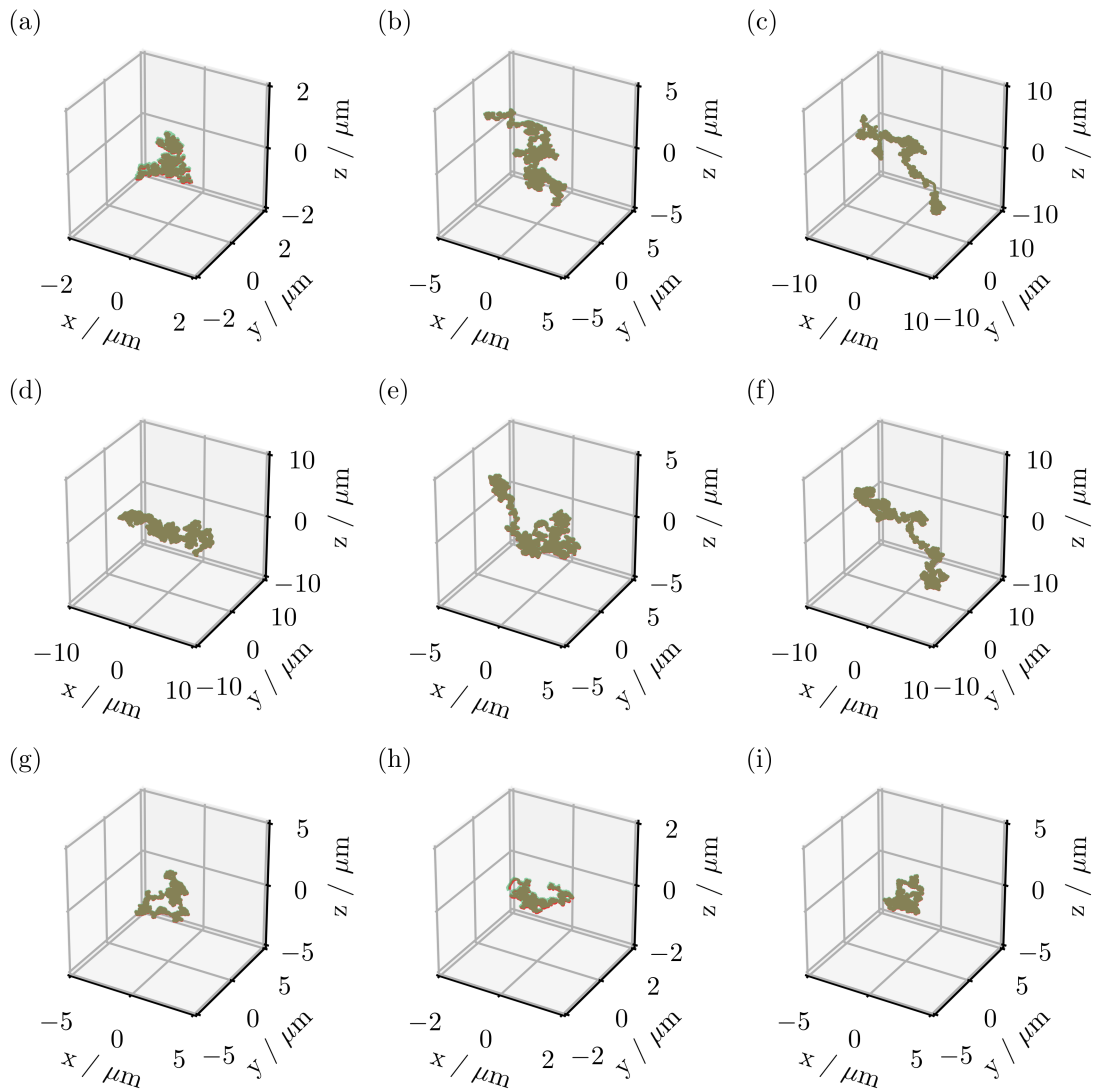


Figure E.8.: Recorded 2C3D-SPOT trajectories. Each graph is a single measurement of two color channels, with channel 1 drawn in red and channel 2 in green. For the eye, the overlap of both channels is perfect and due to the slight transparency of the channels, the visual impression is that of a mixed color in ocher.

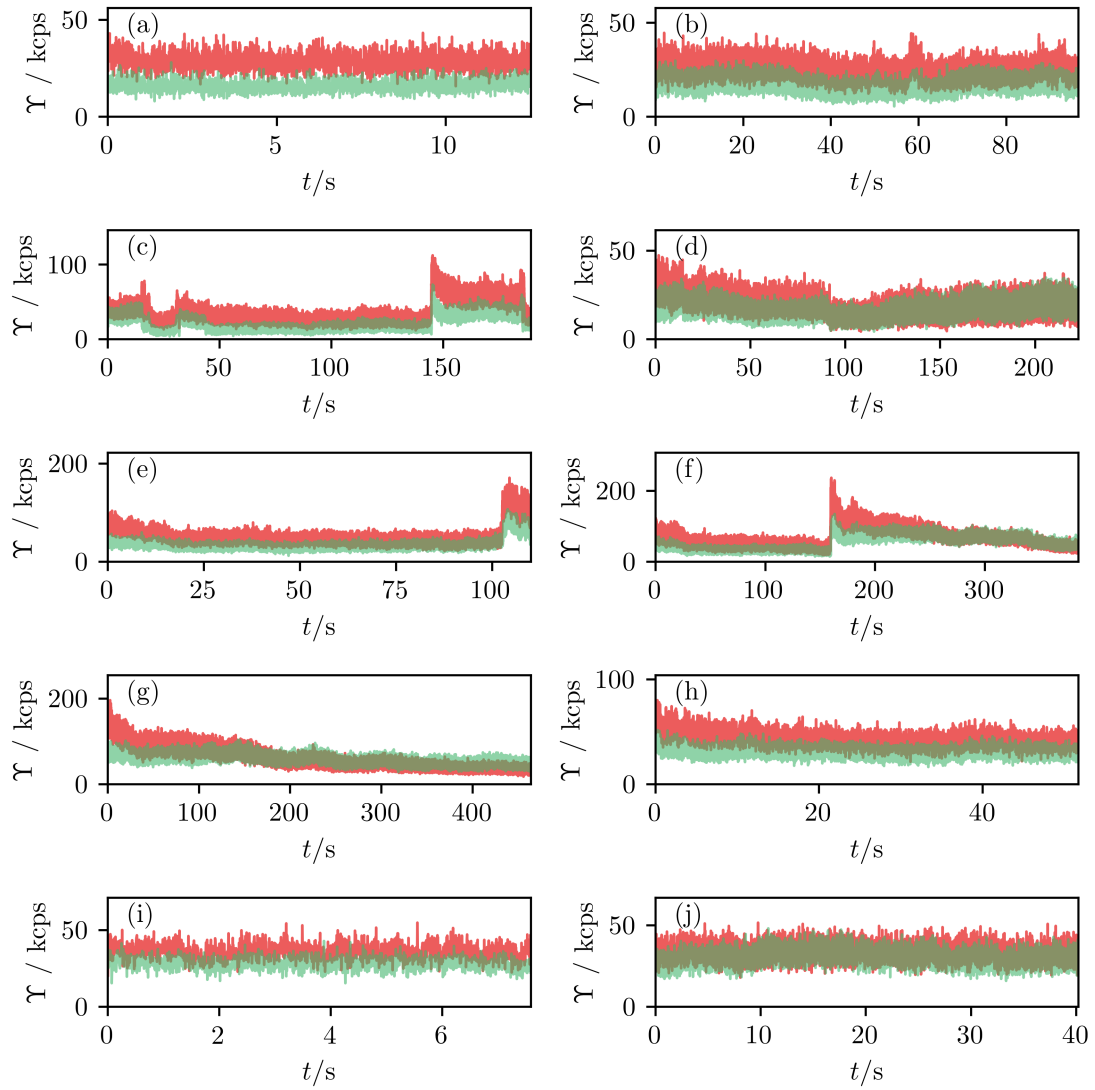


Figure E.9.: Detected fluorescence rates of the respective trajectories in fig. E.8. The alphabetic labeling of the experiments as (a), (b), etc. is the same as in the trajectory overview.

ABBREVIATIONS, SYMBOLS AND CONVENTIONS

CONVENTIONS

- Bold symbols \mathbf{x} are multidimensional variables like vectors or matrices; Non-bold symbols x are scalars or scalar functions.
- The dependency of a function on a continuous-time variable is expressed in round brackets, e.g., $f(t)$; The dependency on a discrete-time variable is expressed in square brackets, e.g., $f[k]$.
- A symbol with an hat, for example \hat{f} represents the measured or estimated value of the corresponding variable f .
- Time-derivatives are expressed by a dot on top of the symbol. The time-derivative of $f(t)$ is written as $\dot{f}(t)$, for instance.
- Cartesian coordinates are symbolized by x , y and z , where the first two are the lateral coordinates and the z -direction is the axial direction
- The complex conjugate of a number z is noted as z^*
- Cylinder coordinates are symbolized by the radial distance ρ , the azimuthal angle φ and the height z . Cylinder coordinates are related to Cartesian coordinates via $x = \rho \cos \varphi$, $y = \rho \sin \varphi$ and $z = z$.

LIST OF ABBREVIATIONS AND ACRONYMS

AOD	Acusto optical deflector
AOTF	Acusto optical tunable filter
APD	Avalanche photodiode
CLA	Chord length analysis
CTRW	Continuous-time random walk
eSEM	Environmental scanning electron microscopy
FBM	Fractional Brownian motion
FCS	Fluorescence correlation spectroscopy
FFT	Fast Fourier transformation
FLE	Fractional Langevin equation
FRET	Fluorescence resonance energy transfer
GUI	Graphical user interface
LCST	Lower critical solution temperature
LTI	Linear time-invariant system
MDF	Molecule detection efficiency function
MIMO	Multiple input/multiple output system
MINFLUX	Minimal emission flux microscopy
MSD	Mean squared displacement
NIPS	Non-solvent induced phase separation
nVACF	Normalized velocity autocorrelation function
PD	Probability density
PID	Proportional–integral–derivative (controller)
SEM	Scanning electron microscopy
SISO	Single input/single output system
SNIPS	Self-assembly and non-solvent induced phase separation
SPOT	Single-particle orbit tracking
SPT	Single-particle tracking
STED	Stimulated-emission-depletion
TDE	2,2'-thiodiethanol
TTL	Transistor–transistor logic
UIR	Unit impulse response
USR	Unit step response
VCO	Voltage controlled oscillator

LIST OF SYMBOLS

$\mathbb{1}$	Unity matrix
$\mathbf{A}, \mathbf{A}(t)$	System or dynamic matrix
A_1, A_2	Confinement geometry factors
$A_l(\rho_p, z_p)$	Auxiliary variable, constant signal amplitude
A_{void}	Void area
a	Particle diameter
a_{\circlearrowleft}	Aperture diameter (projected into the sample plane)
$\text{adj}(\mathbf{X})$	Adjugate matrix \mathbf{X}
$\mathbf{B}, \mathbf{B}(t)$	Input matrix
$\mathcal{B}(t)$	Brownian motion process
$\mathbf{B}_\nu, \mathbf{B}_\nu(t)$	Input matrix of a noise term
\mathbf{B}_{f_1, f_2}	Ray transfer matrix of a beam-expander system
$\mathbf{b}_{\text{in}}^{x,y}, \mathbf{b}_{\text{out}}^{x,y}$	Input and output beam state vectors along x - or y -direction
\mathbf{C}	Output matrix
c_s	speed of sound c_s inside a crystal
$\mathcal{C}\{f(t)\}(\omega)$	Cosine transformation of function $f(t)$ into ω -domain
$c(t, \mathbf{r})$	Concentration profile of a substance
$\text{circ}(\mathbf{r})$	disk function
\mathbf{D}	Feed forward matrix
D	Diffusion coefficient
$D_\alpha, \tilde{D}_\alpha$	Generalized diffusion coefficient
$d_z, d_{z,\text{opt}}$	Axial orbit distance and optimal axial orbit distance
$\text{demod}(t)$	Demodulation function
$\det(\mathbf{X})$	Determinant of a matrix \mathbf{X}
$E_{a,b}(x), E_a(x)$	(Generalized) Mittag-Leffler function
$\mathcal{E}(x)$	Expectation value of x
$e(t), E(s)$	Error signal and its Laplace transform
$e_{\text{dyn}}[k]$	Dynamic localization error
$e_{\text{loc}}[k]$	Localization error
$e_{\text{static}}[k]$	Static localization error
$e_{\text{stat}}[k]$	Statistical localization error
$e_{\text{sys}}[k]$	Systematic localization error
$F(t)$	Fluorescence rate
F_0	Peak fluorescence signal
F_B	Background fluorescence rate
$F_S(t, \mathbf{r}_p)$	Time- and particle position dependent fluorescence rate
$F_t(\omega)$	Time-dependent complex frequency component of a fluorescence rate at ω
$\mathfrak{F}(\mathbf{p}, \mathbf{r}, t), \tilde{\mathfrak{F}}(\mathbf{p}, \mathbf{r}, t)$	Auxiliary symbol for the fluorescence rate distribution
$\mathcal{F}\{f(t)\}, \mathcal{F}\{f(t)\}^{-1}$	Fourier and inverse Fourier transformation of function $f(t)$ into ω -domain
f_i	Focal length of lens L_i
$f_{\text{eG}}(x)$	Gaussian curve with exponential tail
$f_{\text{sG}}(x)$	Stretched Gaussian curve
$f_{\text{exp}}(\tau)$	Exponential saturation law
$f_{\text{ml}}(\tau)$	Mittag-Leffler function based saturation law
$f_{\text{pl}}(\tau)$	Power-law based flattening law
$\mathbf{G}(s), \mathbf{G}[z]$	Transfer function (matrix) and discrete transfer function (matrix)
$\mathbf{G}(\omega)$	Frequency response (matrix)
$\mathbf{G}_{sc}(s), G_{sc}(s)$	Stage- stage controller transfer function (matrix)
$G_{\text{multi-parameter}}(s)$	Multi-parameter model of a transfer function

$G_{\text{forced osci.}}(s)$	Transfer function of a forced oscillator
$G_{\text{PID, osci.}}(s)$	Transfer function of a PID controlled oscillator
$\mathbf{g}(t)$	Unit impulse response (matrix), UIR
H	Hurst exponent
$I_{\text{exc}}(\mathbf{p}, \mathbf{r})$	Laser excitation profile centered at \mathbf{p}
$I_n(x)$	Modified Bessel function of the n th kind of order one and argument x
i	Running index
$J_n(x)$	Bessel function of the n th kind of order one and argument x
$j_l(x)$	Spherical Bessel function of the l th kind of order one and argument x
j	Imaginary unit or running index (dependent on context)
\mathbf{K}	Gain matrix of a feedback system
$\mathcal{K}_{\text{fgn}}(t - t')$	Fractional gaussian noise memory kernel
K_p, K_i, K_d	Proportional, integral and derivative controller gain
k	Running index
k_B	Boltzmann constant, $1.380\,649 \times 10^{-23} \text{ J K}^{-1}$
k_{dc}	DC gain of a second order system
k_{ou}	Inverse Ornstein-Uhlenbeck noise relaxation time
k_ω	Spring constant
$L, \hat{\mathcal{L}}, \hat{L}$	Confinement size, Measured and corrected confinement size
\mathcal{L}_f	Ray transfer matrix of a thin lens with focal length f
$\mathcal{L}\{f(t)\}, \mathcal{L}\{f(t)\}^{-1}$	Laplace and inverse Laplace transformation of function $f(t)$ into s -domain
$M(a, b, x)$	Kummer function
\mathcal{M}	Demodulation matrix
$\mathcal{M}^{x,y}(z)$	Ray transfer analysis matrix for x - or y -deflection
$\text{MDF}(\mathbf{r})$	Molecule detection efficiency function
$\text{MDF}_{\text{mGL}}(t, \mathbf{r}),$	Modified Gaussian-Lorentzian molecule detection efficiency function
$\text{MSD}(\tau)$	Mean squared displacement
m	Mass
m_{void}	Circularity parameter
NA	Numerical aperture
$N_{\text{particles}}$	Particle number
N_{ph}	Integrated fluorescence signal
N_{max}	Integrated peak fluorescence signal
N_{pos}	Number of recorded positions
N_τ	Number of MSD points within a given interval for τ
$\mathcal{N}(a, b)$	Normal distribution with mean a and standard deviation b
$n_{ph}[k]$	Binned photon trace
\tilde{n}	Refractive index
n	Noise density
$n(t)$	Time-dependent noise density
n_{cycles}	Number of position estimation cycles before feedback application
n_s	Number of photon counting sampling points per scan period
$\text{nVACF}_{\Delta\tau}(\tau)$	Normalized velocity autocorrelation function
n_{sp}	Number of scan periods
P_1, P_2	Position correlation functions
$P_{k\Gamma}$	k -Gamma distribution
P_{CLA}	Morphological pore size distribution
$\mathcal{P}(r, t), \mathcal{P}(r, t r', t)$	Positional probability density function
$\mathcal{P}_{\text{ctrw}}(r, t)$	Positional probability density function of a continuous-time random walk
$\mathcal{P}_{\text{fbm}}(r, t)$	Positional probability density function of a fractional Brownian motion
$\text{PSF}(\mathbf{r})$	Point-spread function

p_i	Coefficients of a polynomial
$\mathbf{Q}(t), \mathbf{Q}_\infty$	Time-dependent and steady-state process variance matrix
R, R_{opt}	Orbit radius and optimal orbit radius
$\mathbf{R}_\nu(\tau)$	Covariance vector
\mathcal{R}	Ray transfer matrix of a relay system
$\mathcal{R}(z)$	"Detection waist" function
\mathcal{R}_0	Minimal "detection waist"
\mathcal{R}_z	Characteristic length scale of "detection waist" divergence
$\mathbf{r}, r, \hat{\mathbf{r}}, \hat{r}$	Particle position (three or one dimensional) and its estimate
$\mathbf{r}_p, \hat{\mathbf{r}}_p$	Particle position with respect to the center point and its estimate
$\mathbf{r}_s, \hat{\mathbf{r}}_s$	Stage position and its estimate
$\tilde{\mathbf{r}}[i]$	Noise-free stage response
$\bar{\mathbf{r}}[k]$	Mean particle position of a scan period
$\langle r^2 \rangle_{\text{th}}, \langle r^2 \rangle_{\alpha, \text{th}}$	mean thermal squared position
\mathbf{r}_L	Scan path of a laser focus
r_ν	Covariance of the Brownian kick-term $\nu(t)$
$S(s)$	(Pure) stage transfer function
$\mathcal{S}^x, \mathcal{S}^y$	Ray transfer matrix for x - and y -beam deflection
$S\{f(t)\}(\omega)$	Sinus transformation of function $f(t)$ into ω -domain
$Sq\{f(t)\}(\omega)$	Square wave transformation of function $f(t)$ into ω -domain
s	Laplace space variable, complex frequency
$\text{sqw}(x)$	Square wave function with argument x
\mathcal{T}_d	Ray transfer matrix of a translation by d
T	Duration, time span
\mathcal{T}	Temperature
\mathcal{T}_d	Ray transfer matrix of a free space translation by a distance d
t	Time
U_{defl}	Voltage applied to the FREQ IN input of the AOD driver
$U_{\text{intensity}}$	Voltage applied to the MOD IN input of the AOD driver
$U_\omega(r)$	Harmonic potential
$\mathbf{u}(t), \mathbf{U}(s)$	Input vector and its Laplace transform
$\mathbf{u}_{\text{tar}}(t), \mathbf{U}_{\text{tar}}(s)$	Reference/target signal and its Laplace transform
$u_\nu(t)$	Stage control voltage
$\mathbf{V}, \mathbf{V}(\tau)$	Covariance amplitude
$w(z)$	Laser beam waist function
w_c	Lateral $1/e^2$ -laser beam waist in the center plane of a two orbit geometry
$w_{1,2}(z_p)$	Auxiliary variable, beam waist in orbit plane
w_n	Wiener process for photon counting
$w_p, W_p(s)$	Wiener process for particle position noise and its Laplace transform
w_{xy}	Lateral $1/e^2$ -laser beam waist
w_z	Axial laser beam waist
$\mathbf{x}(t), \mathbf{X}(s)$	System state and its Laplace transform
$\mathbf{x}[k], \mathbf{X}[z]$	Discrete system state and its z -Transform
$\mathbf{y}(t), \mathbf{Y}(s)$	Output vector and its Laplace transform
$\mathbf{y}[k], \mathbf{Y}[z]$	Discrete output vector and its z -Transform
$\mathbf{y}_{\text{USR}}(t)$	Unit step response (matrix), USR
z	z -space, variable, complex frequency
z_{focus}	Focus position with respect to focal plane
$\alpha, \bar{\alpha}, \alpha(\tau)$	Anomaly parameter and averaged and lag time-dependent anomaly
$\Gamma(x)$	Gamma function
$\Gamma(z, x)$	Complementary incomplete Gamma function

$\delta(t)$	Dirac-delta distribution
$\Delta \mathbf{r}_{\Delta\tau}(t)$	Increment vector
Δt	Time difference, time step of a single position estimation cycle
δt	Photon-sampling time bin in simulation and experiment
ϵ_u	Nanopositioning stage noise vector
ζ_{PSF}	Auxiliary normalization factor
$\eta, \tilde{\eta}$	Dynamic viscosity and generalized dynamic viscosity
η_Q	Fluorescence quantum yield
θ_{defl}	Beam deflection angle with respect to the optical axis
$\kappa(z)$	Collection efficiency amplitude
$\Lambda_{xy}(\xi_\rho, \xi_z)$	Lateral scan pattern geometry function
$\Lambda_z(\xi_\rho, \xi_z)$	Axial scan pattern geometry function
λ	Damping coefficient
λ_{ctrw}	Increment distribution of a continuous-time random walk
λ_{exc}	Central excitation wavelength
λ_{em}	Central excitation wavelength
$\nu(t)$	Stochastic noise term
$\tilde{\nu}(t)$	Correlated noise term
$\nu_{\text{bm}}(t)$	Stochastic kick-magnitude of Brownian motion
$\nu_{\text{fgn}}(t)$	Fractional Gaussian noise
ν_{ou}	Ornstein-Uhlenbeck noise amplitude
ν_{RF}	(Electrical) radio frequency
ν_s	Acoustic wave frequency
ξ, ξ_α	Friction coefficient and generalized friction coefficient
π	Archimedes' constant, 3.141 592 653 59....
ρ	Radial coordinate
σ	Standard deviation of a particle localization
σ_t	Total tracking error (Average over a trajectory)
σ_u	Standard deviation of nanopositioning stage noise
$\sigma_{\Delta r}$	Standard deviation of particle displacements
τ	Lag time
$\tilde{\tau}$	Characteristic waiting time of a continuous-time random walk
$\Upsilon(t)$	Stochastic record of the fluorescence rate
$\Upsilon_t(\omega)$	Time-dependent complex frequency component of $\Upsilon(t)$ at frequency ω
$\Phi(s)$	Resolvent matrix
$\phi(t, \tau)$	State transition matrix
$\varphi_{\text{in}}, \varphi_{\text{out}}$	Input and output deflection angle
φ_{ampl}	Deflection amplitude
$\phi^{x,y}$	Deflection phase in x or y -direction
χ, χ	Tracking error vector and tracking error
$\psi_{\text{ctrw}}(\tau)$	Waiting time distribution of a continuous-time random walk
$\Omega_{l,t}^{(k)}(\rho_p, z_p)$	Auxiliary variable, azimuthal angle independent fluorescence signal part
$\omega, \tilde{\omega}$	Angular frequency
ω_0	Lateral orbit scan frequency
ω_n	Natural/resonance frequency
$ x $	Absolute value of x
\underline{z}	Phase value of a complex number z
∇	Nabla operator, gradient
Δ	Laplace operator

BIBLIOGRAPHY

- [1] Cristina Buzea, Ivan I. Pacheco, and Kevin Robbie. *Nanomaterials and nanoparticles: Sources and toxicity*. Biointerphases 2.4 (2007), MR17–MR71.
- [2] Florian Krammer, Gavin J.D. Smith, Ron A.M. Fouchier, Malik Peiris, Katherine Kedzierska, Peter C. Doherty, Peter Palese, Megan L. Shaw, John Treanor, Robert G. Webster, and Adolfo García-Sastre. *Influenza*. Nature Reviews Disease Primers 4.1 (2018), pp. 1–21.
- [3] Françoise Barré-Sinoussi, Anna Laura Ross, and Jean François Delfraissy. *Past, present and future: 30 years of HIV research*. Nature Reviews Microbiology 11.12 (2013), pp. 877–883.
- [4] E. Olavi Kajander and Neva Çiftçioglu. *Nanobacteria: An alternative mechanism for pathogenic intra- and extracellular calcification and stone formation*. Proceedings of the National Academy of Sciences of the United States of America 95.14 (1998), pp. 8274–8279.
- [5] Daniel Shegogue and W. Jim Zheng. *Object-oriented biological system integration: A SARS coronavirus example*. Bioinformatics 21.10 (2005), pp. 2502–2509.
- [6] Daniel DiMaio and John B. Liao. *Human Papillomaviruses and Cervical Cancer*. Advances in Virus Research 65.06 (2006), pp. 125–159.
- [7] Michael J. Pitkethly. *Nanomaterials – the driving force*. Materials Today 7.12 (2004), pp. 20–29.
- [8] Wendelin J. Stark, Philipp R. Stoessel, Wendel Wohlleben, and Andreas Hafner. *Industrial applications of nanoparticles*. Chemical Society Reviews 44.16 (2015), pp. 5793–5805.
- [9] Ernst Abbe. *Beiträge zur Theorie des Mikroskops und der mikroskopischen Wahrnehmung*. Archiv für Mikroskopische Anatomie 9.1 (1873), pp. 413–468.
- [10] B. Amos, G. McConnell, and T. Wilson. *Confocal microscopy*. Vol. 2. Elsevier Ltd., 2012, pp. 3–23. ISBN: 9780080957180.
- [11] Eric Betzig, George H. Patterson, Rachid Sougrat, O. Wolf Lindwasser, Scott Olenych, Juan S. Bonifacino, Michael W. Davidson, Jennifer Lippincott-Schwartz, and Harald F. Hess. *Imaging intracellular fluorescent proteins at nanometer resolution*. Science 313.5793 (2006), pp. 1642–1645.
- [12] Michael J. Rust, Mark Bates, and Xiaowei Zhuang. *Sub-diffraction-limit imaging by stochastic optical reconstruction microscopy (STORM)*. Nature Methods 3.10 (2006), pp. 793–795.

- [13] Stefan W. Hell and Jan Wichmann. *Breaking the diffraction resolution limit by stimulated emission: stimulated-emission-depletion fluorescence microscopy*. *Optics Letters* 19.11 (1994), p. 780.
- [14] Patrick Hoyer, Gustavo De Medeiros, Bálint Balázs, Nils Norlin, Christina Besir, Janina Hanne, Hans Georg Kräusslich, Johann Engelhardt, Steffen J. Sahl, Stefan W. Hell, and Lars Hufnagel. *Breaking the diffraction limit of light-sheet fluorescence microscopy by RESOLFT*. *Proceedings of the National Academy of Sciences of the United States of America* 113.13 (2016), pp. 3442–3446.
- [15] Francisco Balzarotti, Yvan Eilers, Klaus C Gwosch, Arvid H Gynnå, Volker Westphal, Fernando D Stefani, Johan Elf, and Stefan W Hell. *Nanometer resolution imaging and tracking of fluorescent molecules with minimal photon fluxes*. *Science* 355.6325 (2017), pp. 606–612.
- [16] Douglas Magde, Elliot L. Elson, and W. W. Webb. *Thermodynamic fluctuations in a reacting system measurement by fluorescence correlation spectroscopy*. *Physical Review Letters* 29.11 (1972), pp. 705–708.
- [17] Douglas Magde, Elliot L. Elson, and Watt W. Webb. *Fluorescence correlation spectroscopy. II. An experimental realization*. *Biopolymers* 13.1 (1974), pp. 29–61.
- [18] Elliot L. Elson and Douglas Magde. *Fluorescence correlation spectroscopy. I. Conceptual basis and theory*. *Biopolymers* 13.1 (1974), pp. 1–27.
- [19] M. Ehrenberg and R. Rigler. *Rotational brownian motion and fluorescence intensity fluctuations*. *Chemical Physics* 4.3 (1974), pp. 390–401.
- [20] Måns Ehrenberg and Rudolf Rigler. *Fluorescence correlation spectroscopy applied to rotational diffusion of macromolecules*. *Quarterly Reviews of Biophysics* 9.1 (1976), pp. 69–81.
- [21] P. Kask, P. Piksarv, and Ü. Mets. *Fluorescence correlation spectroscopy in the nanosecond time range: Photon antibunching in dye fluorescence*. *European Biophysics Journal* 12 (1985), pp. 163–166.
- [22] Jerker Widengren, Rudolf Rigler, and Ülo Mets. *Triplet-state monitoring by fluorescence correlation spectroscopy*. *Journal of Fluorescence* 4.3 (1994), pp. 255–258.
- [23] Elke Haustein and Petra Schwille. *Fluorescence correlation spectroscopy: Novel variations of an established technique*. *Annual Review of Biophysics and Biomolecular Structure* 36 (2007), pp. 151–169.
- [24] Christian Eggeling, Christian Ringemann, Rebecca Medda, Günter Schwarzmann, Konrad Sandhoff, Svetlana Polyakova, Vladimir N. Belov, Birka Hein, Claas v. Middendorff, Andreas Schönle, and Stefan W. Hell. *Direct observation of the nanoscale dynamics of membrane lipids in a living cell*. *Nature* 457.7233 (2009), pp. 1159–1162.
- [25] Carlo Manzo, Thomas S. Van Zanten, and Maria F. Garcia-Parajo. *Nanoscale fluorescence correlation spectroscopy on intact living cell membranes with NSOM probes*. *Biophysical Journal* 100.2 (2011), p. L8.
- [26] Lydia Kisley, Rachel Brunetti, Lawrence J. Tauzin, Bo Shuang, Xiyu Yi, Alec W. Kirkeminde, Daniel A. Higgins, Shimon Weiss, and Christy F. Landes. *Characterization of Porous Materials by Fluorescence Correlation Spectroscopy Super-resolution Optical Fluctuation Imaging*. *ACS Nano* 9.9 (2015), pp. 9158–9166.

-
- [27] Carlo Manzo and Maria F Garcia-Parajo. *A review of progress in single particle tracking: from methods to biophysical insights*. Reports on Progress in Physics 78.12 (2015), p. 124601.
- [28] Oleg Krichevsky and G Bonnet. *Fluorescence correlation spectroscopy: the technique and its applications*. Rep. Prog. Phys. 65 (2002), pp. 251–297.
- [29] Elliot L. Elson. *Fluorescence correlation spectroscopy: Past, present, future*. Biophysical Journal 101.12 (2011), pp. 2855–2870.
- [30] Riccardo Raccis, Arash Nikoubashman, Markus Retsch, Ulrich Jonas, Kaloian Koyanov, Hans-Jürgen Butt, Christos N Likos, and George Fytas. *Confined Diffusion in Periodic Porous Nanostructures*. ACS Nano 5.6 (2011), pp. 4607–4616.
- [31] N. O. Petersen, P. L. Höddelius, P. W. Wiseman, O. Seger, and K. E. Magnusson. *Quantitation of membrane receptor distributions by image correlation spectroscopy: concept and application*. Biophysical Journal 65.3 (1993), pp. 1135–1146.
- [32] David L. Kolin and Paul W. Wiseman. *Advances in image correlation spectroscopy: Measuring number densities, aggregation states, and dynamics of fluorescently labeled macromolecules in cells*. Cell Biochemistry and Biophysics 49.3 (2007), pp. 141–164.
- [33] Michelle A. Digman, Claire M. Brown, Parijat Sengupta, Paul W. Wiseman, Alan R. Horwitz, and Enrico Gratton. *Measuring fast dynamics in solutions and cells with a laser scanning microscope*. Biophysical Journal 89.2 (2005), pp. 1317–27.
- [34] Robert Brown. *XXVII. A brief account of microscopical observations made in the months of June, July and August 1827, on the particles contained in the pollen of plants; and on the general existence of active molecules in organic and inorganic bodies*. The Philosophical Magazine 4.21 (2011), pp. 161–173.
- [35] M. De Brabander, R. Nuydens, G. Geuens, M. Moeremans, and J. De Mey. *The use of submicroscopic gold particles combined with video contrast enhancement as a simple molecular probe for the living cell*. Cell Motility and the Cytoskeleton 6.2 (1986), pp. 105–113.
- [36] M. De Brabander, R. Nuydens, H. Geerts, and C. R. Hopkins. *Dynamic behavior of the transferrin receptor followed in living epidermoid carcinoma (A431) cells with nanovid microscopy*. Cell motility and the cytoskeleton 9.1 (1988), pp. 30–47.
- [37] H. Geerts, M. De Brabander, R. Nuydens, S. Geuens, M. Moeremans, J. De Mey, and P. Hollenbeck. *Nanovid tracking: a new automatic method for the study of mobility in living cells based on colloidal gold and video microscopy*. Biophysical Journal 52.5 (1987), pp. 775–782.
- [38] Mary C. Beckerle. *Microinjected fluorescent polystyrene beads exhibit saltatory motion in tissue culture cells*. The Journal of cell biology 98.6 (1984), pp. 2126–32.
- [39] B J Schnapp, J Gelles, and M P Sheetz. *Nanometer-scale measurements using video light microscopy*. Cell Motility and the Cytoskeleton 10.1-2 (1988), pp. 47–53.
- [40] I. Roy, T. Y. Ohulchanskyy, D. J. Bharali, H. E. Pudavar, R. A. Mistretta, N. Kaur, and P. N. Prasad. *Optical tracking of organically modified silica nanoparticles as DNA carriers: A nonviral, nanomedicine approach for gene delivery*. Proceedings of the National Academy of Sciences 102.2 (2005), pp. 279–284.

- [41] Th Schmidt, G. J. Schütz, W. Baumgartner, H. J. Gruber, and H. Schindler. *Imaging of single molecule diffusion*. Proceedings of the National Academy of Sciences of the United States of America 93.7 (1996), pp. 2926–2929.
- [42] K. Lindfors, T. Kalkbrenner, P. Stoller, and V. Sandoghdar. *Detection and Spectroscopy of Gold Nanoparticles Using Supercontinuum White Light Confocal Microscopy*. Physical Review Letters 93.3 (2004), pp. 3–6.
- [43] Christian Brunner, Viola Vogel, Volker Jacobsen, Patrick Stoller, and Vahid Sandoghdar. *Interferometric optical detection and tracking of very small gold nanoparticles at a water-glass interface*. Optics Express 14.1 (2006), p. 405.
- [44] Philipp Kukura, Helge Ewers, Christian Müller, Alois Renn, Ari Helenius, and Vahid Sandoghdar. *High-speed nanoscopic tracking of the position and orientation of a single virus*. Nature Methods 6.12 (2009), pp. 923–927.
- [45] Matz Liebel, James T. Hugall, and Niek F. Van Hulst. *Ultrasensitive Label-Free Nanosensing and High-Speed Tracking of Single Proteins*. Nano Letters 17.2 (2017), pp. 1277–1281.
- [46] Ching Ya Cheng, Yi Hung Liao, and Chia Lung Hsieh. *High-speed imaging and tracking of very small single nanoparticles by contrast enhanced microscopy*. Nanoscale 11.2 (2019), pp. 568–577.
- [47] Chia-Lung Hsieh and Yi-Hung Liao. “Coherent brightfield (COBRI) microscopy for ultrahigh-speed single particle tracking on lipid bilayer membranes”. Ed. by Osamu Matoba, Yasuhiro Awatsuji, Toyohiko Yatagai, and Yoshihisa Aizu. SPIE, 2018, p. 1. ISBN: 9781510619791.
- [48] Howard C. Berg. *How to track bacteria*. Review of Scientific Instruments 42.6 (1971), pp. 868–871.
- [49] Katarina Kis-Petikova and Enrico Gratton. *Distance measurement by circular scanning of the excitation beam in the two-photon microscope*. Microscopy research and technique 63.1 (2004), pp. 34–49.
- [50] Andrew J. Berglund and H. Mabuchi. *Feedback controller design for tracking a single fluorescent molecule*. Applied Physics B: Lasers and Optics 78.5 (2004), pp. 653–659.
- [51] Andrew J. Berglund and H. Mabuchi. *Performance bounds on single-particle tracking by fluorescence modulation*. Applied Physics B 83.1 (2006), pp. 127–133.
- [52] Andrew J. Berglund, Kevin McHale, and Hideo Mabuchi. *Fluctuations in closed-loop fluorescent particle tracking*. Optics express 15.12 (2007), pp. 7752–73.
- [53] Andrew J. Berglund and Hideo Mabuchi. *Tracking-FCS: Fluorescence correlation spectroscopy of individual particles*. Optics express 13.20 (2005), pp. 8069–82.
- [54] Kevin McHale, Andrew J. Berglund, and Hideo Mabuchi. *Quantum dot photon statistics measured by three-dimensional particle tracking*. Nano letters 7.11 (2007), pp. 3535–9.
- [55] Kevin McHale and Hideo Mabuchi. *Precise Characterization of the Conformation Fluctuations of Freely Diffusing DNA: Beyond Rouse and Zimm*. Journal of the American Chemical Society 131.49 (2009), pp. 17901–17907.

-
- [56] Valeria Levi, QiaoQiao Ruan, K Kis-Petikova, and Enrico Gratton. *Scanning FCS, a novel method for three-dimensional particle tracking*. Biochemical Society transactions 31.Pt 5 (2003), pp. 997–1000.
- [57] Paolo Annibale, Alexander Dvornikov, and Enrico Gratton. *Electrically tunable lens speeds up 3D orbital tracking*. Biomedical Optics Express 6.6 (2015), p. 2181.
- [58] L Lanzanò and Enrico Gratton. *Orbital single particle tracking on a commercial confocal microscope using piezoelectric stage feedback*. Methods and Applications in Fluorescence 2.2 (2014), p. 024010.
- [59] Valeria Levi, QiaoQiao Ruan, and Enrico Gratton. *3-D Particle Tracking in a Two-Photon Microscope: Application to the Study of Molecular Dynamics in Cells*. Biophysical Journal 88.4 (2005), pp. 2919–2928.
- [60] Laura C. Estrada and Enrico Gratton. *3D nanometer images of biological fibers by directed motion of gold nanoparticles*. Nano Letters 11.11 (2011), pp. 4656–4660.
- [61] Francesco Cardarelli, Luca Lanzano, and Enrico Gratton. *Fluorescence Correlation Spectroscopy of Intact Nuclear Pore Complexes*. Biophysical Journal 101.4 (2011), pp. L27–L29.
- [62] Francesco Cardarelli, Luca Lanzano, and Enrico Gratton. *Capturing directed molecular motion in the nuclear pore complex of live cells*. Proceedings of the National Academy of Sciences of the United States of America 109.25 (2012), pp. 9863–9868.
- [63] Paolo Annibale and Enrico Gratton. *Advanced fluorescence microscopy methods for the real-time study of transcription and chromatin dynamics*. Transcription 5.May (2014), pp. 1–9.
- [64] Paolo Annibale and Enrico Gratton. *Single cell visualization of transcription kinetics variance of highly mobile identical genes using 3D nanoimaging*. Scientific Reports 5.1 (2015), p. 9258.
- [65] Yoshihiko Katayama, Ondrej Burkacky, Martin Meyer, Christoph Bräuchle, Enrico Gratton, and Don C. Lamb. *Real-Time Nanomicroscopy via Three-Dimensional Single-Particle Tracking*. ChemPhysChem 10.14 (2009), pp. 2458–2464.
- [66] Fabian Wehnekamp, Gabriela Plucińska, Rachel Thong, Thomas Misgeld, and Don C. Lamb. *Nanoresolution real-time 3D orbital tracking for studying mitochondrial trafficking in vertebrate axons in vivo*. eLife 8 (2019), pp. 1–22.
- [67] Nigel F. Reuel, Aurélie Dupont, Olivier Thouvenin, Don C. Lamb, and Michael S. Strano. *Three-dimensional tracking of carbon nanotubes within living cells*. ACS Nano 6.6 (2012), pp. 5420–5428.
- [68] A Dupont, M Gorelashvili, V Schüller, F Wehnekamp, D Arcizet, Y Katayama, Don C. Lamb, and D Heinrich. *Three-dimensional single-particle tracking in live cells: news from the third dimension*. New Journal of Physics 15.7 (2013), p. 075008.
- [69] Aurélie Dupont and Don C. Lamb. *Nanoscale three-dimensional single particle tracking*. Nanoscale 3.11 (2011), pp. 4532–41.
- [70] C. Shan Xu, Hu Cang, Daniel Montiel, and Haw Yang. *Rapid and Quantitative Sizing of Nanoparticles Using Three-Dimensional Single-Particle Tracking*. The Journal of Physical Chemistry C 111.1 (2007), pp. 32–35.
- [71] Hu Cang, C Shan Xu, Daniel Montiel, and Haw Yang. *Guiding a confocal microscope by single fluorescent nanoparticles*. Optics Letters 32.18 (2007), p. 2729.

- [72] Hu Cang, C. Shan Xu, and Haw Yang. *Progress in single-molecule tracking spectroscopy*. Chemical Physics Letters 457.4-6 (2008), pp. 285–291.
- [73] Guillaume A. Lessard, Peter M. Goodwin, and James H. Werner. “Three-dimensional tracking of fluorescent particles”. Ed. by Jörg Enderlein and Zygmunt K. Gryczynski. Vol. 6092. 609205. 2006, p. 609205.
- [74] Guillaume A. Lessard, Peter M. Goodwin, and James H. Werner. *Three-dimensional tracking of individual quantum dots*. Applied Physics Letters 91.22 (2007), p. 224106.
- [75] Kevin Welsher and Haw Yang. *Multi-resolution 3D visualization of the early stages of cellular uptake of peptide-coated nanoparticles*. Nature Nanotechnology 9.3 (2014), pp. 198–203.
- [76] Shangguo Hou, Xiaoqi Lang, and Kevin Welsher. *Robust real-time 3D single-particle tracking using a dynamically moving laser spot*. Optics Letters 42.12 (2017), p. 2390.
- [77] Alexander P. Fields and Adam E. Cohen. *Optimal tracking of a Brownian particle*. Optics express 20.20 (2012), pp. 22585–601.
- [78] Shangguo Hou and Kevin Welsher. *An Adaptive Real-Time 3D Single Particle Tracking Method for Monitoring Viral First Contacts*. Small 15.44 (2019), p. 1903039.
- [79] Evan P Perillo, Yen-Liang Liu, Khang Huynh, Cong Liu, Chao-Kai Chou, Mien-Chie Hung, Hsin-Chih Yeh, and Andrew K Dunn. *Deep and high-resolution three-dimensional tracking of single particles using nonlinear and multiplexed illumination*. Nature communications 6.91 (2015), p. 7874.
- [80] Zhuang Liu, Wei Wang, Rui Xie, Xiao-Jie Ju, and Liang-Yin Chu. *Stimuli-responsive smart gating membranes*. Chemical Society reviews 45.3 (2016), pp. 460–75.
- [81] Adam E. Cohen. *Control of nanoparticles with arbitrary two-dimensional force fields*. Physical Review Letters 94.11 (2005), pp. 1–4.
- [82] Adam E. Cohen and William E. Moerner. *The anti-Brownian electrophoretic trap (ABEL trap): fabrication and software*. Imaging, Manipulation, and Analysis of Biomolecules and Cells: Fundamentals and Applications III 5699 (2005), p. 296.
- [83] Alexander P. Fields and Adam E. Cohen. *Electrokinetic trapping at the one nanometer limit*. Proceedings of the National Academy of Sciences of the United States of America 108.22 (2011), pp. 8937–8942.
- [84] Adam E. Cohen and W. E. Moerner. *Method for trapping and manipulating nanoscale objects in solution*. Applied Physics Letters 86.9 (2005), pp. 1–3.
- [85] Adam E. Cohen and W. E. Moerner. *Controlling Brownian motion of single protein molecules and single fluorophores in aqueous buffer*. Optics express 16.10 (2008), pp. 6941–56.
- [86] Q. Wang and W. E. Moerner. *Optimal strategy for trapping single fluorescent molecules in solution using the ABEL trap*. Applied Physics B: Lasers and Optics 99.1-2 (2010), pp. 23–30.
- [87] Yan Jiang, Nicholai R. Douglas, Nicholas R. Conley, Erik J. Miller, Judith Frydman, and W. E. Moerner. *Sensing cooperativity in ATP hydrolysis for single multisubunit enzymes in solution*. Proceedings of the National Academy of Sciences of the United States of America 108.41 (2011), pp. 16962–16967.

- [88] Allison H. Squires, Peter D. Dahlberg, Haijun Liu, Nikki Cecil M. Magdaong, Robert E. Blankenship, and W. E. Moerner. *Single-molecule trapping and spectroscopy reveals photophysical heterogeneity of phycobilisomes quenched by Orange Carotenoid Protein*. *Nature Communications* 10.1 (2019).
- [89] Yvan Eilers, Haisen Ta, Klaus C. Gwosch, Francisco Balzarotti, and Stefan W. Hell. *MINFLUX monitors rapid molecular jumps with superior spatiotemporal resolution*. *Proceedings of the National Academy of Sciences* 115.24 (2018), pp. 6117–6122.
- [90] Klaus C. Gwosch, Jasmin K. Pape, Francisco Balzarotti, Philipp Hoess, Jan Ellenberg, Jonas Ries, and Stefan W. Hell. *MINFLUX nanoscopy delivers 3D multicolor nanometer resolution in cells*. *Nature Methods* 17.2 (2020), pp. 217–224.
- [91] Cong Liu, Yen Liang Liu, Evan P. Perillo, Andrew K. Dunn, and Hsin Chih Yeh. *Single-Molecule Tracking and Its Application in Biomolecular Binding Detection*. *IEEE Journal of Selected Topics in Quantum Electronics* 22.4 (2016).
- [92] Melanie Bergmann, Lars Gutow, and Michael Klages. *Marine Anthropogenic Litter*. Ed. by Melanie Bergmann, Lars Gutow, and Michael Klages. Springer International Publishing, 2015, pp. 1–447. ISBN: 978-3-319-16509-7.
- [93] Messika Revel, Amélie Châtel, and Catherine Mouneyrac. *Micro(nano)plastics: A threat to human health?* *Current Opinion in Environmental Science & Health* 1 (2018), pp. 17–23.
- [94] Yini Ma, Anna Huang, Siqi Cao, Feifei Sun, Lianhong Wang, Hongyan Guo, and Rong Ji. *Effects of nanoplastics and microplastics on toxicity, bioaccumulation, and environmental fate of phenanthrene in fresh water*. *Environmental Pollution* 219 (2016), pp. 166–173.
- [95] Hans Bouwmeester, Peter C.H. Hollman, and Ruud J.B. Peters. *Potential Health Impact of Environmentally Released Micro- and Nanoplastics in the Human Food Production Chain: Experiences from Nanotoxicology*. 2015.
- [96] Baorong Jiang, Alexandra E. Kauffman, Lei Li, Wayne McFee, Bo Cai, John Weinstein, Jamie R. Lead, Saurabh Chatterjee, Geoffrey I. Scott, and Shuo Xiao. *Health impacts of environmental contamination of micro- And nanoplastics: A review*. *Environmental Health and Preventive Medicine* 25.1 (2020), pp. 1–15.
- [97] Mathias Ulbricht. *Advanced functional polymer membranes*. *Polymer* 47.7 (2006), pp. 2217–2262.
- [98] Mark A. Shannon, Paul W. Bohn, Menachem Elimelech, John G. Georgiadis, Benito J. Mariñas, and Anne M. Mayes. *Science and technology for water purification in the coming decades*. *Nature* 452.7185 (2008), pp. 301–310.
- [99] Seung Y. Yang, Incheol Ryu, Hwang Y. Kim, Jin K. Kim, Sung K. Jang, and Thomas P. Russell. *Nanoporous membranes with ultrahigh selectivity and flux for the filtration of viruses*. *Advanced Materials* 18.6 (2006), pp. 709–712.
- [100] A. Chahboun, R. Coratger, F. Ajustron, J. Beauvillain, P. Aimar, and V. Sanchez. *Comparative study of micro- and ultrafiltration membranes using STM, AFM and SEM techniques*. *Ultramicroscopy* 41.1-3 (1992), pp. 235–244.
- [101] Sahadevan Rajesh, Kavalapara H. Shobana, Selvaraj Anitharaj, and Doraiswamy R. Mohan. *Preparation, morphology, performance, and hydrophilicity studies of poly(amide-imide) incorporated cellulose acetate ultrafiltration membranes*. *Industrial and Engineering Chemistry Research* 50.9 (2011), pp. 5550–5564.

- [102] Anju Thekkedath, Wahib M. Naceur, Karima Kecili, Mohammed Sbai, Audrey Elana, Laurent Auret, Hervé Suty, Claire Machinal, and Maxime Pontié. *Macroscopic and microscopic characterizations of a cellulosic ultrafiltration (UF) membrane fouled by a humic acid cake deposit: First step for intensification of reverse osmosis (RO) pre-treatments*. *Comptes Rendus Chimie* 10.9 (2007), pp. 803–812.
- [103] Markus Retsch and Ulrich Jonas. *Hierarchically Structured, Double-Periodic Inverse Composite Opals*. *Advanced Functional Materials* 23.43 (2013), pp. 5381–5389.
- [104] William A. Phillip, Rachel Mika Dorin, Jörg Werner, Eric M.V. Hoek, Ulrich Wiesner, and Menachem Elimelech. *Tuning structure and properties of graded triblock terpolymer-based mesoporous and hybrid films*. *Nano Letters* 11.7 (2011), pp. 2892–2900.
- [105] Thippahaya Cherdhirankorn, Markus Retsch, Ulrich Jonas, Hans-Jürgen Butt, and Kaloian Koynov. *Tracer diffusion in silica inverse opals*. *Langmuir* 26.Xx (2010), pp. 10141–10146.
- [106] Michael J. Skaug and Daniel K. Schwartz. *Tracking nanoparticle diffusion in porous filtration media*. *Industrial and Engineering Chemistry Research* 54.16 (2015), pp. 4414–4419.
- [107] Don S Lemons, Anthony Gythiel, and Paul Langvin. *Paul Langevin’s 1908 paper “On the Theory of Brownian Motion”*. *American Journal of Physics* 533.1908 (1997), pp. 1079–1081.
- [108] S. C. Kou. *Stochastic modeling in nanoscale biophysics: Subdiffusion within proteins*. *Annals of Applied Statistics* 2.2 (2008), pp. 501–535.
- [109] G. E. Uhlenbeck and L. S. Ornstein. *On the Theory of the Brownian Motion*. *Physical Review* 36.5 (1930), pp. 823–841.
- [110] Ralf Metzler, Jae-Hyung Jeon, Andrey G Cherstvy, and Eli Barkai. *Anomalous diffusion models and their properties: non-stationarity, non-ergodicity, and ageing at the centenary of single particle tracking*. *Physical chemistry chemical physics: PCCP* 16.44 (2014), pp. 24128–64.
- [111] A. Einstein. *Über die von der molekularkinetischen Theorie der Wärme geforderte Bewegung von in ruhenden Flüssigkeiten suspendierten Teilchen [AdP 17, 549 (1905)]*. *Annalen der Physik* 14.S1 (2005), pp. 182–193.
- [112] Norbert Wiener. *Norbert Wiener: Collected Works, Volume 1*. Ed. by P. Masani. 1976. ISBN: 9780262230704.
- [113] Léon Van Hove. *Correlations in space and time and born approximation scattering in systems of interacting particles*. *Physical Review* 95.1 (1954), pp. 249–262.
- [114] Paul Hopkins, Andrea Fortini, Andrew J. Archer, and Matthias Schmidt. *The van Hove distribution function for Brownian hard spheres: Dynamical test particle theory and computer simulations for bulk dynamics*. *Journal of Chemical Physics* 133.22 (2010), pp. 1–18.
- [115] Anna S. Bodrova, Aleksei V. Chechkin, Andrey G. Cherstvy, and Ralf Metzler. *Ultraslow scaled brownian motion*. *New Journal of Physics* 17.6 (2015).
- [116] Vincent Tejedor and Ralf Metzler. *Anomalous diffusion in correlated continuous time random walks*. *Journal of Physics A: Mathematical and Theoretical* 43.8 (2010).

- [117] Adam D. Douglass and Ronald D. Vale. *Single-molecule microscopy reveals plasma membrane microdomains created by protein-protein networks that exclude or trap signaling molecules in T cells*. *Cell* 121.6 (2005), pp. 937–950.
- [118] Catherine Tardin, Laurent Cognet, Cécile Bats, Brahim Lounis, and Daniel Choquet. *Direct imaging of lateral movements of AMPA receptors inside synapses*. *EMBO Journal* 22.18 (2003), pp. 4656–4665.
- [119] Songwan Jin, Peter M Haggie, and a S Verkman. *Single-particle tracking of membrane protein diffusion in a potential: simulation, detection, and application to confined diffusion of CFTR Cl⁻ channels*. *Biophysical journal* 93.3 (2007), pp. 1079–88.
- [120] Kumud R. Poudel, David J. Keller, and James a. Brozik. *Single particle tracking reveals corralling of a transmembrane protein in a double-cushioned lipid bilayer assembly*. *Langmuir* 27.1 (2011), pp. 320–327.
- [121] Takahiro K. Fujiwara, Kokoro Iwasawa, Ziya Kalay, Taka A. Tsunoyama, Yusuke Watanabe, Yasuhiro M. Umemura, Hideji Murakoshi, Kenichi G.N. Suzuki, Yuri L. Nemoto, Nobuhiro Morone, and Akihiro Kusumi. *Confined diffusion of transmembrane proteins and lipids induced by the same actin meshwork lining the plasma membrane*. *Molecular Biology of the Cell* 27.7 (2016), pp. 1101–1119.
- [122] Thorsten Kues, Reiner Peters, and Ulrich Kubitscheck. *Visualization and tracking of single protein molecules in the cell nucleus*. *Biophysical Journal* 80.6 (2001), pp. 2954–2967.
- [123] Jing Fan, Shuaijun Li, Ziqian Wu, and Zi Chen. *Diffusion and mixing in microfluidic devices*. Elsevier Inc., 2018, pp. 79–100. ISBN: 9780128126592.
- [124] Peng Bai, Emmanuel Haldoupis, Paul J. Dauenhauer, Michael Tsapatsis, and J. Ilja Siepmann. *Understanding Diffusion in Hierarchical Zeolites with House-of-Cards Nanosheets*. *ACS Nano* 10.8 (2016), pp. 7612–7618.
- [125] Angela B. Grommet, Moran Feller, and Rafal Klajn. *Chemical reactivity under nanoconfinement*. *Nature Nanotechnology* 15.4 (2020), pp. 256–271.
- [126] Mengen Wang, Mengen Wang, Chen Zhou, Chen Zhou, Nusnin Akter, Nusnin Akter, Wilfred T. Tysoe, J. Anibal Boscoboinik, and Deyu Lu. *Mechanism of the Accelerated Water Formation Reaction under Interfacial Confinement*. *ACS Catalysis* 10.11 (2020), pp. 6119–6128.
- [127] Xin Yan, Ryan M. Bain, and R. Graham Cooks. *Organic Reactions in Microdroplets: Reaction Acceleration Revealed by Mass Spectrometry*. *Angewandte Chemie - International Edition* 55.42 (2016), pp. 12960–12972.
- [128] Bert M. Weckhuysen, Susumu Kitagawa, and Michael Tsapatsis. *Reactions in Confined Spaces*. *ChemPhysChem* 19.4 (2018), pp. 339–340.
- [129] Francisco Rodrigues, Thomas Georgelin, Guillaume Gabant, Baptiste Rigaud, Fabrice Gaslain, Guanzheng Zhuang, Maria Gardênnia Da Fonseca, Valentin Valtchev, David Touboul, and Maguy Jaber. *Confinement and time immemorial: prebiotic synthesis of nucleotides on a porous mineral nanoreactor*. *Journal of Physical Chemistry Letters* 10.15 (2019), pp. 4192–4196.
- [130] Sarah Maurer. *The impact of salts on single chain amphiphile membranes and implications for the location of the origin of life*. *Life* 7.4 (2017).

- [131] Stephen Mann. *The origins of life: Old problems, new chemistries*. *Angewandte Chemie - International Edition* 52.1 (2013), pp. 155–162.
- [132] Caitlin E. Cornell, Roy A. Black, Mengjun Xue, Helen E. Litz, Andrew Ramsay, Moshe Gordon, Alexander Mileant, Zachary R. Cohen, James A. Williams, Kelly K. Lee, Gary P. Drobny, and Sarah L. Keller. *Prebiotic amino acids bind to and stabilize prebiotic fatty acid membranes*. *Proceedings of the National Academy of Sciences of the United States of America* 116.35 (2019), pp. 17239–17244.
- [133] Dominique Ernst, Marcel Hellmann, Jürgen Köhler, and Matthias Weiss. *Fractional Brownian motion in crowded fluids*. *Soft Matter* 8.18 (2012), p. 4886.
- [134] Thomas Bickel. *A note on confined diffusion*. *Physica A: Statistical Mechanics and its Applications* 377.1 (2007), pp. 24–32.
- [135] Simon F. Nørrelykke and Henrik Flyvbjerg. *Harmonic oscillator in heat bath: Exact simulation of time-lapse-recorded data and exact analytical benchmark statistics*. *Physical Review E* 83.4 (2011), p. 041103.
- [136] Jae-Hyung Jeon and Ralf Metzler. *Inequivalence of time and ensemble averages in ergodic systems: Exponential versus power-law relaxation in confinement*. *Physical Review E* 85.2 (2012), p. 021147.
- [137] Jae-Hyung Jeon, Natascha Leijnse, Lene B. Oddershede, and Ralf Metzler. *Anomalous diffusion and power-law relaxation of the time averaged mean squared displacement in worm-like micellar solutions*. *New Journal of Physics* 15 (2013).
- [138] S. Burov, R. Metzler, and E. Barkai. *Aging and nonergodicity beyond the Khinchin theorem*. *Proceedings of the National Academy of Sciences of the United States of America* 107.30 (2010), pp. 13228–13233.
- [139] Thomas Neusius, Igor M. Sokolov, and Jeremy C. Smith. *Subdiffusion in time-averaged, confined random walks*. *Physical Review E - Statistical, Nonlinear, and Soft Matter Physics* 80.1 (2009), pp. 1–5.
- [140] Jae Hyung Jeon, Vincent Tejedor, Stas Burov, Eli Barkai, Christine Selhuber-Unkel, Kirstine Berg-Sørensen, Lene Oddershede, and Ralf Metzler. *In vivo anomalous diffusion and weak ergodicity breaking of lipid granules*. *Physical Review Letters* 106.4 (2011), pp. 2–5.
- [141] Shan-Lin Qin and Yong He. *Confined subdiffusion in three dimensions*. *Chinese Physics B* 23 (2014), p. 110206.
- [142] R. K. Saxena, A. M. Mathai, and H. J. Haubold. *On generalized fractional kinetic equations*. *Physica A: Statistical Mechanics and its Applications* 344.3-4 SPEC. ISS. (2004), pp. 657–664.
- [143] Thomas Dertinger, Victor Pacheco, Iris Von Der Hocht, Rudolf Hartmann, Ingo Gregor, and Jörg Enderlein. *Two-focus fluorescence correlation spectroscopy: A new tool for accurate and absolute diffusion measurements*. *ChemPhysChem* 8.3 (2007), pp. 433–443.
- [144] C. B. Müller, A. Loman, V. Pacheco, F. Koberling, D. Willbold, W. Richtering, and Jörg Enderlein. *Precise measurement of diffusion by multi-color dual-focus fluorescence correlation spectroscopy*. *EPL (Europhysics Letters)* 83.4 (2008), p. 46001.

-
- [145] Lutz Langguth, Agata Szuba, Sander a. Mann, Erik C. Garnett, Gijsje H. Koenderink, and a. Femius Koenderink. *Nano-antenna enhanced two-focus fluorescence correlation spectroscopy*. Scientific Reports 7.1 (2017), p. 5985.
- [146] Anastasia Loman, Thomas Dertinger, Felix Koberling, and Jörg Enderlein. *Comparison of optical saturation effects in conventional and dual-focus fluorescence correlation spectroscopy*. Chemical Physics Letters 459.1-6 (2008), pp. 18–21.
- [147] Andrew J. Berglund. *Feedback Control of Brownian Motion for Single-Particle Fluorescence Spectroscopy*. PhD thesis. 2007.
- [148] Matthias Weiss. *Single-particle tracking data reveal anticorrelated fractional Brownian motion in crowded fluids*. Physical Review E 88.1 (2013), p. 010101.
- [149] Stephanie C. Weber, Andrew J. Spakowitz, and Julie A. Theriot. *Bacterial chromosomal loci move subdiffusively through a viscoelastic cytoplasm*. Physical Review Letters 104.23 (2010), pp. 27–30.
- [150] V Calandrini, E Pellegrini, P Calligari, K Hinsen, and G R Kneller. *nMoldyn-Interfacing spectroscopic experiments, molecular dynamics simulations and models for time correlation functions*. Collection SFN 12 (2011), pp. 201–232.
- [151] Guo Ying Gu and Li Min Zhu. *Motion control of piezoceramic actuators with creep, hysteresis and vibration compensation*. Sensors and Actuators, A: Physical 197 (2013), pp. 76–87.
- [152] National Center for Biotechnology Information. *PubChem Database. Fluorescein, CID = 16850*.
- [153] National Center for Biotechnology Information. *PubChem Database. Nile red, CID = 65182*.
- [154] National Center for Biotechnology Information. *PubChem Database. Rhodamine 6G, CID = 13806*.
- [155] National Center for Biotechnology Information. *PubChem Database. Rhodamine B, CID = 6694*.
- [156] Stephen K. Burley, Helen M. Berman, Charmi Bhikadiya, Chunxiao Bi, Li Chen, and et. al. *Protein Data Bank: The single global archive for 3D macromolecular structure data*. Nucleic Acids Research 47.D1 (2019), pp. D520–D528.
- [157] M. Orm, A. B. Cubitt, K. Kallio, L. A. Gross, R. Y. Tsien, and S. J. Remington. *Crystal Structure of the Aequorea victoria Green Fluorescent Protein*. Science 273.5280 (1996), pp. 1392–1395.
- [158] George H. Patterson and Jennifer Lippincott-Schwartz. *A photoactivatable GFP for selective photolabeling of proteins and cells*. Science 297.5588 (2002), pp. 1873–1877.
- [159] Osamu Shimomura, Frank H. Johnson, and Yo Saiga. *Extraction, Purification and Properties of Aequorin, a Bioluminescent Protein from the Luminous Hydromedusa, Aequorea*. Journal of Cellular and Comparative Physiology 59.3 (1962), pp. 223–239.
- [160] Charles Limouse, Jason C. Bell, Colin J. Fuller, Aaron F. Straight, and Hideo Mabuchi. *Measurement of Mesoscale Conformational Dynamics of Freely Diffusing Molecules with Tracking FCS*. Biophysical Journal 114.7 (2018), pp. 1539–1550.

- [161] Nathan C. Shaner, Michael Z. Lin, Michael R. McKeown, Paul A. Steinbach, Kristin L. Hazelwood, Michael W. Davidson, and Roger Y. Tsien. *Improving the photostability of bright monomeric orange and red fluorescent proteins*. *Nature Methods* 5.6 (2008), pp. 545–551.
- [162] Dan Yu, Michelle A. Baird, John R. Allen, Elizabeth S. Howe, Matthew P. Klassen, Anna Reade, Kalpana Makhijani, Yuanquan Song, Songmei Liu, Zehra Murthy, Shao Qing Zhang, Orion D. Weiner, Thomas B. Kornberg, Yuh Nung Jan, Michael W. Davidson, and Xiaokun Shu. *A naturally monomeric infrared fluorescent protein for protein labeling in vivo*. *Nature Methods* 12.8 (2015), pp. 763–765.
- [163] Te Tuan Yang, Linzhao Cheng, and Steven R. Kain. *Optimized codon usage and chromophore mutations provide enhanced sensitivity with the green fluorescent protein*. *Nucleic Acids Research* 24.22 (1996), pp. 4592–4593.
- [164] Takeharu Nagai, Keiji Iyata, Eun Sun Park, Mie Kubota, Katsuhiko Mikoshiba, and Atsushi Miyawaki. *A variant of yellow fluorescent protein with fast and efficient maturation for cell-biological applications*. *Nature Biotechnology* 20.1 (2002), pp. 87–90.
- [165] Nadya G. Gurskaya, Vladislav V. Verkhusha, Alexander S. Shcheglov, Dmitry B. Staroverov, Tatyana V. Chepurnykh, Arkady F. Fradkov, Sergey Lukyanov, and Konstantin A. Lukyanov. *Engineering of a monomeric green-to-red photoactivatable fluorescent protein induced by blue light*. *Nature Biotechnology* 24.4 (2006), pp. 461–465.
- [166] Mate Puljiz, Michael Orlishausen, Werner Köhler, and Andreas M. Menzel. *Thermophoretically induced large-scale deformations around microscopic heat centers*. *The Journal of Chemical Physics* 144.18 (2016), p. 184903.
- [167] Haipeng Lu, Gerard M. Carroll, Nathan R. Neale, and Matthew C. Beard. *Infrared Quantum Dots: Progress, Challenges, and Opportunities*. *ACS Nano* 13 (2019), pp. 939–953.
- [168] X. Michalet, F. F. Pinaud, L. A. Bentolila, J. M. Tsay, S. Doose, J. J. Li, G. Sundaresan, A. M. Wu, S. S. Gambhir, and S. Weiss. *Quantum dots for live cells, in vivo imaging, and diagnostics*. 2005.
- [169] Benoit Dubertret. *In Vivo Imaging of Quantum Dots Encapsulated in Phospholipid Micelles*. *Science* 298.5599 (2002), pp. 1759–1762.
- [170] Ron Hardman. *A toxicologic review of quantum dots: Toxicity depends on physico-chemical and environmental factors*. *Environmental Health Perspectives* 114.2 (2006), pp. 165–172.
- [171] Jennifer L. Pelley, Abdallah S. Daar, and Marc A. Saner. *State of academic knowledge on toxicity and biological fate of quantum dots*. *Toxicological Sciences* 112.2 (2009), pp. 276–296.
- [172] Gangcheng Yuan, Daniel E. Gómez, Nicholas Kirkwood, Klaus Boldt, and Paul Mulvaney. *Two Mechanisms Determine Quantum Dot Blinking*. *ACS Nano* 12.4 (2018), pp. 3397–3405.
- [173] Shunchao Gu, Naoto Anzai, Daisuke Nagao, Yoshio Kobayashi, and Mikio Konno. *Short communication: Preparation of fluorescent polymer particles by emulsion polymerization*. *E-Polymers* 064 (2005), pp. 1–5.

- [174] R. P.A. Dullens, E. M. Claesson, and W. K. Kegel. *Preparation and properties of cross-linked fluorescent poly(methyl methacrylate) latex colloids*. Langmuir 20.3 (2004), pp. 658–664.
- [175] Otto S. Wolfbeis. *An overview of nanoparticles commonly used in fluorescent bioimaging*. Chemical Society Reviews 44.14 (2015), pp. 4743–4768.
- [176] A. Yu Menshikova, T. G. Evseeva, Yu O. Skurkis, T. B. Tennikova, and S. S. Ivanchev. *Monodisperse carboxylated polystyrene particles: Synthesis, electrokinetic and adsorptive properties*. Polymer 46.4 SPEC. ISS. (2005), pp. 1417–1425.
- [177] Shao Chie Huang, Mark D. Stump, Robert Weiss, and Karin D. Caldwell. *Binding of biotinylated DNA to streptavidin-coated polystyrene latex: Effects of chain length and particle size*. Analytical Biochemistry 237.1 (1996), pp. 115–122.
- [178] a. Scotti, W. Liu, J. S. Hyatt, E. S. Herman, H. S. Choi, J. W. Kim, L. a. Lyon, U. Gasser, and a. Fernandez-Nieves. *The CONTIN algorithm and its application to determine the size distribution of microgel suspensions*. The Journal of chemical physics 142.23 (2015), p. 234905.
- [179] Dominique Ernst and Jürgen Köhler. *How the number of fitting points for the slope of the mean-square displacement influences the experimentally determined particle size distribution from single-particle tracking*. Physical chemistry chemical physics: PCCP 15.10 (2013), pp. 3429–32.
- [180] Michael J. Skaug, Liang Wang, Yifu Ding, and Daniel K. Schwartz. *Hindered Nanoparticle Diffusion and Void Accessibility in a Three-Dimensional Porous Medium*. ACS Nano 9.2 (2015), pp. 2148–2156.
- [181] Klaus-Viktor Peinemann, Volker Abetz, and Peter F W Simon. *Asymmetric superstructure formed in a block copolymer via phase separation*. Nature materials 6.12 (2007), pp. 992–996.
- [182] Felix A Plamper, Markus Ruppel, Alexander Schmalz, Oleg Borisov, Matthias Ballauff, and Axel H. E. Müller. *Tuning the Thermoresponsive Properties of Weak Polyelectrolytes: Aqueous Solutions of Star-Shaped and Linear Poly(N,N- dimethylaminoethyl Methacrylate)*. Macromolecules 40.23 (2007), pp. 8361–8366.
- [183] Matthew I. Gibson and Rachel K. O’reilly. *To aggregate, or not to aggregate? Considerations in the design and application of polymeric thermally-responsive nanoparticles*. Chemical Society Reviews 42.17 (2013), pp. 7204–7213.
- [184] L. Chu, R. Xie, and X. Ju. *Stimuli-responsive Membranes: Smart Tools for Controllable Mass-transfer and Separation Processes*. Chinese Journal of Chemical Engineering 19.6 (2011), pp. 891–903.
- [185] Sidney. Loeb and Sirinivasa Sourirajan. *High Flow Porous Membranes for separating water from saline solutions*. 1964.
- [186] Dominique Ernst, Stefan Hain, and Jürgen Köhler. *Setup for single-particle orbit tracking: artifacts and corrections*. Journal of the Optical Society of America. A, Optics, image science, and vision 29.7 (2012), pp. 1277–87.
- [187] Shangguo Hou, Jack Exell, and Kevin Welsher. *Real-time 3D single molecule tracking*. Nature Communications 11.1 (2020).

- [188] Christian Dietrich, Bing Yang, Takahiro Fujiwara, Akihiro Kusumi, and Ken Jacobson. *Relationship of lipid rafts to transient confinement zones detected by single particle tracking*. Biophysical Journal 82.1 (2002), pp. 274–284.
- [189] Douglas S Martin, Martin B Forstner, and Josef a Käs. *Apparent subdiffusion inherent to single particle tracking*. Biophysical Journal 83.4 (2002), pp. 2109–17.
- [190] Thierry Savin and Patrick S Doyle. *Static and dynamic errors in particle tracking microrheology*. Biophysical journal 88.1 (2005), pp. 623–638.
- [191] M Goulian and S M Simon. *Tracking single proteins within cells*. Biophysical Journal 79.4 (2000), pp. 2188–98.
- [192] Stefan Wieser and Gerhard J. Schütz. *Tracking single molecules in the live cell plasma membrane-Do’s and Don’t’s*. Methods 46.2 (2008), pp. 131–140.
- [193] Andrew J. Berglund, Kevin McHale, and Hideo Mabuchi. *Feedback localization of freely diffusing fluorescent particles near the optical shot-noise limit*. Optics Letters 32.2 (2007), p. 145.
- [194] Awad H. Al-Mohy and Nicholas J Higham. *A New Scaling and Squaring Algorithm for the Matrix Exponential*. SIAM Journal on Matrix Analysis and Applications 31.3 (2010), pp. 970–989.
- [195] Dominique Ernst and Jürgen Köhler. *Measuring a diffusion coefficient by single-particle tracking: statistical analysis of experimental mean squared displacement curves*. Physical chemistry chemical physics: PCCP 15.3 (2013), pp. 845–9.
- [196] ML Sheely. *Glycerol viscosity tables*. Industrial & Engineering Chemistry 24.9 (1932).
- [197] Nian-Sheng Cheng. *Formula for the Viscosity of a Glycerol-Water Mixture*. Industrial & Engineering Chemistry Research 47.9 (2008), pp. 3285–3288.
- [198] F. Carrasco, E. Chornet, R. P. Overend, and J. Costa. *A generalized correlation for the viscosity of dextrans in aqueous solutions as a function of temperature, concentration, and molecular weight at low shear rates*. Journal of Applied Polymer Science 37.8 (1989), pp. 2087–2098.
- [199] J.F. Swindells, C. F. Snyder, R. C. Hardy, and P. E. Golden. *Viscosities of Sucrose Solutions at Various Temperatures: Tables of Recalculated Values* (1958).
- [200] Massimo Migliori, Domenico Gabriele, Rosa Di Sanzo, Bruno De Cindio, and Sebastiano Correr. *Viscosity of multicomponent solutions of simple and complex sugars in water*. Journal of Chemical and Engineering Data 52.4 (2007), pp. 1347–1353.
- [201] Iyyaswami Regupathi, Rajendran Govindarajan, Samuthira Pandian Amaresh, and Thanapalan Murugesan. *Densities and Viscosities of Polyethylene Glycol 6000 + Triammonium Citrate + Water Systems*. Journal of Chemical & Engineering Data 54.12 (2009), pp. 3291–3295.
- [202] Robert Holyst, Anna Bielejewska, Jędrzej Szymański, Agnieszka Wilk, Adam Patkowski, Jacek Gapiński, Andrzej Zywockiński, Tomasz Kalwarczyk, Ewelina Kalwarczyk, Marcin Tabaka, Natalia Ziebac, and Stefan a Wieczorek. *Scaling form of viscosity at all length-scales in poly(ethylene glycol) solutions studied by fluorescence correlation spectroscopy and capillary electrophoresis*. Physical chemistry chemical physics: PCCP 11.40 (2009), pp. 9025–32.

- [203] Dominique Ernst, Jürgen Köhler, and Matthias Weiss. *Probing the type of anomalous diffusion with single-particle tracking*. Physical chemistry chemical physics: PCCP 16.17 (2014), pp. 7686–91.
- [204] Daniel Zalami, Oliver Grimm, Felix H. Schacher, Uwe Gerken, and Jürgen Köhler. *Non-invasive study of the three-dimensional structure of nanoporous triblock terpolymer membranes*. Soft Matter (2018), pp. 9750–9754.
- [205] Elizabeth A. Jackson and Marc A. Hillmyer. *Nanoporous membranes derived from block copolymers: From drug delivery to water filtration*. ACS Nano 4.7 (2010), pp. 3548–3553.
- [206] Felix Schacher, Mathias Ulbricht, and Axel H. E. Müller. *Self-Supporting, Double Stimuli-Responsive Porous Membranes From Polystyrene- block -poly(N , N -dimethylaminoethyl methacrylate) Diblock Copolymers*. Advanced Functional Materials 19.7 (2009), pp. 1040–1045.
- [207] Felix Schacher, Markus Müllner, Holger Schmalz, and Axel H. E. Müller. *New Block Copolymers with Poly(N,N -dimethylaminoethyl methacrylate) as a Double Stimuli-Responsive Block*. Macromolecular Chemistry and Physics 210.3-4 (2009), pp. 256–262.
- [208] Chandrashekhara R. Haramagatti, Felix H. Schacher, Axel H. E. Müller, and Jürgen Köhler. *Diblock copolymer membranes investigated by single-particle tracking*. Phys. Chem. Chem. Phys. 13.6 (2011), pp. 2278–2284.
- [209] Nobuyuki Otsu. *A Threshold Selection Method from Gray-Level Histograms*. IEEE Transactions on Systems, Man, and Cybernetics 9.1 (1979), pp. 62–66.
- [210] T. Aste and T. Di Matteo. *Emergence of Gamma distributions in granular materials and packing models*. Physical Review E - Statistical, Nonlinear, and Soft Matter Physics 77.2 (2008), pp. 1–8.
- [211] Daniela Stoeckel, Christian Kübel, Kristof Hormann, Alexandra Höltzel, Bernd M. Smarsly, and Ulrich Tallarek. *Morphological Analysis of Disordered Macroporous–Mesoporous Solids Based on Physical Reconstruction by Nanoscale Tomography*. Langmuir 30.30 (2014), pp. 9022–9027.
- [212] Firoozeh Babayekhorasani, Dave E. Dunstan, Ramanan Krishnamoorti, and Jacinta C. Conrad. *Nanoparticle diffusion in crowded and confined media*. Soft Matter 12.40 (2016), pp. 8407–8416.
- [213] E. Marx and G.W. Mulholland. *Size and Refractive Index Determination of Single Polystyrene Spheres*. Journal of Research of the National Bureau of Standards 88.5 (1983), p. 321.
- [214] Chundong Xue, Xu Zheng, Kaikai Chen, Yu Tian, and Guoqing Hu. *Probing Non-Gaussianity in Confined Diffusion of Nanoparticles*. Journal of Physical Chemistry Letters 7.3 (2016), pp. 514–519.
- [215] Andrey G. Cherstvy, Samudrajit Thapa, Caroline E. Wagner, and Ralf Metzler. *Non-Gaussian, non-ergodic, and non-Fickian diffusion of tracers in mucin hydrogels*. Soft Matter 15.12 (2019), pp. 2526–2551.
- [216] Stas Burov, Jae-Hyung Jeon, Ralf Metzler, and Eli Barkai. *Single particle tracking in systems showing anomalous diffusion: the role of weak ergodicity breaking*. Physical Chemistry Chemical Physics 13.5 (2011), p. 1800.

- [217] Zhaolong Shen and Sean B. Andersson. *Tracking nanometer-scale fluorescent particles in two dimensions with a confocal microscope*. IEEE Transactions on Control Systems Technology 19.5 (2011), pp. 1269–1278.
- [218] Zhaolong Shen and Sean B. Andersson. “Tracking multiple fluorescent particles in two dimensions in a confocal microscope”. Vol. 19. 5. IEEE, 2009, pp. 6052–6057. ISBN: 978-1-4244-3871-6.
- [219] Barbara K. Müller, Evgeny Zaychikov, Christoph Bräuchle, and Don C. Lamb. *Pulsed interleaved excitation*. Biophysical Journal 89.5 (2005), pp. 3508–3522.
- [220] D. Lamb, B. Muller, and C. Brauchle. *Enhancing the Sensitivity of Fluorescence Correlation Spectroscopy by Using Time-Correlated Single Photon Counting*. Current Pharmaceutical Biotechnology 6.5 (2005), pp. 405–414.
- [221] Oya Tagit, Dominik Jańczewski, Nikodem Tomczak, Ming Yong Han, Jennifer L. Herek, and G. Julius Vancso. *Nanostructured thermoresponsive quantum dot/PNIPAM assemblies*. European Polymer Journal 46.7 (2010), pp. 1397–1403.
- [222] Samuel T. Jones, Zarah Walsh-Korb, Steven J. Barrow, Sarah L. Henderson, Jesús Del Barrio, and Oren A. Scherman. *The Importance of Excess Poly(*N*-isopropylacrylamide) for the Aggregation of Poly(*N*-isopropylacrylamide)-Coated Gold Nanoparticles*. ACS Nano 10.3 (2016), pp. 3158–3165.
- [223] Wen He, Yefei Ma, Xing Gao, Xiaoxia Wang, Xia Dai, and Jibing Song. *Application of Poly(*N*-isopropylacrylamide) As Thermosensitive Smart Materials*. Journal of Physics: Conference Series 1676.1 (2020).
- [224] Maria Guix, Sonja M. Weiz, Oliver G. Schmidt, and Mariana Medina-Sánchez. *Self-Propelled Micro/Nanoparticle Motors*. Particle and Particle Systems Characterization 35.2 (2018), pp. 1–31.
- [225] Juan Ruben Gomez-Solano, Alex Blokhuis, and Clemens Bechinger. *Dynamics of Self-Propelled Janus Particles in Viscoelastic Fluids*. Physical Review Letters 116.13 (2016), pp. 2–6.
- [226] Christina Kurzthaler, Clémence Devailly, Jochen Arlt, Thomas Franosch, Wilson C.K. Poon, Vincent A. Martinez, and Aidan T. Brown. *Probing the Spatiotemporal Dynamics of Catalytic Janus Particles with Single-Particle Tracking and Differential Dynamic Microscopy*. Physical Review Letters 121.7 (2018), pp. 1–6.
- [227] Naor Granik, Lucien E. Weiss, Elias Nehme, Maayan Levin, Michael Chein, Eran Perlson, Yael Roichman, and Yoav Shechtman. *Single particle diffusion characterization by deep learning*. Biophysical Journal 117.2 (2019), pp. 185–192.
- [228] Yu Matsuda, Itsuo Hanasaki, Ryo Iwao, Hiroki Yamaguchi, and Tomohide Niimi. *Estimation of diffusive states from single-particle trajectory in heterogeneous medium using machine-learning methods*. Physical Chemistry Chemical Physics 20.37 (2018), pp. 24099–24108.
- [229] Patrice Dosset, Patrice Rassam, Laurent Fernandez, Cedric Espenel, Eric Rubinstein, Emmanuel Margeat, and Pierre Emmanuel Milhiet. *Automatic detection of diffusion modes within biological membranes using back-propagation neural network*. BMC Bioinformatics 17.1 (2016), pp. 1–12.
- [230] Patrycja Kowalek, Hanna Loch-Olszewska, and Janusz Szwabiński. *Classification of diffusion modes in single-particle tracking data: Feature-based versus deep-learning approach*. Physical Review E 100.3 (2019), pp. 1–13.

-
- [231] Elbert Hendricks, Ole Jannerup, and Paul Haase Sørensen. *Linear Systems Control*. Springer Berlin Heidelberg, 2008, pp. 1–555. ISBN: 978-3-540-78485-2.
- [232] H.H. Rosenbrock. *Transfer-function matrixes*. Electronics Letters 2.9 (1966), p. 331.
- [233] C. M. Cheng, Z. K. Peng, W. M. Zhang, and G. Meng. *Volterra-series-based non-linear system modeling and its engineering applications: A state-of-the-art review*. Mechanical Systems and Signal Processing 87.March 2016 (2017), pp. 340–364.
- [234] Harvey Scher and Elliott W. Montroll. *Anomalous transit-time dispersion in amorphous solids*. Physical Review B 12.6 (1975), pp. 2455–2477.
- [235] Elliott W. Montroll and George H. Weiss. *Random Walks on Lattices. II*. Journal of Mathematical Physics 6.2 (1965), pp. 167–181.
- [236] I. Y. Wong, M. L. Gardel, D. R. Reichman, Eric R. Weeks, M. T. Valentine, A. R. Bausch, and D. A. Weitz. *Anomalous diffusion probes microstructure dynamics of entangled F-actin networks*. Physical Review Letters 92.17 (2004), pp. 30–33.
- [237] Harvey Scher, Gennady Margolin, and Brian Berkowitz. *Towards a unified framework for anomalous transport in heterogeneous media*. Chemical Physics 284.1-2 (2002), pp. 349–359.
- [238] Marco Dentz, Andrea Cortis, Harvey Scher, and Brian Berkowitz. *Time behavior of solute transport in heterogeneous media: Transition from anomalous to normal transport*. Advances in Water Resources 27.2 (2004), pp. 155–173.
- [239] Tomasz Gubiec and Ryszard Kutner. *Backward jump continuous-time random walk: An application to market trading*. Physical Review E - Statistical, Nonlinear, and Soft Matter Physics 82.4 (2010), pp. 1–10.
- [240] Ralf Metzler and Joseph Klafter. *The restaurant at the end of the random walk: Recent developments in the description of anomalous transport by fractional dynamics*. Journal of Physics A: Mathematical and General 37.31 (2004).
- [241] W. R. Schneider and W. Wyss. *Fractional diffusion and wave equations*. Journal of Mathematical Physics 30.1 (1989), pp. 134–144.
- [242] Eli Barkai, Ralf Metzler, and Joseph Klafter. *From continuous time random walks to the fractional Fokker-Planck equation*. Physical Review E 61.1 (2000), pp. 132–138.
- [243] Ralf Metzler and Joseph Klafter. *The random walk’s guide to anomalous diffusion: a fractional dynamics approach*. Physics Reports 339.1 (2000), pp. 1–77.
- [244] Enrico Scalas, Rudolf Gorenflo, and Francesco Mainardi. *Uncoupled continuous-time random walks: Solution and limiting behavior of the master equation*. Physical Review E - Statistical Physics, Plasmas, Fluids, and Related Interdisciplinary Topics 69.1 (2004), p. 8.
- [245] Daniel Fulger, Enrico Scalas, and Guido Germano. *Monte Carlo simulation of uncoupled continuous-time random walks yielding a stochastic solution of the space-time fractional diffusion equation*. Physical Review E - Statistical, Nonlinear, and Soft Matter Physics 77.2 (2008), pp. 1–7.
- [246] Jae Hyung Jeon, Eli Barkai, and Ralf Metzler. *Noisy continuous time random walks*. Journal of Chemical Physics 139.12 (2013).

- [247] Benoit B. Mandelbrot and John W. Van Ness. *Fractional Brownian Motions, Fractional Noises and Applications*. SIAM Review 10.4 (1968), pp. 422–437.
- [248] Abdelnaser Adas. *Traffic models in broadband networks*. IEEE Communications Magazine 35.7 (1997), pp. 82–89.
- [249] Will E. Leland, Murad S. Taqqu, and Daniel V. Wilson. *On the Self-Similar Nature of Ethernet Traffic (Extended Version)*. IEEE/ACM Transactions on Networking 2.1 (1994), pp. 1–15.
- [250] J. Lévy Véhel and R. Riedi. *Fractional Brownian motion and data traffic modeling: The other end of the spectrum*. Fractals in Engineering (1997), pp. 185–202.
- [251] Jedrzej Szymanski and Matthias Weiss. *Elucidating the origin of anomalous diffusion in crowded fluids*. Physical Review Letters 103.3 (2009), pp. 1–4.
- [252] S. Rostek and R. Schöbel. *A note on the use of fractional Brownian motion for financial modeling*. Economic Modelling 30.1 (2013), pp. 30–35.
- [253] Wei Lin Xiao, Wei Guo Zhang, Xi Li Zhang, and Ying Luo Wang. *Pricing currency options in a fractional Brownian motion with jumps*. Economic Modelling 27.5 (2010), pp. 935–942.
- [254] Jae-Hyung Jeon and Ralf Metzler. *Fractional Brownian motion and motion governed by the fractional Langevin equation in confined geometries*. Physical Review E - Statistical, Nonlinear, and Soft Matter Physics 81 (2010), pp. 1–11.
- [255] J. R.M. Hosking. *Modeling persistence in hydrological time series using fractional differencing*. Water Resources Research 20.12 (1984), pp. 1898–1908.
- [256] Eric Lutz. *Fractional Langevin equation*. Physical Review E - Statistical Physics, Plasmas, Fluids, and Related Interdisciplinary Topics 64.5 (2001), p. 4.
- [257] Trifce Sandev. *Generalized Langevin Equation and the Prabhakar Derivative*. Mathematics 5.4 (2017), p. 66.
- [258] H. Qian and Elliot L. Elson. *Analysis of confocal laser-microscope optics for 3-D fluorescence correlation spectroscopy*. Applied optics 30.10 (1991), pp. 1185–95.
- [259] R. Rigler, Ü . Mets, J. Widengren, and P. Kask. *Fluorescence correlation spectroscopy with high count rate and low background: analysis of translational diffusion*. European Biophysics Journal 22.3 (1993), pp. 169–175.
- [260] Travis E. Oliphant. *Guide to NumPy*. Vol. 17. 3. 2006, pp. 209–224.
- [261] Eric Jones, Travis Oliphant, and Pearu Peterson. *SciPy: Open source scientific tools for Python*. 2001.
- [262] Matthew Newville, Till Stensitzki, Daniel B. Allen, and Antonino Ingargiola. *LM-FIT: Non-Linear Least-Square Minimization and Curve-Fitting for Python*. 2014.
- [263] Wes McKinney. *Data Structures for Statistical Computing in Python*. Proc. of the 9th Python Science Conference (SCIPY 2010) (2010), pp. 51–56.
- [264] J. G. Ziegler and N. B. Nichols. *Optimum settings for automatic controllers*. InTech 42.6 (1995), pp. 94–100.
- [265] G. H. Cohen and G. A. COON. *Theoretical Consideration of Retarded Control*. Transactions of ASME 75 (1953), pp. 827–834.

-
- [266] Guo Ying Gu, Li Min Zhu, Chun Yi Su, and Han Ding. *Motion control of piezoelectric positioning stages: Modeling, controller design, and experimental evaluation*. IEEE/ASME Transactions on Mechatronics 18.5 (2013), pp. 1459–1471.
- [267] Jie Ling, Zhao Feng, Min Ming, and Xiaohui Xiao. *Model reference adaptive damping control for a nanopositioning stage with load uncertainties*. Review of Scientific Instruments 90.4 (2019), p. 045101.
- [268] Yu Xie, Jing Li Fu, and Ben Yong Chen. *Parameter identification of hysteresis nonlinear dynamic model for piezoelectric positioning system based on the improved particle swarm optimization method*. Advances in Mechanical Engineering 9.6 (2017), pp. 1–12.
- [269] Yuen Kuan Yong, Sumeet S. Aphale, and S. O. Reza Moheimani. *Design, analysis and control of a fast nanopositioning stage*. IEEE/ASME International Conference on Advanced Intelligent Mechatronics, AIM August (2008), pp. 451–456.
- [270] Fu Cheng Wang, Yan Chen Tsai, Chin Hui Hsieh, Lian Sheng Chen, and Chung Huang Yu. *Robust control of a two-axis piezoelectric nano-positioning stage*. Vol. 44. 1 PART 1. IFAC, 2011, pp. 3539–3544. ISBN: 9783902661937.
- [271] Pankaj Mehta, Marin Bukov, Ching Hao Wang, Alexandre G.R. Day, Clint Richardson, Charles K. Fisher, and David J. Schwab. *A high-bias, low-variance introduction to Machine Learning for physicists*. Physics Reports 810 (2019), pp. 1–124.
- [272] Sumeet S. Aphale, Santosh Devasia, and S. O. Reza Moheimani. *High-bandwidth control of a piezoelectric nanopositioning stage in the presence of plant uncertainties*. Nanotechnology 19.12 (2008).
- [273] Chih Jer Lin and Po Ting Lin. *Tracking control of a biaxial piezo-actuated positioning stage using generalized Duhem model*. Computers and Mathematics with Applications 64.5 (2012), pp. 766–787.
- [274] Linlin Li, Guoying Gu, and LiMin Zhu. *Fractional repetitive control of nanopositioning stages for tracking high-frequency periodic inputs with nonsynchronized sampling*. Review of Scientific Instruments 90.5 (2019), p. 055108.
- [275] Andrew J. Fleming. *Nanopositioning system with force feedback for high-performance tracking and vibration control*. IEEE/ASME Transactions on Mechatronics 15.3 (2010), pp. 433–447.
- [276] Kenneth Levenberg. *A method for the solution of certain non-linear problems in least squares*. Quarterly of Applied Mathematics 2.2 (1944), pp. 164–168.
- [277] Donald W. Marquardt. *An Algorithm for Least-Squares Estimation of Nonlinear Parameters*. Journal of the Society for Industrial and Applied Mathematics 11.2 (1963), pp. 431–441.
- [278] Michael Wahl, Ingo Gregor, Mattias Patting, and Jörg Enderlein. *Fast calculation of fluorescence correlation data with asynchronous time-correlated single-photon counting*. Optics express 11.26 (2003), pp. 3583–91.
- [279] Emanuel Eichhammer. *QCustomPlot - Qt C++ widget for plotting and data visualization, Version 2.0.0*. 2019.